Ligand assisted molecular electrocatalysis and molecular charge storage

विद्या वाचस्पति की
उपाधि की अपेक्षाओं की आंशिक पूर्ति में प्रस्तुत शोध प्रबंध

A thesis submitted in partial fulfillment of the requirements of the degree of Doctor of Philosophy

द्वारा / By

संचयिता मुखोपाध्याय / Sanchayita Mukhopadhyay

पंजीकरण सं. / Registration No.:
20183605

शोध प्रबंध पर्यवेक्षक / Thesis Supervisor:
Prof. Muhammed Musthafa O. T.

भारतीय विज्ञान शिक्षा एवं अनुसंधान संस्थान पुणे
INDIAN INSTITUTE OF SCIENCE EDUCATION AND RESEARCH PUNE
2024

Dedicated to my

beloved parents

CERTIFICATE

Certified that the work incorporated in the thesis entitled **"Ligand assisted molecular electrocatalysis and molecular charge storage"** Submitted by **Ms. Sanchayita Mukhopadhyay** was carried out by the candidate, under my supervision. The work presented here or any part of it has not been included in any other thesis submitted previously for the award of any degree or diploma from any other University or institution.

Prof. Muhammed Musthafa O. T.   **Date: 11th April, 2024**

Associate Professor,

Department of Chemistry,

IISER Pune

Declaration by Student

Name of Student: **Sanchayita Mukhopadhyay**

Reg. No.: **20183605**

Thesis Supervisor(s): **Muhammed Musthafa O. T.**

Department: **Chemistry**

Date of joining program: **01/08/2018**

Date of Pre-Synopsis Seminar: **09/11/2023**

Title of Thesis: **Ligand assisted molecular electrocatalysis and molecular charge storage**

I declare that this written submission represents my idea in my own words and where others' ideas have been included; I have adequately cited and referenced the original sources. I declare that I have acknowledged collaborative work and discussions wherever such work has been included. I also declare that I have adhered to all principles of academic honesty and integrity and have not misrepresented or fabricated or falsified any idea/data/fact/source in my submission. I understand that violation of the above will be cause for disciplinary action by the Institute and can also evoke penal action from the sources which have thus not been properly cited or from whom proper permission has not been taken when needed.

The work reported in this thesis is the original work done by me under the guidance of

Dr./Prof. **Muhammed Musthafa O. T.**

Date: **11/04/2024**

Signature of the student:

ACKNOWLEDGEMENTS

The successful culmination of my doctoral thesis was made possible through the invaluable guidance and support extended by a multitude of individuals. I wish to extend my sincere appreciation to a select group, though my profound gratitude encompasses all those who played pivotal roles in transforming this envisioned achievement into a tangible reality.

Firstly, I extend my deepest thanks to my supervisor, Dr. Muhammed Musthafa O. T., for his unwavering support and guidance throughout my Ph.D. journey. His provision of excellent lab facilities and a conducive working environment, along with the freedom to explore various projects, has been invaluable. I am grateful for his scientific insights, patient mentorship, and constructive feedback, which have shaped me into an independent thinker. His emphasis on technical proficiency and scientific ethics, conveyed through one-on-one meetings and informal discussions, has been instrumental in my development as a researcher and a responsible individual.

I also express my sincere gratitude and respect to my RAC members, Prof. V. G. Anand from IISER Pune and Prof C.P. Vinod from NCL Pune, for their continuous support and invaluable scientific inputs during the past four years, particularly in RAC meetings. I extend my deepest regards to former director Prof. Jayant Udgaonkar and current director Prof. Sunil Bhagwat for providing cutting-edge facilities, robust research infrastructure, and a vibrant academic atmosphere at the institute. I am thankful to IISER Pune MHRD for the Ph.D. fellowship over the last five years, as well as to the faculties of the chemistry and physics departments for providing their support with various instrument facilities in their labs.

The accomplishment of this work owes much to the unwavering assistance and backing extended by my lab mates, both current and former. I express deep appreciation to a remarkable group of seniors in my lab, namely Dr.

Table of Contents

Synopsis of the thesis entitled "Ligand assisted molecular electrocatalysis and molecular charge storage"

The widespread global energy crisis, primarily caused by the extensive use of fossil fuels, has turned renewable energy conversion into a critical focus for the international scientific community. Within this context, electrochemical transformation through electrocatalysis has garnered significant research attention for its potential to convert abundant feedstocks into valuable products.[1-3] Consequently, there has been a concerted effort in designing and developing various metal-based and molecular electrocatalysts.[4,5] Molecular electrocatalysts such as phthalocyanines and porphyrins have gained a lot of attention mainly because of their superior chemical and thermal stability and highly flexible optoelectronic nature.[6-8] In electrochemical processes using molecular systems, the eventual fate of the process is often dictated by the central metal ion and therefore, little attention has been paid on the contribution of the surrounding ligand.[9-12] In these lines, the central objective of this thesis is to unveil the distinct impact of ligands on both electrocatalysis and charge storage, utilizing cobalt as the consistent central metal ion. The investigation explores the role of ligands by varying the nature as well as isomerization of ligands in the N_4 macrocyclic framework during challenging electrochemical processes. The thesis is structured into seven chapters.

The first Chapter emphasizes the significance of N_4 macrocyclic complexes, particularly focusing on the electrochemical properties of metal phthalocyanines. It delves into detailed discussions on their pivotal roles in

diverse electrocatalytic transformations and supercapacitive charge storage. The chapter highlights the influence of the central metal ion in modulating molecular electrocatalysis and charge storage, drawing attention to existing gaps in understanding the structure-activity and structure-charge storage relationships in the context of the ligands.

The second Chapter elucidates the synthesis process of $-NO_2$, $-COOH$, and $-NH_2$ substituted phthalocyanine molecules, α-NO_2 and β-NO_2 substituted isomeric phthalocyanine molecules along with unsubstituted phthalocyanine molecules, **Figure 1**. The discussion extends to the integration of these molecules on carbon-supported platforms, encompassing applications in electrocatalysis, metal-air batteries and molecular charge storage. The chapter also delves into the utilization of various physico-chemical techniques for characterizing the synthesized compounds.

M = Co, Ni, Cu, Fe

X , Y = NO_2 , COOH , NH_2
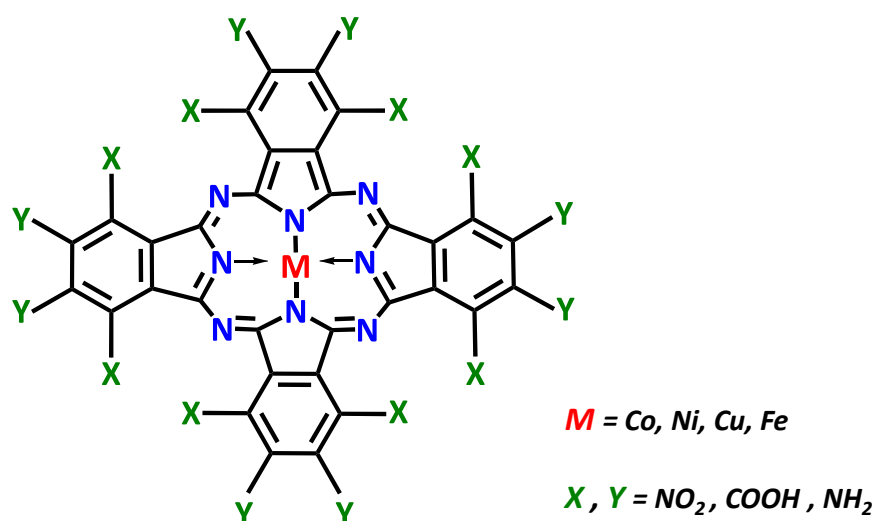
Figure 1. Structure of metal phthalocyanine where M represents the central metal and X and Y represents the α and β positions in the macrocyclic ring respectively where functionalities can be attached.

Synopsis

The third Chapter provides insight into the influence of regioisomerism of ligands on tuning the reaction kinetics and mechanisms of oxygen reduction reaction (ORR) and oxygen evolution Reaction (OER) around the same catalytic Co centre. The oxidative activation observed in the β-isomeric electrocatalyst, attributed to the combined presence of –R and –I effects, in contrast to the diminishing -R effect in the α-isomeric electrocatalyst, significantly enhances the kinetics of both ORR and OER in the former. This chapter also showcases the practical applicability of ligand isomerism in electrocatalysis by integrating them in an aqueous Zn-air battery system. The results such as polarisation curve, charge-discharge cycling, in-situ mass spectrometry data highlight the β-isomer outperforms the α-isomer, exhibiting superior charging voltage, round-trip efficiency, and excellent cycling stability, **Figure 2**.
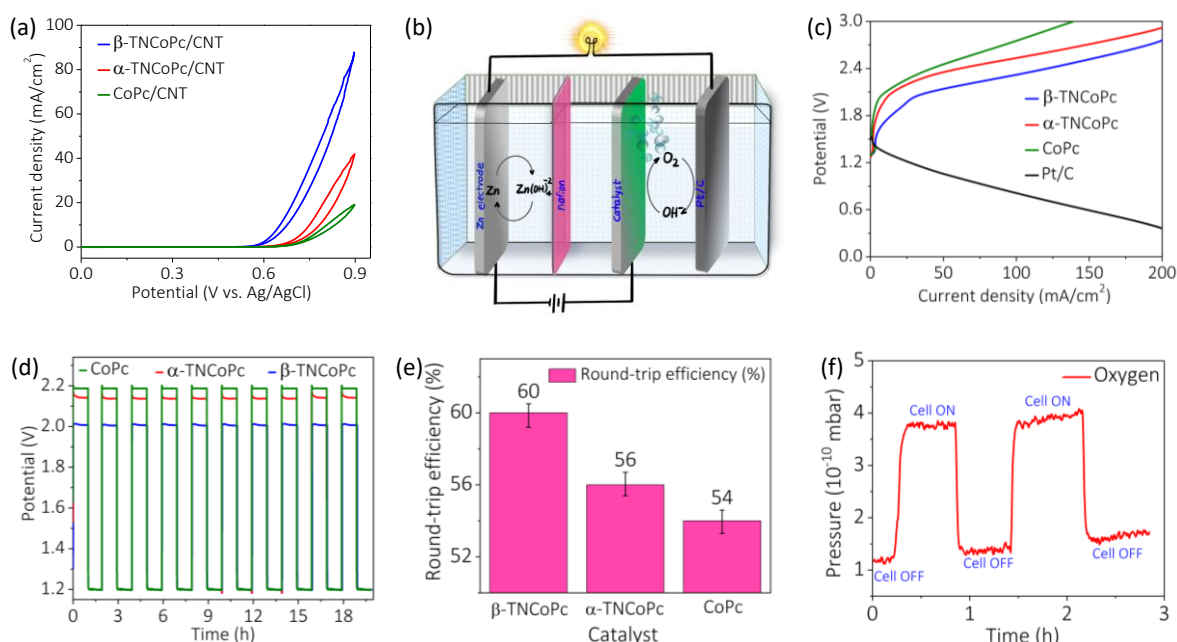
Figure 2. (a) Cyclic voltammograms for oxygen evolution reaction with CoPc, α-TNCoPc and β-TNCoPc isomeric molecules in pH=14 electrolyte at a scan

---

rate of 10mV/s. (b) Tri-electrode configuration for a rechargeable Zn-air battery. (c) Charge-discharge profiles of rechargeable zinc–air battery. Discharge (black) and charge (blue, red, green) polarization curves were obtained with Pt/C as the ORR catalyst and β-TNCoPc, α-TNCoPc and unsubstituted CoPc as the OER catalysts respectively. (d) Charge-discharge cycling data for zinc–air battery with the isomeric molecular electrocatalysts at a current density of 20 mA/cm^2. (e) Comparison of the round-trip efficiency at a current density of 20 mA/cm^2 for unsubstituted CoPc, α-TNCoPc and β-TNCoPc isomers. (f) In-situ electrochemical mass spectrometry with β-TNCoPc isomer during the charge chemistry of Zn-air battery demonstrating the sustainability in oxygen evolution.

The fourth Chapter showcases how the nature of the ligand contributes counterintuitively to electrocatalysis through a proton charge assembly during water oxidation and chlorine evolution reactions. To understand the pristine behaviour of the molecular platform, quartz crystal microbalance (QCM) technique was used to study the monolayer of the carboxy, nitro and unsubstituted CoPc molecules. Contrary to the position in the spectrochemical series, the catalytic entity with the carboxy-functionalized ligand exhibited higher electrochemical activity compared to the more electron-withdrawing nitro-functionalized ligand. Various analyses including zeta potential measurements and XPS studies indicate a higher degree of proton charge assembly on the carboxy ligand that in turn facilitates the enrichment of catalytically active species in the corresponding central metal, **Figure 3**. This study demonstrates that merely selecting a ligand based on the spectrochemical series may not suffice; its interaction with the surrounding medium must also be taken into consideration to fully exploit the maximum potential of the molecules in electrocatalysis.
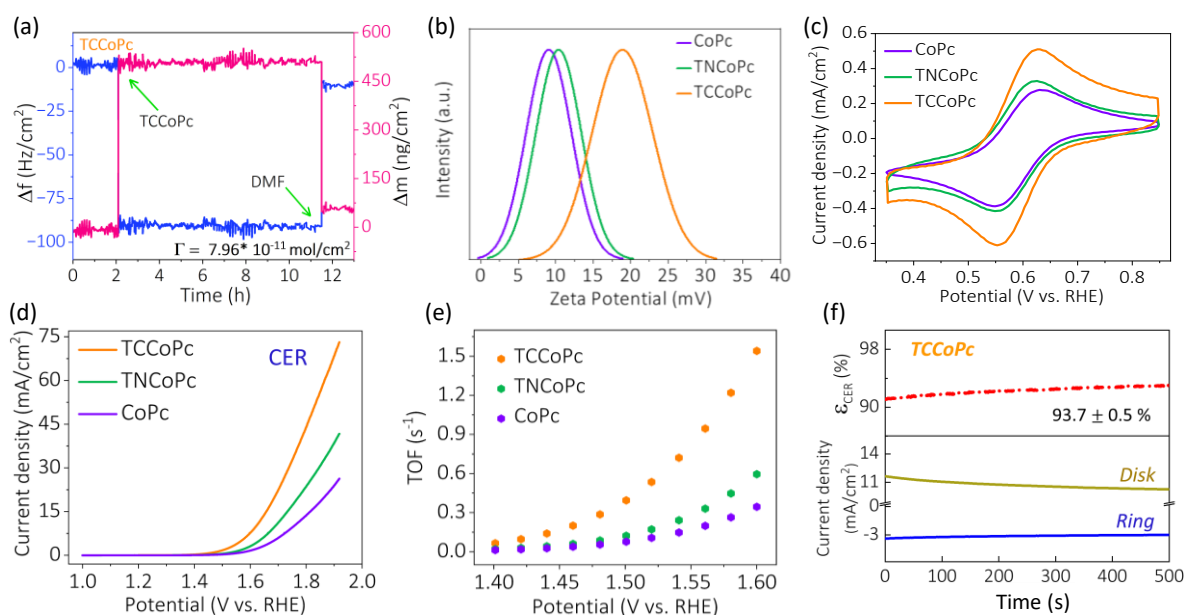
Figure 3. (a) Quartz crystal microbalance (QCM) profile during the adsorption of the molecules from a 0.5 mM solution of TCCoPc in dimethyl formamide (DMF). Blue trace shows the frequency change during adsorption and the pink trace shows the mass change calculated using Saurbrey equation. Surface coverage (Γ) value of TCCoPc molecule is provided in the image. (b) Zeta potential measurement in acidic medium and (c) Cyclic voltammogram in 0.1 M $HClO_4$ medium collected at a scan rate of 20 mV/s for 10 mM ferricyanide solution with CoPc, TNCoPc and TCCoPc molecules. (d) Linear sweep voltammograms (LSV) recorded at a scan rate of 10 mV/s at a rotation rate of 1600 rpm for chlorine evolution reaction (CER) in 0.1 M $HClO_4$ solution containing 1 M NaCl and (e) Calculated turnover frequencies (TOFs) for CER with CoPc, TNCoPc and TCCoPc molecules. (f) Efficiency of CER for TCCoPc molecule obtained with hydrodynamic method.

The fifth Chapter illustrates how a ligand functionality devoid of any redox activity can enhance the charge storage capability of the electric double layer through a non-electrochemical proton charge assembly. The double layer charge storage is found to be higher for carboxy and amine substituted molecules to nearly similar extents compared to nitro substituted and unsubstituted molecule, which is augmented to the extensive proton charge

assembly in the former molecular platforms in acidic medium. Consequently, there is a higher local density of anions in the electric double layer (EDL), which enhances the energy density of the supercapacitor device without compromising its power capability. Galvanostatic charge-discharge study along with impedance analysis demonstrated carboxy substituted molecule to be a better supercapacitive platform than unsubstituted molecule, **Figure 4**. The showcased enhancement of supercapacitive charge storage through proton charge assembly by non-redox active functionalities contributes to the rational design of ligands for energy storage applications.
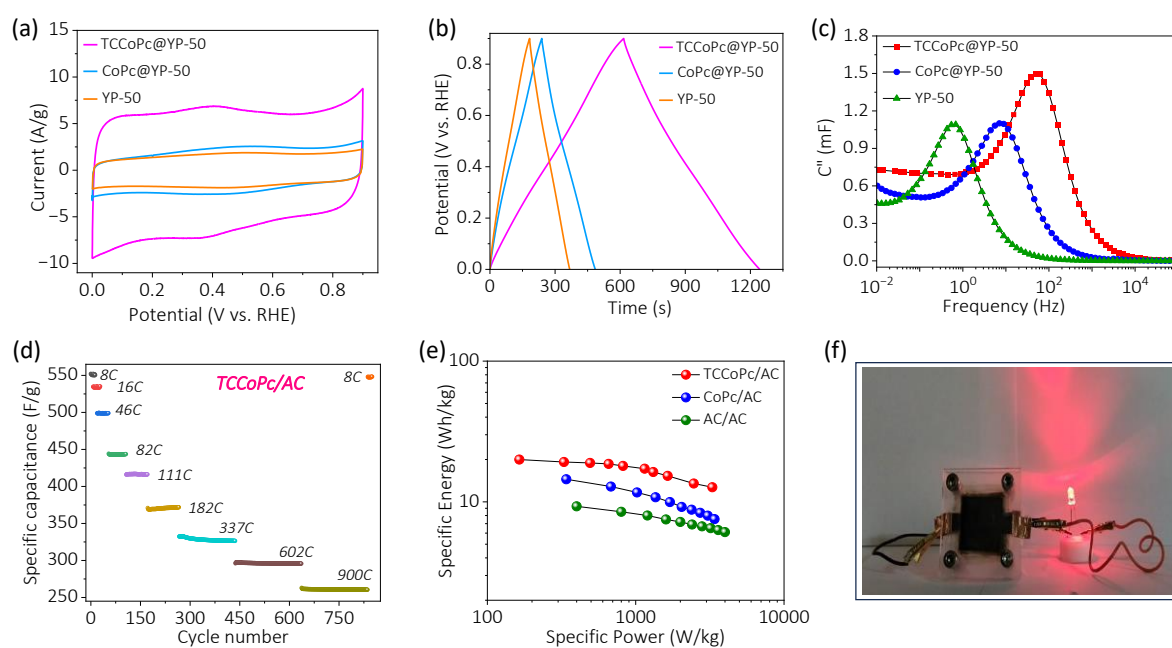
Figure 4. (a) Cyclic voltammograms (CVs) at a scan rate of 5mV/s and (b) galvanostatic charge-discharge at a current rate of 1A/g for YP-50 and its composites namely CoPc@YP-50 and TCCoPc@YP-50. (c) Plot of the imaginary part of capacitance (C″) vs. frequency acquired in the frequency range of 100 kHz to 5 mHz with a 10 mV (peak to peak) AC excitation signal at the open circuit voltage (OCV). (d) Capacity retention plot for the TCCoPc/AC split cell with increasing C rates. The rate is brought back to 8C after cycling it up to a high rate of 900C. (e) Ragone plots for the

asymmetric two-electrode split cell. (f) Practical viability of the device is shown by powering a 2 V LED with the TCCoPc/AC split cell.

The sixth Chapter presents a unique finding with carboxy-functionalized cobalt phthalocyanine (TCCoPc) in the context of the oxygen reduction reaction (ORR) in aqueous medium. Typically, ORR in such conditions follows either a 2-electron or 4-electron pathway, resulting in peroxide or water as the main products, respectively. However, the combination of this ligand and Co central metal (TCCoPc) surprisingly leads to a 1-electron ORR, forming superoxide in aqueous medium. Hydrodynamic voltammetric techniques, including rotating disk electrode (RDE) and rotating ring disk electrode (RRDE), support the evidence of superoxide ion formation with TCCoPc. Notably, this 1-electron ORR phenomenon is unique to the cobalt and carboxy combination and not observed with other carboxy-substituted transition metal phthalocyanines namely (Fe, Ni, and Cu), **Figure 5,** suggesting an interplay between the nature of the ligand and nature of the central metal.
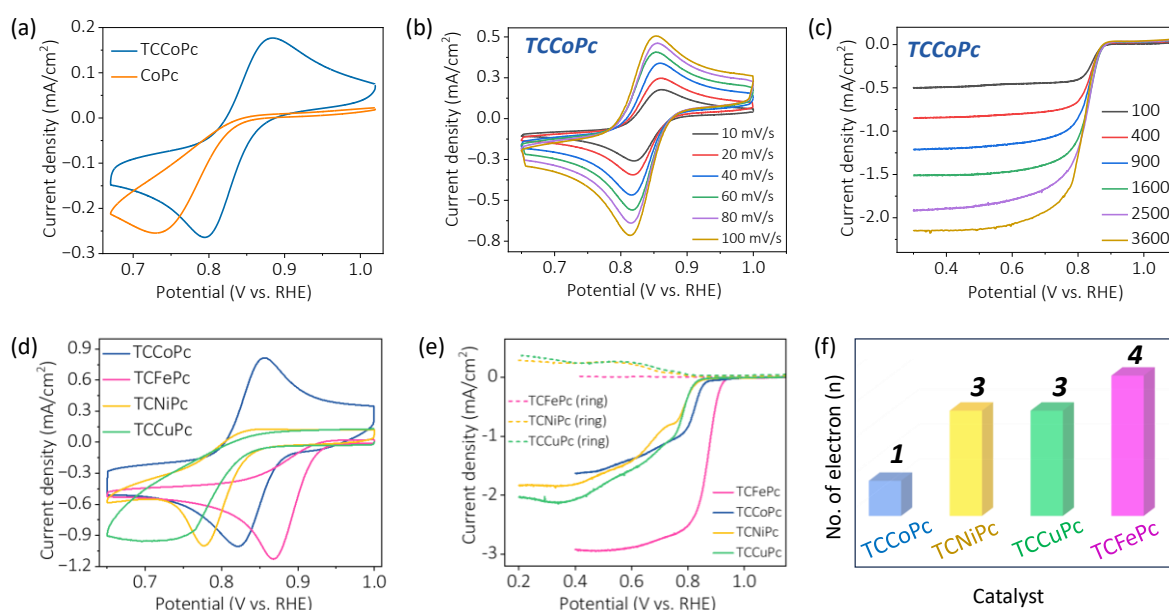
Figure 5. (a) Cyclic voltammograms of CoPc and TCCoPc molecules in 1 M KOH at a scan rate of 10mV/s. (b) Scan rate dependence study of TCCoPc molecule in 1 M KOH at various scan rates ranging from 10 mV/s to 100 mV/s. (c) RDE measurement for ORR with TCCoPc at various rotation rates of 100 to 3600 rpm at a scan rate of 5 mV/s in 1 M KOH. (d) Comparison of cyclic voltammograms of different metal carboxy molecules namely carboxy substituted Fe (TCFePc), Co (TCCoPc), Ni (TCNiPc) and Cu (TCCuPc) phthalocyanines at a scan rate of 10 mV/s in 1 M KOH. (e) RRDE study at a rotation rate of 1600 rpm with TCFePc, TCCoPc, TCNiPc and TCCuPc molecules. (f) Bar diagram showing number of electrons for ORR with TCFePc, TCCoPc, TCNiPc and TCCuPc molecules.

The seventh Chapter summarizes the work with a future outlook. The work presented in this thesis reveals the importance of ligand in the field of electrocatalysis as well as charge storage in molecular systems, Scheme 1. While the central metal ion significantly influences electrocatalysis and charge storage, the ligand-induced contribution provides a distinctive avenue to exploit the molecule's maximum potential for complex electrochemical transformations and charge storage applications. Moreover, the structure-activity relations of molecules remain incomplete without considering the role of the ligand, as demonstrated by its significant impact. It is imperative to emphasize that this phenomenon lacks generalizability across the spectrochemical series, as the correlation is distinct for each substituent. This underscores the necessity for meticulous investigations at the molecular level for individual substituents to comprehend their specific activity or charge storage relationships. This is principally due to non-electrochemical interactions frequently intertwining the molecule's electrochemical properties with the nature of the functionality as well as its

surrounding medium, as elucidated in this thesis. These interactions typically manifest as substituent-specific, presenting a myriad of prospects for researchers within the molecular electrocatalysis and charge storage domain. The elucidation of metal-ligand activity relationships, in tandem with the influence of the surrounding medium, within N_4-macrocyclic molecules, is expected to remedy deficiencies and knowledge gaps in their structure-activity correlations. This contribution is expected to notably propel the evolution of next-generation electrodes applicable to electrocatalysis and energy storage and conversion devices.

Scheme 1. The role of ligand in molecular electrocatalysis and charge storage.

Synopsis

References:

[1]   Tang, C.; Zheng, Y.; Jaroniec, M.; Qiao, S. Z. Electrocatalytic Refinery for Sustainable Production of Fuels and Chemicals. *Angew. Chemie - Int. Ed.* **2021**, *60* (36), 19572–19590.

[2]   Lucas, F. W. S.; Grim, R. G.; Tacey, S. A.; Downes, C. A.; Hasse, J.; Roman, A. M.; Farberow, C. A.; Schaidle, J. A.; Holewinski, A. Electrochemical Routes for the Valorization of Biomass-Derived Feedstocks: From Chemistry to Application. *ACS Energy Lett.* **2021**, *6* (4), 1205–1270.

[3]   Martín, A. J.; Pérez-Ramírez, J. Heading to Distributed Electrocatalytic Conversion of Small Abundant Molecules into Fuels, Chemicals, and Fertilizers. *Joule* **2019**, *3* (11), 2602–2621.

[4]   (1)   Lee, B.-H.; Shin, H.; Rasouli, A. S.; Choubisa, H.; Ou, P.; Dorakhan, R.; Grigioni, I.; Lee, G.; Shirzadi, E.; Miao, R. K.; Wicks, J.; Park, S.; Lee, H. S.; Zhang, J.; Chen, Y.; Chen, Z.; Sinton, D.; Hyeon, T.; Sung, Y.-E.; Sargent, E. H. Supramolecular Tuning of Supported Metal Phthalocyanine Catalysts for Hydrogen Peroxide Electrosynthesis. *Nat. Catal.* **2023**, *6* (3), 234–243.

[5]   Zhong, H.; Wang, M.; Ghorbani-Asl, M.; Zhang, J.; Ly, K. H.; Liao, Z.; Chen, G.; Wei, Y.; Biswal, B. P.; Zschech, E.; Weidinger, I. M.; Krasheninnikov, A. V; Dong, R.; Feng, X. Boosting the Electrocatalytic Conversion of Nitrogen to Ammonia on Metal-Phthalocyanine-Based Two-Dimensional Conjugated Covalent Organic Frameworks. *J. Am. Chem. Soc.* **2021**, *143* (47), 19992–20000.

[6]   Costentin, C.; Savéant, J.-M. Towards an Intelligent Design of Molecular Electrocatalysts. *Nat. Rev. Chem.* **2017**, *1* (11), 87.

[7]   Sobbi, A. K.; Wöhrie, D.; Schlettwein, D. Photochemical Stability of Various Porphyrins in Solution and as Thin Film Electrodes. *J. Chem. Soc. Perkin Trans. 2* **1993**, No. 3, 481–488.

[8]   Bottari, G.; de la Torre, G.; Guldi, D. M.; Torres, T. Covalent and Noncovalent Phthalocyanine-Carbon Nanostructure Systems:

Synthesis, Photoinduced Electron Transfer, and Application to Molecular Photovoltaics. *Chem. Rev.* **2010**, *110* (11), 6768–6816.

[9] Cao, R.; Thapa, R.; Kim, H.; Xu, X.; Kim, M. G.; Li, Q.; Park, N.; Liu, M.; Cho, J. Promotion of Oxygen Reduction by a Bio-Inspired Tethered Iron Phthalocyanine Carbon Nanotube-Based Catalyst. *Nat. Commun.* **2013**, *4*, 1–7.

[10] Fukuzumi, S.; Lee, Y. M.; Nam, W. Mechanisms of Two-Electron versus Four-Electron Reduction of Dioxygen Catalyzed by Earth-Abundant Metal Complexes. *ChemCatChem* **2018**, *10* (1), 9–28.

[11] Chen, K.; Cao, M.; Ni, G.; Chen, S.; Liao, H.; Zhu, L.; Li, H.; Fu, J.; Hu, J.; Cortés, E.; Liu, M. Nickel Polyphthalocyanine with Electronic Localization at the Nickel Site for Enhanced CO2 Reduction Reaction. *Appl. Catal. B Environ.* **2022**, *306*, 121093.

[12] Kusama, S.; Saito, T.; Hashiba, H.; Sakai, A.; Yotsuhashi, S. Crystalline Copper (II) Phthalocyanine Catalysts for Electrochemical Reduction of Carbon Dioxide in Aqueous Media. *ACS Catal.* **2017**, *7* (12), 8382–8385.

Chapter 1

Introduction

Chapter 1

Given the pivotal roles of electrocatalysts in critical domains such as energy conversion/storage, analytical chemistry, and green chemistry, considerable focus has been directed toward unraveling their structure to activity relationships.[1–6] Among various types of electrocatalysts, the activity of the conventional electrocatalysts can be enhanced by interfacial modifications, engineering the surface-to-volume ratio, modified synthetic strategies to expose highly reactive crystal planes, etc. Often, these electrocatalysts are based on precious metals like platinum, palladium, ruthenium, iridium, etc.[7, 8] Molecular electrocatalysts having the N_4 macrocyclic framework such as metal phthalocyanines, metal porphyrins, and similar molecules (MN_4 electrocatalysts) supported on carbon and graphitic structures have been widely investigated as viable non-precious molecular electrocatalysts for a wide range of electrochemical applications, biosensing applications, energy storage applications and many more due to their chemical and thermal stabilities and highly tunable optoelectronic properties.[3, 9,10] Their redox processes are often very fast involving minimal reorganizational energies and can function as redox mediators in electron transfer processes involving a great variety of substrates.[11–13] This chapter presents an overview of N_4 macrocyclic systems, focusing on their electrochemical aspects, including electrocatalysis and charge storage. The chapter emphasizes the existing inadequacies and knowledge gaps in understanding their structure-activity relations. Through approaches based on electrochemical and spectroscopic analyses, a ligand structure-activity relation is elucidated in molecular electrocatalysis and charge storage, that

in turn contributes to the evolution of less obvious ligands to be indispensable in electrochemical processes.

1.1. N$_4$ macrocyclic metal complexes:

Delving into the captivating realm of N$_4$ macrocyclic metal complexes (MN$_4$), illustrated by Figure 1.1 featuring Metalloporphyrins (MPs) and metallophthalocyanines (MPcs), unveils a symphony of unique physical, chemical, and spectral attributes.[14–16] These 18 π-electron aromatic macrocycles, adorned with intricate structural features, transcend scientific boundaries, finding purpose in optical, photochemical, coordination, catalytic, and electrochemical domains.[15] The enchantment intensifies as we explore the reversible redox chemistry of N$_4$ metal macrocyclic complexes, strategically immobilized on diverse electrode surfaces, unveiling myriad electrochemical possibilities.[14,15] In a harmonious convergence of structure and function, phthalocyanines emerge as versatile molecular models, illuminating the physicochemical intricacies of both synthetic and naturally occurring MN$_4$ complexes, particularly captivating the scientific landscape of electrochemistry.

The fundamental distinction between porphyrin and phthalocyanine rings lies in their respective structures. Porphyrins form from the cyclization of four pyrrole rings linked by methine (=CH-) bridges, while phthalocyanines boast imine (=N-) bridges and a fused benzene ring at the 3, 4 positions of the pyrrole rings.[15] Both macrocycles exhibit a square planar coordination site with four-fold axial symmetry, allowing chelation with various ions.[15–18] The robust equatorial bonds enable the delocalization

of metal electronic density across the π-system, influencing axial ligands and enhancing catalytic and electrocatalytic processes.[12,15,17] In phthalocyanines, specific structural features, such as electronegative nitrogen atoms at meso-positions and an expanded π-aromatic system, contribute unique electronic, charge transfer, and redox properties.

The foundational structure of N_4 macrocyclic systems, as depicted in Figure 1.1, is amenable to modification through substituents at the ring periphery. Phthalocyanines undergo substitution at the carbon atoms of the fused benzene ring, while porphyrins offer dual possibilities: substitution at the meso- and/or beta pyrrolic positions. These tailored modifications impart specific physicochemical properties, providing precise control over the interactions and behavior of these macrocyclic derivatives. [15,18] Inspired by biological systems, which serve as models for organizing structures in complex systems, this adaptability leads to the creation of functional molecular machines.[15] Metallophthalocyanines, synthetic counterparts closely mirroring metalloporphyrins, display enhanced attributes like low flexibility, increased thermal stability, solubility, and improved electronic conductivity, making them efficacious electron transfer mediators. This versatility positions phthalocyanines as promising molecular platforms for energy conversion, green synthesis, and electrochemical sensing, with potential applications in photocatalysis, solar cells, and electrochromic materials.[12, 19–22]

Porphyrin **Phthalocyanine**
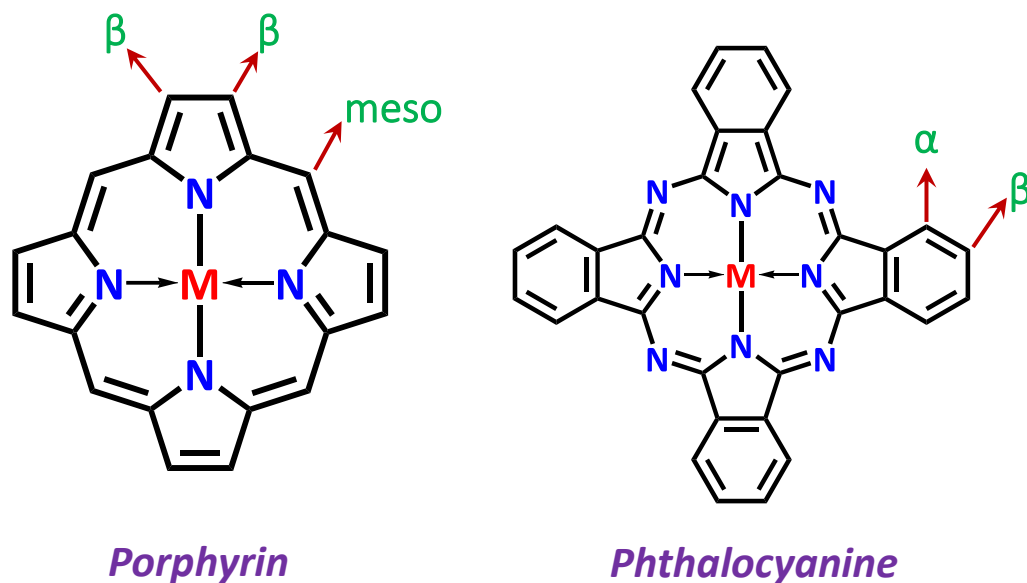
Figure 1.1. Molecular structures of metal porphyrin and metal phthalocyanine complexes denoting the positions where substitutions are possible in both the molecules.

1.2. Metal Phthalocyanines:

Discovered in 1928, phthalocyanines have since been the focal point of extensive investigations across various research fields, emerging as engineered analogues of naturally occurring phthalocyanines.[23–27] These planar aromatic macrocycles are composed of four isoindole sub-units, forming a delocalized 18 π electron aromatic cloud over an arrangement of alternating nitrogen and carbon atoms. Synthesis efforts have yielded diverse metal phthalocyanines, with substitutions ranging from tetra and octa to hexadeca. Peripheral hydrogen atoms at the secondary sphere of phthalocyanine molecules are replaced by functional groups such as COOH, NH_2, NO_2, Cl, Br, F, SO_3H, CH_3, etc. and the central metal ions can be Co,

Fe, Ni, Cu, etc. forming bonds with nitrogen atoms of the isoindole units in both unsubstituted and substituted metal phthalocyanines.[28–33]

1.3. Synthesis of metal phthalocyanines:

The synthesis of phthalocyanines can be accomplished through various methods, each offering distinct advantages and tailored outcomes. One common approach is the classical cyclotetramerization method, where phthalonitrile reacts with metal salts or oxides under high-temperature conditions, resulting in the formation of metal phthalocyanine macrocycles. [14–16, 23] This method provides a straightforward route but may require elevated temperatures and long reaction times. Another widely employed technique is the template synthesis, where metal ions coordinated to specific templates guide the cyclotetramerization process, influencing the structure and properties of the resulting phthalocyanines.[34–36] This method allows for better control over the metal center and can lead to higher yields of specific isomeric forms. Metal insertion reactions involve introducing metal ions into pre-formed phthalocyanine frameworks, allowing for post-synthetic modification and control over the metal composition.[15,16,23–25] This method provides versatility in tuning the properties of the resulting phthalocyanine. Additionally, green synthesis methods, utilizing environmentally friendly conditions and sustainable reactants, have gained attention. Microwave-assisted synthesis and sonochemical methods have been explored for their efficiency and reduced environmental impact. Ultimately, the choice of synthesis method depends on the desired phthalocyanine properties, the specific metal centre, and the intended

applications, reflecting the diverse strategies available for tailoring these versatile macrocyclic compounds. Both unsubstituted and substituted phthalocyanines, can be synthesised from various starting materials, including aromatic ortho-dicarboxylic acid derivatives, phthalonitriles, phthalic anhydrides, phthalimides, diiminoisoindolines, and 2-cyanobenzamides,[37–41] as depicted in Figure 1.2.
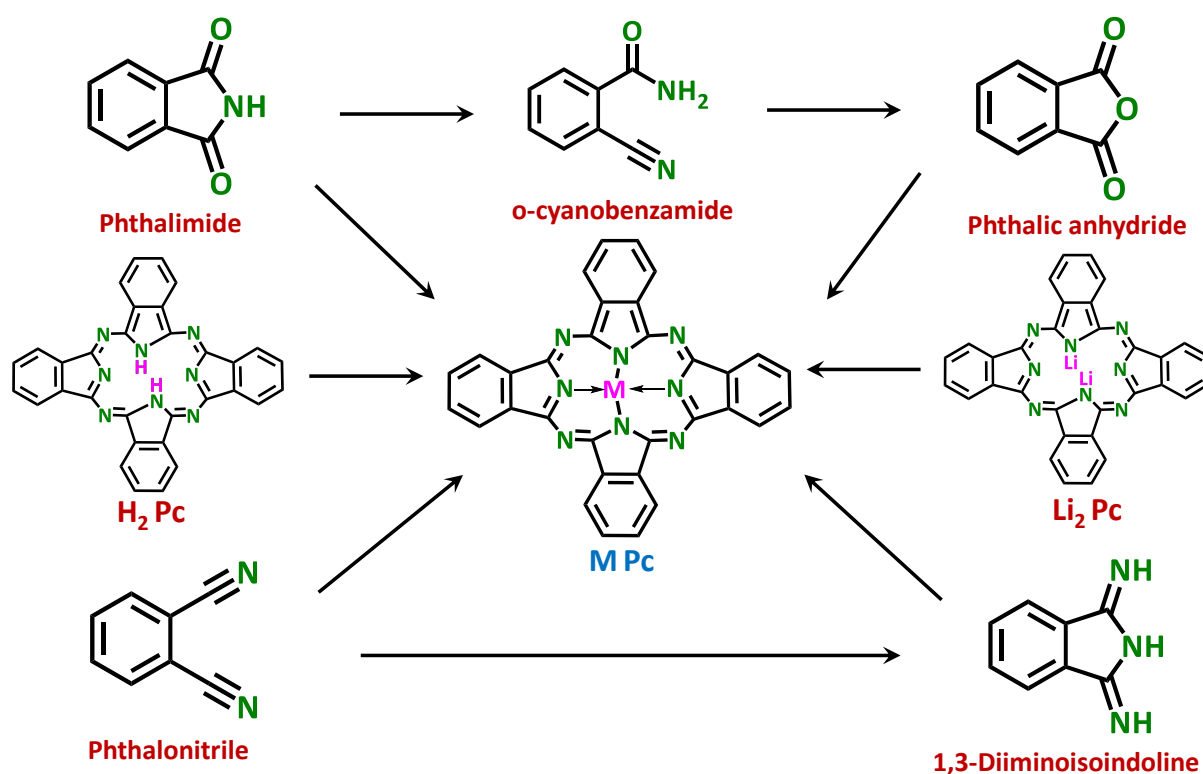
Figure 1.2. Various synthesis routes of metal phthalocyanines.

1.4. Characteristics of metal phthalocyanines:

Phthalocyanine (Pcs) molecules emerge as noteworthy ligands distinguished by their prominent features in the domain of coordination chemistry. Particularly, Pcs display distinctive characteristics, with their remarkable redox behavior standing out prominently. This behavior

originates from the extensive network of conjugated electrons—eighteen of which are aromatic—delocalized over four isoindoline units bridged by eight azamethines in the Pc macrocycle (refer to Figure 1.1).[14] The stable electronic conformation of the Pc macrocycle constrains its reactivity primarily to redox or substitution reactions, involving the exchange of electrons or hydrogen atoms, respectively. These reactions are facilitated by suitable oxidizing/reducing agents or electrophilic/nucleophilic reactants.[12,15,42] While additions and ring openings are infrequent due to stringent conditions leading to Pc skeleton disruption,[43–45] reactions preserving the aromatic character, such as acid-base reactions[46–48] or transformations of the central metal ion,[49–51] are more commonly observed.

In the realm of electrochemical applications, phthalocyanines (Pcs) exhibit compelling electrical properties, robust thermal and chemical stabilities, and adjustable optoelectronic features.[9,1013,52] Their swift redox processes, involving minimal reorganizational energies, position them as exceptional redox mediators in electron transfer processes across diverse substrates.[11–13] Notably, their flexibility allows for the transfer of over 70-80 metals from the two hydrogen atoms within the central cavity, with various alternatives combinable in the secondary sphere positions of the N_4 macrocycle. This adaptability enables fine-tuning of their electronic properties, positioning Pcs as promising candidates for non-precious molecular platforms, particularly in energy conversion/storage, green chemistry, electrochromic windows, and sensing applications as shown in Figure 1.3.[14,19,53] The rich electrochemistry of Pcs extends to their

applicability in electrochemical capacitors designed for charge storage applications,[54–61] offering tunability through linkage with appropriate functional units.
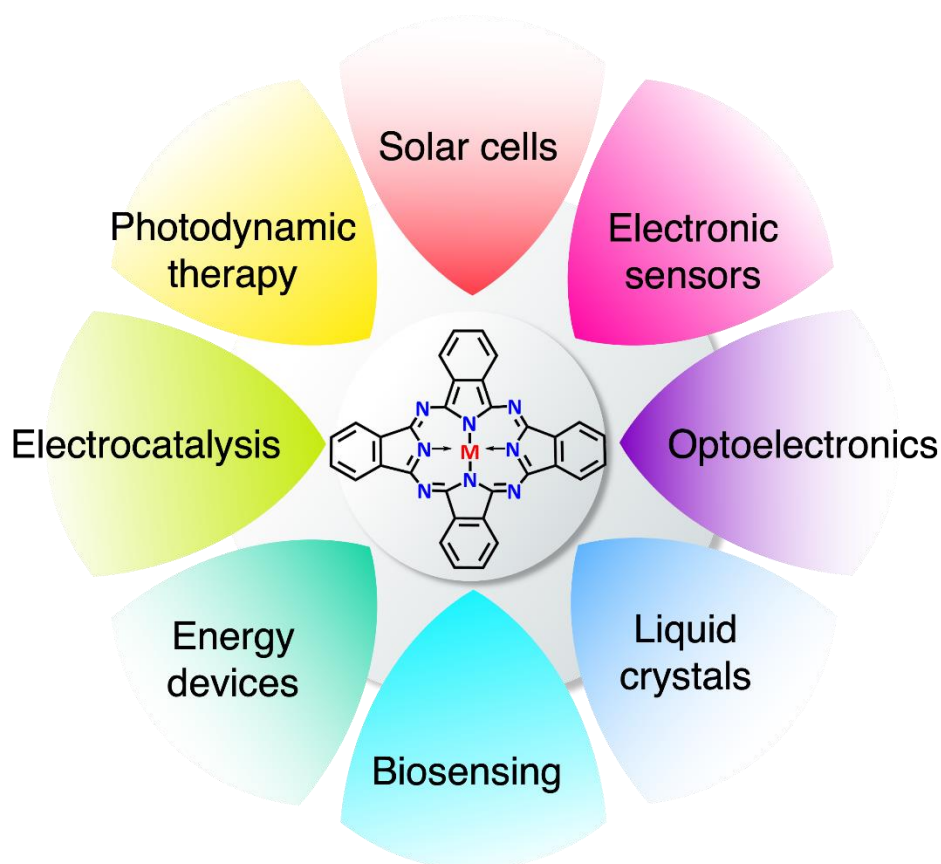
Figure 1.3. Various applications of metal phthalocyanines.

1.5. Metal phthalocyanines as supercapacitors:

Researchers have extensively explored metallophthalocyanine (MPc) complexes, which are N_4-macrocyclic metal compounds, as electrode materials for the design of molecular supercapacitors.[55–57,62–70] Unlike conventional capacitors, a supercapacitor stands out in terms of its energy storage capacity. It possesses a capacity value higher than that of typical parallel plate capacitors, bridging the gap between traditional capacitors and rechargeable batteries.[71–74] Generally, a high-capacity capacitor can

store 10 to 100 times more energy per unit volume or mass than regular capacitors. It can rapidly get charged and discharged as compared to batteries, enduring many more charge and discharge cycles than rechargeable batteries.[75,76] Supercapacitors typically utilize porous carbon material as electrodes and store charge electrostatically. They find application in situations requiring immediate power. It is important to highlight that in electrochemical capacitors, charge storage is predominantly surface-confined, in contrast to the bulk charge storage observed in batteries. This characteristic contributes to the well-known energy deficiency of high-power supercapacitors and the moderate power capability of high-energy batteries. Future-generation electrochemical devices aim to achieve both high energy and high-power capabilities.[77–84]

There are two main types of supercapacitors based on charge storage mechanisms: a) Electrochemical Double Layer Capacitors (EDLCs) and b) Pseudocapacitors. The EDLC operates by the non-Faradaic separation of charges at the electric double layer, whereas the pseudocapacitors majorly involve surface confined Faradaic redox reactions. EDLC-type materials such as activated carbon or carbon nanotube undergo reversible adsorption/desorption of electrolyte ions at the electrode-electrolyte interface during charging/discharging. This process is solely dependent on the active surface area of the electrodes, and since the charge storage mechanism depends only on the physical reorientation of ion charge assembly at the interface, the energy density is much lower in EDLCs, as compared to pseudocapacitive materials. As mentioned earlier, the charge

storage mechanism of pseudocapacitive materials primarily involve surface limited redox reactions.[55,85–87] Typically, during the process of charging/discharging, there will be a change in the redox state of the species involved, that in turn demand intercalation/deintercalation of counter ions.[88–90] Therefore, materials that can exhibit multiple redox transitions are often preferred in developing high energy density capacitor device. This conventional wisdom that multiple redox transition within the electrode has a direct link with the attainable energy density is affirmed by the classical demonstrations of charge storage in electrode materials including RuO_2, NiO, Co_3O_4, MnO_2, conducting polymers etc., and they all exhibited very high charge storage capability in their available potential window.[88–90] In molecular systems, such as N_4 macrocyclic complexes, there have been a few demonstrations aimed at enhancing their charge storage capability. Additionally, functional carbon nanostructures, such as graphene and carbon nanotubes (CNTs), have been employed as surfaces to anchor MN_4 macrocyclic complexes, thereby improving their overall charge storage properties.[91–95]

For instance, Priya Madhuri et al. have explored electrochemical capacitance applications of nickel phthalocyanine (NiPc) nanofibres and its composite with reduced graphene oxide (rGO). The composite material demonstrated a specific capacitance of 223.28 F/g at 1A/g current rate, along with good cycling stability for 1000 cycles.[67] Deyab et al. used Co-phthalocyanine/CNT (PcCo@CNTs) as a supercapacitor in 6M KOH electrolyte and obtained a specific capacitance of 1112 F/g at a current of 1

A/g and energy density of 55.6 Wh/kg.[96] Non-peripheral octamethyl-substituted copper(II) phthalocyanine (N-CuMe$_2$Pc) demonstrated impressive charge storage capability.[69] A Zn-ion hybrid supercapacitor with β-form zinc phthalocyanine (ZnPc) molecular crystal as the cathode material provided maximum energy density of 86.2 Wh/kg at 0.22 kW/kg and maintained a capacitance retention of 73.4% after 100,000 cycles.[97] Composites of cobalt-based phthalocyanines with MWCNTs and nickel-based phthalocyanines with graphene-based electrodes exhibited superior charge storage capability. In similar lines, researchers have investigated charge storage in various metallophthalocyanine complexes, and these demonstrations undeniably indicate their potential to excel as electrodes for supercapacitive charge storage.[62–70]

1.6. Metal phthalocyanines as electrocatalysts:

Electrochemical energy conversion/storage systems, such as fuel cells, metal-air batteries, and CO$_2$ reduction technologies, offer promising solutions for a sustainable energy future. However, the challenge lies in the development of electrocatalysts with optimal properties, as many of these reaction pathways involve multi-electron transfers and suffer from sluggish kinetics and catalyst poisoning.[98–101] Therefore, a crucial requirement exists for electrocatalysts characterized by high efficiency and affordability, enabling the initiation of electrochemical transformations at reduced overpotentials, while also exhibiting advanced selectivity. In this perspective, electrocatalysts assume a pivotal role in influencing the framework of renewable energy.

Achieving appreciable rates in electrochemical reactions often necessitates a notable overpotential.[102] This becomes particularly evident in reactions that go beyond outer-sphere electron transfers and involve significant bond rearrangements, as well as bond breaking and formation. Such reactions, encompass multiple reactants and products, potentially leading to the uptake or release of additional electrons. In such scenarios, catalysis of the electrochemical reaction is pursued to enhance the reaction current, ideally approaching the equilibrium potential.[103]

The term "electrocatalysis" is conventionally employed for reactions in which metals play a chemical role in the catalytic process.[103,104] While the chemical properties of the electrode material are crucial for catalytic efficiency, geometric and crystallographic features, as well as the nature and number of defects, also impact electrocatalysis.[103–105] The catalysis and electrochemistry communities have devised volcano plots based on thermodynamic properties to swiftly analyze extensive datasets, aiming to comprehend various aspects of electrocatalysis. The volcano plot for exchange current density (jo) concerning the Gibbs free energy change in the adsorption/desorption step (e.g., $\Delta G_{H+}/\Delta G_{OOH+}$) in most electrochemical transformations indicates that platinum-based electrocatalysts serve as the benchmark.[106–108]

Various types of electrocatalysts are available, including metal surfaces or metal nanoparticles, coordination complexes (molecular), and enzymes. Noble-metal-based materials, such as platinum (Pt), are considered state-of-the-art electrocatalysts for diverse electrochemical

reactions, including the oxygen reduction reaction,[109–111] hydrogen evolution reaction and hydrogen oxidation reaction.[112–114] Additionally, ruthenium (Ru)/iridium (Ir) oxide is recognized as a benchmark catalyst for the oxygen evolution reaction,[115–118] while gold and silver have been employed for catalyzing the carbon dioxide reduction reaction.[119–121] However, metal-based electrocatalysts come with drawbacks such as limited earth reserves, low selectivity, inadequate durability, and high cost during operation, restricting their widespread integration into renewable energy technologies. Consequently, the development of cost-effective, earth-abundant electrocatalysts with high activity and durability is crucial for the practical implementation of clean energy technologies.[122–124] Presently, an expanding array of molecular catalysts is involved in the electrochemical transformations of valued added substrates, with a primary focus on comprehending their structure-activity relationships—an essential aspect for designing improved molecular electrocatalysts.

Extensively studied within the realm of non-precious molecular electrocatalysts, the family of molecular electrocatalysts, such as MPcs with N_4 macrocyclic frameworks, and MPcs supported on carbon and other graphitic structures, shows promise for a wide array of electrochemical reactions—from energy conversion to biosensing applications.[125–127] These electrocatalysts exhibit proficiency in catalyzing diverse electrooxidation reactions, including those involving carbon monoxide, glucose, and nitrogen monoxide.[128–133] Additionally, they showcase capability in electroreduction reactions, such as the reduction of molecular oxygen, hydrogen peroxide,

molecular nitrogen, and nitrate. Beyond their technological significance, metal-based phthalocyanines offer valuable insights into the interplay between their electrochemical properties and structural characteristics.

Amidst the current energy challenges, significant strides have been made in recent years toward comprehending the structure-activity relationships of molecular electrocatalysts. This progress has facilitated the development of tools for catalyst benchmarking, paving the way for the intelligent design of new molecular electrocatalysts. In their molecular form, MPc molecules comprise a central metal ion surrounded by N-containing ligand groups. It is known that the reaction mechanism and the final product of any electrochemical transformation reaction is majorly governed by the central metal ion. For example, Cao et al., Zhang et al. and Chen et al. have demonstrated oxygen reduction reaction with an iron based phthalocyanine proceeds via a four-electron pathway giving water as the final product[134–136] whereas Fukuzumi et al., Chen et al. and Sun et al. showed with a cobalt based phthalocyanine oxygen reduction reaction proceeds via a two-electron pathway giving peroxide as the final product.[137–139] Kejun et al. found CO_2 reduction reaction with nickel polyphthalocyanine leads to CO as the end product with an ultrahigh selectivity of 99.7%.[140] Kusama et al. demonstrated with crystalline copper (II) phthalocyanine C_2H_4 is obtained as the major product of CO_2 reduction reaction.[141] Gong et al. showed cobalt phthalocyanine anchored on nitrogen-doped hollow carbon spheres gave CO with a faradic efficiency of 96% as the major product of CO_2 reduction reaction.[142] Liu et al. explored metal phthalocyanines as

model electrocatalysts for selective alkyne semihydrogenation and found cobalt phthalocyanine gives best performance with high ethylene faradaic efficiency under a pure acetylene stream.[143] Ebadi et al. showed a dinuclear ruthenium phthalocyanine gives N_2O and NH_3 as the main products of nitrite reduction at pH 4 – 8 at high and low nitrite concentration respectively.[144] Nyokong et al. explored various metallophthalocyanine (MPc) for the detection of nitric oxide (NO) and found phthalocyanines containing electroactive central metals such as CoPc and FePc generally show better catalytic activity towards the detection of NO than complexes containing electro inactive central metals.[145] Chen et al. demonstrated binuclear iron phthalocyanine catalyzes the dechlorination of atrazine giving 2-hydroxy-4-ethylamino-6-isopropylamino-1,3,5- triazine as the main product.[146] Chen et al. showed a composite of cobalt phthalocyanine with graphene oxide (GO) exhibits an efficient hydrogen evolution reaction giving a low overpotential of ~253 mV at a current density of 10 mA cm^{-2} in alkaline media.[147] Genc et al. studied the effect of central metal atom for the photocatalytic water splitting by hydrogen evolution reaction. The photocatalytic activities of $ZnPc/TiO_2$ and $CoPc/TiO_2$ were compared and the rate of hydrogen production was found to be higher in $ZnPc/TiO_2$ than $CoPc/TiO_2$.[148]

Moreover, it has been discovered that heat treatment processes involving a mixture of metal macrocyclic molecules and carbon materials can enhance both the activity and durability of the resulting composite materials. For example, Kumar et al. investigated the bifunctional electrocatalytic activity toward ORR and OER of mixed metal (FeNi, FeMn

and FeCo) phthalocyanine modified multiwalled carbon nanotubes (MWCNTs) prepared by a pyrolysis method. FeCo and FeMn catalysts showed better ORR activity whereas FeNi was better OER catalyst. The FeCo and FeMn catalysts also displayed good performance as cathodes in anion exchange membrane fuel cells (AEMFCs).[149] Furthermore, functional carbon nanostructures, including reduced graphene oxide and carbon nanotubes (CNT), have been employed as substrates for MN_4 macrocyclic complexes to enhance their catalytic performance. Notably, various composites of graphene/MWCNT macrocyclic complexes, assembled through π-π interactions, were characterized and assessed for their electrocatalytic properties.

Taken together, up to the present moment, metallophthalocyanines (MPcs) have been successfully integrated as active components in various electrochemical applications, including electrocatalysis and charge storage. The preceding discussion emphasizes that the electrochemical properties of phthalocyanine molecules are contingent upon the central metal ion and the structure of the ligand. It is essential to note that the examples provided here serve as demonstrative instances within the extensive literature on metal phthalocyanines in electrochemistry. The overarching conclusion is that their electrocatalytic activities are predominantly dictated by the central metal ion, while the charge storage capabilities can be adjusted by the N_4 macrocyclic framework and the nature of the support material.

1.7. Aim and scope of the thesis:

As discussed in the above sections, MPc molecules are utilised for catalyzing various electrochemical transformations and charge storage applications. It is well established that in metal phthalocyanines the central metal ion is the one which dictates the reaction mechanism and ultimately controls the final products of the electrochemical reactions.[134–142] The primary aim of this thesis is to elucidate the exclusive role of ligand in electrocatalysis as well as charge storage. For this, the central metal ion is taken to be cobalt which is kept same throughout the thesis. The role of ligand is investigated by varying the nature of the ligand as well as the isomerism of the ligand in the N_4 macrocyclic framework towards various electrochemical proceses. The thesis is divided into following chapters.

Chapter 1 delivers a comprehensive introduction to N_4 macrocyclic complexes, focusing on their electrochemical properties. It explores their significant contributions to electrocatalytic reactions and supercapacitive charge storage applications, emphasizing the central metal ion's role in molecular electrocatalysis and charge storage based on the existing literature. The chapter concludes by outlining the aim and objectives of the current research work.

Chapter 2 outlines the synthesis of $-NO_2$, $-COOH$, and $-NH_2$ substituted phthalocyanine molecules, including isomeric $-NO_2$ molecules. The discussion extends to integrating these molecules on carbon-supported platforms for applications in electrocatalysis, metal-air batteries, and

molecular charge storage. Various physico-chemical techniques are explored for unambiguously characterizing the synthesized compounds.

Chapter 3 illustrates how ligand isomerism in -NO_2 substituted molecular catalysts influences the reaction kinetics and mechanisms of oxygen reduction reaction (ORR) and oxygen evolution reaction (OER). The β-isomeric electrocatalyst exhibits an enhanced oxidative activation due to the combined –R and –I effects, in contrast to diminishing -R effect in the α-isomeric electrocatalyst. This enhancement noticeably improves the kinetics of both ORR and OER in the β-isomeric electrocatalyst without altering their respective reaction mechanisms. Furthermore, the integration of β-isomeric electrocatalyst was found to noticeably improve the round-trip efficiency of a Zn-air battery as compared to the α-isomeric molecule. This investigation presents an innovative approach in designing efficient molecular electrocatalysts for targeted electrochemical reactions relevant to energy storage and conversion.

Chapter 4 demonstrates the counterintuitive contribution of ligands to electrocatalysis through a proton charge assembly, during water oxidation and chlorine evolution reactions. Contrary to their position in the spectrochemical series, the experimental trends on the same catalytic Co centre were found to be opposite with an unexpectedly high activity with the carboxy functionalized ligand than the more electron withdrawing nitro functionalized ligand. Electrochemical and spectroscopic analyses indicate the enrichment of the catalytically active Co entity in the carboxy functionalized ligand due to extensive proton charge assembly, that in turn

accelerates the overall OER and CER processes. This study illustrates that selecting a ligand based solely on the spectrochemical series may not be adequate; considering its interaction with the surrounding medium is crucial to fully harness the maximum potential of the molecule in electrocatalysis.

Chapter 5 showcases how a non-redox active ligand functionality can elevate the charge storage capability of the electric double layer through a non-electrochemical proton charge assembly. The double layer charge storage enhancement for carboxy and amine substituted molecules to a similar extent compared to nitro substituted and unsubstituted molecules is attributed to extensive proton charge assembly in acidic medium for the former sets of molecules. This results in a higher local density of anions in the electric double layer (EDL), enhancing the energy density of the supercapacitor device without compromising its power capability. Various analyses including electrochemical and spectroscopic techniques confirm the superior charge storage capability of the carboxy substituted molecule is independent of the central metal ion, attributing its origin to ligand characteristics. A real-life application is demonstrated by powering a 2 V LED with the supercapacitor based on carboxy functionalised molecule. This idea of a non-redox active functionality contributing to supercapacitive charge storage through a non-electrochemical proton charge assembly presents an opportunity for designing ligands for energy storage applications.

Chapter 6 demonstrates a result obtained exclusively with carboxy functionalised cobalt phthalocyanine (TCCoPc) molecule towards oxygen reduction reaction in aqueous medium. Generally, ORR in aqueous medium proceeds via either 2 electron or 4 electron pathway giving peroxide or water as main products respectively. However, the carboxy functionalized ligand and a central Co metal combination (TCCoPc) leads to a surprising 1 electron ORR forming superoxide in aqueous medium. Hydrodynamic voltametric techniques including rotating disk electrode and rotating ring disk electrode points towards superoxide ion formation with TCCoPc. Furthermore, this 1 electron ORR was not observed with other carboxy substituted transition metal phthalocyanines including Fe, Cu and Ni, suggesting an interplay between the nature of the ligand and nature of the central metal.

Chapter 7 provides a concise summary and outlines future perspectives for the research presented in the thesis.

1.8. References

[1]   Chung, M.; Maalouf, J. H.; Adams, J. S.; Jiang, C.; Román-Leshkov, Y.; Manthiram, K. Direct Propylene Epoxidation via Water Activation over Pd-Pt Electrocatalysts. *Science* **2024**, *383*, 49–55.

[2]   Vaddypally, S.; Tomlinson, W.; O'Sullivan, O. T.; Ding, R.; Van Vliet, M. M.; Wayland, B. B.; Hooper, J. P.; Zdilla, M. J. Activation of C–H, N–H, and O–H Bonds via Proton-Coupled Electron Transfer to a Mn(III) Complex of Redox-Noninnocent Octaazacyclotetradecadiene, a

Catenated-Nitrogen Macrocyclic Ligand. *J. Am. Chem. Soc.* **2019**, *141* (14), 5699–5709.

[3]   Costentin, C.; Savéant, J.-M. Towards an Intelligent Design of Molecular Electrocatalysts. *Nat. Rev. Chem.* **2017**, *1* (11), 87.

[4]   Liang, Y.; McLaughlin, D.; Csoklich, C.; Schneider, O.; Bandarenka, A. S. The Nature of Active Centers Catalyzing Oxygen Electro-Reduction at Platinum Surfaces in Alkaline Media. *Energy Environ. Sci.* **2019**, *12* (1), 351–357.

[5]   Löffler, T.; Meyer, H.; Savan, A.; Wilde, P.; Garzón Manjón, A.; Chen, Y. T.; Ventosa, E.; Scheu, C.; Ludwig, A.; Schuhmann, W. Discovery of a Multinary Noble Metal–Free Oxygen Reduction Catalyst. *Adv. Energy Mater.* **2018**, *8* (34), 1–7.

[6]   Chen, H.; Cai, R.; Patel, J.; Dong, F.; Chen, H.; Minteer, S. D. Upgraded Bioelectrocatalytic N2 Fixation: From N2 to Chiral Amine Intermediates. *J. Am. Chem. Soc.* **2019**, *141* (12), 4963–4971.

[7]   Ali, A.; Shen, P. K. Recent Advances in Graphene-Based Platinum and Palladium Electrocatalysts for the Methanol. *J. Mater. Chem. A,* **2019**, *7,* 22189–22217.

[8]   Roca-Ayats, M.; Herreros, E.; García, G.; Peña, M. A.; Martínez-Huerta, M. V. Promotion of Oxygen Reduction and Water Oxidation at Pt-Based Electrocatalysts by Titanium Carbonitride. *Appl. Catal. B Environ.* **2016**, *183,* 53–60.

[9]   Sobbi, A. K.; Wöhrie, D.; Schlettwein, D. Photochemical Stability of Various Porphyrins in Solution and as Thin Film Electrodes. *J. Chem. Soc. Perkin Trans. 2* **1993**, No. 3, 481–488.

[10]   Bottari, G.; de la Torre, G.; Guldi, D. M.; Torres, T. Covalent and Noncovalent Phthalocyanine-Carbon Nanostructure Systems: Synthesis, Photoinduced Electron Transfer, and Application to Molecular Photovoltaics. *Chem. Rev.* **2010**, *110* (11), 6768–6816.

[11]   Huang, S.; Chen, K.; Li, T.-T. Porphyrin and Phthalocyanine Based Covalent Organic Frameworks for Electrocatalysis. *Coord. Chem. Rev.* **2022**, *464,* 214563.

[12] Leznoff, C.C.; Lever, A.B.P. Phthalocyanines, Properties and Applications, **1989**, 1–4, VCH Publishers Inc., New York.

[13] Zagal, J. H.; Griveau, S.; Silva, J. F.; Nyokong, T.; Bedioui, F. Metallophthalocyanine-based molecular materials as catalysts for electrochemical reactions. *Coord. Chem. Rev.* **2010**, *254*, 2755–2791.

[14] Zagal, J.H.; Bedioui, F.; Dodelet, J. P. *N4-macrocyclic metal complexes.* Springer, New York. **2006**; volume 1; Energy.

[15] Zagal, J.H.; Bedioui, F. *Electrochemistry of N4-macrocyclic metal complexes.* Springer, New York. **2006**; volume 1-2.

[16] Yang, Y.-J.; Li, S.-X.; Chen, D.-L.; Long, Z.-W. Geometric and Electronic Properties of Metal-Free Phthalocyanine. *ACS Omega* **2022**, *7* (45), 41266–41274.

[17] Ishihara, S.; Labuta, J.; Van Rossom, W.; Ishikawa, D.; Minami, K.; Hill J. P.; Ariga, K. Porphyrin-based sensor nano architectonics. *Phys Chem Chem Phys.* **2014**, *16* (21), 9713-9746.

[18] De La Torre, G.; Bottari, G.; Sekita, M.; Hausmann, A.; Guldi, D. M.; Torres, T. A Voyage into the Synthesis and Photophysics of Homo- and Heterobinuclear Ensembles of Phthalocyanines and Porphyrins. *Chem. Soc. Rev.* **2013**, *42* (20), 8049-8105.

[19] Sorokin, A. B. Phthalocyanine Metal Complexes in Catalysis. *Chem. Rev.* **2013**, *113* (10), 8152-8191.

[20] De La Torre, G.; Claessens, C. G.; Torres, T. Phthalocyanines: Old Dyes, New Materials. *Chem. Commun.* **2007**, *20*, 2000-2015.

[21] Rezaee, E.; Khan, D.; Cai, S.; Dong, L.; Xiao, H.; Silva, S. R. P.; Liu, X.; Xu, Z. X. Phthalocyanine in Perovskite Solar Cells: A Review. *Mater. Chem. Front.* **2023**, 1704–1736.

[22] Milaeva, E. R.; Speier, G.; Lever, A. B. P. *The redox chemistry of metallophthalocyanines in solution.* Wiley, New York, **1992**, 162-227.

[23] Kadish K. M.; Smith K. M.; Guilard R. *The porphyrin handbook,* Academic, San Diego. **2003**, volume 16-20.

[24] Yang, S.; Yu, Y.; Gao, X.; Zhang, Z.; Wang, F. Recent Advances in Electrocatalysis with Phthalocyanines. *Chem. Soc. Rev.* **2021**, *50* (23), 12985–13011.

[25] Akyüz, D.; Özçifçi, Z.; Menteşe, E.; Akçay, H. T. Novel Peripheral and Non-Peripheral Substituted Cobalt Phthalocyanines: Synthesis, Electrochemistry, Spectroelectrochemistry. *J. Electroanal. Chem.* **2022**, *924*, 116864.

[26] De la Torre, G.; Vázquez, P.; Agulló-López, F.; Torres, T. Role of Structural Factors in the Nonlinear Optical Properties of Phthalocyanines. *Chem. Rev.* **2004**, *104* (9), 3723-3750.

[27] Jiang, J.; Dennis, K. P. N. G. A Decade Journey in the Chemistry of Sandwich-Type Tetrapyrrolato-Rare Earth Complexes. *Acc. Chem. Res.* **2009**, *42* (1), 79-88.

[28] Zhu, W.; Liu, S.; Zhao, K.; Ye, G.; Huang, K.; He, Z. Revealing a Double-Volcano-Like Structure-Activity Relationship for Substitution-Functionalized Metal-Phthalocyanine Catalysts toward Electrochemical CO2 Reduction. *Small* **2024**, *20* (4), 2306144.

[29] Francisco Silva, J.; Griveau, S.; Richard, C.; Zagal, J. H.; Bedioui, F. Glassy Carbon Electrodes Modified with Single Walled Carbon Nanotubes and Cobalt Phthalocyanine and Nickel Tetrasulfonated Phthalocyanine: Highly Stable New Hybrids with Enhanced Electrocatalytic Performances. *Electrochem. commun.* **2007**, *9* (7), 1629-1634.

[30] Hirabaru, O.; Nakase, T.; Hanabusa, K.; Shirai, H.; Hojo, N.; Takemoto, K. Functional Metal-Porphyrazine Derivatives and Their Polymers. Part 11. Secondary Fuel Cells based on Oxygen Reduction at a Platinum Electrode modified by Metal-2,9,16,23-Tetracarboxyphthalocyanine covalently bound to Poly(2-vinylpyridine-styrene). *Dalton Trans.* **1984**, *8,* 1485-1489.

[31] Masa, J.; Ozoemena, K.; Schuhmann, W.; Zagal, J. H. Oxygen Reduction Reaction Using N4-Metallomacrocyclic Catalysts: Fundamentals on Rational Catalyst Design. *J. Porphyr. Phthalocyanines* **2012**, *16* (7-8), 761-784.

[32] Kumar, A.; Kumar Vashistha, V.; Kumar Das, D. Recent Development on Metal Phthalocyanines Based Materials for Energy Conversion and Storage Applications. *Coord. Chem. Rev.* **2021**, *431*, 213678.

[33] Preethi, N.; Shinohara, H.; Nishide, H. Reversible Oxygen-Binding and Facilitated Oxygen Transport in Membranes of Polyvinylimidazole Complexed with Cobalt- Phthalocyanine. *React. Funct. Polym.* **2006**, *66* (8), 851-855.

[34] Szymczak, J.; Rębiś, T.; Mielcarek, J.; Kryjewski, M. Electrochemical, Spectrochemical and Catalytical Properties of Cobalt(II) Phthalocyanine Regioisomers Studies. *Synth. Met.* **2022**, *283*, 116971.

[35] Zhou, W.; Yutronkie, N. J.; Lessard, B. H.; Brusso, J. L. From Chemical Curiosity to Versatile Building Blocks: Unmasking the Hidden Potential of Main-Group Phthalocyanines in Organic Field-Effect Transistors. *Mater. Adv.* **2021**, *2* (1), 165–185.

[36] Harmandar, K.; Saglam, M. F.; Sengul, I. F.; Ekineker, G.; Balcik-Ercin, P.; Göksel, M.; Atilla, D. Novel Triazole Containing Zinc(II)Phthalocyanine Schiff Bases: Determination of Photophysical and Photochemical Properties for Photodynamic Cancer Therapy. *Inorganica Chim. Acta* **2021**, *519*, 120286.

[37] Byrne, T.; Linstead, R. P.; Lowe, A. R.; Phthalocyanines. Part II. The preparation of phthalocyanine and some metallic derivatives from o-cyanobenzamide and phthalimide. *J. Chem. Soc.,* **1934**, *10*, 1017-1022.

[38] Öztürk, N. F.; Özdemir, S.; Giray, G.; Aftab, J.; Bayır, Z. A. Biological Applications of The Newly Designed Phthalocyanine-Modified Gold Nanorods. *Chemistry Select* **2024**, *9* (1), e202303907.

[39] Güleç, Ö.; Bilgiçli, A. T.; Hepokur, C.; Günsel, A.; Arslan, M.; Nilüfer Yarasir, M. Novel and Effective Peripheral Tetra-Substituted Phthalocyanines with Quinazoline Groups for Cancer Treatment: Synthesis, Photophysical and Photochemical Properties, and in-Vitro Studies. *J. Photochem. Photobiol. A Chem.* **2024**, *452*, 115587.

[40] Grundke, C.; Silva, R. C.; Kitzmann, W. R.; Heinze, K.; de Oliveira, K. T.; Opatz, T. Photochemical α-Aminonitrile Synthesis Using Zn-Phthalocyanines as Near-Infrared Photocatalysts. *J. Org. Chem.* **2022**, *87* (9), 5630–5642.

[41] Moser, F. H.; Thomas, A. L. Phthalocyanine Compounds. *J. Chem. Educ.* **1964**, *41* (5), 245-249.

[42] Hanack, M.; Lang, M. Conducting Stacked Metallophthalocyanines and Related Compounds *Adv. Mater.* **1994**, *6* (11), 819-833.

[43] Nath, A.; Prushan, M. J.; Gilbert, J. G. Can super-excited molecules survive fragmentation? *J. Radioanal. Nucl. Chem.* **2001**, *247*, 589.

[44] Lalande, G.; Côté, R.; Tamizhmani, G.; Guay, D.; Dodelet, J. P.; Dignard-Bailey, L.; Weng, L. T.; Bertrand, P. Physical, Chemical and Electrochemical Characterization of Heat-Treated Tetracarboxylic Cobalt Phthalocyanine Adsorbed on Carbon Black as Electrocatalyst for Oxygen Reduction in Polymer Electrolyte Fuel Cells. *Electrochim. Acta* **1995**, *40* (16), 2635-2646.

[45] Eley, D. D.; Hazeldine, D. J.; Palmer, T. F. Mass spectra, ionization potentials and related properties of metal-free and transition metal phthalocyanines *J. Chem. Soc., Faraday Trans. 2* **1973**, *69*, 1808.

[46] Weitman, H.; Schatz, S.; Gottlieb, H. E.; Kobayashi, N.; Ehrenberg, B. Spectroscopic Probing of the Acid-Base Properties and Photosensitization of a Fluorinated Phthalocyanine in Organic Solutions and Liposomes. *Photochem. Photobiol.* **2007**, *73* (5), 473-481.

[47] Nagao, K.; Kayo, A.; Tetsuo, O. Some Spectroscopic, Electrochemical and Spectroelectrochemical Properties of Tetrapyrazinoporphyrazine and Its Iron and Cobalt Complexes. *Anal. Sci.* **1990**, *6* (3), 449-453.

[48] Gaspard, S.; Viovy, R. Protonation of phthalocyanines. III-Case of free phthalocyanine: H_2Pc *J. Chim. Phys.,* **1981**, *78*, 851-853.

[49] Schneider, T.; Heckmann, H.; Barthel, M.; Hanack, M. Synthesis and Characterization of Soluble Chloro- and Aryl (naphthalocyaninato) indium (III) Complexes and Their Precursors. *Eur. J. Org. Chem.* **2001**, *16*, 3055-3065.

[50] Cook, M. J.; Dunn, A. J.; Howe, S. D.; Thomson, A. J.; Harrison, K. J. Octa-alkoxy phthalocyanine and naphthalocyanine derivatives: dyes with Q-band absorption in the far red or near infrared. *J. Chem. Soc. Perkin Trans. 1* **1988**, *8*, 2453-2458.

[51] Barthel, M.; Hanack, M. Axially substituted titanium (IV) phthalocyanines. *J. Porphyrins Phthalocyanines* **2000**, *4* (7), 635-638.

[52] González-Rodríguez, D.; Bottari, G. Phthalocyanines, Subphthalocyanines and Porphyrins for Energy and Electron Transfer Applications. *J. Porphyr. Phthalocyanines* **2009**, *13* (4-5), 624-636.

[53] Rigsby, M. L.; Wasylenko, D. J.; Pegis, M. L.; Mayer, J. M. Medium Effects Are as Important as Catalyst Design for Selectivity in Electrocatalytic Oxygen Reduction by Iron-Porphyrin Complexes. *J. Am. Chem. Soc.* **2015**, *137* (13), 4296-4299.

[54] Kotz, R.; Carlen, M. Principles and applications of electrochemical capacitors. *Electrochim. Acta* **2000**, *45*, 2483-2498.

[55] Chidembo, A. T.; Ozoemena, K. I.; Agboola, B. O.; Gupta, V.; Wildgoose, G. G.; Compton, R. G. Nickel (II) Tetra-Aminophthalocyanine Modified MWCNTs as Potential Nanocomposite Materials for the Development of Supercapacitors. *Energy Environ. Sci.* **2010**, *3* (2), 228-236.

[56] Agboola, B. O.; Ozoemena, K. I. Synergistic Enhancement of Supercapacitance upon Integration of Nickel (II) Octa [(3,5-Biscarboxylate)-Phenoxy] Phthalocyanine with SWCNT-Phenylamine. *J. Power Sources* **2010**, *195* (12), 3841-3848.

[57] Mu, J.; Shao, C.; Guo, Z.; Zhang, M.; Zhang, Z.; Zhang, P.; Chen, B.; Liu, Y. Solvothermal Synthesis and Electrochemical Properties of 3D Flower-like Iron Phthalocyanine Hierarchical Nanostructure. *Nanoscale* **2011**, *3* (12), 5126-5131.

[58] Sakthivel K, Munichadraiah N and Scanlon LG. *J. Electrochem Soc.* **2005**, *152*, C756-C763.

[59] Li, R.; Zhang, X.; Zhu, P.; Ng, D. K. P.; Kobayashi, N.; Jiang, J. Electron-Donating or -Withdrawing Nature of Substituents Revealed by the Electrochemistry of Metal- Free Phthalocyanines. *Inorg. Chem.* **2006**, *45* (5), 2327-2334.

[60] Silva, N.; Calderón, S.; Páez, M. A.; Oyarzún, M. P.; Koper, M. T. M.; Zagal, J. H. Probing the Fen +/Fe(n-1) + Redox Potential of Fe Phthalocyanines and Fe Porphyrins as a Reactivity Descriptor in the Electrochemical Oxidation of Cysteamine. *J. Electroanal. Chem.* **2018**, *819,* 502-510.

[61] Rajić, N. Z.; Stojaković, D. R. Synthesis and Characterization of Some Nitro- Substituted Phthalocyanines of Nickel (II), Cobalt (II) and Copper (II). *J. Coord. Chem.* **2009**, *19* (4), 295-301.

[62] Chidembo, A. T.; Огʌeтeпa, K. 1. Electrochemical Capacitive Behaviour of Multiwalled Carbon Nanotubes Modified with Electropolymeric Films of Nickel Tetraaminophthalocyanine. *Electroanalysis* **2010**, *22* (21), 2529-2535.

[63] Makgopa, K.: Ejikeme, P. M.; Ozoemena, K. 1. Graphene Oxide-Modified Nickel (II) Tetra-Aminophthalocyanine Nanocomposites for High-Power Symmetric Pseudocapacitor. *Electrochim. Acta* **2016**, *212*, 876-882.

[64] Xu, Z.; Li, Z.; Holt, C. M. B.; Tan, X.; Wang, H.; Amirkhiz. B. S.; Stephenson, T Mitlin, D. Electrochemical Supercapacitor Electrodes from Sponge-like Graphene Nanoarchitectures with Ultrahigh Power Density. *J. Phys. Chem. Lett.* **2012**, *3* (20), 2928-2933.

[65] Bakandritsos, A; Chronopoulos, D. D.; Jakubec, P., Pykal, M.; Cépe, K., Steriotis, T.: Kalytchuk, S.; Peu, M.; Zbožil. R.; Otyepka, M. High-Performance Supercapacitors Based on a Zwirterionic Nerwork of Covalently Functionalized Graphene with Iron Tetraminophthalocyanine. *Adv. Funct. Mater.* **2018**, *28* (29), 1-9.

[66] Wang, M.: Shi, H.; Zhang, P.: Liao, Z.; Wang, M.: Zhong, H.: Schwotzer. F.: Nia, A. S.; Zschech, E.; Zhou, S.; Kaskel, S.; Dong, R.; Feng, X. Phthalocyanine-Based 2D Conjugated Metal-Organic Framework Nanosheets for High-Performance Micro- Supercapacitors. *Adv. Funct. Mater.* **2020**, *30* (30).

[67] Madhuri, K. P.: John, N. S. Supercapacitor Application of Nickel Phthalocyanine Nanofibres and Its Composite with Reduced Graphene Oxide. *Appl. Surf. Sci.* **2018**, 449 528-536.

[68] Lu, Y.; Zheng, Q.; Wu, J.; Yu, Y. Enhanced Electrochemical Charge Storage Performance by Doping of Copper Phthalocyanine-3,4',4'',4'''-Terrasulfonic Acid Tetrasodium Salt into Polypyrrole/Multi-Walled Carbon Nanotubes 3D-Nanostructured Electrodes. *Electrochim. Acta* **2018**, *265*, 594-600.

[69] Ramachandran, R.; Hu, Q.; Wang, F. Xu, Z. X. Synthesis of N-CuMe$_2$Pc Nanorods/Graphene Oxide Nanocomposite for Symmetric Supercapacitor Electrode with Excellent Cyclic Stability. *Electrochim. Acta* **2019**, *298*, 770-777.

[70] Taşaltln, N. Taşaltin. C. Aydin, H.; Şahinrürk. Uz Gürek, A. G. Hexylsulfanyl substituted CoPc and GO-CoPc on Ni Foam as Electroactive Material for Supercapacitors. *J. Porphyr. Phthalocyanines* **2019**, *23* (11-12), 1616-1621.

[71] Frackowiak, E.; Fic, K.; Meller, M.; Lota, G. Electrochemistry Serving People and Nature: High-Energy Ecocapacitors Based on Redox-Active Electrolytes. *ChemSusChem* **2012**, *5* (7), 1181-1185.

[72] Akinwolemiwa, B.; Peng, C.; Chen, G. Z. Redox Electrolytes in Supercapacitors. *J. Electrochem. Soc.* **2015**, *162* (5), A5054-A5059.

[73] Jost, K.; Dion, G.; Gogotsi, Y. Textile Energy Storage in Perspective. *J. Mater. Chem. A* **2014**, *2* (28), 10776-10787.

[74] Zhang, S. W.; Chen, G. Z. Manganese Oxide Based Materials for Supercapacitors. *Energy Mater. Mater. Sci. Eng. Energy Syst.* **2008**, *3* (3), 186-200.

[75] Guan, L.; Yu, L.; Chen, G. Z. Capacitive and Non-Capacitive Faradaic Charge Storage. *Electrochim. Acta* **2016**, *206*, 464-478.

[76] Huang, J.; Sumpter, B. G.; Meunier, V. A Universal Model for Nanoporous Carbon Supercapacitors Applicable to Diverse Pore Regimes, Carbon Materials, and Electrolytes. *Chem. - A Eur. J.* **2008**, *14* (22), 6614-6626.

[77] Gogotsi, Y. What Nano Can Do for Energy Storage. *ACS Nano* **2014**, *8* (6), 5369-5371.

[78] Ke, Q.; Wang, J. Graphene-Based Materials for Supercapacitor Electrodes - A Review. *J. Mater.* **2016**, *2* (1), 37-54.

[79] Lukatskaya, M. R.; Dunn, B.; Gogotsi, Y. Multidimensional Materials and Device Architectures for Future Hybrid Energy Storage. *Nat. Commun.* **2016**, *7*, 1-13.

[80] Wang, F.; Wu, X.; Yuan, X.; Liu, Z.; Zhang, Y.; Fu, L.; Zhu, Y.; Zhou, Q.; Wu, Y.; Huang, W. Latest Advances in Supercapacitors: From New

Electrode Materials to Novel Device Designs. *Chem. Soc. Rev.* **2017**, *46* (22), 6816-6854.

[81] Tehrani, Z.; Thomas, D. J.; Korochkina, T.; Phillips, C. O.; Lupo, D.; Lehtimäki, S.; O'Mahony, J.; Gethin, D. T. Large-Area Printed Supercapacitor Technology for Low- Cost Domestic Green Energy Storage. *Energy* **2017**, *118*, 1313-1321.

[82] Dubal, D. P.; Chodankar, N. R.; Kim, D. H.; Gomez-Romero, P. Towards Flexible Solid-State Supercapacitors for Smart and Wearable Electronics. *Chem. Soc. Rev.* **2018**, *47* (6), 2065-2129.

[83] Mourad, E.; Coustan, L.; Lannelongue, P.; Zigah, D.; Mehdi, A.; Vioux, A.; Freunberger, S. A.; Favier, F.; Fontaine, O. Biredox Ionic Liquids with Solid-like Redox Density in the Liquid State for High-Energy Supercapacitors. *Nat. Mater.* **2017**, *16* (4), 446-454.

[84] Simon, P.; Gogotsi, Y. Materials for Electrochemical Capacitors. *Nat. Mater.* **2008**, *7*, 845-854.

[85] Yuan, J.; Qiu, M.; Hu, X.; Liu, Y.; Zhong, G.; Zhan, H.; Wen, Z. Pseudocapacitive Vanadium Nitride Quantum Dots Modified One-Dimensional Carbon Cages Enable Highly Kinetics-Compatible Sodium Ion Capacitors. *ACS Nano* **2022**, *16* (9), 14807–14818.

[86] Gorduk, O.; Gencten, M.; Gorduk, S.; Sahin, M.; Sahin, Y. Electrochemical Fabrication and Supercapacitor Performances of Metallo Phthalocyanine / Functionalized - Multiwalled Carbon Nanotube / Polyaniline Modified Hybrid Electrode Materials. *J. Energy Storage* **2021**, *33*, 102049.

[87] Chen, J. J.; Ye, J. C.; Zhang, X. G.; Symes, M. D.; Fan, S. C.; Long, D. L.; Zheng, M. Sen; Wu, D. Y.; Cronin, L.; Dong, Q. F. Design and Performance of Rechargeable Sodium Ion Batteries, and Symmetrical Li-Ion Batteries with Supercapacitor-Like Power Density Based upon Polyoxovanadates. *Adv. Energy Mater.* **2018**, *8* (6), 1–6.

[88] Sarkar, D.; Das, D.; Das, S.; Kumar, A.; Patil, S.; Nanda, K. K.; Sarma, D. D.; Shukla, A. Expanding Interlayer Spacing in MoS_2 for Realizing an Advanced Supercapacitor. *ACS Energy Lett.* **2019**, *4* (7), 1602–1609.

[89] Åvall, G.; A. Ferrero, G.; Janßen, K. A.; Exner, M.; Son, Y.; Adelhelm, P. In Situ Pore Formation in Graphite Through Solvent Co-Intercalation: A New Model for The Formation of Ternary Graphite Intercalation Compounds Bridging Batteries and Supercapacitors. *Adv. Energy Mater.* **2023**, *2301944*, 1–13.

[90] He, S.; Mo, Z.; Shuai, C.; Liu, W.; Yue, R.; Liu, G.; Pei, H.; Chen, Y.; Liu, N.; Guo, R. Pre-Intercalation δ-MnO_2 Zinc-Ion Hybrid Supercapacitor with High Energy Storage and Ultra-Long Cycle Life. *Appl. Surf. Sci.* **2022**, *577*, *151904*.

[91] Zhang, Q. Z.; Zhang, D.; Miao, Z. C.; Zhang, X. L.; Chou, S. L. Research Progress in MnO_2–Carbon Based Supercapacitor Electrode Materials. *Small* **2018**, *14* (24), 1702883.

[92] Alharbi, F. F.; Waheed, M. S.; Aman, S.; Ahmad, N.; Farid, H. M. T.; Mohaymen Taha, T. A. Facile Development of Mn Doped NiO Nanoarrays Supported on a Reduced Graphene Oxide Nanocomposite as a Supercapacitor. *Energy and Fuels* **2023**, *37* (16), 12225–12235.

[93] Zhang, W.; Yu, S.; Hu, H.; Fei, Y.; Chen, L.; Zhang, T. Binder-Free Self-Supporting Electrodes Formed by Intercalation of RuO_2 on Wood-Derived Carbon for Supercapacitor. *Appl. Surf. Sci.* **2023**, *640*, 158285.

[94] Halder, S.; Roy, S.; Roy, S.; Chakraborty, C. Enriching Oxygen Vacancy in Co_3O_4 by Solution Combustion Synthesis for Enhanced Supercapacitive Property. *J. Phys. Chem. C* **2023**, *127*, 18279–18290.

[95] Arun Kumar, S.; Sarasamreen, I.; Balaji, C.; Gowdhaman, A.; Ramesh, R.; Anbarasan P. M. Elevates the electrochemical stability performance of hydrothermally synthesized Co_3O_4 nanowires/NF for hybrid supercapacitors. *Inorg. Chem. Commun.* **2023**, *158*, 111506.

[96] Deyab, M. A.; Mohsen, Q.; Slavcheva, E. Co-Phthalocyanin/CNTs Nanocomposites: Synthesis, Characterizations, and Application as an Efficient Supercapacitor. *J. Mol. Liq.* **2022**, *359*, 119319.

[97] Han, D.; Wang, W.; Yu, S.; Qi, W.; Ling, R.; Yang, C.; Liu, G. Stable β-Form Zinc Phthalocyanine Cathodes for Flexible Zn-Ion Hybrid Supercapacitors with Ultra-Long Cycling Life. *Chem. Eng. J.* **2023**, *468*, 143875.

[98]   Chen, X.; Paul, R.; Dai, L. Carbon-Based Supercapacitors for Efficient Energy Storage. *Natl. Sci. Rev.* **2017**, *4* (3), 453-489.

[99]   She, Z. W.; Kibsgaard, J.; Dickens, C. F.; Chorkendorff, I.; Nørskov, J. K.; Jaramillo, T. F. Combining Theory and Experiment in Electrocatalysis: Insights into Materials Design. *Science* **2017**, *355*, 6321.

[100] Wang, Z. L.; Xu, D.; Xu, J. J.; Zhang, X. B. Oxygen Electrocatalysts in Metal-Air Batteries: From Aqueous to Nonaqueous Electrolytes. *Chem. Soc. Rev.* **2014**, *43* (22), 7746-7786.

[101] Dai, L.; Xue, Y.; Qu, L.; Choi, H. J.; Baek, J. B. Metal-Free Catalysts for Oxygen Reduction Reaction. *Chem. Rev.* **2015**, *115* (11), 4823-4892.

[102] Pingarrón, J. M.; Labuda, J.; Barek, J.; Brett, C. M. A.; Camões, M. F.; Fojta, M.; Hibbert, D. B. Terminology of Electrochemical Methods of Analysis (IUPAC Recommendations 2019). *Pure Appl. Chem.* **2020**, *92* (4), 641-694.

[103] Costentin, C.; Robert, M.; Savéant, J. M. Molecular Catalysis of Electrochemical Reactions. *Curr. Opin. Electrochem.* **2017**, *2* (1), 26-31.

[104] Savéant, J. M. Molecular Catalysis of Electrochemical Reactions. Mechanistic Aspects. *Chem. Rev.* **2008**, *108*, 2348-2378.

[105] Guerrini, E.; Trasatti, S. Recent Developments in Understanding Factors of Electrocatalysis. *Russ. J. Electrochem.* **2006**, *42* (10), 1017-1025.

[106] Quaino, P.; Juarez, F.; Santos, E.; Schmickler, W. Volcano Plots in Hydrogen Electrocatalysis-Uses and Abuses. *Beilstein J. Nanotechnol.* **2014**, *5* (1), 846-854.

[107] Toulhoat, H.; Raybaud, P. Prediction of Optimal Catalysts for a given Chemical Reaction. *Catal. Sci. Technol.* **2020**, *10* (7), 2069-2081.

[108] Jiao, Y.; Zheng, Y.; Jaroniec, M.; Qiao, S. Z. Design of Electrocatalysts for Oxygen- and Hydrogen-Involving Energy Conversion Reactions. *Chem. Soc. Rev.* **2015**, *44* (8), 2060-2086.

[109] Bezerra, C. W. B.; Zhang, L.; Lee, K.; Liu, H.; Marques, A. L. B.; Marques, E. P.; Wang, H.; Zhang, J. A Review of Fe-N/C and Co-N/C

Chapter 1

Catalysts for the Oxygen Reduction Reaction. *Electrochim. Acta* **2008**, *53* (15), 4937-4951.

[110] Lin, L.; Zhu, Q.; Xu, A. W. Noble-Metal-Free Fe-N/C Catalyst for Highly Efficient Oxygen Reduction Reaction under both Alkaline and Acidic Conditions. *J. Am. Chem. Soc.* **2014**, *136* (31), 11027-11033.

[111] Yin, P.; Yao, T.; Wu, Y.; Zheng, L.; Lin, Y.; Liu, W.; Ju, H.; Zhu, J.; Hong, X.; Deng, Z.; Zhou, G.; Wei, S.; Li, Y. Single Cobalt Atoms with Precise N-Coordination as Superior Oxygen Reduction Reaction Catalysts. *Angew. Chemie - Int. Ed.* **2016**, *55* (36), 10800-10805.

[112] Wu, J.; Yang, H. Platinum-Based Oxygen Reduction Electrocatalysts. *Acc. Chem. Res.* **2013**, *46* (8), 1848-1857.

[113] Esposito, D. V.; Hunt, S. T.; Stottlemyer, A. L.; Dobson, K. D.; McCandless, B. E.; Birkmire, R. W.; Chen, J. G. Low-Cost Hydrogen-Evolution Catalysts Based on Monolayer Platinum on Tungsten Monocarbide Substrates. *Angew. Chemie - Int. Ed.* **2010**, *49* (51), 9859-9862.

[114] Morales-Guio, C. G.; Hu, X. Amorphous Molybdenum Sulfides as Hydrogen Evolution Catalysts. *Acc. Chem. Res.* **2014**, *47* (8), 2671-2681.

[115] Antolini, E. Iridium as Catalyst and Co-catalyst for Oxygen Evolution/Reduction in Acidic Polymer Electrolyte Membrane Electrolyzers and Fuel Cells. *ACS Catal.* **2014**, *4* (5), 1426-1440.

[116] Ma, T. Y.; Dai, S.; Jaroniec, M.; Qiao, S. Z. Metal-Organic Framework Derived Hybrid Co3O4-Carbon Porous Nanowire Arrays as Reversible Oxygen Evolution Electrodes. *J. Am. Chem. Soc.* **2014**, *136* (39), 13925-13931.

[117] Huang, J.; Chen, J.; Yao, T.; He, J.; Jiang, S.; Sun, Z.; Liu, Q.; Cheng, W.; Hu, F.; Jiang, Y.; Pan, Z.; Wei, S. CoOOH Nanosheets with High Mass Activity for Water Oxidation. *Angew. Chemie - Int. Ed.* **2015**, *54* (30), 8722-8727.

[118] Wang, Y.; Xie, C.; Zhang, Z.; Liu, D.; Chen, R.; Wang, S. In Situ Exfoliated, N-Doped, and Edge-Rich Ultrathin Layered Double

Hydroxides Nanosheets for Oxygen Evolution Reaction. *Adv. Funct. Mater.* **2018**, *28* (4), 1-6.

[119] Trindell, J. A.; Clausmeyer, J.; Crooks, R. M. Size Stability and H_2/CO Selectivity for Au Nanoparticles during Electrocatalytic CO_2 Reduction. *J. Am. Chem. Soc.* **2017**, *139* (45), 16161-16167.

[120] Weng, Z.; Jiang, J.; Wu, Y.; Wu, Z.; Guo, X.; Materna, K. L.; Liu, W.; Batista, V. S.; Brudvig, G. W.; Wang, H. Electrochemical CO_2 Reduction to Hydrocarbons on a Heterogeneous Molecular Cu Catalyst in Aqueous Solution. *J. Am. Chem. Soc.* **2016**, *138* (26), 8076-8079.

[121] Weng, Z.; Zhang, X.; Wu, Y.; Huo, S.; Jiang, J.; Liu, W.; He, G.; Liang, Y.; Wang, H. Self-Cleaning Catalyst Electrodes for Stabilized CO_2 Reduction to Hydrocarbons. *Angew. Chemie - Int. Ed.* **2017**, *56* (42), 13135-13139.

[122] Lu, C.; Tranca, D.; Zhang, J.; Rodríguez Hernández, F.; Su, Y.; Zhuang, X.; Zhang, F.; Seifert, G.; Feng, X. Molybdenum Carbide-Embedded Nitrogen-Doped Porous Carbon Nanosheets as Electrocatalysts for Water Splitting in Alkaline Media. *ACS Nano* **2017**, *11* (4), 3933-3942.

[123] Wu, Y.; Liu, X.; Han, D.; Song, X.; Shi, L.; Song, Y.; Niu, S.; Xie, Y.; Cai, J.; Wu, S.; Kang, J.; Zhou, J.; Chen, Z.; Zheng, X.; Xiao, X.; Wang, G. Electron Density Modulation of NiCo2S4 Nanowires by Nitrogen Incorporation for Highly Efficient Hydrogen Evolution Catalysis. *Nat. Commun.* **2018**, *9,* 1425.

[124] Sun, T.; Xu, L.; Li, S.; Chai, W.; Huang, Y.; Yan, Y.; Chen, J. Cobalt-Nitrogen-Doped Ordered Macro-/Mesoporous Carbon for Highly Efficient Oxygen Reduction Reaction. *Appl. Catal. B Environ.* **2016**, *193*, 1-8.

[125] Li, L.; Tang, X.; Huang, S.; Lu, C.; Lützenkirchen-Hecht, D.; Yuan, K.; Zhuang, X.; Chen, Y. Longitudinally Grafting of Graphene with Iron Phthalocyanine-Based Porous Organic Polymer to Boost Oxygen Electroreduction. *Angew. Chemie Int. Ed.* **2023**, *62* (22), e202301642.

[126] Nguyen, T. Q.; Escaño, M. C. S.; Kasai, H. Nitric Oxide Adsorption Effects on Metal Phthalocyanines. *J. Phys. Chem. B* **2010**, *114* (31), 10017-10021.

[127] Medina, W. S. G.; Santos, N. A. G. dos Curti, C.; Tedesco, A. C.; Santos, A. C. dos. Effects of Zinc Phthalocyanine Tetrasulfonate-Based Photodynamic Therapy on Rat Brain Isolated Mitochondria. *Chem. Biol. Interact.* **2009**, *179* (2-3), 402-406.

[128] Boutin, E.; Wang, M.; Lin, J. C.; Mesnage, M.; Mendoza, D.; Lassalle-Kaiser, B.; Hahn, C.; Jaramillo, T. F.; Robert, M. Aqueous Electrochemical Reduction of Carbon Dioxide and Carbon Monoxide into Methanol with Cobalt Phthalocyanine. *Angew. Chemie Int. Ed.* **2019**, *58* (45), 16172–16176.

[129] Villagra, E.; Bedioui, F.; Nyokong, T.; Canales, J. C.; Sancy, M.; Páez, M. A.; Costamagna, J.; Zagal, J. H. Tuning the Redox Properties of Co-N_4 Macrocyclic Complexes for the Catalytic Electrooxidation of Glucose. *Electrochim. Acta* **2008**, *53* (14), 4883-4888.

[130] Vilakazi, S. L.; Nyokong, T. Voltammetric Determination of Nitric Oxide on Cobalt Phthalocyanine Modified Microelectrodes. *J. Electroanal. Chem.* **2001**, *512* (1-2), 56-63.

[131] Adeniyi, O.; Nwahara, N.; Mwanza, D.; Nyokong, T.; Mashazi, P. High-Performance Non-Enzymatic Glucose Sensing on Nanocomposite Electrocatalysts of Nickel Phthalocyanine Nanorods and Nitrogen Doped-Reduced Graphene Oxide Nanosheets. *Appl. Surf. Sci.* **2023**, *609*, 155234.

[132] Zhong, H.; Wang, M.; Ghorbani-Asl, M.; Zhang, J.; Ly, K. H.; Liao, Z.; Chen, G.; Wei, Y.; Biswal, B. P.; Zschech, E.; Weidinger, I. M.; Krasheninnikov, A. V; Dong, R.; Feng, X. Boosting the Electrocatalytic Conversion of Nitrogen to Ammonia on Metal-Phthalocyanine-Based Two-Dimensional Conjugated Covalent Organic Frameworks. *J. Am. Chem. Soc.* **2021**, *143* (47), 19992–20000.

[133] Shibata, M.; Furuya, N. Simultaneous Reduction of Carbon Dioxide and Nitrate Ions at Gas-Diffusion Electrodes with Various Metallophthalocyanine Catalysts. *Electrochim. Acta* **2003**, *48* (25-26), 3953-3958.

[134] Cao, R.; Thapa, R.; Kim, H.; Xu, X.; Kim, M. G.; Li, Q.; Park, N.; Liu, M.; Cho, J. Promotion of Oxygen Reduction by a Bio-Inspired Tethered Iron

Phthalocyanine Carbon Nanotube-Based Catalyst. *Nat. Commun.* **2013**, *4*, 1–7.

[135] Zhang, Z.; Dou, M.; Ji, J.; Wang, F. Phthalocyanine Tethered Iron Phthalocyanine on Graphitized Carbon Black as Superior Electrocatalyst for Oxygen Reduction Reaction. *Nano Energy* **2017**, *34*, 338–343.

[136] Chen, K.; Liu, K.; An, P.; Li, H.; Lin, Y.; Hu, J.; Jia, C.; Fu, J.; Li, H.; Liu, H.; Lin, Z.; Li, W.; Li, J.; Lu, Y. R.; Chan, T. S.; Zhang, N.; Liu, M. Iron Phthalocyanine with Coordination Induced Electronic Localization to Boost Oxygen Reduction Reaction. *Nat. Commun.* **2020**, *11* (1), 1–8.

[137] Fukuzumi, S.; Lee, Y. M.; Nam, W. Mechanisms of Two-Electron versus Four-Electron Reduction of Dioxygen Catalyzed by Earth-Abundant Metal Complexes. *ChemCatChem* **2018**, *10* (1), 9–28.

[138] Chen, P.; Lau, H.; Habermeyer, B.; Gros, C. P.; Barbe, J. M.; Kadish, K. M. Electrochemistry, Spectroelectrochemistry and Catalytic Activity of Biscobalt Bisporphyrin Dyads towards Dioxygen Reduction. *J. Porphyr. Phthalocyanines* **2011**, *15* (5–6), 467–479.

[139] Sun, B.; Ou, Z.; Meng, D.; Fang, Y.; Song, Y.; Zhu, W.; Solntsev, P. V.; Nemykin, V. N.; Kadish, K. M. Electrochemistry and Catalytic Properties for Dioxygen Reduction Using Ferrocene-Substituted Cobalt Porphyrins. *Inorg. Chem.* **2014**, *53* (16), 8600–8609.

[140] Chen, K.; Cao, M.; Ni, G.; Chen, S.; Liao, H.; Zhu, L.; Li, H.; Fu, J.; Hu, J.; Cortés, E.; Liu, M. Nickel Polyphthalocyanine with Electronic Localization at the Nickel Site for Enhanced CO2 Reduction Reaction. *Appl. Catal. B Environ.* **2022**, *306*, 121093.

[141] Kusama, S.; Saito, T.; Hashiba, H.; Sakai, A.; Yotsuhashi, S. Crystalline Copper (II) Phthalocyanine Catalysts for Electrochemical Reduction of Carbon Dioxide in Aqueous Media. *ACS Catal.* **2017**, *7* (12), 8382–8385.

[142] Gong, S.; Wang, W.; Xiao, X.; Liu, J.; Wu, C.; Lv, X. Elucidating Influence of the Existence Formation of Anchored Cobalt Phthalocyanine on Electrocatalytic CO_2-to-CO Conversion. *Nano Energy* **2021**, *84*, 105904.

[143] Liu, Z.; Chen, Z.; Bu, J.; Ma, W.; Zhang, L.; Zhong, H.; Cheng, L.; Li, S.; Wang, T.; Zhang, J. Metal Phthalocyanines as Efficient Electrocatalysts for Acetylene Semihydrogenation. *Chem. Eng. J.* **2022**, *431*, 134129.

[144] Ebadi, M.; Lever, A. B. P. Electroreduction of Nitrite Catalyzed by a Dinuclear Ruthenium Phthalocyanine Modified Graphite Electrode. *J. Porphyr. Phthalocyanines* **2003**, *7* (8), 529–539.

[145] Nyokong, T.; Vilakazi, S. Phthalocyanines and Related Complexes as Electrocatalysts for the Detection of Nitric Oxide. *Talanta* **2003**, *61* (1), 27–35.

[146] Chen, X.; Hu, X.; An, L.; Zhang, N.; Xia, D.; Zuo, X.; Wang, X. Electrocatalytic Dechlorination of Atrazine Using Binuclear Iron Phthalocyanine as Electrocatalysts. *Electrocatalysis* **2014**, *5* (1), 68–74.

[147] Chen, L.; Sagar, R. U. R.; Chen, J.; Liu, J.; Aslam, S.; Nosheen, F.; Anwar, T.; Hussain, N.; Hou, X.; Liang, T. Cobalt Phthalocyanine as an Efficient Catalyst for Hydrogen Evolution Reaction. *Int. J. Hydrogen Energy* **2021**, *46* (37), 19338–19346.

[148] Genc, E.; Yüzer, A. C.; Yanalak, G.; Harputlu, E.; Aslan, E.; Ocakoglu, K.; Ince, M.; Patir, I. H. The Effect of Central Metal in Phthalocyanine for Photocatalytic Hydrogen Evolution via Artificial Photosynthesis. *Renew. Energy* **2020**, *162*, 1340–1346.

[149] Kumar, Y.; Kibena-Põldsepp, E.; Kozlova, J.; Rähn, M.; Treshchalov, A.; Kikas, A.; Kisand, V.; Aruväli, J.; Tamm, A.; Douglin, J. C.; Folkman, S. J.; Gelmetti, I.; Garcés-Pineda, F. A.; Galán-Mascarós, J. R.; Dekel, D. R.; Tammeveski, K. Bifunctional Oxygen Electrocatalysis on Mixed Metal Phthalocyanine-Modified Carbon Nanotubes Prepared via Pyrolysis. *ACS Appl. Mater. Interfaces* **2021**, *13* (35), 41507–41516.

Chapter 2

Materials and Methods

This Chapter elaborates the experimental protocols adopted in the thesis along with the chemicals and materials used.

2.1. Materials.

The chemicals such as Trimellitic anhydride (97%), 4-nitro phthalimide (98%), 3-nitro phthalimide (98%), phthalimide (99%), cobalt (II) chloride hexahydrate (≥98%), copper (II) chloride dihydrate (≥98%), zinc (II) chloride hydrate (99.99%), nickel (II) chloride hexahydrate (≥98%), iron (III) chloride hexahydrate (≥98%), ammonium molybdate (99.99%), ammonium chloride (≥98%), sodium sulfide nonahydrate (≥98%), urea (99%), nitrobenzene (99%), toluene (99.5%), methanol (99%), ethanol (95%), isopropyl alcohol (99%), potassium hydroxide (99.98 %), sodium chloride (99%), hexane (95%), sulfuric acid (96%) and N,N dimethyl formamide (DMF) (99%) were obtained from Alfa Aesar, India. The carbon nanotubes (CNTs) were procured from C-Nano (FT 9000). The YP-50 carbon was purchased from Kuraray chemicals, India. Hydrochloric acid (HCl) (37%), perchloric acid (HClO$_4$) (70%), sodium hydroxide (≥99%), hydrogen peroxide (30%), dimethyl sulfoxide-d$_6$ (DMSO-d$_6$) (99.9 atom % D) and Nafion solutions (5 wt. %) were received from Sigma Aldrich, India.

2.2. Synthesis of metal phthalocyanines and their composite with carbon materials.

2.2.1. Synthesis of cobalt (II) phthalocyanine (CoPc), 1,8,15,22-tetra nitro cobalt (II) phthalocyanine (α-TNCoPc) and 2,9,16,23-tetra nitro cobalt (II) phthalocyanine (β-TNCoPc), 1,8,15,22-tetra nitro zinc (II) phthalocyanine

(α-TNZnPc) and 2,9,16,23-tetra nitro zinc (II) phthalocyanine (β-TNZnPc) molecules

Reported procedures were followed for the synthesis purpose.[1-3] For the synthesis of α-TNCoPc and β-TNCoPc, 3-nitro phthalimide/4- nitro phthalimide (3.86 g), urea (6 g), ammonium molybdate (0.05 g), ammonium chloride (0.5 g) and 30 mL of nitrobenzene were taken in a 250 mL round bottomed flask after finely grinding and mixing them together. Cobalt (II) chloride hexahydrate (1.2 g) was added into the reaction mixture after stirring it for 10 minutes, followed by vigorous stirring at 100°C for 30 minutes. The temperature was increased to 180°C at a ramping rate of 10°C per 30 minutes and was refluxed at this temperature for 4 hours. Following this the mixture was diluted with toluene (50 mL) and the resulting precipitate was filtered and washed thoroughly with hot water, methanol and hexane. Finally, the precipitate was dried in an oven at 80°C overnight. For the synthesis of CoPc, the same procedure was followed only nitro phthalimide was replaced with phthalimide whereas for the synthesis of α-TNZnPc and β-TNZnPc, same procedure was adopted by replacing the metal salt with zinc (II) chloride in place of cobalt (II) chloride.

2.2.2. Synthesis of 2,9,16,23-tetra carboxylic acid cobalt (II) phthalocyanine (TCCoPc), 2,9,16,23-tetra carboxylic acid copper (II) phthalocyanine (TCCuPc), 2,9,16,23-tetra carboxylic acid nickel (II) phthalocyanine (TCNiPc) and 2,9,16,23-tetra carboxylic acid iron (III) phthalocyanine (TCFePc) molecules

The synthesis was carried out as per the reported literature.[4-7] For the synthesis of TCCoPc, 8.3 g (34.9 mmol) of cobalt (II) chloride hexahydrate was pulverized with 27.5 g (143 mmol) of trimellitic anhydride, 50 g (0.833 mol) of urea, 0.574 g (2.14 mmol) of ammonium molybdate tetrahydrate, and 3.75 g (70 mmol) of ammonium chloride in a mortar until homogeneous mixture was obtained and until the color changed from white to dark purple. Subsequently, the mixture was placed in a three-necked flask and heated for 2 hours at 120^oC along with stirring and refluxing. Subsequently, the temperature was increased to 230^oC and maintained for 6 hours. The precipitate gradually changed from purple to bluish black. The mixture was cooled to room temperature and immersed in dilute hydrochloric acid for 1 hour. After washing it thoroughly with water, tetraamide phthalocyanine was obtained. The precipitate was dissolved in 1M NaOH-saturated NaCl solution (500 mL) and then refluxed and stirred for 24 hours at 98^oC. Then, the pH was adjusted to 2 using dilute hydrochloric acid and the resultant precipitate was separated through filtration. Ethanol and water were used to further rinse the precipitate until neutral. Finally, it was dried in a vacuum oven at 80^oC overnight to obtain tetra carboxylic acid cobalt (II) phthalocyanine (TCCoPc). Same procedure was adopted for the synthesis of copper, nickel and iron carboxylic acid phthalocyanine by replacing the metal salt with copper (II) chloride, nickel (II) chloride and iron (III) chloride respectively.

2.2.3. Synthesis of 2,9,16,23-tetra amino cobalt (II) phthalocyanine (TACoPc) molecule

The synthesis of 2,9,16,23-tetra amino cobalt (II) phthalocyanine was done by reducing the synthesised 2,9,16,23-tetra nitro cobalt (II) phthalocyanine according to reported procedure.[1-3] Firstly, tetra nitro cobalt (II) phthalocyanine (0.75 g), sodium sulfide nonahydrate (3 g) and 30 mL of DMF was taken in a 250 mL round bottomed flask and heated to 80°C for 2 hours. The resulting mixture was then cooled down to room temperature and diluted with 200 mL of ice water. The precipitate formed was filtered and washed thoroughly multiple times with hot water, methanol and finally hexane. Lastly the resultant precipitate was dried overnight at 80°C in a vacuum oven to obtain the TACoPc molecule.

2.2.4. Synthesis of metal phthalocyanine composite with carbon nanotubes (CNTs) of CoPc@CNT, α-TNCoPc@CNT, β-TNCoPc@CNT, TCCoPc@CNT, TCNiPc@CNT, TCCuPc@CNT and TCFePc@CNT

A known amount of the phthalocyanines were mixed separately with carbon nanotubes (CNTs) in a stoichiometric ratio of 3:7 (w/w) in DMF and sonicated for 30 minutes to obtain a well-mixed suspension. The resulting suspension was stirred under ambient temperature (25°C) for 24 hours. The precipitate was obtained by centrifugation which was thoroughly washed with DMF followed by ethanol. The product was dried overnight to get the final composite.[8, 9]

2.2.5. Synthesis of metal phthalocyanine composite with YP-50 carbon of CoPc@YP-50, TCCoPc@YP-50, TCCuPc@YP-50, TNCoPc@YP-50 and TACoPc@YP-50

The composite was prepared by sonicating a known amount of the phthalocyanine molecules with the YP-50 support in a stoichiometric weight ratio of 2:1 in N, N-dimethyl formamide (DMF) for 30 minutes. A well-mixed suspension was obtained which was further stirred at 80°C for ~ 24 hours. Following that the mixture was centrifuged and the resulting precipitate obtained was thoroughly washed with DMF and ethanol multiple times. Finally, the precipitate was dried overnight to get the final composite product.[8, 9]

2.3. Material characterization:

Matrix-assisted laser desorption ionization time-of-flight (MALDI-TOF) mass spectrometry was carried out with AB SCIEX 4800 Plus TOF/TOF instrument. UV-Visible, Fourier transform infrared (FTIR) and Raman spectroscopic measurements of the molecules as well as the molecules integrated with CNT and YP-50 (composites) were carried out with the Perkin Elmer Lambda 950, Bruker Alpha ATR-FTIR and LabRAM HR, Horbia Jobin Yvon spectrometer respectively for all the systems. Zeiss Ultraplus-4095 instrument was used to carry out the scanning electron microscopy (SEM) with energy dispersive X-ray (EDX) measurement. Nuclear magnetic resonance (NMR) spectra of the molecules were recorded with Bruker 400 MHz spectrometer. X-ray photo electron spectroscopy (XPS) was carried out using Thermo Scientific Kalpha+ spectrometer. The

measurements were carried out using a monochromatic Al Kα (1486.6 eV) X-ray source (72 W power) with a spot size of 400 µm. For electron energy analysis, a 180⁰ double focusing hemispherical analyzer with 128 channel detector was used. An ultralow energy co-axial electron beam and Ar+ ion beam was used for charge compensation. The final spectra were cross verified for charge accumulation with C1s standard value at 284.6 eV. The base pressure of the spectrometer was always better than ~5×10^{-9} mbar and ~1×10^{-7} mbar during data acquisition with flood gun on. The survey scan was collected at 200 eV pass energy and individual core-levels at 50 eV. Peak fitting was carried out using XPS Peak Fit software with a smart background.

In-situ electrochemical mass spectrometry was carried out with an HPR-40 R&D (Hiden analytical) Quadruple mass analyzer with a standard QIC inlet. The intensity count is represented as relative pressure with respect to a carrier gas. Quartz crystal microbalance (QCM) measurements were performed using EG&G QCM922A with carbon coated quartz crystals. Zetasizer Nano ZS90 Analyser (Malvern) instrument was used to perform the zeta potential measurements. Contact angle measurements were carried out using Holmarc's Contact Angle Meter. The specific surface area was calculated by the BET method with a Micromeritics-3-FLEX pore and a surface area analyser.

2.4. Electrochemical measurements:

2.4.1. Three electrode configurations

The electrochemical experiments were performed using the Biologic potentiostat (VMP 300) at 25°C and 1 atm pressure. For the electrochemical measurements, a three-electrode cell (10 ml volume, 2 mm electrode distance) configuration was used with a 3 mm diameter glassy carbon disk as the working electrode, a platinum wire as the counter electrode and an Ag/AgCl/Cl⁻ (3.5 M KCl) as the reference electrode. The hydrodynamic measurements (Rotating disk electrode technique (RDE) and Rotating ring disk electrode technique (RRDE)) was carried out with the PINE instrument integrated with PARSTAT MC (AMETEK) potentiostat at different rotation rates. All the potentials were finally converted to reversible hydrogen scale (RHE scale) based on the redox potentials for hydrogen redox reactions obtained on a Pt disc working electrode. The electrochemical investigations in chapter 3 were performed in 1 M KOH alkaline solution (pH 14) at a rotation rate of 1600 rpm with (CoPc), (α-TNCoPc) isomer and (β-TNCoPc) isomer modified glassy carbon electrodes. Drop casting method was used for the preparation of the electrodes. At first a homogenous dispersion of the catalyst (composites of phthalocyanine molecules with CNT) was prepared by sonicating a known amount of the composite material in isopropyl alcohol with 5 wt % nafion as the binder for an hour. Following that the prepared ink was drop casted on the glassy carbon disk electrode which was cleaned each time by polishing with 0.005 μm alumina powder followed by electrochemical cycling in the supporting electrolyte. Before starting the experiment, the solutions were purged with nitrogen gas for about 15 minutes. In chapter 4 the electrochemical investigations were carried out in an acidic solution without chloride ions (0.1 M HClO₄) and with chloride

ions (0.1 M $HClO_4$ + 1 M NaCl) at a rotation rate of 1600 rpm with all the three catalysts namely CoPc, TNCoPc and TCCoPc modified glassy carbon disk electrodes. All the experiments were carried out in Ar saturated solutions. Rotating Ring Disk Electrode (RRDE) method with a E7 RRDE (AFE7R9GCPT, Pine Research Instrumentation) having a glassy carbon as the disk electrode and platinum as the ring (GC-Pt) electrode was used to confirm the chlorine evolution reaction (CER). Linear sweep voltammetry was carried out on the disc electrode whereas a constant potential (0.95 V vs. RHE) where Cl_2 would get reduced to Cl^- was applied on the ring electrode. In chapter 5 the electrochemical investigations were done in 0.5 M sulfuric acid medium with CoPc, TCCoPc, TCCuPc, TACoPc and TNCoPc modified glassy carbon disk electrode. The same procedure as CNT was followed for preparation of the electrodes with YP-50 composite. All the experiments were carried out in Ar saturated solutions. In chapter 6 the electrochemical investigations were performed in 1M KOH medium with CoPc, TCCoPc, TCCuPc, TCNiPc and TCFePc modified glassy carbon disk electrode. The experiments were carried out in N_2 saturated solutions and O_2 saturated solutions for carrying out the oxygen reduction reaction (ORR).

2.4.2. Zn-air battery configuration:

Polarization and constant current tests for the battery were performed in a tri-electrode two-compartment flood cell configuration in full cell mode (Scheme 3.2) at 25^oC and 1 atm pressure. The two half-cells were separated by a Nafion-117 membrane. The anodic compartment contained zinc metal dipped in 0.2 M Zn $(OAc)_2$ solution dissolved in 6 M KOH solution (30 mL).

Cathodic compartment contained oxygen purged (100 ml/min) 6 M KOH solution (30 mL). The cathodic compartment housed both the ORR catalyst i.e., Pt/C with a catalyst loading of 0.5 mg/cm^2 as well as the OER catalyst i.e., β-TNCoPc, α-TNCoPc and unsubstituted CoPc with a catalyst loading of 2 mg/cm^2 on a carbon paper. The catalyst inks were prepared by dispersing a known amount of the phthalocyanine/CNT (30:70) in isopropyl alcohol with 5 wt % Nafion dispersion as the binder.

2.4.3. Electrochemical cell construction for Cl$_2$ estimation:

A three-electrode system was built in a two-compartment cell to separate the working electrode from the counter electrode. The reference electrode was placed at the same compartment as that of the working electrode. A Nafion 117 membrane was used to separate both the compartments of the cell. The Nafion membrane was pretreated with 5% H$_2$O$_2$ and heated at 60°C for an hour prior to its use. A Toray carbon paper having a catalyst loading of 2 mg/cm^2, a Pt disk electrode, and a KCl-saturated Ag/AgCl electrode were used as the working, counter, and reference electrodes respectively. The anodic chamber contained 0.1 M HClO$_4$ + 1 M NaCl as the electrolyte whereas the catholyte was 0.1 M HClO$_4$.

2.4.4. Supercapacitor Measurements (two electrode configuration):

Two-electrode cells consisted of composite (CoPc@YP-50 and TCCoPc@YP-50) electrode and an activated caron (AC) counter electrode. The device was assembled into two electrodes split test cell (MTI Cooperation, USA). The composite electrodes were fabricated using carbon paper (AvCarb MGL190) as the current collector. The counter AC electrode

fabrication was carried out by mixing 95 wt.% AC and 5 wt.% of Nafion binder manually in isopropyl alcohol until a homogenous ink was obtained. The ink was coated onto carbon paper sheets with a thickness of ~0.15 mm as supercapacitor electrodes (1.4 cm diameter), with a mass loading of ~7 mg/cm². Two-electrode split test cell were assembled according to established protocols.[10, 11] Briefly, with the molecular system a circular composite electrode (1.4 cm diameter) was fabricated with a mass loading of nearly 3.5 mg/cm². These electrodes were stacked with a glass fiber filter paper separator (thickness = 0.20 mm) wetted with 400 µL of 0.5 M H_2SO_4 aqueous electrolyte. The stack was enclosed in a split test cell and assembled with silicone O ring rubber to prevent electrolyte evaporation and short circuiting.

2.5. Formation of self-assembled monolayers (SAM) of CoPc, TNCoPc and TCCoPc on glassy carbon (GC) electrodes:

To understand the pristine behaviour of the phthalocyanine molecules, electrochemical investigations were performed by forming self-assembled monolayers of these molecules on glassy carbon electrode. The monolayer was formed by following the below mentioned procedure. Firstly a 2 mM solution of the phthalocyanine molecules were prepared by ultrasonicating for 30 minutes in DMF. The GC electrodes were initially polished by alumina powder followed by electrochemical cleaning. The polished GCs were electrochemically cleaned by cycling within the potential range 0 V to 1.3 V vs. RHE in 0.5M H_2SO_4 medium until reproducible cyclic voltammograms were obtained. Following this the GC electrodes were

thoroughly washed with water followed by DMF and dipped in the respective phthalocyanine solutions for 6 hours undisturbed. The modified electrodes were washed with fresh DMF to remove any physiosorbed molecules and finally washed with distilled water. The monolayer electrodes are now ready for electrochemical investigation.

2.6. Quartz crystal microbalance (QCM) studies:

To ensure the monolayer formation, Quartz Crystal Microbalance studies (QCM) were performed. The formation and surface coverage of the monolayers were confirmed by the QCM studies. It was carried out in a flow cell mode. Carbon coated quartz resonator (9.120 MHz) was used as the base crystal. A 0.5 mM molecular catalyst solution in dimethyl formamide (DMF) was flowed through the cell at a flow rate of 1 mL/min. Firstly, to get a stable background signal DMF solution was flowed for 2 hours. Following this, the catalyst solution was circulated through the cell for around 7 hours continuously to allow the formation of monolayer of molecules on the electrode surface. Finally, to remove any weakly adsorbed molecular catalyst on the surface of the carbon resonator, fresh DMF solution was passed again for 2 hours. To find the mass of adsorbed molecules on the crystal surface, Sauerbrey equation was used which correlates the frequency shift (Δ f) to mass change (Δ m) as shown in Equation 2.1:[12-14]

$$\Delta m = -c(\Delta f/n) \qquad \text{............ (2.1)}$$

where, Δ f is the net resonance frequency shift due to adsorption of the molecules, n is the overtone number which is taken as 1. The sensitivity (c)

of the QCM crystal was 5.608 ng cm^{-2}Hz^{-1}. The surface coverage (Γ, mol cm^{-2}) was calculated using equation 2.2:

$$\Gamma = \frac{\Delta m}{molecular\ mass} \qquad \ldots\ldots\ldots\ldots (2.2)$$

2.7. Density functional theory (DFT) calculations:

All calculations were done using the Quantum ESPRESSO (QE) software (version 7.0),[15, 16] which relies on a plane wave-based implementation of spin polarized density functional theory. In order to account for the electron-ion interactions, ultrasoft pseudopotentials were used.[17] The wavefunctions and charge densities were expanded using a plane wave basis with kinetic energy cut-offs 55 Ry and 550 Ry, respectively. The following valence electronic configurations were used for each of the species:

Co: $3s^2 3p^6 3d^7 4s^2$; N: $2s^2 2p^3$; C: $2s^2 2p^2$; H: $1s^1$; O: $2s^2 2p^4$
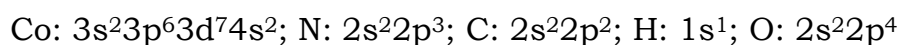
Perdew, Burke, and Ernzerhof (PBE) parametrization of the generalized gradient approximation (GGA) was used to describe the electron-electron exchange and correlation energies.[18] To correctly account for the strong Coulomb and exchange interactions between the Co-d electrons, we have used the Cococcioni and Gironcoli implementation of DFT+ U method.[19] Based on a recent study by Sanyal et al., we have used an Ueff = 4.0 eV.[20] Grimme's Dispersion (DFT-D2)[21, 22] corrections were introduced to describe non-local van der Waals interactions, which are not captured by conventional GGA exchange correlation functionals. Brillouin zone integrations were performed using the Γ-point only. To speed up

convergence, we have used Gaussian smearing, with a smearing width of 0.002 Ry. In order to minimize the interactions between the periodic images, we have placed the molecules in a big box with dimensions 32 Å × 32 Å × 15 Å. This results in a vacuum of about 15 Å along all the three directions. The charges on the Co atoms are computed using the Density Derived Electrostatic and Chemical (DDEC) method of charge partitioning.[23-28]

The reactivity of these molecules can be characterized by computing some of their properties, namely, gap between the highest occupied molecular orbital (HOMO) and lowest unoccupied molecular orbital (LUMO), Chemical Hardness (η), Chemical softness (1/η), Chemical Potential (μ) and Electronegativity, (x). These are computed as shown below:

(1) HOMO-LUMO gap (E_g): The HOMO-LUMO gap is given by

$$E_g = E_{LUMO} - E_{HOMO} \qquad .... (2.3)$$

Where E_{LUMO} and E_{HOMO} are the positions of the LUMO and HOMO of the molecule.

(2) Chemical Hardness (η): The chemical hardness is computed as follows:

$$\eta = \frac{1}{2}(IP - EA) \qquad .... (2.4)$$

Where *IP* and *EA* represent the ionization potential and electron affinity respectively. Within the limitations of Koopman's theorem, the IP and EA are the negative of the HOMO and LUMO eigenvalues respectively. Hence, the chemical hardness is half of the HOMO-LUMO gap in the material. We note that since in DFT calculations, the HOMO-LUMO gap is usually

underestimated, our computed values of η are also underestimated. However, the trends in the value of the chemical hardness are usually reproduced qualitatively. The chemical softness is given by the inverse of chemical hardness.

(3) Chemical potential (μ): The chemical potential is computed as:

$$\mu = -\frac{IP+EA}{2} \qquad\qquad .... (2.5)$$

(4) Electronegativity (x): The electronegativity is given as the negative of the chemical potential.

In order to compute the above quantities, we need the absolute values of the positions of HOMO and LUMO. However, in plane wave pseudopotential based DFT calculations, the zero of the energy axes is not well-defined. Hence to compare between different systems, we have set the vacuum energy at zero. The energy eigenvalues for each system have been scaled with respect to the vacuum energy.

2.8. Calculation of number of electron (n) and H_2O_2% yield for ORR:

Rotating Ring Disk Electrode (RRDE) method with GC disk and Au ring electrode was used to calculate number of electrons and H_2O_2 percentage. Linear sweep voltammetry was carried out on the disc electrode whereas the ring was biased at H_2O_2 oxidation potential (1V vs RHE).[29]

The number of electron (n) is calculated using the following equation:

$$n = 4 \times \frac{I_d}{I_d + \frac{I_r}{N_c}} \qquad\qquad \text{............ (2.6)}$$

and the % of peroxide (p) produced was calculated with the following equation:

$$p = 2 \times \frac{\frac{I_r}{N_c}}{I_d + \frac{I_r}{N_c}} \qquad\qquad \text{............ (2.7)}$$

where I_d, I_r and N_c represents the disk current, ring current and collection efficiency of the RRDE respectively. N_c was found to be 0.37 which was calculated by measuring the ratio of disk current to ring current in equimolar concentrations of potassium ferrocyanide and potassium ferricyanide.

2.9. Specific capacitance (C_{sp}), energy density and power density calculations for molecule-based supercapacitor:

2.9.1. For three electrode configurations:

The specific capacitance (C_{sp}) was calculated from cyclic voltammetry (CV) curves at various scan rates using the following equation 2.8.[30-32]

$$C_{sp} = \frac{\int i \, dV}{2 \times m \times v \times \Delta V} \qquad\qquad \text{............ (2.8)}$$

where, C_{sp} is specific capacitance in (F/g), $\int i.dV$ is the integrated area in the cyclic voltammogram, m is the mass of the active material (g), v is the scan rate (mV s^{-1}) and ΔV is the voltage window (V).

The C_{sp} from the galvanostatic charge-discharge (GCD) measurements was calculated using the equation 2.9.

$$C_{sp} = \frac{I \times \Delta t}{m \times \Delta V} \qquad \text{............ (2.9)}$$

where, C_{sp} is specific capacitance (F/g), I is the applied current (A), ΔV represents the potential window (V), Δt signifies discharge time (s) and m is the mass of the active material (g).

2.9.2. For asymmetric two electrode configurations:

The specific capacity, energy, and power for the two-electrode cells were calculated from galvanostatic charge discharge data (discharge cycle). The specific capacity was calculated using the equation 2.10.

$$Q_s = \frac{I \times t}{mc} \qquad \text{............ (2.10)}$$

where I is the applied current, t is the discharge time, and m_c is the mass of active material (CoPc/TCCoPc@YP-50) on the cathode. For calculating specific energy and power of the two-electrode cell, the total mass of cell components was used according to reported literature.[33, 34] Specific energy is calculated using the equation 2.11.

$$E_s = \frac{I \times t \times \Delta V}{mtotal} \qquad \text{............ (2.11)}$$

where ΔV is the potential window and m_{total} is given by equation 2.12.

$$m_{total} = m_a + m_c \qquad \text{............ (2.12)}$$

where m_a is the mass of Activated carbon (AC) required to balance the measured discharge Q or C, respectively.

Specific power was calculated using the equation 2.13.

$$P_s = \frac{I \times \Delta V}{mtotal} \qquad \text{............ (2.13)}$$

2.10. Capacitive contributions analysis:

The capacitive contribution to the current response can be obtained by analysing the cyclic voltammograms. The current response at different potentials is expressed as being the combination of surface capacitive effects and diffusion-controlled processes.[35, 36] The capacitive effects were characterized by analyzing the cyclic voltammetry data at various sweep rates as per equation 2.14. Plot of $i/v^{1/2}$ vs. $v^{1/2}$ for both the molecules will provide the non-faradaic and faradaic contributions at various potentials. In equation 2.14, $k_1 v$ and $k_2 v^{1/2}$ correspond to the current contributions from the surface capacitive effects and the diffusion-controlled process, respectively. Thus, by determining k_1 and k_2, it is possible to quantify, the current fraction arising out of these contributions. The capacitive currents and diffusion currents are determined from the total current using equation 2.14.

$$i\,(V) = k_1 v + k_2 v^{1/2} \qquad \text{............. (2.14)}$$

2.11. Characteristic time constant (τ_0), self-discharge current (i_{sd}) and leakage current (i_{lk}) measurements:

The time constant (τ_0) (also known as the relaxation time) indicates the minimum time required to fully discharge the capacitor.[37-39] It is estimated using the equation 2.15.

$$\tau_0 = 1/f_0 \qquad \text{............. (2.15)}$$

The frequency also known as "knee" or "onset" frequency (f_0) which reflects the power capability of a supercapacitor, is calculated by plotting imaginary part of capacitance (C") as a function of frequency. The C" is associated with the energy loss and the real part (C') reflects the deliverable capacitance and these can be calculated according to the following equations 2.16 and 2.17.[38, 40]

$$C''(\omega) = Z'(\omega) \ / \ \omega \, |Z(\omega)|^2 \qquad \ldots\ldots\ldots\ldots \text{(2.16)}$$

$$C'(\omega) = -Z''(\omega) \ / \ \omega \, |Z(\omega)|^2 \qquad \ldots\ldots\ldots\ldots \text{(2.17)}$$

where $|Z(\omega)|$ is the impedance modulus and $C''(\omega)$ and $C'(\omega)$ is imaginary and real parts of capacitance.

Self-discharge measurements were performed by measuring the time within which the voltage dropped from the completely charged state to the potential equal to mean of charged state and the open circuit voltage (OCV). Leakage current was calculated by holding the potential at full charge and the current required to maintain the fully charged state was measured over time.[41-43] Before self-discharge and leakage current measurements, initially, the system was charged with a rate of 1 mA g^{-1} to 1 V and then held at this voltage for 4 hours. After a full charge, the system was allowed to undergo self-discharge for ~15 hours while monitoring the open circuit voltage decay. The self-discharge currents were estimated by using equation 2.18.[42]

$$i_{sd} = C \times \frac{(V1 - V2)}{\Delta t} \qquad \ldots\ldots\ldots\ldots \text{(2.18)}$$

Where V_1 represents the potential of charged state, V_2 represents the mean potential between charged state and the open circuit voltage and Δt is the time taken in seconds to reach V_2.

2.12. References:

[1]   Lukyanets, E. A.; Nemykin, V. N. The key role of peripheral substituents in the chemistry of phthalocyanines and their analogs. *J. Porphyr. Phthalocyanines,* **2010**, *14*, 1–40.

[2]   Al-lami, A. K.; Majeed, N. N.; Al-mowali, A. H. Synthesis, Mesomorphic and Molar Conductivity Studies of Some Macrocyclic Phthalocyanine Palladium (II). *Chem. Mater. Res.* **2013**, *3* (4), 59.

[3]   Kottaichamy, A. R.; Makri Nimbegondi Kotresh, H.; Devendrachari, M. C.; Thimmappa, R.; Paswan, B.; Tiwari, O.; Chanda, V.; Gaikwad, P.; Thotiyl, M. O. *J. Phys. Chem. C,* **2015**, *119*, 28276–28284.

[4]   Chen, C.; Ma, Z.; Zhou, S.; Li, T.; Sun, X. Cobalt-Tetracarboxyl-Phthalocyanine Linked with Fe_3O_4/Chitosan Microsphereas—Efficient Catalyst for Dye Degradation. *Catal. Letters* **2017**, *147* (9), 2399–2409.

[5]   Sun, X.; Wang, L.; Tan, Z. Improved Synthesis of Soluble Metal-Free/Metal Phthalocyanine Tetracarboxylic Acids and Their Application in the Catalytic Epoxidation of Cyclohexene. *Catal. Letters* **2015**, *145* (4), 1094–1102.

[6]   Achar, B. N.; Fohlen, G. M.; Parker, J. A.; Keshavayya, J. Preparation & Structural Investigations of Copper (II), Cobalt (II), Nickel (II) & Zinc (II) Derivatives of 2,9, 16,23-Phthalocyanine Tetracarboxylic Acid. *Indian J. Chem.* **1988**, *27*, 411–416.

[7]   Hosu, I. S.; Wang, Q.; Vasilescu, A.; Peteu, S. F.; Raditoiu, V.; Railian, S.; Zaitsev, V.; Turcheniuk, K.; Wang, Q.; Li, M.; Boukherroub, R.; Szunerits, S. Cobalt Phthalocyanine Tetracarboxylic Acid Modified Reduced Graphene Oxide: A Sensitive Matrix for the Electrocatalytic

Detection of Peroxynitrite and Hydrogen Peroxide. *RSC Adv.* **2015**, *5* (2), 1474–1484.

[8]   Cao, R.; Thapa, R.; Kim, H.; Xu, X.; Kim, M. G.; Li, Q.; Park, N.; Liu, M.; Cho, J. Promotion of Oxygen Reduction by a Bio-Inspired Tethered Iron Phthalocyanine Carbon Nanotube-Based Catalyst. *Nat. Commun.* **2013**, *4*, 1–7.

[9]   Zhu, M.; Chen, J.; Guo, R.; Xu, J.; Fang, X.; Han, Y.-F. Cobalt Phthalocyanine Coordinated to Pyridine-Functionalized Carbon Nanotubes with Enhanced CO_2 Electroreduction. *Appl. Catal. B Environ.* **2019**, *251*, 112–118.

[10]   Li, H.; Lang, J.; Lei, S.; Chen, J.; Wang, K.; Liu, L.; Zhang, T.; Liu, W.; Yan, X. A High-Performance Sodium-Ion Hybrid Capacitor Constructed by Metal–Organic Framework–Derived Anode and Cathode Materials. *Adv. Funct. Mater.* **2020**, *8* (30), 1–12.

[11]   Singh, T. I.; Rajeshkhanna, G.; Kshetri, T.; Kim, N. H.; Lee, J. H. High-performance solid-state hybrid supercapacitor enabled by metal-organic framework-derived multi-component hybrid electrodes of Co-N-C nanofibers and Co2-xFexP-N-C micropillars *J. Mater. Chem. A*, **2018**, *8*, 26158–26174.

[12]   Somashekarappa, M. P.; Keshavayya, J.; Sampath, S. Self-Assembled Molecular Films of Tetraamino Metal (Co, Cu, Fe) Phthalocyanines on Gold and Silver. Electrochemical and Spectroscopic Characterization. *Pure Appl. Chem.* **2002**, *74* (9), 1609–1620.

[13]   Makinde, Z. O.; Louzada, M.; Mashazi, P.; Nyokong, T.; Khene, S. Electrocatalytic Behaviour of Surface Confined Pentanethio Cobalt (II) Binuclear Phthalocyanines towards the Oxidation of 4-Chlorophenol. *Appl. Surf. Sci.* **2017**, *425*, 702–712.

[14]   Fleming, B. D.; Praporski, S.; Bond, A. M.; Martin, L. L. Electrochemical Quartz Crystal Microbalance Study of Azurin Adsorption onto an Alkanethiol Self-Assembled Monolayer on Gold. *Langmuir* **2008**, *24* (1), 323–327.

[15]   Giannozzi, P.; Baroni, S.; Bonini, N.; Calandra, M.; Car, R.; Cavazzoni, C.; Ceresoli, D.; Chiarotti, G. L.; Cococcioni, M.; Dabo, I.; Dal Corso, A.;

De Gironcoli, S.; Fabris, S.; Fratesi, G.; Gebauer, R.; Gerstmann, U.; Gougoussis, C.; Kokalj, A.; Lazzeri, M.; Martin-Samos, L.; Marzari, N.; Mauri, F.; Mazzarello, R.; Paolini, S.; Pasquarello, A.; Paulatto, L.; Sbraccia, C.; Scandolo, S.; Sclauzero, G.; Seitsonen, A. P.; Smogunov, A.; Umari, P.; Wentzcovitch, R. M. QUANTUM ESPRESSO: A Modular and Open-Source Software Project for Quantum Simulations of Materials. *J. Phys. Condens. Matter* **2009**, *21*, 395502.

[16] Giannozzi, P.; Andreussi, O.; Brumme, T.; Bunau, O.; Nardelli, M. B.; Calandra, M.; Car, R.; Cavazzoni, C.; Ceresoli, D.; Cococcioni, M.; others. Advanced Capabilities for Materials Modelling with Quantum ESPRESSO. *J. Phys. Condens. Matter* **2017**, *29* (46), 465901.

[17] Vanderbilt, D. Soft self-consistent pseudopotentials in a generalized eigenvalue formalism, Phys. Rev. B **1990**, *41*, 7892.

[18] Perdew, J. P.; Burke, K.; Ernzerhof, M.; Generalized Gradient Approximation Made Simple. *Phys. Rev. Lett.,* **1996,** *77*, 3865-3868.

[19] Cococcioni, M.; Gironcoli, S. D. Linear response approach to the calculation of the effective interaction parameters in the LDA+U method, *Phys. Rev. B* **2005**,*71*, 035105.

[20] Brumboiu, I. E.; Haldar, S.; Lüder, J.; Eriksson, O.; Herper, H. C.; Brena, B.; Sanyal, B. Influence of Electron Correlation on the Electronic Structure and Magnetism of Transition-Metal Phthalocyanines, *J. Chem. Theory Comput.* **2016**, *12* (4), 1772–1785.

[21] Grimme, S. Semiempirical GGA-Type Density Functional Constructed with a Long-Range Dispersion Correction, *J.Comp. Chem.* **2006**, *27*, 1787.

[22] Barone, V.; Casarin, M.; Forrer, D.; Pavone, M.; Sambi, M.; Vittadini, A. Role and Effective Treatment of Dispersive Forces in Materials: Polyethylene and Graphite Crystals as Test Cases. *J. Comp. Chem.* **2009**, *30*, 934.

[23] Manz, T. A. Introducing DDEC6 atomic population analysis: part 3. Comprehensive method to compute bond orders. *RSC Advances,* **2017,** *7,* 45552-45581.

[24] Gabaldon Limas, N.; Manz, T. A. Introducing DDEC6 atomic population analysis: part 2. Computed results for a wide range of periodic and nonperiodic materials, *RSC Advances*, **2016**, *6*, 45727-45747.

[25] Manz, T. A.; Gabaldon Limas, N. Introducing DDEC6 atomic population analysis: part 1. Charge partitioning theory and methodology. *RSC Advances*, **2016**, *6*, 47771-47801.

[26] Manz, T. A.; Sholl, D. S. Improved Atoms-in-Molecule Charge Partitioning Functional for Simultaneously Reproducing the Electrostatic Potential and Chemical States in Periodic and Non-Periodic Materials. *J. Chem. Theory Comput.* **2012**, *8*, 2844-2867.

[27] Manz, T. A.; Sholl, D. S. Methods for Computing Accurate Atomic Spin Moments for Collinear and Noncollinear Magnetism in Periodic and Nonperiodic Materials. *J. Chem. Theory Comput.,* **2011**, *7*, 4146-4164.

[28] Manz, T. A.; Sholl, D. S. Chemically Meaningful Atomic Charges that Reproduce the Electrostatic Potential in Periodic and Nonperiodic Materials. *J. Chem. Theory Comput.,* **2010**, *6,* 2455-2468.

[29] Zhou, R.; Zheng, Y.; Jaroniec, M.; Qiao, S. Z. Determination of the Electron Transfer Number for the Oxygen Reduction Reaction: From Theory to Experiment. *ACS Catal.* **2016**, *6* (7), 4720–4728.

[30] Wu, H.; Lou, Z.; Yang, H.; Shen, G. A Flexible Spiral-Type Supercapacitor Based on ZnCo2O4 Nanorod Electrodes. *Nanoscale* **2015**, *7* (5), 1921–1926.

[31] Wang, Q.; Wang, X.; Xu, J.; Ouyang, X.; Hou, X.; Chen, D.; Wang, R.; Shen, G. Flexible Coaxial-Type Fiber Supercapacitor Based on NiCo2O4 Nanosheets Electrodes. *Nano Energy* **2014**, *8*, 44–51.

[32] Bae, J.; Song, M. K.; Park, Y. J.; Kim, J. M.; Liu, M.; Wang, Z. L. Fiber Supercapacitors Made of Nanowire-Fiber Hybrid Structures for Wearable/Flexible Energy Storage. *Angew. Chemie - Int. Ed.* **2011**, *50* (7), 1683–1687.

[33] Ramachandran, R.; Hu, Q.; Wang, F.; Xu, Z. X. Synthesis of N-CuMe 2 Pc Nanorods/Graphene Oxide Nanocomposite for Symmetric Supercapacitor Electrode with Excellent Cyclic Stability. *Electrochim. Acta* **2019**, *298*, 770–777.

[34] Madhuri, K. P.; John, N. S. Supercapacitor Application of Nickel Phthalocyanine Nanofibres and Its Composite with Reduced Graphene Oxide. *Appl. Surf. Sci.* **2018**, *449*, 528–536.

[35] Wang, J.; Polleux, J.; Lim, J.; Dunn, B. Pseudocapacitive Contributions to Electrochemical Energy Storage in TiO_2 (Anatase) Nanoparticles. *J. Phys. Chem. C* **2007**, *111* (40), 14925–14931.

[36] Han, D.; Wang, W.; Yu, S.; Qi, W.; Ling, R.; Yang, C.; Liu, G. Stable β-Form Zinc Phthalocyanine Cathodes for Flexible Zn-Ion Hybrid Supercapacitors with Ultra-Long Cycling Life. *Chem. Eng. J.* **2023**, *468*, 143875.

[37] Yang, K.; Cho, K.; Kim, S. Effect of Carbon Black Addition on Thermal Stability and Capacitive Performances of Supercapacitors. *Sci. Rep.* **2018**, *8* (1), 11989.

[38] Taberna, P. L.; Simon, P.; Fauvarque, J. F. Electrochemical Characteristics and Impedance Spectroscopy Studies of Carbon-Carbon Supercapacitors. *J. Electrochem. Soc.* **2003**, *150* (3), A292.

[39] Yoo, Y.; Kim, M. S.; Kim, J. K.; Kim, Y. S.; Kim, W. Fast-Response Supercapacitors with Graphitic Ordered Mesoporous Carbons and Carbon Nanotubes for AC Line Filtering. *J. Mater. Chem. A* **2016**, *4* (14), 5062–5068.

[40] Rodrigues, A. C.; Da Silva, E. L.; Quirino, S. F.; Cuña, A.; Marcuzzo, J. S.; Matsushima, J. T.; Gonçalves, E. S.; Baldan, M. R. Ag@Activated Carbon Felt Composite as Electrode for Supercapacitors and a Study of Three Different Aqueous Electrolytes. *Mater. Res.* **2018**, *22*, 1–9.

[41] Wang, X.; Song, T. Buckypaper Templating Ni-Co Hydroxide Nanosheets as Free-Standing Electrodes for Ultrathin and Flexible Supercapacitors. *New J. Chem.* **2016**, *40* (9), 8006–8011.

[42] Mourad, E.; Coustan, L.; Lannelongue, P.; Zigah, D.; Mehdi, A.; Vioux, A.; Freunberger, S. A.; Favier, F.; Fontaine, O. Biredox Ionic Liquids with Solid-like Redox Density in the Liquid State for High-Energy Supercapacitors. *Nat. Mater.* **2017**, *16* (4), 446–454.

[43] El-Kady, M. F.; Kaner, R. B. Scalable Fabrication of High-Power Graphene Micro-Supercapacitors for Flexible and on-Chip Energy Storage. *Nat. Commun.* **2013**, *4* (1), 1475.

Chapter 3

Ligand Assisted Oxygen Redox Chemistry for Energy Efficient Zinc-Air Battery

Chapter 3

ABSTRACT: This Chapter elucidates the role of ligand via its regioisomerism in oxygen redox chemistry. The role of ligand-isomerism in modulating the mechanisms and kinetics associated with charge/discharge-chemistry of an aqueous metal-air battery are also investigated. The dominant electron-withdrawing inductive effect (-I effect) and the diminished electron-withdrawing resonance effect (-R effect) in the α-NO$_2$ isomeric molecule noticeably diminishes the rate of oxygen reduction (ORR) and oxygen evolution reactions (OER) on the catalytic Co centre. In the β-NO$_2$ isomeric molecule, the absence of repulsive field-effect due to the spatial separation of functionality, leads to combined involvement of –I and –R effects which noticeably enhances the OER and ORR kinetics on the same catalytic Co centre. This chapter demonstrates that, the regioisomerism of the -NO$_2$ functionality, does not alter the mechanistic pathways of OER/ORR but rather influence their respective kinetics. When isomeric molecules are integrated as molecular electrocatalysts to aid the charge-chemistry of an aqueous Zn-air battery, the overpotential required could be decreased by ~250 mV in case of β-NO$_2$ isomer compared to the α-NO$_2$ isomer at all current densities leading to a round trip efficiency as high as 60%. This work opens up alternative strategies in the design of new and novel molecular platforms to target the overall energy efficiency of electrochemical energy storage and conversion devices.
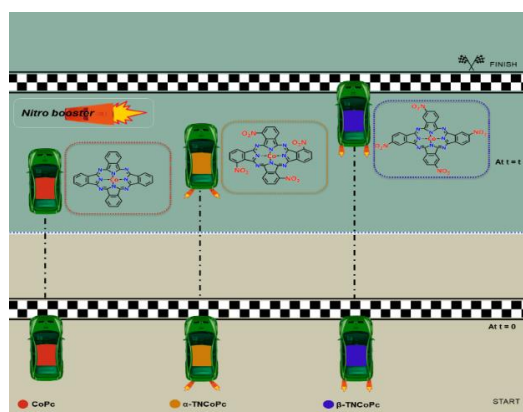
3.1. Introduction:

The oxygen redox chemistry, encompassing the electrochemical reduction of oxygen (ORR) and the water oxidation reaction (OER), stands as vital processes in electrochemical energy systems, including fuel cells[1-6] and rechargeable metal-air batteries.[7-11] Nevertheless, the slow kinetics associated with breaking the molecular oxygen bonds, even on noble metal electrocatalysts, poses a limitation to the efficiency of ORR in electrochemical energy systems.[1-12] While noble metals like platinum, gold, and silver, as well as metal oxides and mixed oxides such as spinels and perovskites, have been extensively studied as electrocatalysts for ORR, platinum remains the benchmark ORR electrocatalyst.[13-17] However, challenges related to its availability and cost constrain its practical viability in electrochemical power systems.[12,16-18] Consequently, there is a need to design and develop low-cost catalysts using earth-abundant metals capable of catalyzing ORR at lower overpotential through a direct four-electron transfer to molecular oxygen.[15,18-22] Similarly, the oxygen evolution reaction is also associated with a number of challenges, the most important ones being requirement of high overvoltage for the water splitting reaction which hampers the long-term stability of the catalysts. Also, till date the benchmark electrocatalysts for OER is based on the high-cost noble metal catalysts such as IrO_2 and RuO_2. Therefore, the need of the hour is to develop alternative oxygen reduction reaction (ORR)/oxygen evolution reaction (OER) catalysts based on earth-abundant metals with high activity and durability.[23-26] In this context, molecular electrocatalysts like metal

phthalocyanines (MPcs) and metal porphyrins (MPs) have emerged at the forefront of energy research due to their high degree of tunability in electronic and geometric parameters.[27-31] Among these phthalocyanines, the Co based systems are explored as they have been found to be electrocatalytically active towards ORR/OER.[32-35]

In this Chapter, the role of ligand in molecular electrocatalysts is explored in the ubiquitous oxygen redox chemistry. The active role of ligand in oxygen redox reactions such as oxygen reduction reactions (ORR) and oxygen evolution recations (OER) are particluarly investigated by tuning the ligand isomerism (α and β-TNCoPc isomers) around the same catalytic Co centre. Interestingly, when nitro substituted cobalt phthalocyanines (TNCoPc) were explored for oxygen redox chemistry, it has been observed β isomerization of the ligand tunes the OER kinetics without altering the mechanistic pathways of the reaction. For these reasons, β-TNCoPc isomer catalyst is further explored for Zinc-air battery (ZAB) to target their overall round-trip efficiency. The present work demonstrates an alternative approach in the design of efficient molecular electrocatalysts to target electrochemical reactions relevant to energy storage and conversion.

3.2. Results and Discussions:

The primary aim of this Chapter is to explore, whether the isomerism of a ligand functionality influences the reaction mechanism or reaction kinetics with respect to a specific reaction pathway. To shed light into these, nitro substituted phthalocyanines containing earth abundant central metals like Co are explored to target oxygen reduction (ORR) and oxygen

evolution (OER) reactions. This is because, the complexity of ORR/OER is the limiting factor which dictates the round-trip efficiency of aqueous metal-air batteries and reversible fuel cells.[36–38]

## 3.2.1. Characterisation of CoPc, the isomeric nitro molecules and their composites with CNTs.

To explore the implications of ligand isomerism in ORR/OER; the regioisomers of tetra-nitro cobalt phthalocyanine (TNCoPc) with -NO$_2$ substitution at the α (α-TNCoPc) and β (β-TNCoPc) positions were synthesized and characterized, Scheme 3.1 (please refer to chapter 2, section 2.2.1, pages 50-51 for more information).[28–35] High-resolution mass spectrometry (HRMS) demonstrated the parent ion peak at m/z value of ~751 for the α and β isomers and at ~573 for unsubstituted cobalt phthalocyanine (CoPc) which are close to their molecular masses, (Figure 3.1). UV-vis spectra of these molecules demonstrated absorption bands in the range of 550-750 nm and 300-400 nm respectively which are characteristic Q and B bands of metal phthalocyanines (Figure 3.2a). The absorption band close to 320 nm is attributed to the charge transfer band in metal phthalocyanines.[17,28,30] A comparison of the isomeric molecule's UV-vis spectra suggests a red-shifted Q band in the β isomer reflecting comparatively extensive delocalization of charge density in the β isomer compared to the α isomer.[39–41] FTIR spectra of synthesized unsubstituted CoPc and the isomeric molecules (Figure 3.2b), show the respective spectral bands as mentioned in Table 3.1. Raman spectra (Figure 3.2c), reveals all the phthalocyanine signature peaks (Table 3.2), as reported in the

literature.[42–44] NMR spectroscopic analysis of α and β-TNCoPc isomers were further carried out, for more in-depth structural elucidation of the isomeric molecules by using the corresponding Zn based diamagnetic nitro phthalocyanines (α-TNZnPc and β-TNZnPc). The distinct chemical shifts of aromatic protons labelled as H_A, H_B and H_C (Figure 3.2d) in the NMR spectra of α and β isomers of TNZnPc, indicate distinctly different chemical environments surrounding these protons. The 2D (COSY) NMR further elucidates the formation of the isomeric molecules as shown in Scheme 3.1. In the case of the α isomeric molecule, the H_B proton couples both with the H_A as well as the H_C protons (Figure 3.2e) whereas for the β isomeric molecule there is only one correlation. The H_B proton couples only with the H_A proton (Figure 3.2f). Thus, this difference in the way the protons couple with each further confirm the formation of both the nitro substituted isomeric cobalt phthalocyanine molecules.
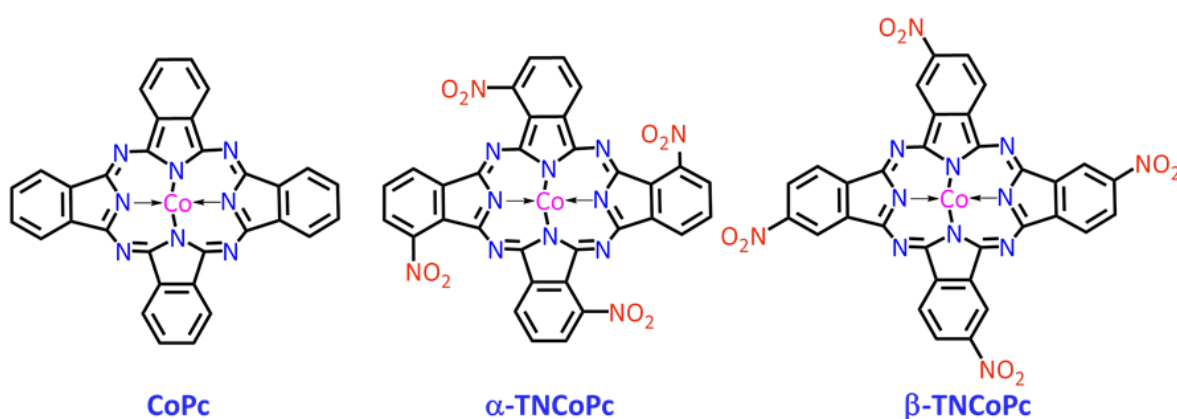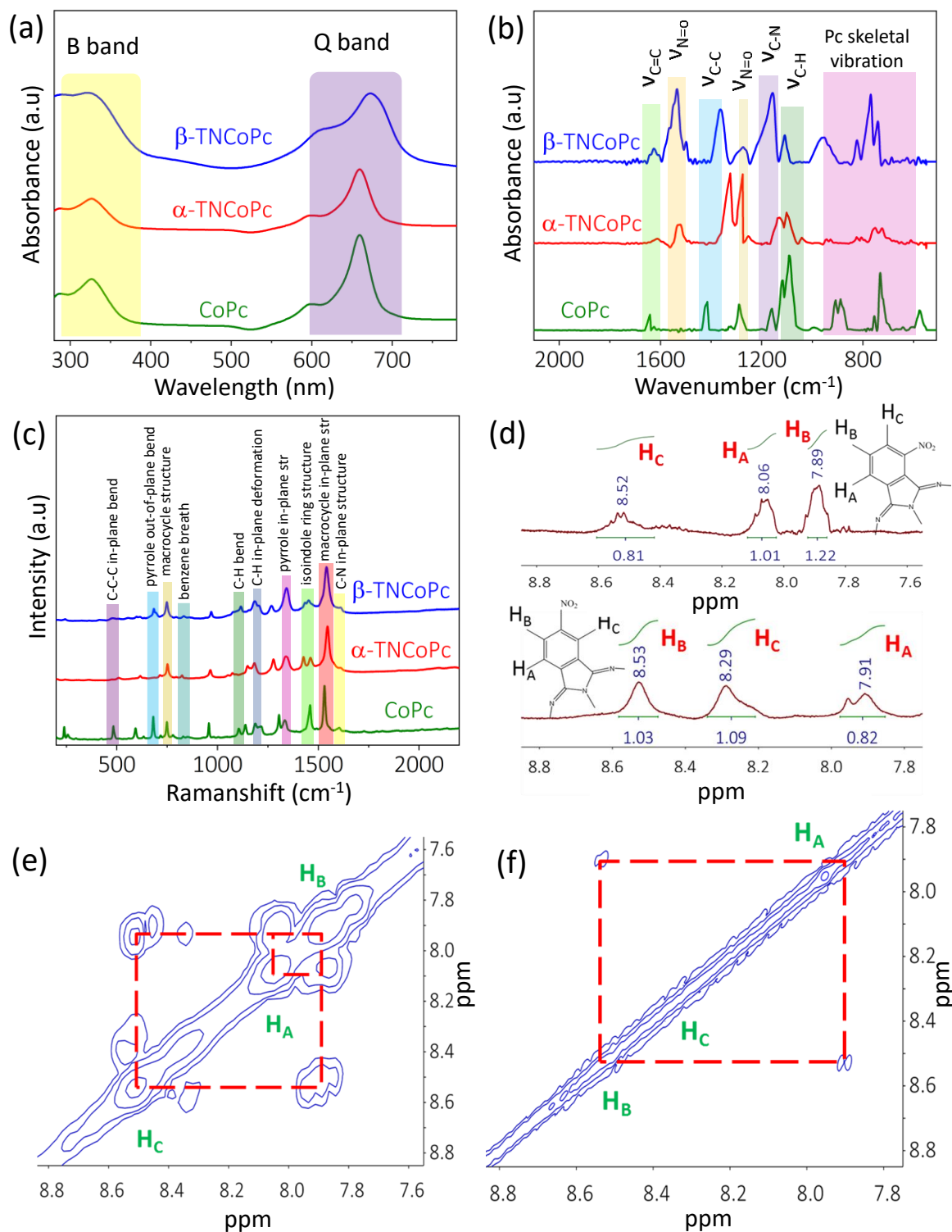

Scheme 3.1. Molecular structures of unsubstituted cobalt phthalocyanine CoPc (Left), and isomeric nitro substituted cobalt phthalocyanines namely the α-TNCoPc (middle) and β-TNCoPc (right) molecules.
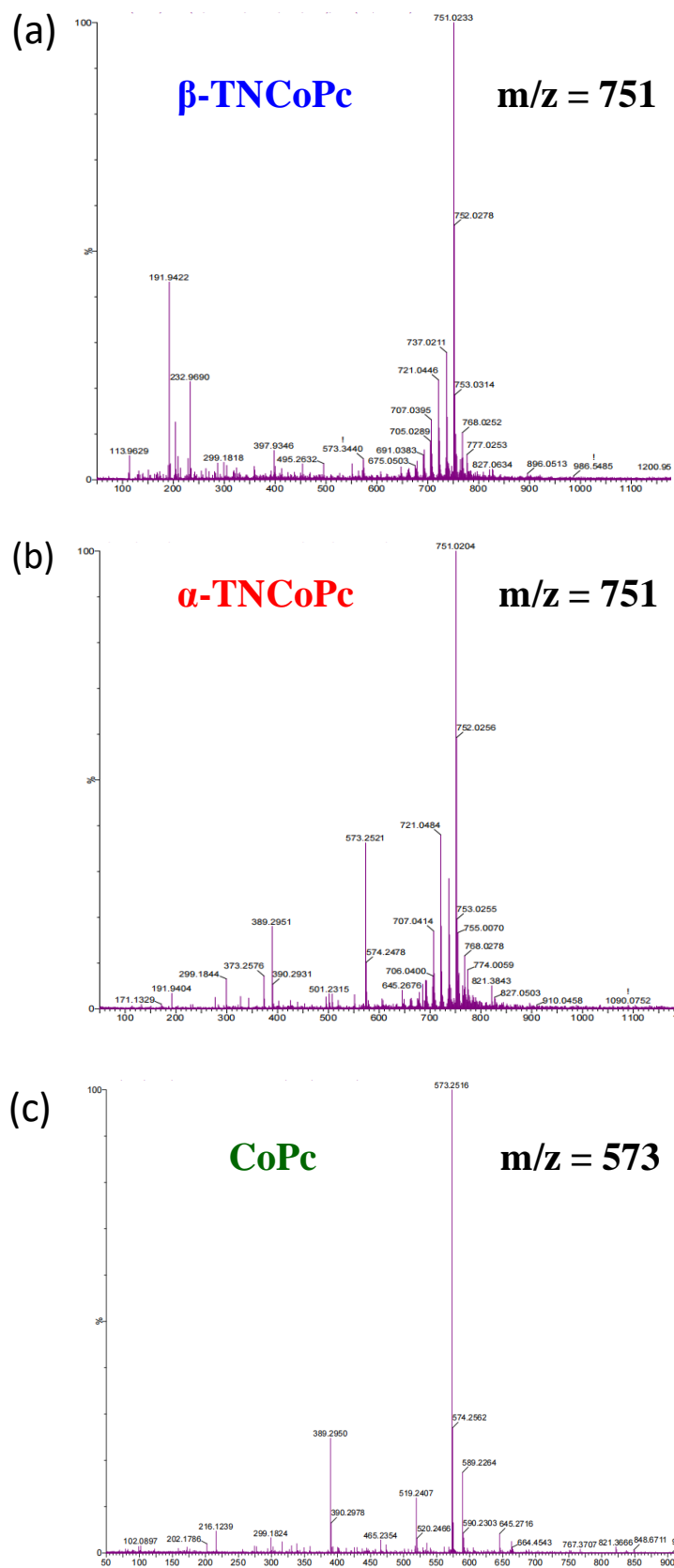
Figure 3.1. High-resolution mass spectrometry (HRMS) of (a) β-TNCoPc isomer, (b) α-TNCoPc isomer and (c) CoPc molecules.

Figure 3.2. (a) UV-Visible spectra of unsubstituted CoPc, α-TNCoPc and β-TNCoPc isomeric molecules. (b) Fourier transform infrared (FTIR) spectroscopy and (c) Raman spectroscopy of unsubstituted CoPc, α-TNCoPc isomer and β-TNCoPc isomer. (d) 1H NMR spectra of α-TNZnPc and β-

TNZnPc isomeric molecules, (e) 2D (COSY) spectra of α-TNZnPc isomer and (f) 2D (COSY) spectra of β-TNZnPc isomeric molecules.

Table 3.1. Allotment of the spectral peaks observed in FTIR spectra of CoPc, α-TNCoPc and β-TNCoPc molecules.

| Wavenumber (cm^{-1})	Band corresponding to
754	Phthalocyanine skeletal vibrations
870	
938	
1023	
1142	C-H stretching vibration
1247	C-C stretching vibration
1371	C-N stretching vibration
1522	N-O stretching vibration
1638	C=C macrocyclic ring vibration

Table 3.2. Allotment of the spectral peaks observed in Raman spectra of CoPc, α-TNCoPc and β-TNCoPc molecules.

| Raman shift (cm^{-1})	Band corresponding to
487	In plane bending of C-C-C
687	Out of plane bending of pyrrole ring
759	Macrocyclic stretching
857	Benzene breathing
1095	C-H bending
1241	In plane deformation of C-H
1397	In plane stretching of C-N
1456	Isoindole ring stretching
1530	In plane stretching of macrocycle
1674	In plane stretching of C-N

The primary aim of this investigation is to understand how the isomerism of the -NO$_2$ functionality influences the reaction mechanism /reaction kinetics of ORR/OER so as to explore their potential to improve the overall energy efficiency of a Zn air battery. Toward this, isomeric

molecular catalysts were first anchored on carbon nanotubes (CNT) because of its known capability to aid electron transport.[45–49] α and β-TNCoPcs and
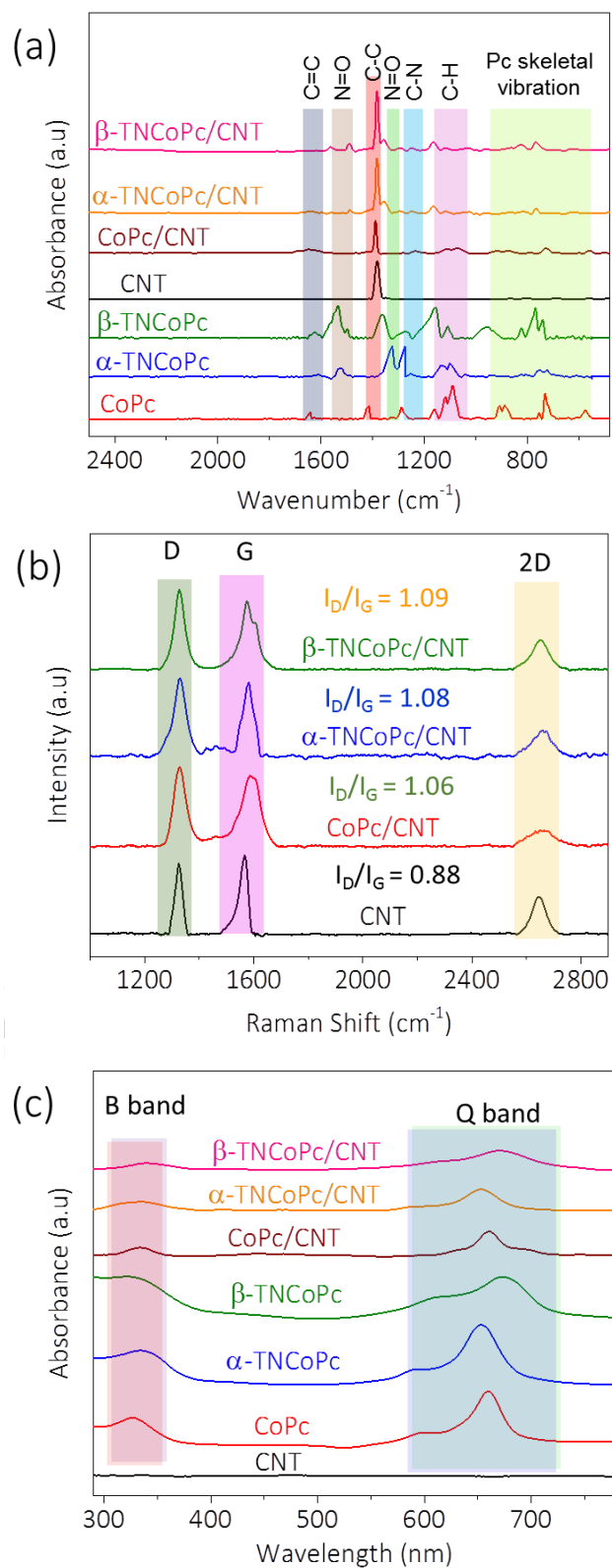
Figure 3.3. (a) Fourier transform infrared (FTIR) spectroscopy, (b) Raman spectroscopy and (c) UV-Visible spectroscopy of β-TNCoPc/CNT isomer, α-TNCoPc/CNT isomer and CoPc/CNT.
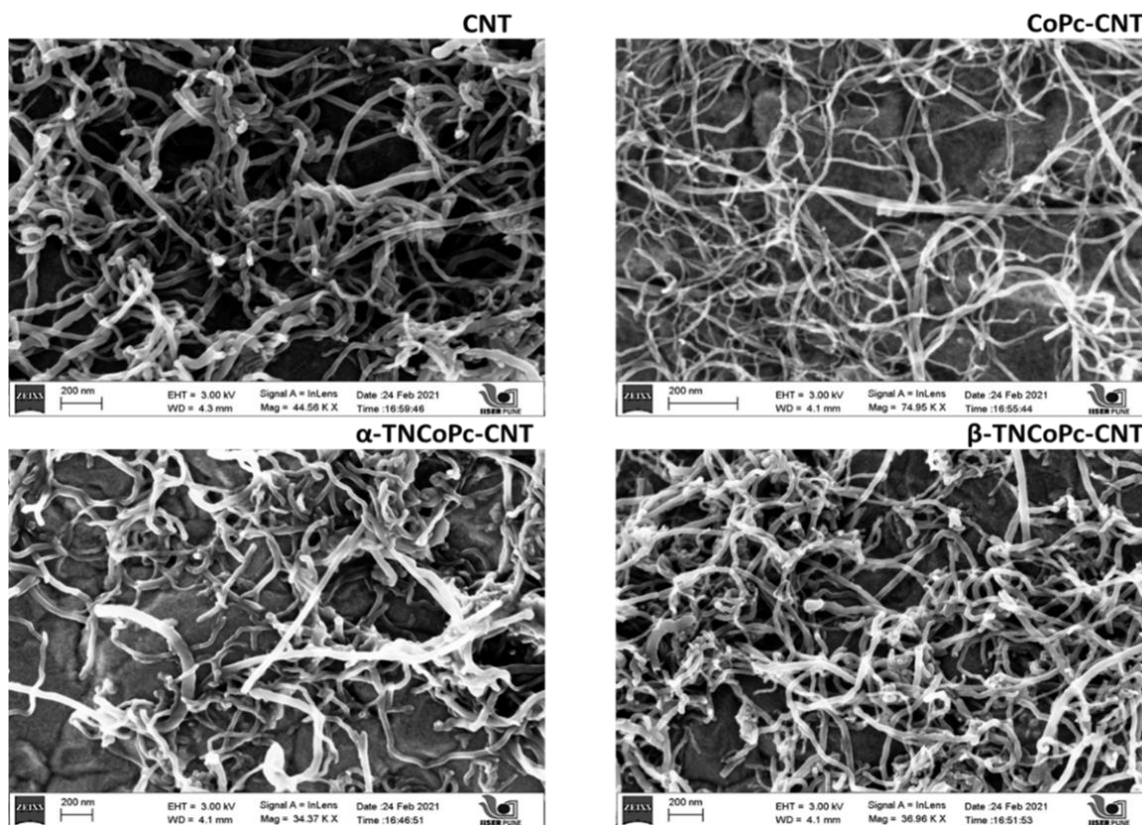
**Figure 3.4.** FESEM images of (a) CNT, (b) CoPc/CNT, (c) α-TNCoPc/CNT and (d) β-TNCoPc/CNT.

unsubstituted CoPc anchored on CNT (α-TNCoPc/CNT, β-TNCoPc/CNT and CoPc/CNT) were synthesized and characterized thoroughly (kindly refer to chapter 2, section 2.2.4, page 53). The features of CNT in the TNCoPc/CNT catalytic system in the FTIR and Raman spectra (Figure 3.3a, b) suggest the formation of CNT composite catalytic systems. Though, the features of phthalocyanines were almost masked by the presence of defect and graphitic bands in the Raman spectra of CNT composite catalytic systems; the alterations in the I_D/I_G (intensity of defect band/intensity of graphitic

band) ratio in the catalysts indicate the formation of composite catalytic systems.[48, 49]
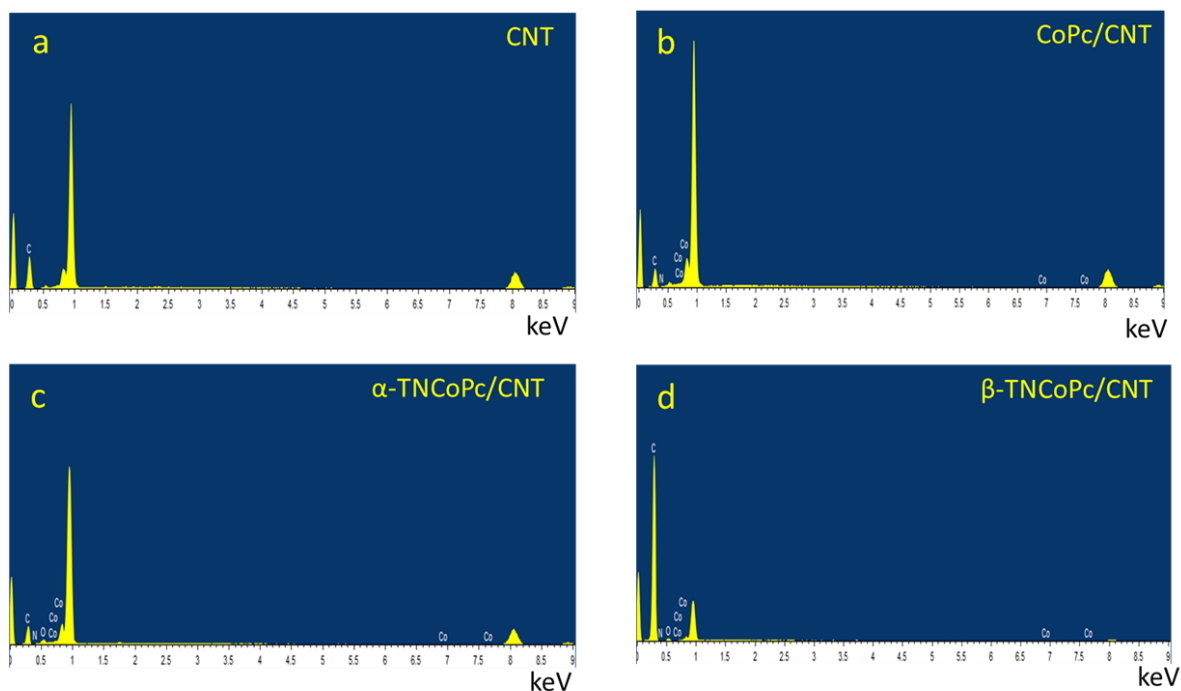
Figure 3.5. EDS pattern of (a) CNT, (b) CoPc/CNT, (c) α-TNCoPc/CNT and (d) β-TNCoPc/CNT.

Table 3.3. Weight and atomic percentage of the elements extracted from EDS data for all the three catalysts.

α-TNCoPc			β-TNCoPc			CoPc		
Element	Weight %	Atomic %	Element	Weight %	Atomic %	Element	Weight %	Atomic %
C K	82.58	85.33	C K	82.49	85.4	C K	89.37	92.89
N K	9.03	8.57	N K	8.96	8.39	N K	8.65	7.56
Co K	1.78	0.38	Co K	1.81	0.39	Co K	1.98	0.45
O K	6.61	5.72	O K	6.74	5.82			
Total:	100.0		Total:	100.0		Total:	100.0	

Scanning electron microscopy (SEM) images, (Figure 3.4) along with energy dispersive X-ray spectroscopy (EDS), (Figure 3.5) further indicate nanotubular morphology of CNT and confirm the presence of Co, C, N and O (EDS pattern) in composite CNT catalytic systems which suggest the successful incorporation of TNCoPcs on the CNT. The EDS data (Figure 3.5 and Table 3.3) confirm the amount of Co present in all the three composite catalytic system is maintained more or less the same.

3.2.2. Kinetic and mechanistic investigations of ORR.
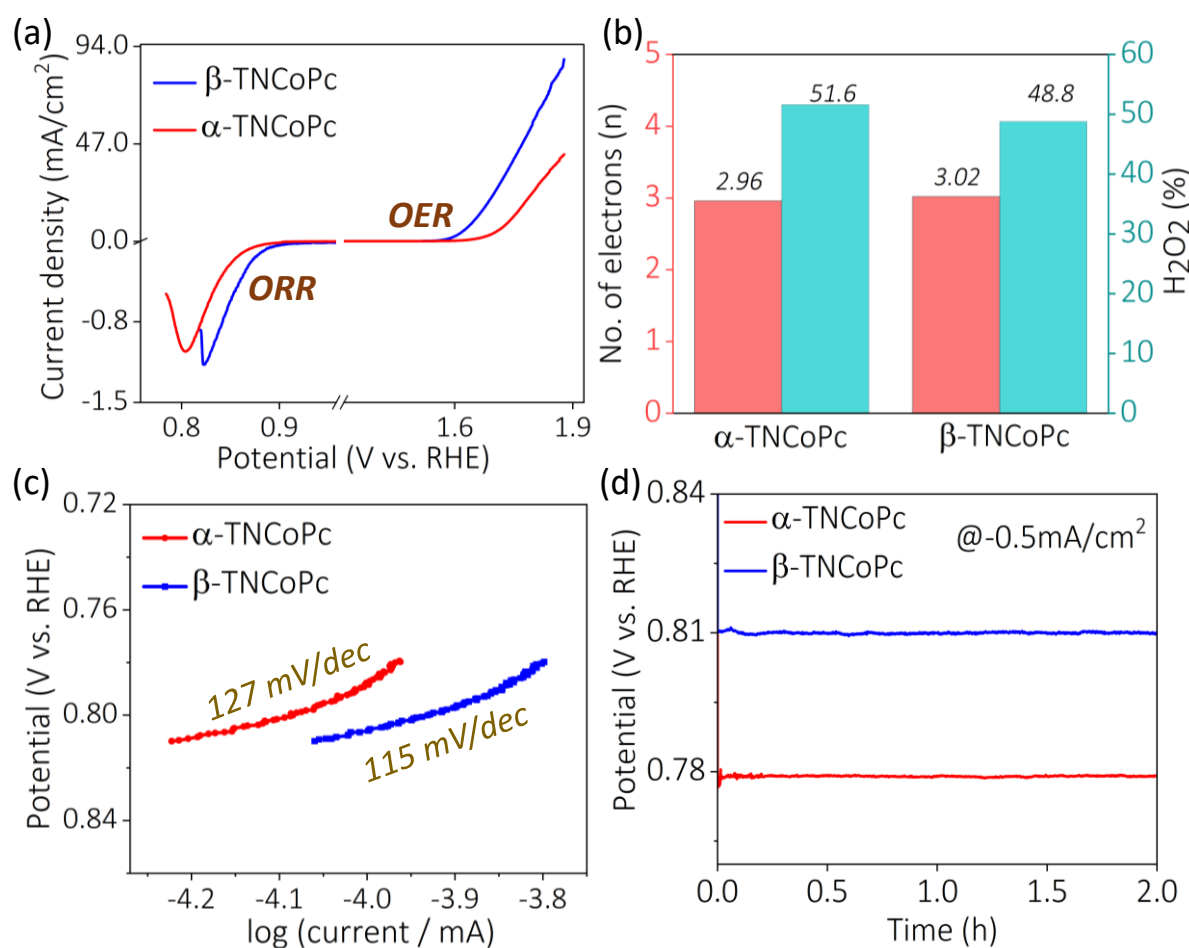
Figure 3.6. (a) Linear sweep voltammograms for ORR as well as OER on α-TNCoPc and β-TNCoPc isomeric molecules. (b) Plot showing the number of electrons and % of H_2O_2 formed with α-TNCoPc and β-TNCoPc isomeric

molecules at a potential of 0.79 V vs. RHE. (c) Tafel slopes for ORR with α-TNCoPc and β-TNCoPc isomers. (d) Chronopotentiometric measurements for ORR at a constant current density of 0.5 mA/cm^2 for α-TNCoPc and β-TNCoPc isomeric molecules.

Linear sweep voltammograms (Figure 3.6a), suggest that the activity of β-TNCoPc isomer towards the half-cell ORR/OER is superior to its α counterpart which is clear from the onset potential and potential required for achieving a particular rate (Table 3.4). Since the catalytic domain is the central metal ion (cobalt ion), voltametric investigation reveals that ligand isomerism can tune the catalytic metal center with the 'β' isomer demonstrating enhanced ORR/OER activities compared to the corresponding 'α' isomer, (Figure 3.6a). This will be beneficial for improving the round-trip efficiency in metal-air batteries as ORR/OER is their discharge/charge reactions respectively. Hydrodynamic voltammetry for ORR shows that, the number of electrons transferred is close to 3 and % of peroxide is close to 50 % for both the isomeric molecules, suggesting that ORR proceeds with the intermediacy of peroxide, Figure 3.6b (please refer to chapter 2 section 2.8 pages 63-64 for details). The Tafel analysis (Figure 3.6c) suggest a lower Tafel slope for the β isomer indicating a facile kinetics in this isomer. The long-term stability is then subsequently investigated on isomeric electrocatalysts in the half-cell modes by chronopotentiometric analysis. Clearly, the potential required to achieve the same current density is substantially lower in β-isomer compared to α-isomer, (Figure 3.6d). This indicate that isomerism of -NO$_2$ functionality does not change the ORR reaction mechanism. However, it does change the kinetics of ORR

substantially, with a higher activity in favour of the β-isomer compared to the α-isomer. Secondly, this pathway with the intermediacy of peroxide is desirable for the electrosynthesis of peroxide but detrimental for energy conversion devices, as peroxide is known to poison the electrocatalytic domains.

Table 3.4. Comparison of the onset potential and the potential required for achieving a particular current density for ORR and OER with α-TNCoPc and β-TNCoPc.

| Catalyst	OER		ORR	
	Onset potential (V vs. RHE)	Potential (V vs. RHE) @10mA/cm^2	Onset potential (V vs. RHE)	Potential (V vs. RHE) @0.5mA/cm^2
β-TNCoPc	1.56	1.65	0.85	0.81
α-TNCoPc	1.65	1.75	0.83	0.78

3.2.3. Kinetic and mechanistic investigations of OER.
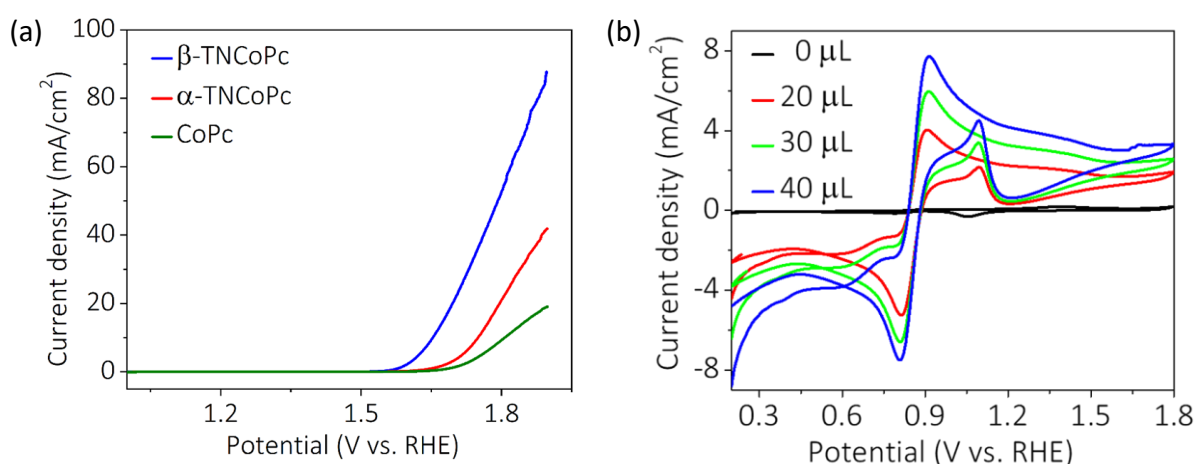
Figure 3.7. (a) Linear sweep voltammograms recorded at a scan rate of 5 mV/s for oxygen evolution reaction in pH=14 electrolyte at a rotation rate of 1600 RPM. (b) Cyclic voltammogram of bare Au in 1M KOH with different concentrations of H_2O_2.

Though water oxidation is superior in β-isomer over the corresponding α-isomer (Figure 3.6a and Figure 3.7a), it is known that water oxidation can lead to the formation of peroxide (2e$^-$ pathway) or O_2 (4e$^-$ pathway, OER) as the products.[50–52] The former is desirable for peroxide electrosynthesis but the latter for energy conversion devices.[53–55] To prove this unambiguously, rotating ring disk electrode (RRDE) measurements were carried out by performing linear sweep voltammetry at the disk for OER and biasing the ring (Au ring) at ORR potential (0.7 V vs. RHE) and peroxide oxidation potential (1 V vs. RHE), (Figure 3.8a). The corresponding potentials were determined from the cyclic voltammogram, (Figure 3.7b) for oxygen reduction reaction and peroxide oxidation on Au electrodes. When the ring is biased at ORR potentials (0.7 V vs. RHE), the ring current appears as soon as the disk potentials cross the water oxidation regime. However, no ring current is seen when it is biased at peroxide oxidation potential, (Figure 3.8a). This clearly suggests O_2 is the primary product during water oxidation at the disk and not the peroxide. The Tafel plot, (Figure 3.8b), shows a facile kinetics on the β-isomer compared to α-isomer and unsubstituted CoPc. The long-term stability with a higher activity is observed on the β-isomer compared to the α-isomer, (Figure 3.8c). All these indicate that, the isomerism of the -NO$_2$ functionality does not change the reaction mechanism of OER, however, it rather influences the reaction kinetics. Taken together, the ligand isomerism via the isomerism of -NO$_2$ functionality in the secondary sphere does not change the reaction dynamics of OER/ORR but it significantly influences their respective electrochemical kinetics. The data outlined in (Figure 3.6 and Figure 3.8) further

demonstrate that ligand isomerism via the regio-isomerism of -NO$_2$ functionality can be utilized for aiding the charge reaction of an aqueous metal air battery and not the discharge chemistry due to the involvement of peroxide intermediacy in the latter.
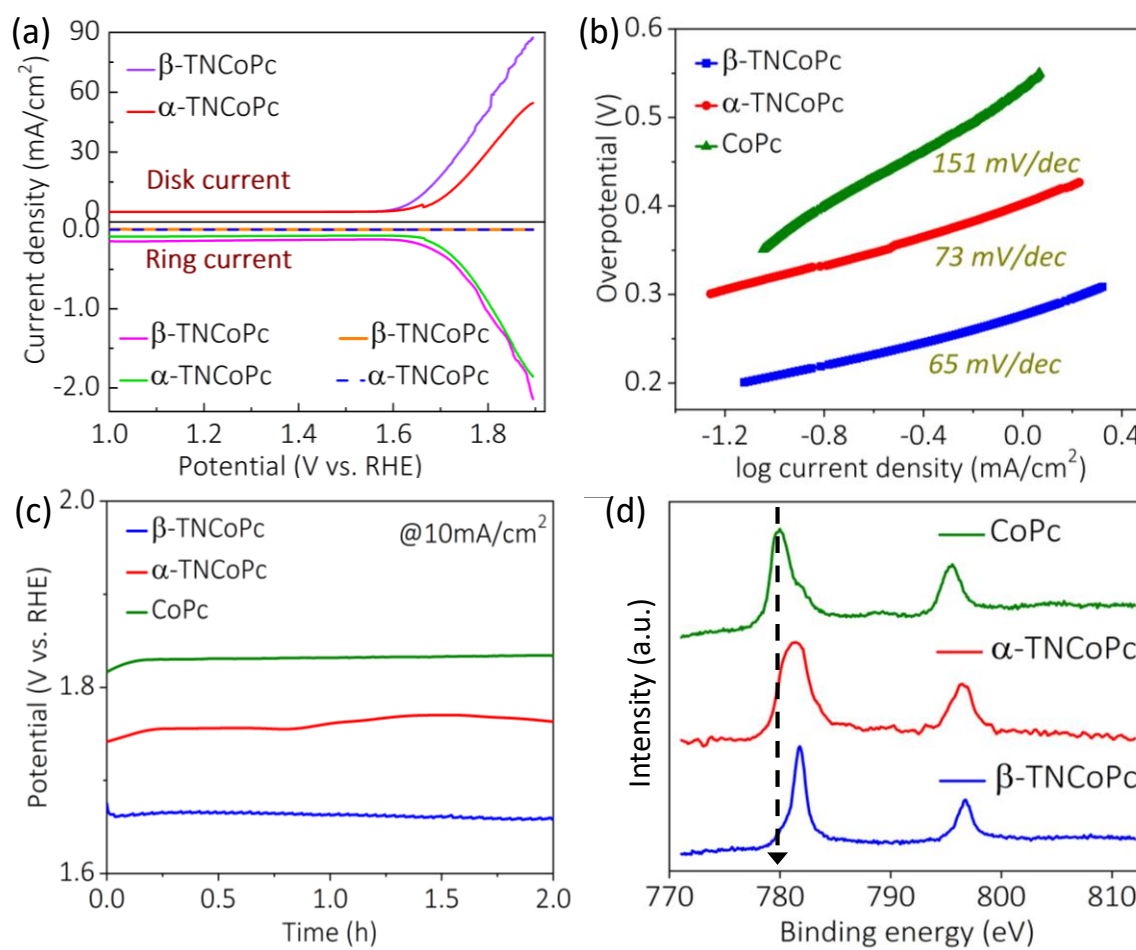

Figure 3.8. (a) RRDE measurements during OER at the disk (red trace and violet trace) using α and β-TNCoPc isomeric molecules by biasing the Au ring at 0.7 V vs. RHE (pink and green trace) for ORR and at 1 V vs. RHE (orange and blue trace) for peroxide oxidation at 1600 RPM. (b) Tafel plots along with their Tafel slopes for OER with unsubstituted CoPc, α-TNCoPc and β-TNCoPc isomers. (c) Chronopotentiometric measurements at a constant current density of 10 mA/cm^2 for oxygen evolution reaction in pH=14 electrolyte at a rotation rate of 1600 RPM for unsubstituted CoPc, α-

TNCoPc isomer and β-TNCoPc isomer. (d) XPS spectra of pristine CoPc, α-TNCoPc and β-TNCoPc isomeric molecules.

The reason for this fascinating behaviour with respect to regioisomerism can be primarily attributed to the electron withdrawing resonance effect (-R) and electron withdrawing inductive effect (-I) of the nitro groups (-NO$_2$) in the isomeric molecules.[32,33] The closeness of 'O' of −NO$_2$ group and the iminic 'N' atom in the macrocyclic ring of the α-isomer may prompt repulsive field effects between these groups which may force the −NO$_2$ group to go out of the molecular plane. This might lead to a reduction in the −R effect between −NO$_2$ group and the macrocycle plane and the electron withdrawing effect may mainly originate from the -I effect. Whereas, for the β isomer, repulsive filed effect between the groups can be negligible as they are well separated spatially. This might favour an in-plane confirmation of −NO$_2$ group in β isomer leading to a dominant −R and −I effect in the molecule. This is in fact responsible for the broadening and red shifting of Q band in the β-TNCoPc isomer with respect to the Q band of α-TNCoPc isomer molecule (Figure 3.2a). Nevertheless, due to these circumstances the central metal ion should be more electron deficient in the β-isomer compared to the α-isomer. This should enhance the contribution of the oxidized Co species in the β-isomeric molecule compared to the α-isomeric molecule. This is reflected in the X- ray photoelectron spectroscopy (XPS) data of these molecules, (Figure 3.8d) wherein the binding energy peak corresponding to Co^{3+} (2p$_{3/2}$) species demonstrated a positive binding energy shift of 0.6 eV in the β-isomeric molecule compared to the α-isomeric molecule. These suggest that, the contribution of oxidized cobalt species is

noticeably enriched in the β-isomer molecule compared to the corresponding α counterpart, (Figure 3.8d), which in turn indicates a positive shift in the redox energy of Co^{3+}/Co^{2+} in the former.[35,56-58] This should lead to a better overlap of Co^{3+}/Co^{2+} redox energy level with the oxygen redox level in the β-isomer molecule which can amplify the oxygen redox reactions. This will be beneficial to boost the round-trip efficiency of ZABs as demonstrated in the next section.
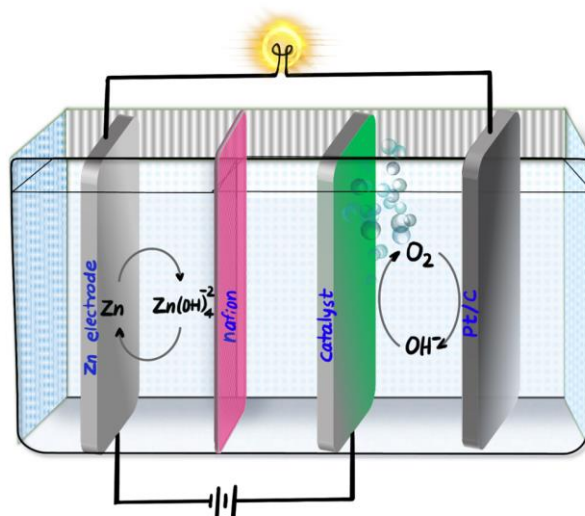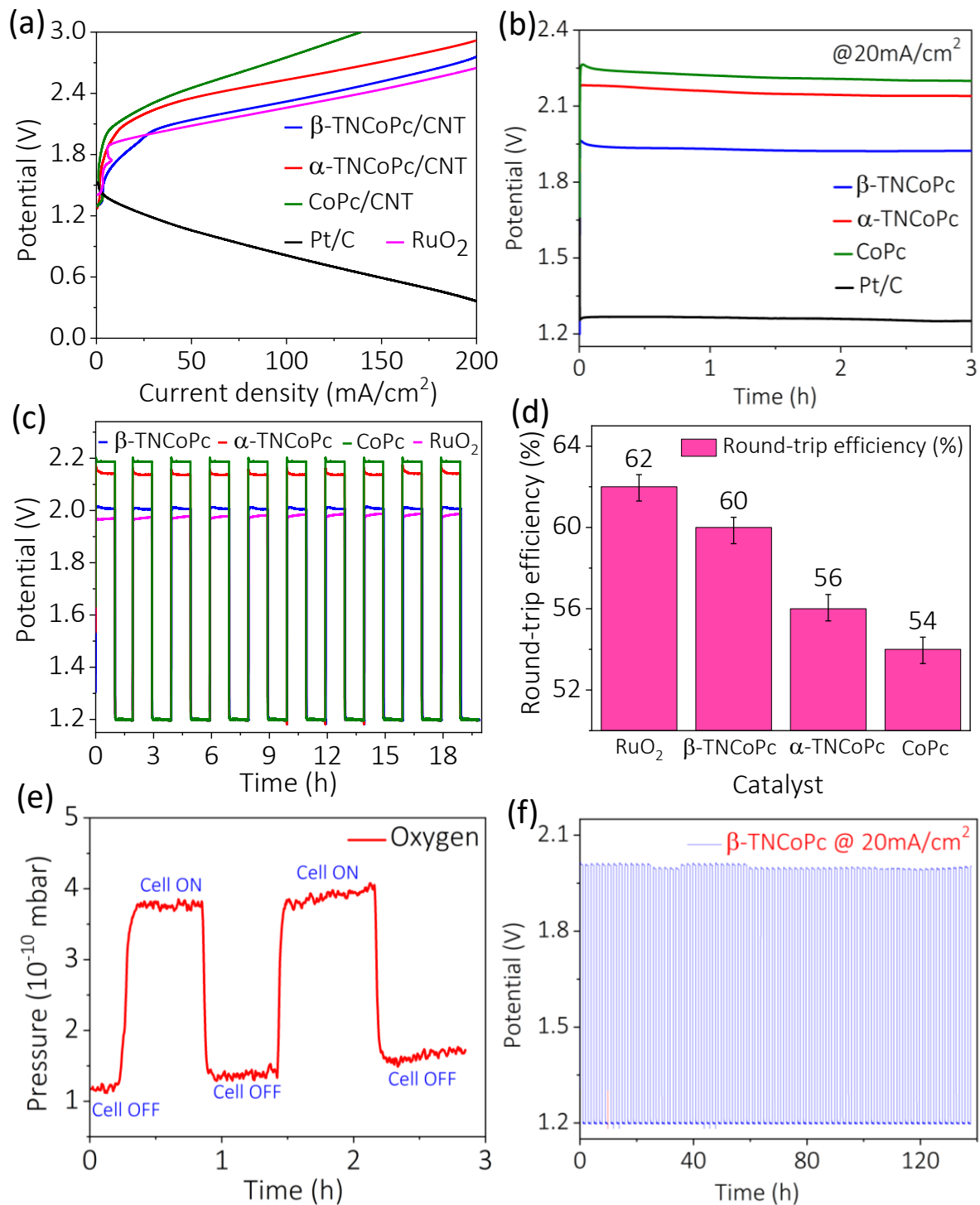

Scheme 3.2. Trielectrode configuration for a rechargeable Zn-air battery.
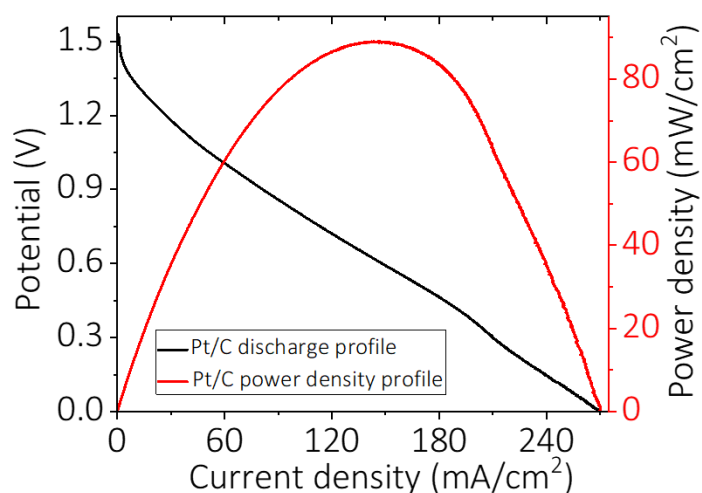
Figure 3.9. Discharge polarization and power density curve of Pt/C in the zinc air battery.

3.2.4. Evaluation of Zinc-air battery performance.

Figure 3.10. (a) Charge-discharge profiles of rechargeable zinc–air batteries, discharge (black) and charge (blue, red, green and pink) polarization curves obtained with Pt/C (0.5 mg/cm^2) as the ORR catalyst and β-TNCoPc, α-TNCoPc, unsubstituted CoPc and RuO$_2$ as the OER catalysts (2 mg/cm^2) respectively. (b) Chronopotentiometric traces at a constant current density of

20 mA/cm^2. (c) Charge-discharge cycling data for ZAB with the isomeric molecular electrocatalysts, CoPc and RuO$_2$ at a current density of 20 mA/cm^2. (d) Comparison of the round-trip efficiency at a current density of 20 mA/cm^2 for RuO$_2$, unsubstituted CoPc, α-TNCoPc and β-TNCoPc isomers. (e) In-situ electrochemical mass spectrometry with β-TNCoPc isomer during the charge reaction. (f) Long-term cycling with β-TNCoPc isomer at a current density of 20 mA/cm^2.

In order to validate the performance of isomeric catalysts in Zn air battery, these molecules anchored on CNT were utilized as the OER catalysts during the charge chemistry in tri-electrode ZAB configuration as shown in (Scheme 3.2) (refer to chapter 2, section 2.4.2, pages 57-58 for details).[59–61] The discharge chemistry was carried out between Zn electrode and a Pt/C based ORR catalyst and the charge chemistry was carried out between the Zn electrode and the isomeric catalysts. The Zn half-cell and ORR/OER half-cells were separated by a Nafion 117 membrane. The discharge polarization curve demonstrated a peak power density of 90 mW/cm^2 at a current density of 150 mA/cm^2 (Figure 3.9), which is in line with the literature with Pt based catalysts.[62,63] The charge polarization curves show that the β isomer outperforms the corresponding α isomer and the charging reaction at all current densities occurs at a lower operating potential in the β isomer than the α isomer, (Figure 3.10a). The long-term stability was investigated by chronopotentiometry at a current density of 20 mA/cm^2 and it further show a lower operating potential in β isomer than the corresponding α isomer, (Figure 3.10b). In order to investigate the stability of metal air battery during repeated charge discharge, cyclic stability of the

Table 3.5. Comparison of charging voltage and round-trip efficiency of different zinc-air batteries involving cobalt-based catalysts.

| Catalysts	Current density (mA/cm²)	Charging voltage (V)	Cycling stability (h)	Round-trip efficiency (%)	Reference
FeCo based BFC	20mA/cm²	2.1V	100 (at 2mA/cm²)	64.6	Pei et al., 2019
Mn/Co:2.5-CB	20mA/cm²	2.18V	30 (at 5mA/cm²)	50.2	Davari et al., 2016
NCNT/ Co$_x$Mn$_{1-x}$O	20mA/cm²	1.9V	12 (at 7mA/cm²)	61.7	Liu et al., 2016
NiCo$_2$O$_4$@NiMn LDH	20mA/cm²	2.1V	83	63.5	Guo et al., 2018
NCNT/CoO-NiO-NiCo	20mA/cm²	2V	25	63.1	Liu et al., 2015
CoMn$_2$O$_4$/ N-rGO	20mA/cm²	1.9V	17	62	Prabu et al., 2014
β-TNCoPc/CNT	20mA/cm²	2V	140	60	**This work**

battery was investigated at a discharge and charge current density of 20 mA/cm², (Figure 3.10c), which further demonstrates that β isomer requires a lower driving force than the corresponding α isomer for achieving the same rate. Therefore, the round-trip efficiency is noticeably improved in the β isomer compared to the α isomer, (Figure 3.10d). In-situ electrochemical mass spectrometric data with the best performing β isomer OER catalyst, show that when the cell is ON, the catalyst evolves oxygen and the oxygen signal decays to the base line when the cell is OFF, and the process is sustainable for several cycles, (Figure 3.10e). Further, the cycling stability test of ZAB with the β isomer was carried out and it shows a stable charging profile for large number of cycles (70 cycles are shown), (Figure 3.10f). All

these studies clearly suggest the β isomer is an efficient material for improving the round-trip efficiency of rechargeable zinc air batteries. Further, a comparison of the performance of our Zn-air battery employing the β isomer was made with the other Zn-air batteries reported in the literature (Table 3.5), which show the charging voltage and round-trip efficiency are comparable to the literature.

3.2.5. Post electrochemical characterisations.

In order to investigate the durability of the β isomer catalyst, post electrochemical characterization were carried after cycling the battery for 70 hours. X-ray photoelectron spectroscopy studies show that the Co signals are intact in the molecule before and after the long-term analysis and no signals of cobalt oxides were observed, (Figure 3.11a). UV-visible, FTIR and Raman spectroscopy reveal that the chemical identity of the molecular catalysts is well preserved even after prolonged electrocatalysis. These spectroscopic characterizations also rule out the possibility of CoOx formation by the degradation of the molecular catalysts. If it would have been formed, FTIR and Raman spectra would have shown characteristics peaks of CoOx which were not observed in the present case (Figure 3.11c and Figure 3.11d).[64–66] Taken together, it is demonstrated that ligand isomerism can be utilized to design non-precious molecular electrocatalysts for targeting the round trip efficiency of ZABs. This demonstration is expected to contribute to the design of future molecular catalysts with improved activities for various electrochemical applications.
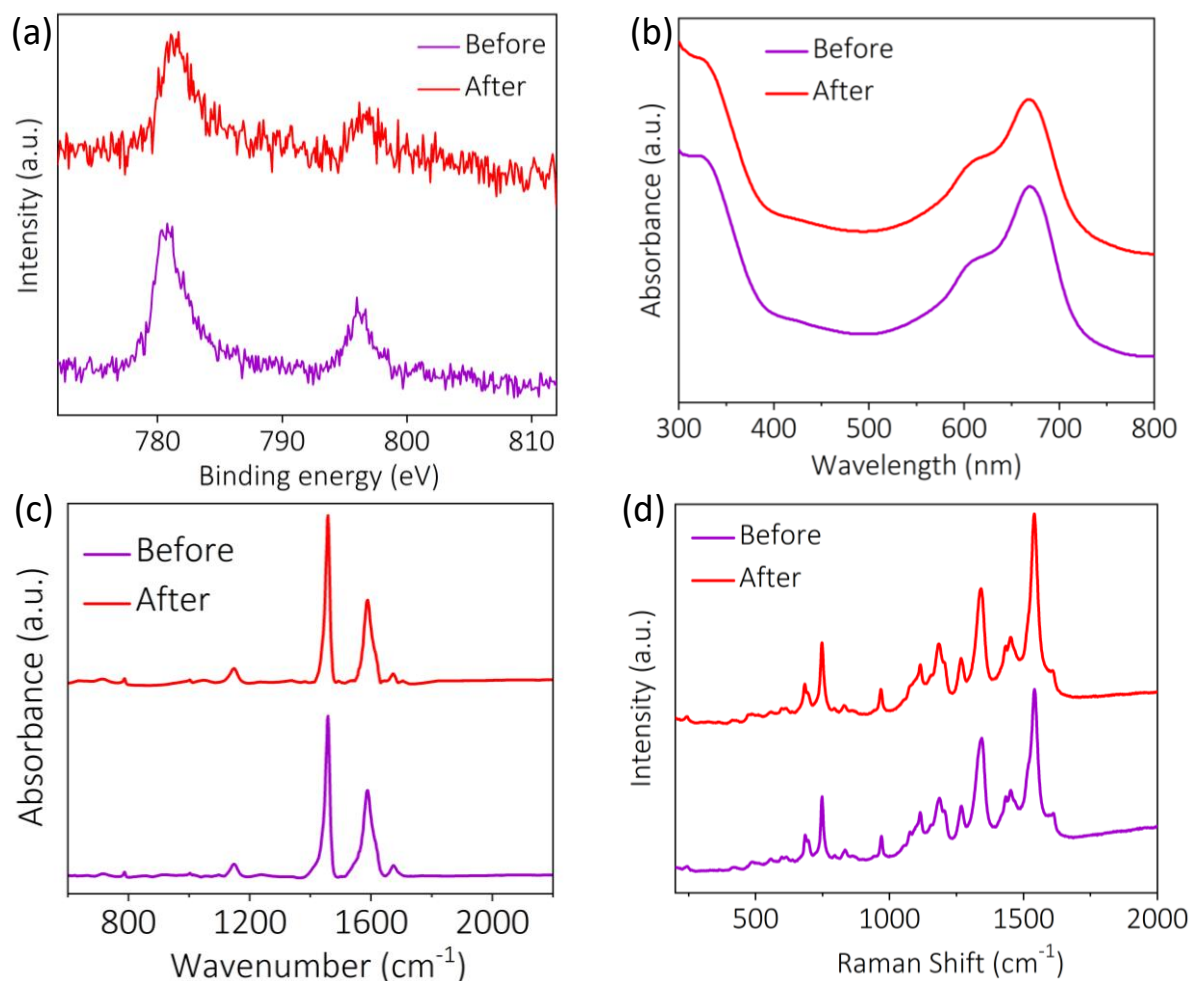
Figure 3.11. (a) XPS spectra of β-TNCoPc composite electrode before (violet) and after (red) long term polarization for 70 hours. (b) UV-visible spectra before (violet) and after (red) long term polarization for 70 hours. (c) FT-IR spectra before (violet) and after (red) long term polarization for 70 hours. (d) Raman spectra before (violet) and after (red) long term polarization for 70 hours.

3.3. Conclusions:

The role of ligand in tuning the reaction kinetics and reaction mechanisms of ORR and OER reactions is eluciated via the regiiosimerism of the ligand around the same catalytic Co centre. Oxidative activation in the β isomeric electrocatalyst due to the combined presence of –R and–I effects as

compared to the only –I effect in the α isomeric electrocatalyst noticeably enhance the ORR and OER kinetics in the former, however, without altering their respective reaction mechanism. With respect to ORR on isomeric electrocatalysts, the number of electrons transferred were close to 3 and the percentage of peroxide was close to 50% on both the electrocatalysts, yet with an improved kinetics in the β-isomer. As far as OER is concerned, a 4 electron pathway was preferred on both the isomeric electrocatalysts, however with a noticeably higher activity in favor of the β-isomer. To show the practical applicability of ligand isomerism in electrocatalysis, how the round-trip efficiency of a Zn-air battery can be targetted by tuning the ligand isomerism is demonstrated. The results show that the β-isomer outperforms the α-isomer in terms of charging voltage and round-trip efficiency with excellent cycling stability. Nevertheless, the isomerism of -NO_2 functionality does not aid the discharge chemistry of Zn-air batteries because of the intermediacy of peroxide in the ORR pathway. However, this can be utilized as an electrocatalyst in peroxide electrosynthesising metal-air batteries and fuel cells. [50–53,67,68] Overall, the work outlined shows a novel strategy towards the design of efficient molecular electrocatalysts to target the overall energy efficiency of future generation energy storage and conversion devices. In the present work, the effect of isomerism of secondary sphere substituents on the charging chemistry is majorly demonstrated. It is to be noted that, by following the strategy outlined in this thesis, it is also possible to develop bifunctional electrocatalysts based on earth abundant metal based phthalocyanines to aid the discharge as well as charge reactions. This is expected to help in the development of precious metal free air batteries.

3.4. References:

[1] Asazawa, K.; Yamada, K.; Tanaka, H.; Oka, A.; Taniguchi, M.; Kobayashi, T. A Platinum-Free Zero-Carbon-Emission Easy Fuelling Direct Hydrazine Fuel Cell for Vehicles. *Angew. Chemie.* **2007**, *119* (42), 8170–8173.

[2] Park, J. S.; Park, S. H.; Yim, S. D.; Yoon, Y. G.; Lee, W. Y.; Kim, C. S. Performance of Solid Alkaline Fuel Cells Employing Anion-Exchange Membranes. *J. Power Sources,* **2008**, *178* (2), 620–626.

[3] Kuttiyiel, K. A.; Sasaki, K.; Choi, Y.; Su, D.; Liu, P.; Adzic, R. R. Bimetallic IrNi Core Platinum Monolayer Shell Electrocatalysts for the Oxygen Reduction Reaction. *Energy Environ. Sci.* **2012**, *5* (1), 5297–5304.

[4] Xu, H.; Fu, Q.; Yao, Y.; Bao, X. Highly Active Pt-Fe Bicomponent Catalysts for CO Oxidation in the Presence and Absence of H2. *Energy Environ. Sci.* **2012**, *5* (4), 6313–6320.

[5] Oezaslan, M.; Hasché, F.; Strasser, P. PtCu3, PtCu and Pt,Cu Alloy Nanoparticle Electrocatalysts for Oxygen Reduction Reaction in Alkaline and Acidic Media. *J. Electrochem. Soc.* **2012**, *159* (4), B444–B454.

[6] Bidault, F.; Brett, D. J. L.; Middleton, P. H.; Brandon, N. P. Review of Gas Diffusion Cathodes for Alkaline Fuel Cells. *J. Power Sources* **2009**, *187* (1), 39–48.

[7] Lee, D. U.; Park, H. W.; Higgins, D.; Nazar, L.; Chen, Z. Highly Active Graphene Nanosheets Prepared via Extremely Rapid Heating as Efficient Zinc-Air Battery Electrode Material. *J. Electrochem. Soc.* **2013**, *160* (9), F910–F915.

[8] Shui, J. L.; Okasinski, J. S.; Kenesei, P.; Dobbs, H. A.; Zhao, D.; Almer, J. D.; Liu, D. J. Reversibility of Anodic Lithium in Rechargeable Lithium-Oxygen Batteries. *Nat. Commun.* **2013**, *4*, 1–7.

[9] Park, H. W.; Lee, D. U.; Nazar, L. F.; Chen, Z. Oxygen Reduction Reaction Using MnO2 Nanotubes/Nitrogen-Doped Exfoliated Graphene Hybrid Catalyst for Li-O2 Battery Applications. *J. Electrochem. Soc.* **2013**, *160* (2), A344–A350.

[10] Zhang, H.; Zhong, X.; Shaw, J. C.; Liu, L.; Huang, Y.; Duan, X. Very High Energy Density Silicide-Air Primary Batteries. *Energy Environ. Sci.* **2013**, *6* (9), 2621–2625.

[11] Chen, Z.; Higgins, D.; Chen, Z.; Lee, D. U. Activated and Nitrogen-Doped Exfoliated Graphene as Air Electrodes for Metal-Air Battery Applications. *J. Mater. Chem. A* **2013**, *1* (7), 2639–2645.

[12] Dai, L.; Xue, Y.; Qu, L.; Choi, H. J.; Baek, J. B. Metal-Free Catalysts for Oxygen Reduction Reaction. *Chem. Rev.* **2015**, *115* (11), 4823–4892.

[13] Zhao, A.; Masa, J.; Xia, W.; Maljusch, A.; Willinger, M. G.; Clavel, G.; Xie, K.; Schlögl, R.; Schuhmann, W.; Muhler, M. Spinel Mn-Co Oxide in N-Doped Carbon Nanotubes as a Bifunctional Electrocatalyst Synthesized by Oxidative Cutting. *J. Am. Chem. Soc.* **2014**, *136* (21), 7551–7554.

[14] Yang, Z.; Yao, Z.; Li, G.; Fang, G.Y.; Nie, H.G.; Liu, Z.; Zhou, X.M.; Chen, X.A.; Huang, S.M. Sulfur-Doped Graphene as an Efficient Metal-Free Cathode Catalyst for Oxygen Reduction. *ACS Nano* **2012**, *6* (1), 205–211.

[15] Liu, Q.; Jin, J.T.; Zhang, J.Y. NiCo2S4@Graphene as a Bifunctional Electrocatalyst for Oxygen Reduction and Evolution Reactions. *ACS Appl. Mater. Interfaces* **2013**, *5* (11), 5002–5008.

[16] Lübke, M.; Sumboja, A.; McCafferty, L.; Armer, C. F.; Handoko, A. D.; Du, Y.; McColl, K.; Cora, F.; Brett, D.; Liu, Z.; Darr, J. A. Transition-Metal-Doped a-MnO2 Nanorods as Bifunctional Catalysts for Efficient Oxygen Reduction and Evolution Reactions. *Chemistry Select* **2018**, *3* (9), 2613–2622.

[17] Zagal, J. H.; Bedioui, F.; Dodelet, J. P. *N₄-Macrocyclic Metal Complexes.* **2007**, *6*, 44–3301.

[18] Zhong, H.; Campos-Roldán, C. A.; Zhao, Y.; Zhang, S.; Feng, Y.; Alonso-Vante, N. Recent Advances of Cobalt-Based Electrocatalysts for Oxygen Electrode Reactions and Hydrogen Evolution Reaction. *Catalysts* **2018**, *8* (11), 559.

[19] Lim, B.; Jiang, M.; Camargo, P. H. C.; Cho, E. C.; Tao, J.; Lu, X.; Zhu, Y.; Xia, Y. Pd-Pt Bimetallic Nanodendrites with High Activity for Oxygen Reduction. *Science* **2009**, *324* (5932), 1302–1305.

[20] Shao, M.; Chang, Q.; Dodelet, J. P.; Chenitz, R. Recent Advances in Electrocatalysts for Oxygen Reduction Reaction. *Chem. Rev.* **2016**, *116* (6), 3594–3657.

[21] Xia, Z.; An, L.; Chen, P.; Xia, D. Non-Pt Nanostructured Catalysts for Oxygen Reduction Reaction: Synthesis, Catalytic Activity and Its Key Factors. *Adv. Energy Mater.* **2016**, *6* (17), 1600458.

[22] Huang, Z. F.; Wang, J.; Peng, Y.; Jung, C. Y.; Fisher, A.; Wang, X. Design of Efficient Bifunctional Oxygen Reduction/Evolution Electrocatalyst: Recent Advances and Perspectives. *Adv. Energy Mater.* **2017**, *7* (23), 1700544.

[23] Özen, Ü. E.; Doğan, E.; Özer, M.; Bekaroğlu, Ö.; Özkaya, A. R. Communication—High-Performance and Non-Precious Bifunctional Oxygen Electrocatalysis with Binuclear Ball-Type Phthalocyanine Based Complexes for Zinc-Air Batteries. *J. Electrochem. Soc.* **2016**, *163* (9), A2001–A2003.

[24] Xu, H.; Ci, S.; Ding, Y.; Wang, G.; Wen, Z. Recent Advances in Precious Metal-Free Bifunctional Catalysts for Electrochemical Conversion Systems. *J. Mater. Chem. A* **2019**, *7* (14), 8006–8029.

[25] Bhowmick, S.; Dhankhar, A.; Sahu, T. K.; Jena, R.; Gogoi, D.; Peela, N. R.; Ardo, S.; Qureshi, M. Low Overpotential and Stable Electrocatalytic Oxygen Evolution Reaction Utilizing Doped Perovskite Oxide, $La_{0.7}Sr_{0.3}MnO_3$, Modified by Cobalt Phosphate. *ACS Appl. Energy Mater.* **2020**, *3* (2), 1279–1285.

[26] Anju, V. G.; Manjunatha, R.; Austeria, P. M.; Sampath, S. Primary and Rechargeable Zinc-Air Batteries Using Ceramic and Highly Stable TiCN as an Oxygen Reduction Reaction Electrocatalyst. *J. Mater. Chem. A* **2016**, *4* (14), 5258–5264.

[27] Wan, X.; Liu, X.; Li, Y.; Yu, R.; Zheng, L.; Yan, W.; Wang, H.; Xu, M.; Shui, J. Fe-N-C Electrocatalyst with Dense Active Sites and Efficient

Mass Transport for High- Performance Proton Exchange Membrane Fuel Cells. *Nat. Catal.* **2019**, *2* (3), 259–268.

[28]   Sorokin, A. B. Phthalocyanine Metal Complexes in Catalysis BT - Chemical Reviews. *Chem. Rev.* **2013**, *113* (10), 8152–8191.

[29]   Sobbi, A. K.; Wöhrie, D.; Schlettwein, D. Photochemical Stability of Various Porphyrins in Solution and as Thin Film Electrodes. *J. Chem. Soc. Perkin Trans.* **1993**, *2*, 481–488.

[30]   Bottari, G.; Torre, G. De; Guldi, D. M. and T. T. Covalent and Noncovalent Phthalocyanine-Carbon Nanostructure Systems Solar Cell. *Chem. Rev.* **2010**, *110*, 6768–6816.

[31]   Rigsby, M. L.; Wasylenko, D. J.; Pegis, M. L.; Mayer, J. M. Medium Effects Are as Important as Catalyst Design for Selectivity in Electrocatalytic Oxygen Reduction by Iron-Porphyrin Complexes. *J. Am. Chem. Soc.* **2015**, *137* (13), 4296–4299.

[32]   Kottaichamy, A. R.; Begum, S.; Nazrulla, M. A.; Dargily, N. C.; Devendrachari, M. C.; Manzoor Bhat, Z.; Thimmappa, R.; Makri Nimbegondi Kotresh, H.; Vinod, C. P.; Thotiyl, M. O. Unprecedented Isomerism-Activity Relation in Molecular Electrocatalysis. *J. Phys. Chem. Lett.* **2020**, *11* (1), 263–271.

[33]   Cong, F. Di; Ning, B.; Yu, H. F.; Cui, X. J.; Chen, B.; Cao, S. G.; Ma, C. Y. The Control of Phthalocyanine Properties through Nitro-Group Electronic Effect. *Spectrochim. Acta - Part A Mol. Biomol. Spectrosc.* **2005**, *62* (1–3), 394–397.

[34]   Fu, Y.; Xu, D.; Wang, Y.; Li, X.; Chen, Z.; Li, K.; Li, Z.; Zheng, L. Single Atoms Anchored on Cobalt-Based Catalysts Derived from Hydrogels Containing Phthalocyanine toward the Oxygen Reduction Reaction. *ACS Sustainable Chem. Eng.* **2020**, 8, 8338–8347.

[35]   Li, C.; Huang, T.; Huang, Z.; Sun, J.; Zong, C.; Yang, J.; Deng, W.; Dai, F. A Sulfonated Cobalt Phthalocyanine/Carbon Nanotube Hybrid as a Bifunctional Oxygen Electrocatalyst. *Dalt. Trans.* **2019**, *48* (46), 17258–17265.

[36]   Liu, X.; Yuan, Y.; Liu, J.; Liu, B.; Chen, X.; Ding, J.; Han, X.; Deng, Y.; Zhong, C.; Hu, W. Utilizing Solar Energy to Improve the Oxygen

Evolution Reaction Kinetics in Zinc–Air Battery. *Nat. Commun.* **2019**, *10* (1), 4767.

[37] Guo, X.; Zheng, T.; Ji, G.; Hu, N.; Xu, C.; Zhang, Y. Core/Shell Design of Efficient Electrocatalysts Based on $NiCo_2O_4$ Nanowires and NiMn LDH Nanosheets for Rechargeable Zinc-Air Batteries. *J. Mater. Chem. A* **2018**, *6* (22), 10243–10252.

[38] Liu, X.; Park, M.; Kim, M. G.; Gupta, S.; Wang, X.; Wu, G.; Cho, J. High-Performance Non-Spinel Cobalt–Manganese Mixed Oxide-Based Bifunctional Electrocatalysts for Rechargeable Zinc–Air Batteries. *Nano Energy* **2016**, *20*, 315–325.

[39] Li, R.; Zhang, X.; Zhu, P.; Ng, D. K. P.; Kobayashi, N.; Jiang, J. Electron-Donating or -Withdrawing Nature of Substituents Revealed by the Electrochemistry of Metal-Free Phthalocyanines. *Inorg. Chem.* **2006**, *45* (5), 2327–2334.

[40] Kobayashi, N.; Miwa, H.; Nemykin, V. N. Adjacent versus Opposite Type Di-Aromatic Ring-Fused Phthalocyanine Derivatives: Synthesis, Spectroscopy, Electrochemistry, and Molecular Orbital Calculations. *J. Am. Chem. Soc.* **2002**, *124* (27), 8007–8020.

[41] Panwar, V.; Kumar, P.; Ray, S. S.; Jain, S. L. Organic Inorganic Hybrid Cobalt Phthalocyanine/Polyaniline as Efficient Catalyst for Aerobic Oxidation of Alcohols in Liquid Phase. *Tetrahedron Lett.* **2015**, *56* (25), 3948–3953.

[42] Topuz, B. B.; Gündüz, G.; Mavis, B.; Çolak, Ü. Synthesis and Characterization of Copper Phthalocyanine and Tetracarboxamide Copper Phthalocyanine Deposited Mica-Titania Pigments. *Dye. Pigment.* **2013**, *96* (1), 31–37.

[43] Zhu, L.; Jing, X.; Song, L.; Liu, B.; Zhou, Y.; Xiang, Y.; Xia, D. Solid-Phase Synthesis and Catalytic Sweetening Performance of Sulfonated Cobalt Phthalocyanine from Sulfonated Phthalic Anhydride Mixture. *New J. Chem.* **2014**, *38* (2), 663–668.

[44] Georgescu, R.; Boscornea, C.; Calinescu, I.; State, R. Raman, IR and UV-Vis Spectroscopic Investigations of Some Substituted Phthalocyanines. *Rev. Chim.* **2015**, *66* (10), 1554–1557.

[45]   Zhang, M.; Gorski, W. Electrochemical Sensing Platform Based on the Carbon Nanotubes/Redox Mediators-Biopolymer System. *J. Am. Chem. Soc.* **2005**, *127* (7), 2058–2059.

[46]   Abbaspour, A.; Mirahmadi, E. Electrocatalytic Activity of Iron and Nickel Phthalocyanines Supported on Multi-Walled Carbon Nanotubes towards Oxygen Evolution Reaction. *Electrochim. Acta* **2013**, *105*, 92–98.

[47]   Chidembo, A. T.; Ozoemena, K. I.; Agboola, B. O.; Gupta, V.; Wildgoose, G. G.; Compton, R. G. Nickel (II) Tetra-Aminophthalocyanine Modified MWCNTs as Potential Nanocomposite Materials for the Development of Supercapacitors. *Energy Environ. Sci.* **2010**, *3*, 228–236.

[48]   Zhu, J.; Li, Y.; Chen, Y.; Wang, J.; Zhang, B.; Zhang, J.; Blau, W. J. Graphene Oxide Covalently Functionalized with Zinc Phthalocyanine for Broadband Optical Limiting. *Carbon N. Y.* **2011**, *49* (6), 1900–1905.

[49]   Zhang, X.; Wu, Z.; Zhang, X.; Li, L.; Li, Y.; Xu, H.; Li, X.; Yu, X.; Zhang, Z.; Liang, Y.; Wang, H. Highly Selective and Active CO_2 Reduction Electrocatalysts Based on Cobalt Phthalocyanine/Carbon Nanotube Hybrid Structures. *Nat. Commun.* **2017**, *8*, 1–8.

[50]   Shi, X.; Back, S.; Gill, T. M.; Siahrostami, S.; Zheng, X. Electrochemical Synthesis of H_2O_2 by Two-Electron Water Oxidation Reaction. *Chem* **2021**, *7* (1), 38–63.

[51]   Xia, C.; Back, S.; Ringe, S.; Jiang, K.; Chen, F.; Sun, X.; Siahrostami, S.; Chan, K.; Wang, H. Confined Local Oxygen Gas Promotes Electrochemical Water Oxidation to Hydrogen Peroxide. *Nat. Catal.* **2020**, *3* (2), 125–134.

[52]   Gill, T. M.; Vallez, L.; Zheng, X. The Role of Bicarbonate-Based Electrolytes in H2O2Production through Two-Electron Water Oxidation. *ACS Energy Lett.* **2021**, *6* (8), 2854–2862.

[53]   Malali, S.; Manzoor, Z.; Ottakam, M. Journal of Colloid and Interface Science A Zinc-Quinone Battery for Paired Hydrogen Peroxide Electrosynthesis. *J. Colloid Interface Sci.* **2020**, *559*, 324–330.

[54]   Zhang, Q.; Zhou, M.; Ren, G.; Li, Y.; Li, Y.; Du, X. Highly Efficient Electrosynthesis of Hydrogen Peroxide on a Superhydrophobic Three-

Phase Interface by Natural Air Diffusion. *Nat. Commun.* **2020**, *11* (1), 1731.

[55] Wu, K.-H.; Wang, D.; Lu, X.; Zhang, X.; Xie, Z.; Liu, Y.; Su, B.-J.; Chen, J.-M.; Su, D.-S.; Qi, W.; Guo, S. Highly Selective Hydrogen Peroxide Electrosynthesis on Carbon: In Situ Interface Engineering with Surfactants. *Chem* **2020**, *6* (6), 1443–1458.

[56] Gu, W.; Hu, L.; Hong, W.; Jia, X.; Li, J.; Wang, E. Noble-Metal-Free Co_3S_4–S/G Porous Hybrids as an Efficient Electrocatalyst for Oxygen Reduction Reaction. *Chem. Sci.* **2016**, *7* (7), 4167–4173.

[57] Rodríguez-fernández, J.; Sun, Z.; Zhang, L.; Tan, T.; Curto, A.; Lauritsen, J. V. Structural and Electronic Properties of Fe Dopants in Cobalt Oxide Nanoislands on Structural and Electronic Properties of Fe Dopants in Cobalt Oxide Nanoislands on Au (111). *J. Chem. Phys.* **2019**, *150*, 041731.

[58] Thapa, S.; Paudel, R.; Blanchet, M. D.; Gemperline, P. T.; Comes, R. B. Probing Surfaces and Interfaces in Complex Oxide Films via in Situ X-Ray Photoelectron Spectroscopy. *J. Mater. Res.* **2021**, *36* (1), 26–51.

[59] Cao, R.; Thapa, R.; Kim, H.; Xu, X.; Kim, M. G.; Li, Q.; Park, N.; Liu, M.; Cho, J. Promotion of Oxygen Reduction by a Bio-Inspired Tethered Iron Phthalocyanine Carbon Nanotube-Based Catalyst. *Nat. Commun.* **2013**, *4*, 1–7.

[60] Tran, T. N. T.; Clark, M. P.; Xiong, M.; Chung, H. J.; Ivey, D. G. A Tri-Electrode Configuration for Zinc-Air Batteries Using Gel Polymer Electrolytes. *Electrochim. Acta* **2020**, *357*, 136865.

[61] Hong, W.; Li, H.; Wang, B. A Horizontal Three-Electrode Structure for Zinc-Air Batteries with Long-Term Cycle Life and High Performance. *Int. J. Electrochem. Sci.* **2016**, *11* (5), 3843–3851.

[62] Yu, Q.; Xu, J.; Wu, C.; Zhang, J.; Guan, L. MnO_2 Nanofilms on Nitrogen-Doped Hollow Graphene Spheres as a High-Performance Electrocatalyst for Oxygen Reduction Reaction. *ACS Appl. Mater. Interfaces* **2016**, *8* (51), 35264–35269.

[63] Yang, T. B.; Zhou, K. Y.; Chen, G. Y.; Zhang, W. X.; Liang, J. C. CoSb3 Alloy Nanoparticles Wrapped with N-Doped Carbon Layers as a Highly

Active Bifunctional Electrocatalyst for Zinc-Air Batteries. *RSC Adv.* **2017**, *7* (52), 33012–33019.

[64]   Li, Y.; Qiu, W.; Qin, F.; Fang, H.; Hadjiev, V. G.; Litvinov, D.; Bao, J. Identification of Cobalt Oxides with Raman Scattering and Fourier Transform Infrared Spectroscopy. *J. Phys. Chem. C* **2016**, *120* (8), 4511–4516.

[65]   Tang, C. W.; Wang, C. Bin; Chien, S. H. Characterization of Cobalt Oxides Studied by FT-IR, Raman, TPR and TG-MS. *Thermochim. Acta* **2008**, *473* (1–2), 68–73.

[66]   Barakat, N. A. M.; Khil, M. S.; Sheikh, F. A.; Kim, H. Y. Synthesis and Optical Properties of Two Cobalt Oxides (CoO and Co_3O_4) Nanoflbers Produced by Electrospinning Process. *J. Phys. Chem. C* **2008**, *112* (32), 12225–12233.

[67]   Brillas, E.; Alcaide, F.; Cabot, P.-L. A Small-Scale Flow Alkaline Fuel Cell for on-Site Production of Hydrogen Peroxide. *Electrochim. Acta* **2002**, *48* (4), 331–340.

[68]   Li, W.; Bonakdarpour, A.; Gyenge, E.; Wilkinson, D. P. Drinking Water Purification by Electrosynthesis of Hydrogen Peroxide in a Power-Producing PEM Fuel Cell. *ChemSusChem* **2013**, *6* (11), 2137–2143.

Chapter 4

Ligand Assisted Molecular

Electrocatalysis

Chapter 4

ABSTRACT: This Chapter discusses how the nature of the ligand tunes the electric double layer leading to counter intuitive trend in electrocatalysis. It is shown that the ability of the ligand to reorganize the electric double layer (EDL) often dominates the electrocatalysis contrary to their inductive effect in the spectrochemical series, leading to counter intuitive electrocatalysis. With water oxidation and chlorine evolution as the probe reactions; the same catalytic entity with carboxy functionalized ligand exhibited surprisingly higher electrochemical activity than aggressively electron-withdrawing nitro functionalized ligands, which is contrary to their actual location in the spectrochemical series. Spectroscopic and electrochemical analyses suggest the enrichment of catalytically active species in the carboxy substituted ligand via proton charge assembly in the EDL that in turn enhances the kinetics of the overall electrochemical process. This demonstration of less obvious ligands becoming indispensable in electrocatalysis, suggests a blind designing of ligands solely based-on their inductive effect should be relooked as it will prevent the utilization of the maximum potential of the molecule in electrocatalysis.
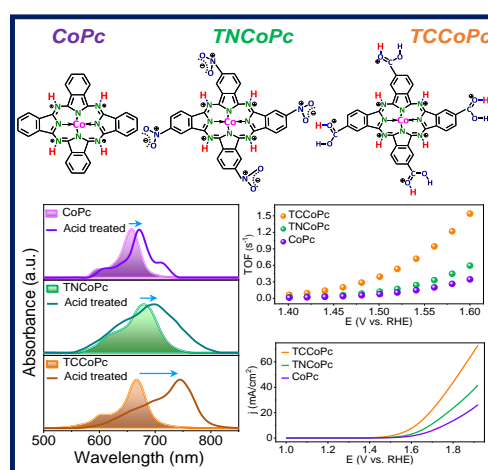
Chapter 4

4.1. Introduction:

In this Chapter, how the nature of the ligand contributes to electrocatalysis counter intuitively via a proton charge assembly is demonstrated. The global energy crisis because of the extensive use of fossil fuels has already become a ubiquitous problem, that in turn makes the domain of renewable energy conversion a hotspot for the global scientific community.[1-3] In this regard, electrochemical transformation via electrocatalysis has become a thrust area of research because of its potential to convert the abundant feedstocks into value-added products.[4-7] This has in turn led to the design and development of various metal based and molecular electrocatalysts.[8-10] Molecular electrocatalysts such as phthalocyanines and porphyrins have gained a lot of attention mainly because of their superior chemical and thermal stability and highly flexible optoelectronic nature.[11-14] For these reasons, the metallophthalocyanines have been explored for catalysis like MEROX process for the sweetening of oils to electrocatalysis in fuel cells and air batteries with undeniable importance in electrochromism, pigment industry, sensing, solar cells, and photodynamic therapy (cancer treatment).[15-19] It is already known that the electrochemical performance of the phthalocyanines can be affected by the redox properties of the central metal which in turn can be altered by changing the metal center or by altering the type, number, and position of the substituents on the macrocyclic ligand.[20-24] It has also been observed that electron withdrawing functionalities such as ($-NO_2$, $-CN$, $-COOH$, $-Cl$) favor oxidation reactions like water electrolysis, oxidation of thiols, ascorbic

acid oxidation, peroxide oxidation etc.[25-28] On the other hand, electron donating substituents like (t-Bu, -NH$_2$, -OH) favor reductive electrocatalysis such as carbon dioxide reduction, oxygen reduction, nitrogen reduction etc.[29-32] So, a correlation between electrocatalytic capability and inductive effect of the ligand functionality has already been arrived, which is widely chosen as a benchmark for designing new molecular platforms for electrochemical transformations.

In this Chapter, an intriguing effect of ligand functionality in electrocatalysis is demonstrated which is irrespective of its position in the spectrochemical series. It demonstrates that the ability of the ligand functionality to alter the electric double layer (EDL) can often surpass the effect anticipated solely based on the spectrochemical series, leading to counter intuitive electrocatalysis. In oxidative electrocatalysis, based on the inductive effect of the ligand functionality, the same catalytic metal centre is expected to demonstrate superior activity with aggressively electron withdrawing nitro (-NO$_2$) functionalized ligand than a carboxy (-COOH) substituted ligand with lesser electron withdrawing power. However, with water oxidation and chlorine evolution reactions as the probe reactions, the experimental trends on the same catalytic Co centre were diametrically opposite with an unexpectedly high activity with the carboxy functionalized ligand than the nitro functionalized ligand. Various electrochemical and spectroscopic analyses suggest the enrichment of the catalytically active Co entity in the carboxy functionalized ligand by its capability to reorganize the electrical double layer (EDL) via proton charge assembly. This

demonstration of the less obvious ligand becoming indispensable in electrocatalysis via their ability to alter the EDL structure, suggest a blind designing of the molecular catalyst by considering only their inductive effect in the spectrochemical series should be reconsidered as it will prevent the utilization of the maximum potential of the molecule in electrocatalysis.

4.2. Results and Discussions:

4.2.1 Characterisation of CoPc, TNCoPc, TCCoPc and their composites with CNTs.

To demonstrate the possibility of counter intuitive electrocatalysis which is irrespective of the inductive effect of the ligand in the spectrochemical series, cobalt phthalocyanine (CoPc) and its substituted derivatives such as nitro substituted cobalt phthalocyanine (TNCoPc) and carboxy substituted cobalt phthalocyanine (TCCoPc) were synthesized and thoroughly characterized as shown in Figure 4.1. As per the spectrochemical series, the electron withdrawing inductive effect (-I effect) of nitro functionalized ligand is more than the carboxy functionalized ligand [33-35], and hence the former is expected to aid oxidative electrocatalysis than the latter. In order to verify this, these molecules were synthesized as per the reported procedure (please refer to chapter 2, section 2.2.1 and 2.2.2, pages 50-52 for details). To ensure the purity of the compounds', detailed characterizations were performed. Matrix-assisted laser desorption ionization time-of-flight mass spectrometry (MALDI-TOF) showed the parent ion peaks at m/z value of ~572, ~751 and ~747 for CoPc ($C_{32}H_{16}CoN_8$),
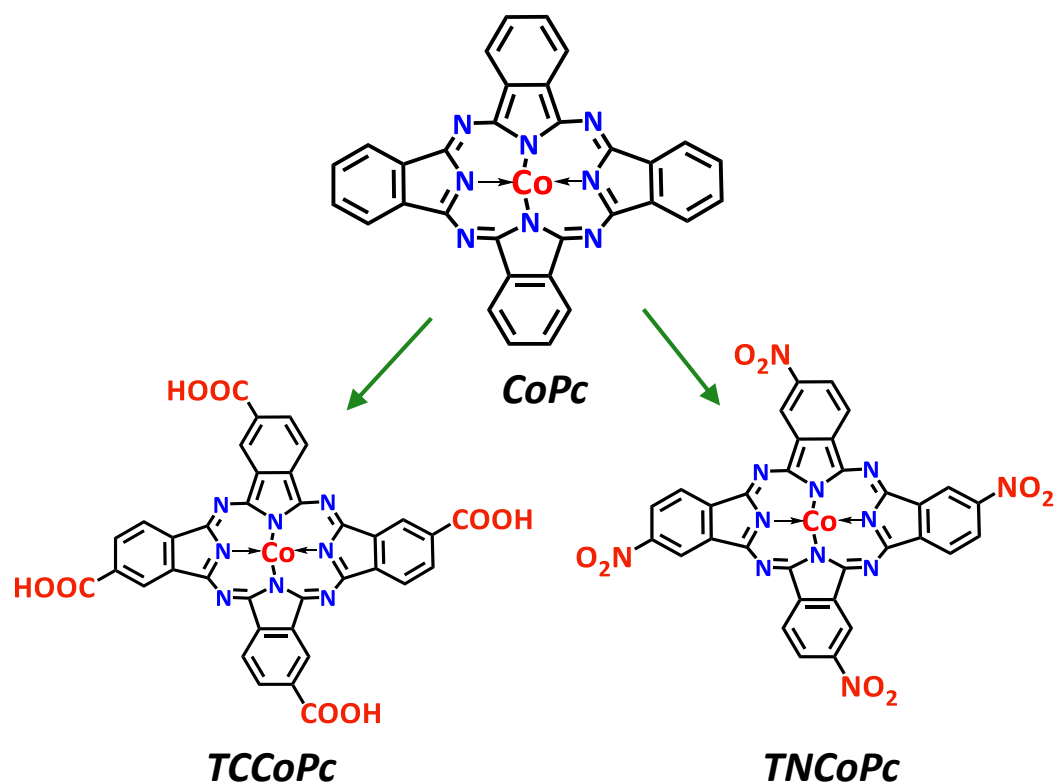
Figure 4.1. Molecular structures of unsubstituted cobalt phthalocyanine (CoPc), nitro substituted cobalt phthalocyanine (TNCoPc) and carboxy substituted cobalt phthalocyanine (TCCoPc).

TNCoPc ($C_{32}H_{12}CoN_{12}O_8$) and TCCoPc ($C_{36}H_{16}CoN_8O_8$) molecules respectively indicating their successful formation (Figure 4.2 a-f). Matrix-assisted laser desorption ionization time-of-flight mass spectrometry (MALDI-TOF) showed the parent ion peaks at m/z value of ~572, ~751 and ~747 for CoPc ($C_{32}H_{16}CoN_8$), TNCoPc ($C_{32}H_{12}CoN_{12}O_8$) and TCCoPc ($C_{36}H_{16}CoN_8O_8$) molecules respectively indicating their successful formation (Figure 4.2 a-c). The Fourier-transform infrared spectroscopy (FTIR) was further carried out to confirm the formation of molecular catalysts. Given the compound comprises of different bonding environments, mainly C=C, C-N and C-C bonds, they should exhibit distinct fingerprints in the FTIR spectra. From FTIR spectra, peaks at ~1643 cm^{-1}, ~1356 cm^{-1}, ~1285 cm^{-1}
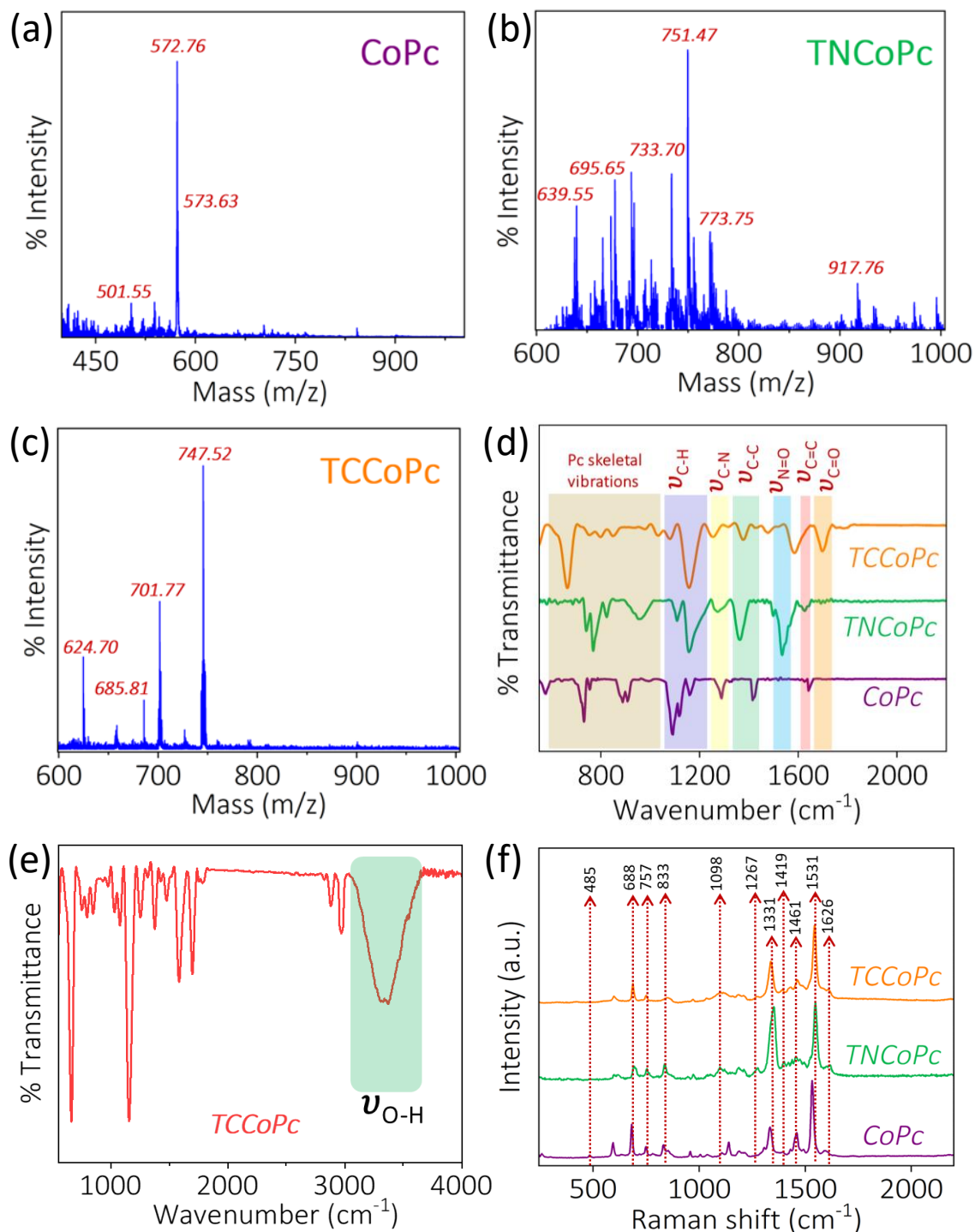
Figure 4.2. (a) Matrix-assisted laser desorption ionization time-of-flight mass spectrometry (MALDI-TOF) of (a) CoPc (b) TNCoPc and (c) TCCoPc molecules. (d) Fourier transform infrared (FTIR) spectroscopy of CoPc, TNCoPc and TCCoPc molecules, (e) Full range Fourier transform infrared (FTIR) spectroscopy of TCCoPc molecule and (f) Raman spectra of CoPc, TNCoPc and TCCoPc molecules.

and ~1133 cm^{-1}, corresponding to C=C macrocycle ring vibration, C-N stretching vibrations, C-C stretching vibrations and C-H stretching vibrations, were observed respectively. Moreover, the vibrations observed at ~730, ~883, ~951 and ~1087 cm^{-1} are attributed to the phthalocyanine skeletal vibration. The stretching frequencies arising due to the functional groups -NO$_2$ and -COOH in the molecule can be observed at ~1532 cm^{-1} (N=O) and ~1700 cm^{-1} (C=O) respectively, (Figure 4.2d).[36-41] The broad peak at ~3445 cm^{-1} as observed in TCCoPc correlates to the O-H stretching vibration of the -COOH group, (Figure 4.2e). The Raman spectra further aids in confirming the formation of molecules. The formation of the molecules accompanies several characteristic Raman shifts related to various functionalities attached to the molecule. C-N stretching, C-C stretching and C-H bending vibrations are observed in the range 800-1200 cm^{-1}. The C-H in-plane deformation in the macrocyclic ring and the stretching vibration of the isoindole ring unit are respectively present at ~1267 cm^{-1} and ~1461 cm^{-1}. The C-N in-plane stretching vibrations are observed at ~1419 cm^{-1} and ~1626 cm^{-1}. C-C-C in-plane bending bands and the macrocyclic stretching vibration bands are present at a Raman shift between 400-600 cm^{-1} and ~757 cm^{-1} respectively, as seen in (Figure 4.2f).[36-39] The ^{1}H NMR demonstrates two double doublets at chemical shift values 9.53 – 9.55 ppm and 8.36 – 8.38 ppm indicating two different types of protons in CoPc. The chemical shift values at 7.85, 8.24 and 8.47 ppm for TNCoPc and at 8.29, 9.39, 10.21 and 12.47 ppm for TCCoPc prove the successful formation of corresponding molecules. The broad peak ~12 ppm for TCCoPc indicate the presence of the acidic group, (Figure 4.3).
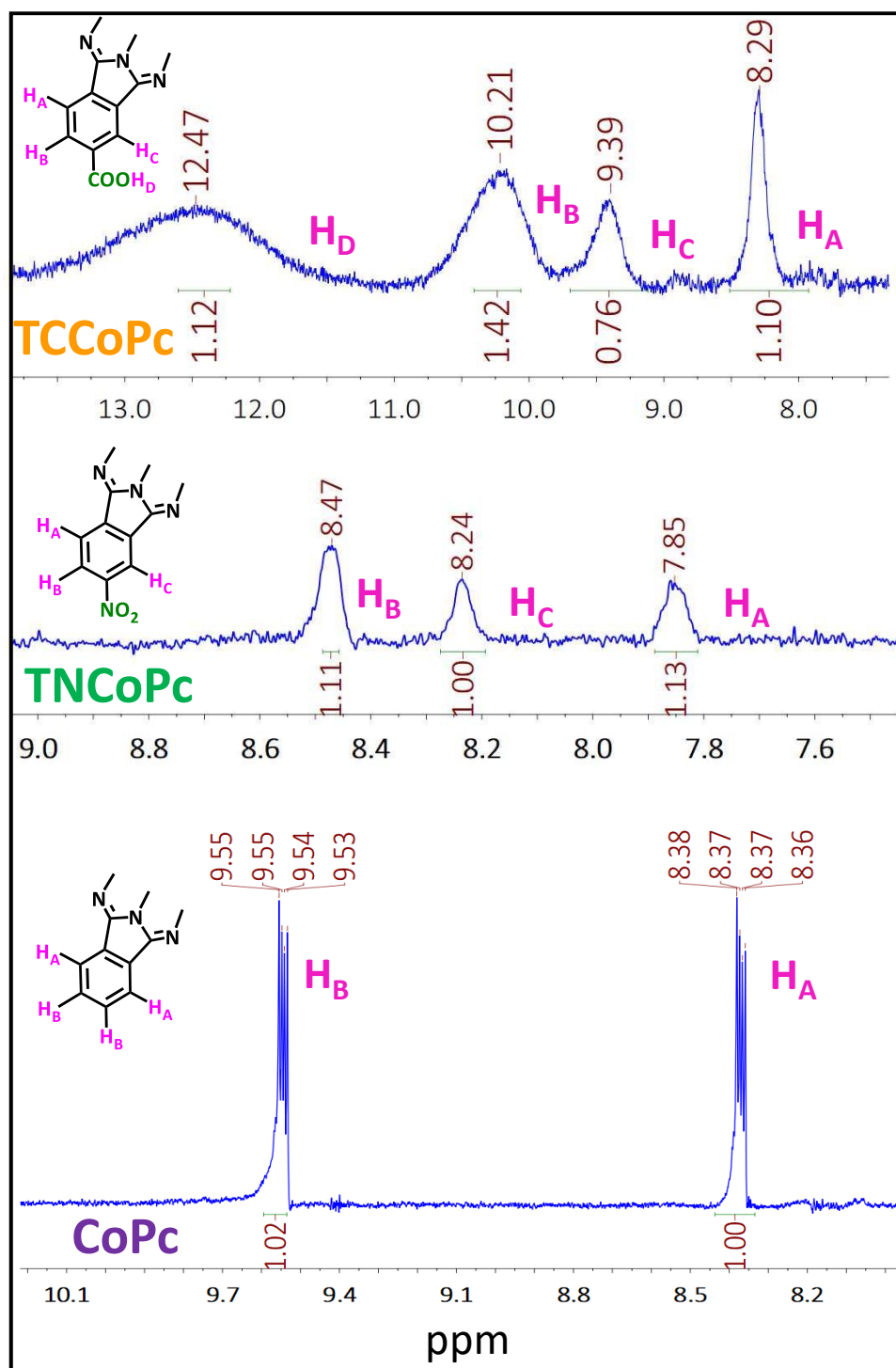
Figure 4.3. Nuclear Magnetic Resonance (^{1}H NMR) spectra of CoPc, TNCoPc and TCCoPc molecules.
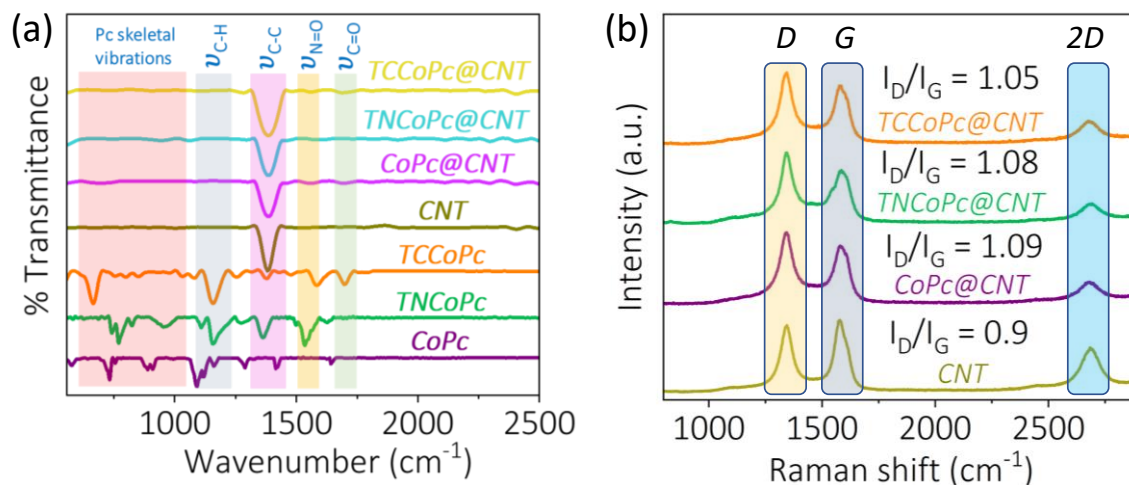
Figure 4.4. (a) Fourier transform infrared (FT-IR) spectroscopy and (b) Raman spectroscopy of CoPc@CNT, TNCoPc@CNT and TCCoPc@CNT composites.

Following the successful formation of all the three pristine molecules, their activity towards oxygen evolution reaction (OER) was probed via electrochemical water oxidation. Towards this, their composites with carbon nanotubes (MWCNT) were made as CNT can improve the overall electronic conductivity.[42-47] The composites namely CoPc@CNT, TNCoPc@CNT and TCCoPc@CNT were synthesized according to procedure reported in chapter 2, section 2.2.4, page 53. Various spectroscopic techniques like FT-IR, Raman spectroscopy etc., were utilized to inspect whether the molecules have undergone a complete integration with the CNT. Successful incorporation of molecular catalysts on CNT can be deciphered from the FT-IR spectra that clearly indicate the peaks affiliated to the phthalocyanine molecules (Figure 4.4a). Similarly, Raman spectroscopy has been performed which clearly exhibits defects and graphitic bands corresponding to the CNT substrate (Figure 4.4b). Incorporation of the molecules in CNT can be identified by calculating the intensity ratio arising from defect (I_D) and

graphitic (I_G) bands. Incorporation of the molecules in CNT should decrease the relative intensity of the graphitic bands due to more defect creation. [44,46,47] After the composite formation, as predicted, the I_D /I_G ratio does increase, rendering the successful incorporation of phthalocyanine in CNTs (Figure 4.4b). Furthermore, scanning electron microscopy (SEM) images, (Figure 4.5) in combination with energy dispersive X-ray spectroscopy (EDS), (Figure 4.6) show characteristics features of CNT and confirm the presence of Co, C, N and O (EDS pattern) in the composite CNT catalytic systems. All these along with the observations made from FTIR and Raman spectroscopy, proves the integration of the phthalocyanine molecules on CNT.
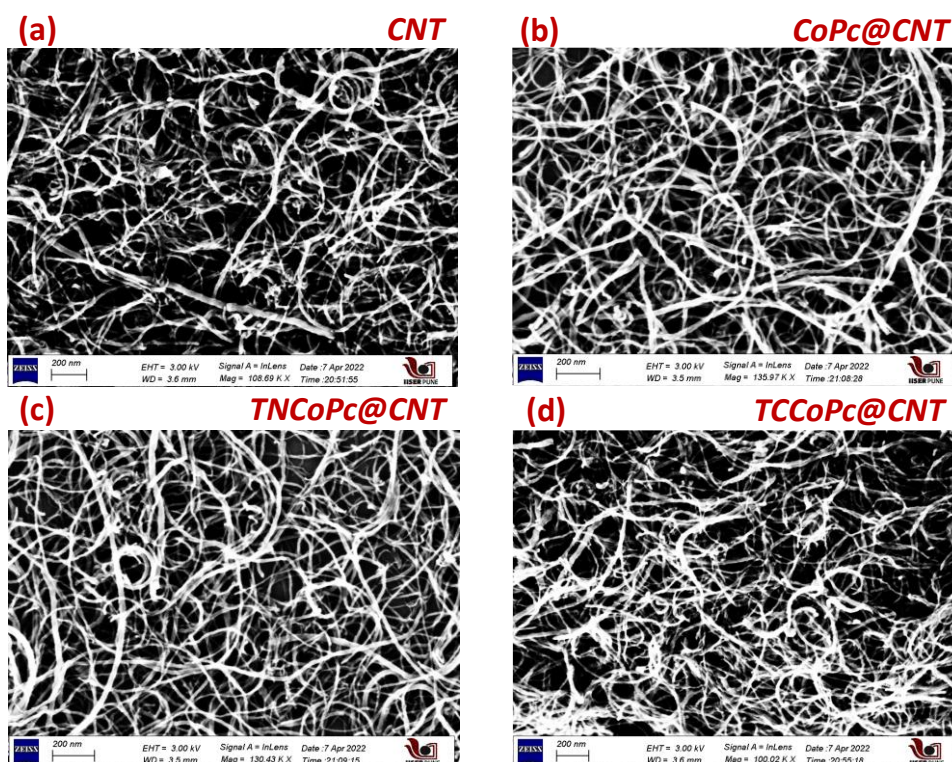
Figure 4.5. FE-SEM images of (a) CNT (b) CoPc@CNT (c) TNCoPc@CNT and (d) TCCoPc@CNT.
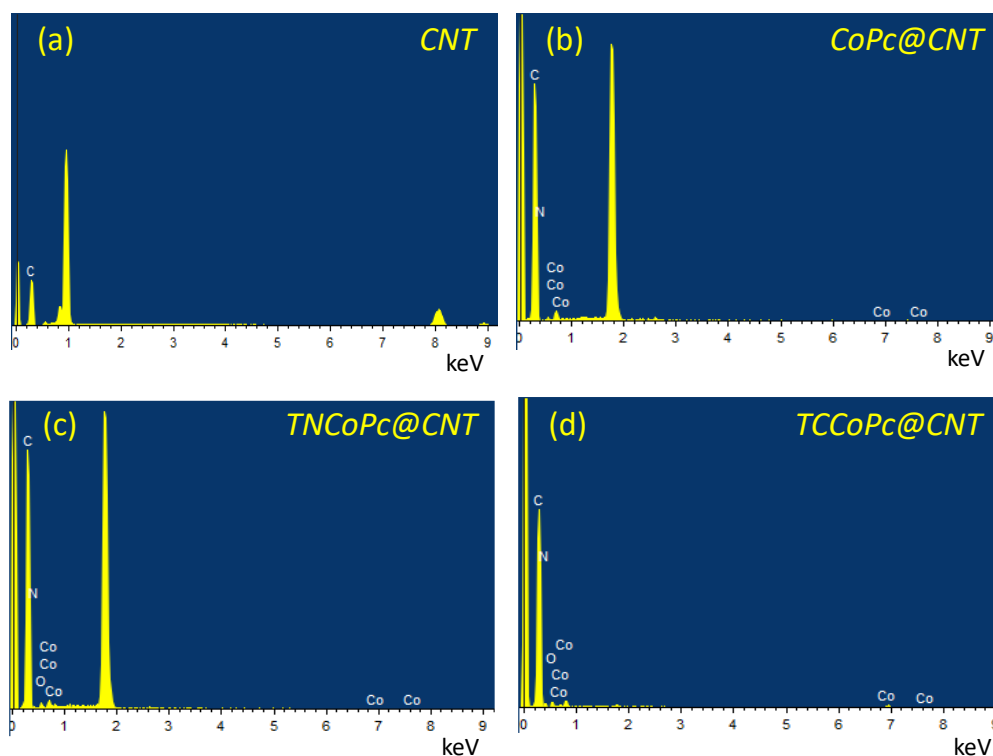
Figure 4.6. EDS pattern of (a) CNT (b) CoPc@CNT (c) TNCoPc@CNT and (d) TCCoPc@CNT.

4.2.2. UV-vis, XPS and DFT analysis of pristine molecules.

It should be noted that nitro functionalized ligand is more electron withdrawing than carboxy functionalized ligand as per the spectrochemical series and hence their oxidative electrocatalysis should follow the same trend. [33-35] This is because more electron withdrawing ligand would favor oxidative activation of the catalytic metal centre which is expected to accelerate their oxidative electrocatalysis. To understand this oxidative activation in CoPc systems, initially UV-Vis and XPS analyses along with theoretical calculations were carried out. UV-visible spectroscopy demonstrated two bands in the range 300-400 nm (B band) and 550-750

nm (Q band) for all the three molecules which are characteristic bands of macrocyclic molecules, Figure 4.7a.
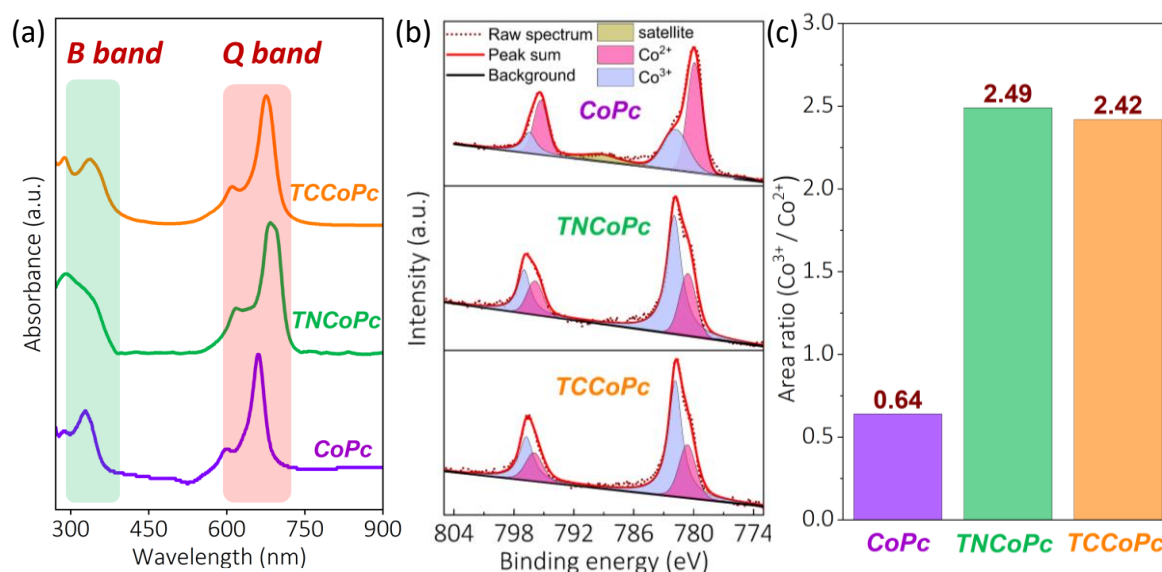
Figure 4.7. (a) UV-visible spectroscopy, (b) X-ray photoelectron spectroscopy (XPS) spectra, and (c) the relative area ratio of Co^{3+} to Co^{2+} of unsubstituted CoPc, TNCoPc and TCCoPc molecules extracted from the XPS spectra demonstrated in Figure 4.7b.

It is reported that the Q-band is more prone to the nature of the ligand [36-38,48], and as can be seen in Figure 4.7a, where the Q-band is more influenced by ligand substitution. UV-vis spectra showed a red shifted Q-band for TNCoPc compared to TCCoPc and unsubstituted CoPc, Figure 4.7a. This is attributed to the increased electronic delocalization due to the substitution of -NO_2 group on the macrocyclic ligand leading to enhanced -I (electron withdrawing inductive effects) and -R (electron withdrawing resonance effects) effects. Further, XPS analysis with the pristine molecular catalysts shows that the percent of the oxidised cobalt species is enriched in TNCoPc than TCCoPc and unsubstituted CoPc, Figure 4.7b and Figure 4.7c. Chemical softness parameter obtained from density functional theory

(DFT) calculations (for details please refer to chapter 2, section 2.7, pages 61-63) was found to be the highest for nitro functionalized ligand than carboxy and unsubstituted ligands, Figure 4.8 and Table 4.1. The higher chemical softness of nitro functionalized ligand is mirrored in their decreased HOMO-LUMO gap. It is known that the activity of a particular catalytic entity can be directly correlated to chemical softness of the molecular catalyst.[49-51] Based on these, it is expected that the same Co catalytic entity to be more active with the nitro functionalized ligand than carboxy and unsubstituted ligands.
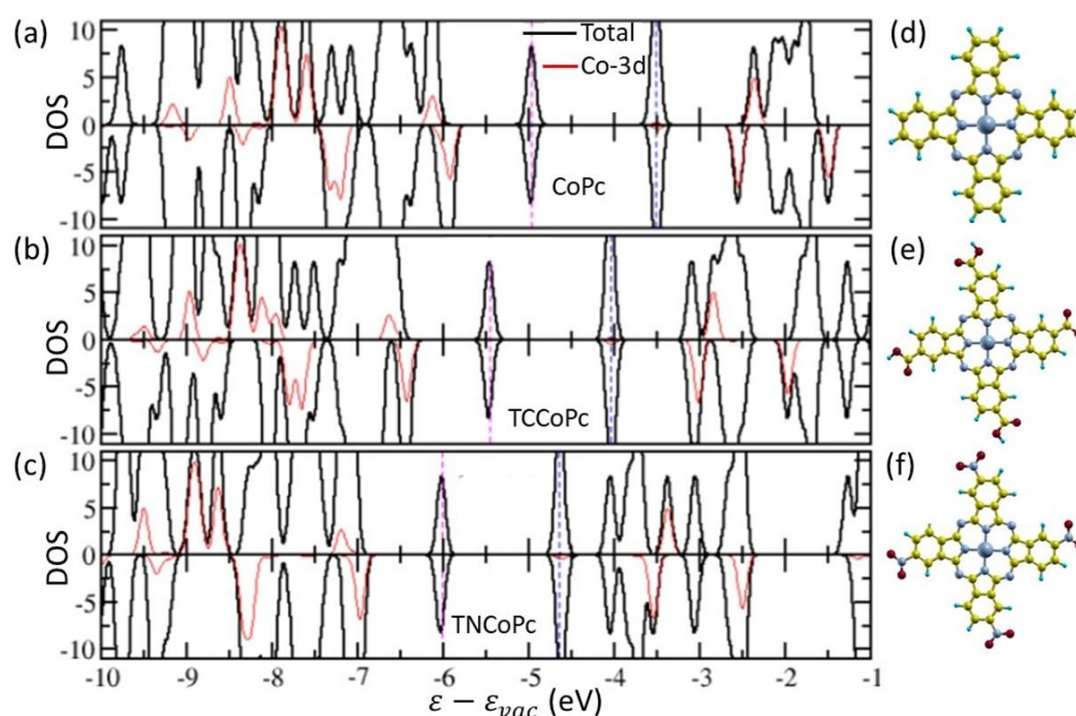
Figure 4.8. (a-c) Density of states (DOS) and (d-f) optimized structures of CoPc, TNCoPc and TCCoPc molecules respectively. The HOMO (LUMO) is marked by red dashed (blue dashed) vertical line. All the energies are shifted with respect to that of the vacuum energy. In (d), (e) and (f) the C, N, H, O and Co atoms are denoted by yellow, grey, turquoise, red and large grey spheres respectively.

Table 4.1. Parameters extracted from DFT calculations (Figure 4.8).

System	CoPc	TCCoPc	TNCoPc
HOMO-LUMO gap (eV)	1.46	1.41	1.39
Chemical Hardness, η (eV)	0.73	0.71	0.69
Chemical softness, $1/\eta$ (eV^{-1})	1.37	1.41	1.45
Chemical Potential, μ (eV)	-4.22	-4.74	-5.37
Electronegativity, χ (eV)	4.22	4.74	5.37
DDEC charge on Co	0.613	0.618	0.621

### 4.2.3 Electrochemical analysis of oxygen evolution reaction.

However, OER electrocatalysis in aqueous acidic medium shows that the onset potential as well as the overpotential required for a particular rate follows the order: TCCoPc < TNCoPc < CoPc, which is counter intuitive with respect to their inductive effects, Figure 4.9a. This is contrary to their position in the spectrochemical series, and the oxidative activation of the catalytic metal center as detailed in Figure 4.7. To understand this intriguing order in electrocatalysis, OER electrocatalysis with the same molecular platforms in alkaline medium was performed, Figure 4.9b. Interestingly, the electrocatalytic capability of the molecular systems followed a trend with a higher activity in favor of nitro functionalized ligand than carboxy and unsubstituted ligands which is as expected by their

location in the spectrochemical series. Taken together, the electrocatalytic capability of the same catalytic entity in acidic medium does not follow the trend dictated by the ligands with respect to their inductive effects. Therefore, the surrounding acidic medium may be playing a role in modulating the electric double layer (EDL) which in turn might be leading to a pronounced oxidative activation of the catalytic Co species in carboxy functionalized ligand than nitro functionalized ligand.
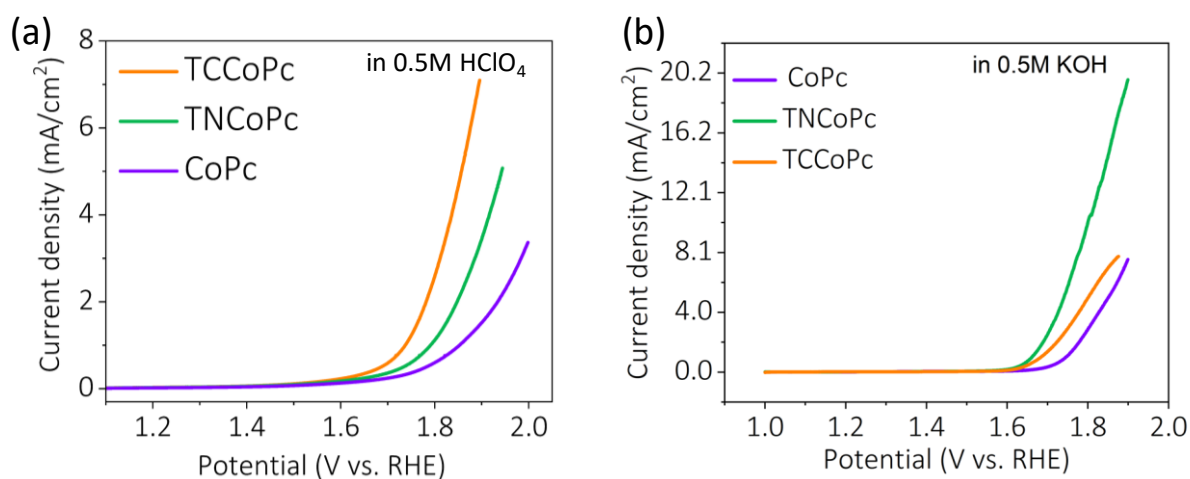

Figure 4.9. Linear sweep voltammetry (LSV) curves for water oxidation reaction recorded at a scan rate of 10 mV/s at a rotation rate of 1600 rpm in (a) 0.5 M $HClO_4$ solution and (b) 0.5 M KOH solution with CoPc, TNCoPc and TCCoPc molecules.

To understand this, initially the surface charge of the molecular catalysts by performing electrochemical analysis with a negatively and positively charged redox probes like ferricyanide and $[Ru(bpy)_3]^{2+}$ was evaluated respectively. It was observed that for the same weight percent of the molecular systems, the redox currents of negatively charged ferricyanide is noticeably enhanced with carboxy functionalized ligand than the nitro functionalized ligand suggesting that the carboxy functionalized ligand has
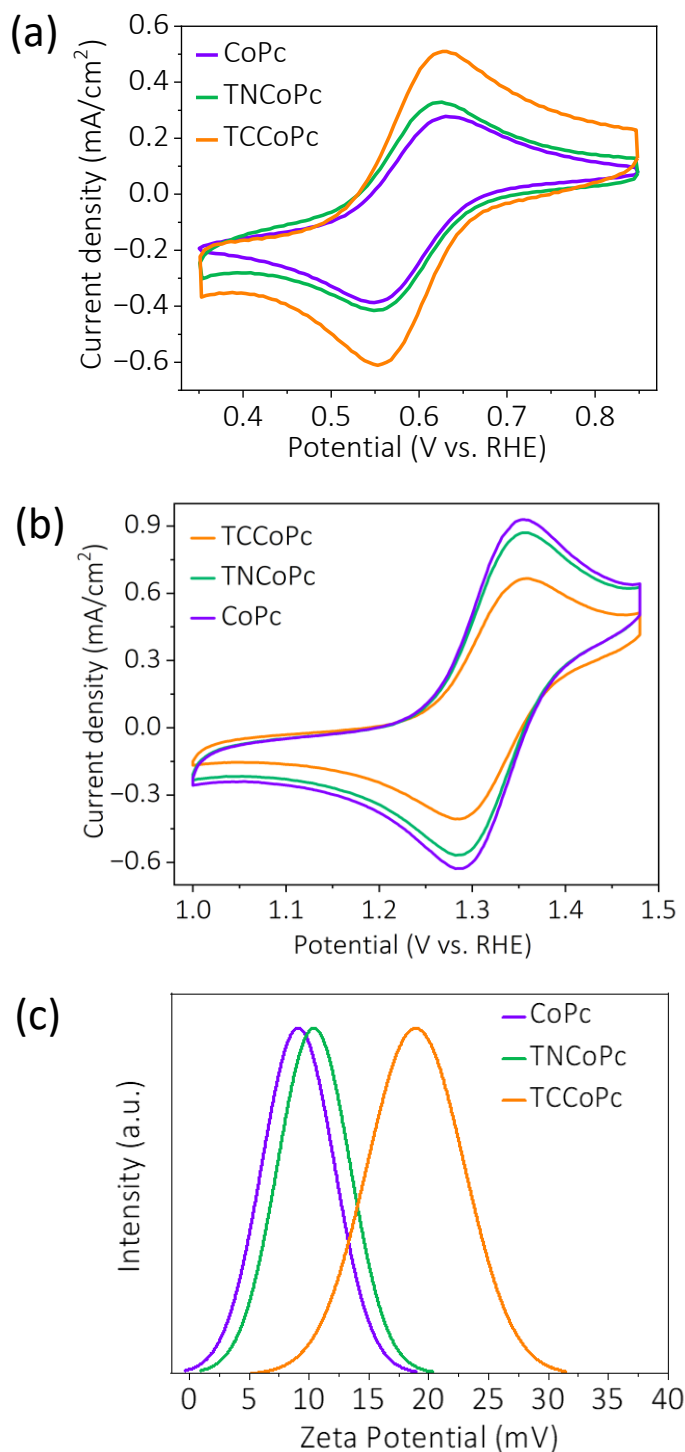
Figure 4.10. Cyclic voltammogram in 0.1 M HClO$_4$ medium collected at a scan rate of 20 mV/s for (a) 10 mM ferricyanide solution and (b) 5 mM [Ru(bpy)$_3$]$^{2+}$ solution with CoPc, TNCoPc and TCCoPc molecules. (c) Zeta potential measurement in acidic medium for CoPc, TNCoPc and TCCoPc molecules.
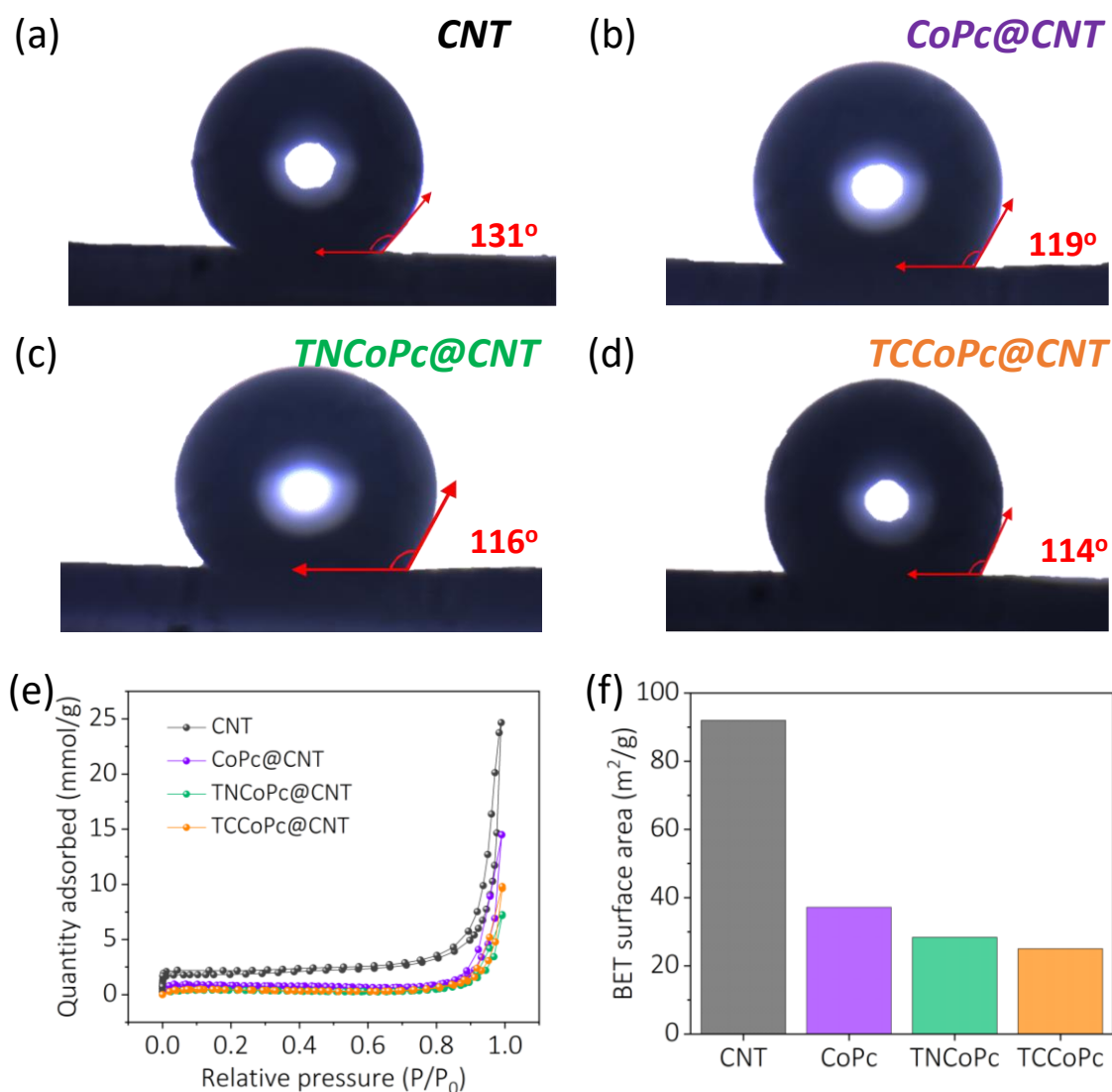
Figure 4.11. Contact angle measurements of (a) CNT, (b) CoPc@CNT, (c) TNCoPc@CNT and (d) TCCoPc@CNT. (e) The N_2 adsorption-desorption isotherm, and (f) BET surface area of pristine CNT, CoPc@CNT, TNCoPc@CNT and TCCoPc@CNT.

a higher amount of positive surface charge as compared to the nitro functionalized ligand, Figure 4.10a. An opposite behaviour was observed with the positively charged redox probe $[Ru(bpy)_3]^{2+}$, further signalling that the surface charge of the carboxy functionalized ligand is more positive than the nitro functionalized ligand, Figure 4.10b. To further commensurate this

result, Zeta potential measurements were carried out and this difference in their surface charge is reflected in their Zeta potential measurements, Figure 4.10c, which suggest the carboxy functionalized ligand (nearly 19 mV) is more positive than the nitro functionalized ligand (nearly 10 mV) and unsubstituted CoPc (nearly 9 mV) in acidic medium. All these analyses suggests that the TCCoPc has a higher positive surface charge assembly than the TNCoPc molecule.

To investigate whether this disparity is because of the difference in surface area or wettability of the composite electrodes or not, contact angle and BET surface area measurements were performed. As shown in Figure 4.11 (a-d), the wettability was found to be almost similar for all the three catalysts. The specific surface area obtained from BET was also found to fall in a similar range for all the three composites, Figure 4.11 (e-f). These rules out the possibility of the surface area and wettability factors contributing to the alterations in the redox currents of the charged redox species and suggests it is primarily due to the surface charge of the molecules in acidic medium.

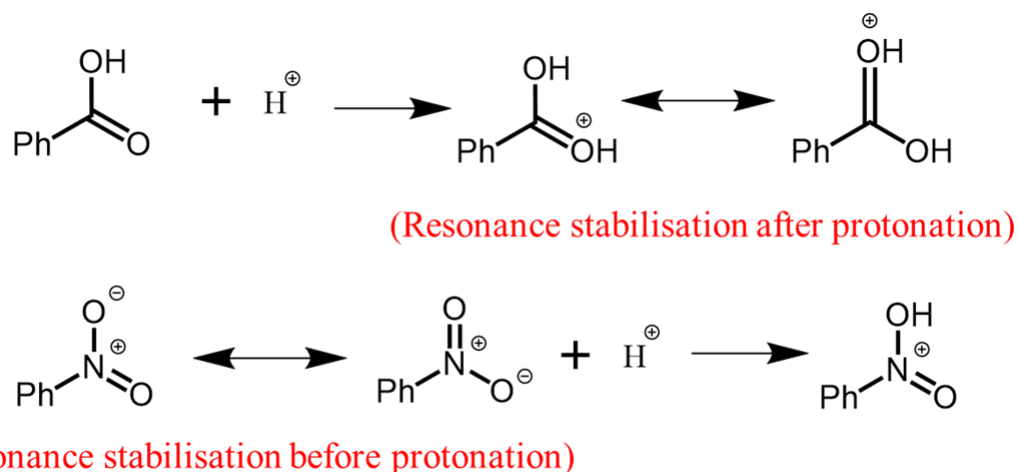### 4.2.4. UV-vis and XPS analysis of acid treated catalysts.

This higher positive surface charge signals the protonation of the carboxy functionality in aqueous acidic medium, which should make the carboxy ligand more electron withdrawing than the nitro functionalized ligand. This is probed by UV-Visible acid titration with and without acid in dimethyl sulfoxide (DMSO) solvent. As can be seen, the carboxy substituted
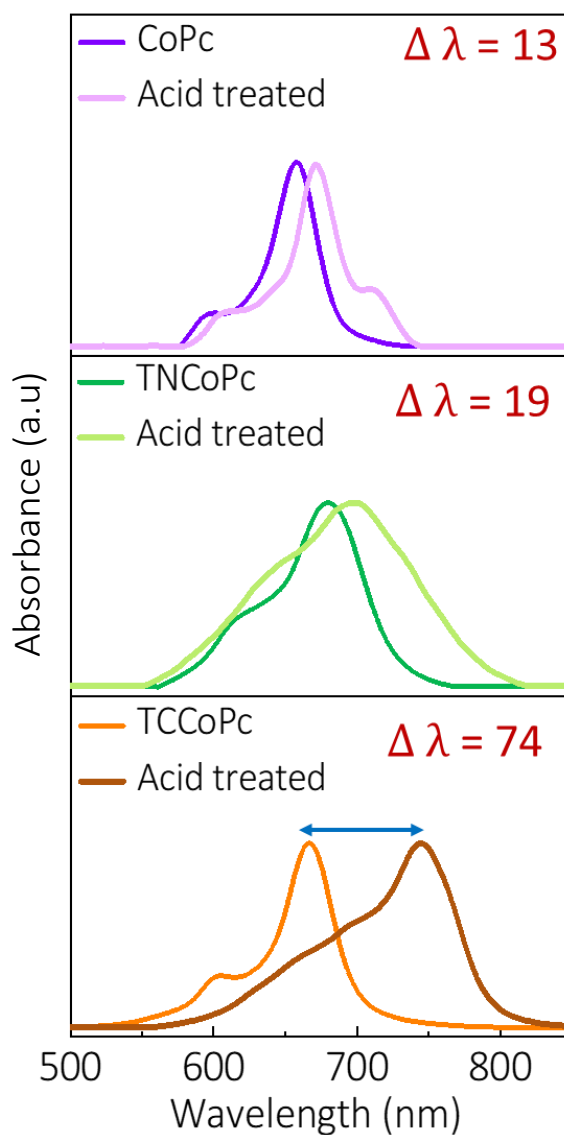
Figure 4.12. UV-vis spectroscopy of TCCoPc, TNCoPc and unsubstituted CoPc in the absence and the presence of acid or H^+.

Table 4.2. pKa values of oxo acids.

Protonated species	pKa values
	-12.4
	-7.8

(Resonance stabilisation after protonation)

(Resonance stabilisation before protonation)

Scheme 4.1. Scheme depicting the resonance stabilization of protonated carboxyl and nitro functionalities.

ligand demonstrated a significant red shift of Q band maxima (by nearly 74 nm) compared to nitro functionalized ligand (by nearly 19 nm) and unsubstituted ligand (by nearly 13 nm), Figure 4.12. So, this possibility of protonation of carboxy ligand ideally suggests that the TCCoPc molecule can undergo 8 protonation whereas the TNCoPc and unsubstituted molecule can undergo only 4 protonation. The pKa values for the protonated forms of aromatic nitro group and aromatic carboxylic acid group are -12.4 and -7.8 respectively, Table 4.2.[52-54] It is well known that lower the pKa value, the stronger is the acid. Thus, based on the pKa values of the protonated groups, it is evident that the extent of protonation at pH = 0 (electrolyte used for the present investigation) will be much more pronounced in the carboxyl group than the nitro group. Secondly, the protonated form of the -COOH group is resonance stabilized whereas the protonation of $-NO_2$ breaks its existing resonance stabilization, Scheme 4.1.
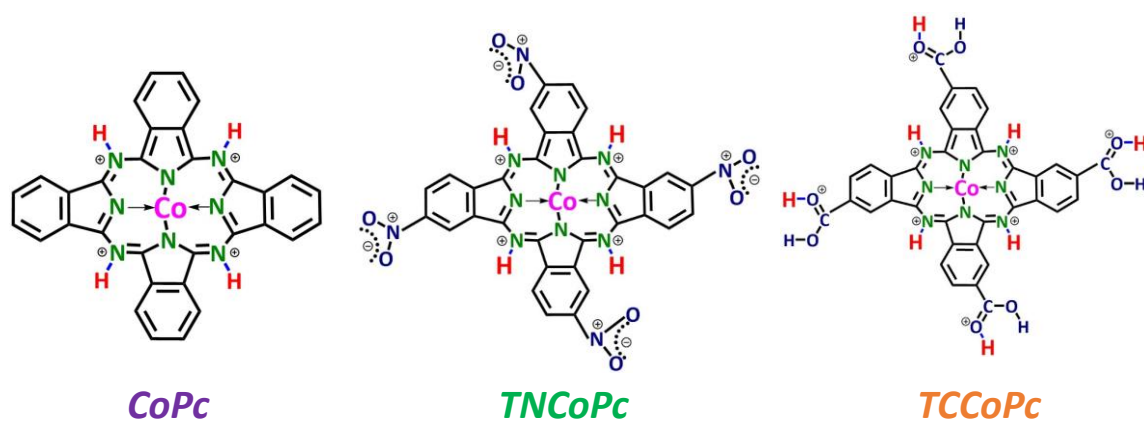
Scheme 4.2. Schematics showing the extent of protonation in TCCoPc, TNCoPc and CoPc molecules.

Based on the above observations, a plausible explanation was predicted as shown in Scheme 4.2, which demonstrates a higher degree of protonation in TCCoPc than TNCoPc. This kind of proton charge assembly should make the carboxy ligand to be more electron withdrawing than the nitro functionalized and unsubstituted ligands, with a higher degree of oxidative activation of the catalytic Co center in the former. This is probed by XPS analysis with acid treated molecular catalysts, Figure 4.13a and 4.13b. Figure 4.13c demonstrates a comparison of the relative oxidized cobalt species for all the three molecules before and after acid treatment. As shown, the percentage of oxidized Co species is enriched in carboxy ligand than the other molecular platforms treated in a similar manner. Therefore, the higher amount of proton charge assembly in the EDL of carboxy ligand explains its counter intuitive activity than nitro functionalized ligand.
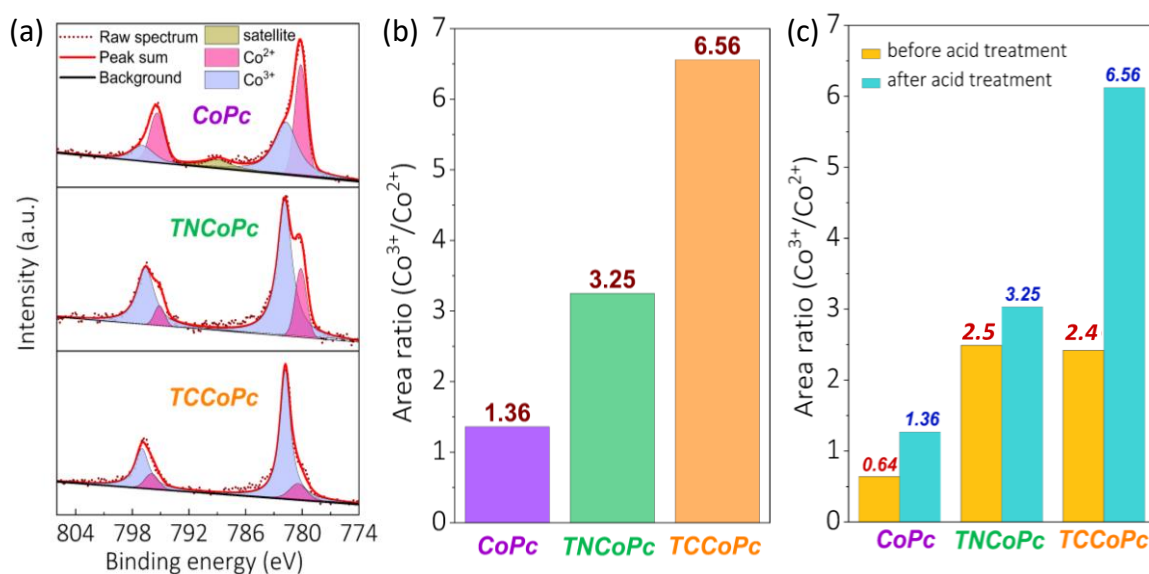
Figure 4.13. (a, b) X-ray photoelectron spectra (XPS) and the relative area ratio of Co^{3+} to Co^{2+} of unsubstituted CoPc, TNCoPc and TCCoPc molecules after treating them with acid. (c) Comparison of the relative oxidized cobalt species for all the three molecules before and after acid treatment.

4.2.5 Electrochemical analysis of chlorine evolution reaction.

The foregoing discussion highlights that oxidative activation of the catalytic metal center is more pronounced and the surrounding ligand is significantly more positive in the carboxy functionalized ligand in acidic medium. These two effects can be exploited together for challenging electrochemical oxidation reactions especially when the electrochemical substrate happens to be negatively charged. This is because the proton charge assembly on the ligand is expected to drag the negatively charged substrate towards the electrode and the pronounced oxidative activation of the catalytic center is expected to aid the removal of electrons from the substrate. In this context, these molecular platforms for chlorine evolution reaction wherein the substrate is negatively charged Cl^- species were explored. The electrochemical activity towards chlorine evolution reaction

(CER) was investigated with CoPc@CNT, TNCoPc@CNT and TCCoPc@CNT by voltametric techniques. Linear sweep voltammogram (LSV), Figure 4.14a, suggest that for the CER process, the onset potential as well as the overpotential required for achieving a particular rate follow the order: TCCoPc < TNCoPc < CoPc. Chronopotentiometric analysis (potential vs. time) was carried out for understanding their long-term stability and durability. The potential required to achieve a particular current density was found to be lowest in case of TCCoPc followed by TNCoPc and CoPc, Figure 4.14b. The kinetic information of the catalysts for CER was obtained from Tafel analyses. The plot between overpotential (η) and log i (current) also called the Tafel plot provided the lowest Tafel slope for the TCCoPc and the highest slope for CoPc suggesting a facile kinetics in the order: TCCoPc > TNCoPc > CoPc, Figure 4.14c. The Tafel slope values for TCCoPc, TNCoPc, CoPc given in Table 4.3 were pointing to a Volmer-Heyrovsky reaction pathway with Volmer step as the rate determining step.[55-58] The intrinsic catalytic activity of electrocatalysts for CER was also assessed in terms of exchange current density (j_0) using Tafel analyses (Table 4.3), further signalling the superior activity of TCCoPc over the other two catalysts. The CER activity of the catalysts was also assessed by calculating the turnover frequencies (TOFs). For the calculation of TOFs, all Co sites in the composite catalyst layer were considered as active sites.[59]

The number of active sites (n) of the catalysts were calculated by the following equation:

$$n = \frac{mCo}{MCo} = \frac{wCo \times VCo \times \rho Co}{100 \times MCo} \qquad \text{.......} (4.1)$$
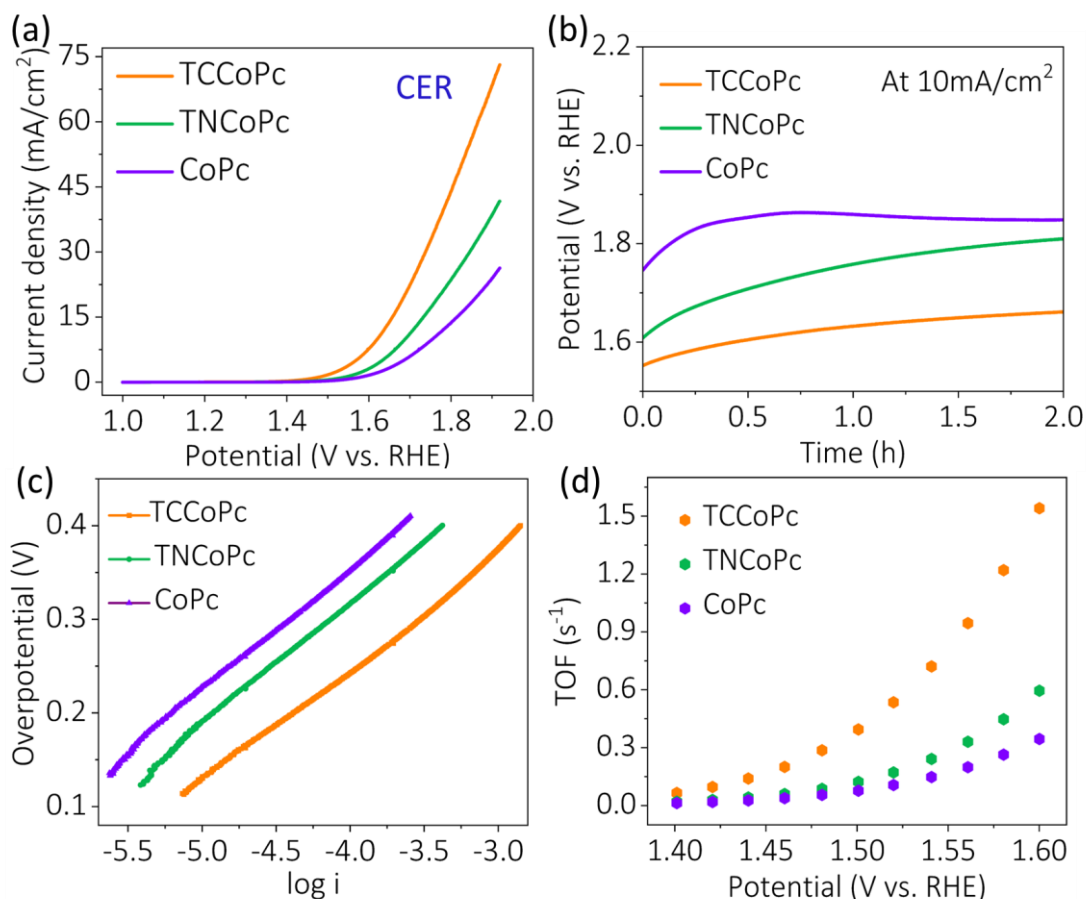
Figure 4.14. (a) Linear sweep voltammetry curves for CER recorded at a scan rate of 10 mV/s at a rotation rate of 1600 rpm in 0.1 M HClO₄ solution containing 1 M NaCl with CoPc, TNCoPc and TCCoPc molecules. (b) Chronopotentiometric measurements at a current density of 10 mA/cm², and (c) Tafel plots for the catalytic systems in 0.1 M HClO₄ + 1 M NaCl solutions. (d) Calculated turnover frequencies (TOFs) for CER with CoPc, TNCoPc and TCCoPc molecules.

where m_{Co} is the amount of Co in the catalyst, M_{Co} is the molar mass of Co (58.33 g mol^{-1}), w_{Co} is the weight percent of Co in the composites, ρ_{Co} is the mass concentration of Co in the catalyst ink, and V_{Co} is the volume of the loaded catalyst ink. The turnover frequency (TOF) of the phthalocyanines is calculated as follows:

$$\text{TOF (s}^{-1}) = \frac{id}{2*n*F} \qquad \text{....... (4.2)}$$

where i_d is the disk current during CER measurement in 0.1 M HClO$_4$ + 1.0 M NaCl, n is the number of active sites and F is the Faraday constant (96484 C). The factor ½ is based on the two electrons that are transferred for the oxidation of two Cl$^-$ ions to one Cl$_2$ molecule (equation 4.3).

$$2 \; Cl^- \; \rightleftharpoons \; Cl_2 + 2e^- \qquad .... \; (4.3)$$
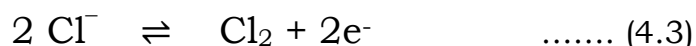
TCCoPc showed 5 times higher TOF than CoPc at an overpotential of 200 mV, Figure 4.14d, thereby deciphering the role of the ligand in activating the electrocatalyst.

Table 4.3. Tafel slopes and exchange current densities of CoPc, TNCoPc and TCCoPc for chlorine evolution reaction extracted from (Figure 4.14c).

System	Tafel slope (mV/dec)	Exchange current density ($\mu A \; cm^{-2}$)
TCCoPc	122	13.2
TNCoPc	138	5.87
CoPc	142	3.46

In order to confirm that CER is the major electrochemical process, rotating ring disk voltametric measurements (RRDE) have been performed. A fixed potential of 0.95V vs. RHE at the Pt ring electrode to reduce Cl$_2$ was applied while scanning the disk electrode towards the CER region.[60, 61] 0.95 V vs. RHE was chosen for Cl$_2$ reduction from the following experiments. Firstly, the electrolyte (0.1 M HClO$_4$ + 1 M NaCl) was purged with nitrogen gas and the cyclic voltammogram was recorded on a Pt electrode (black trace in Figure 4.15a).
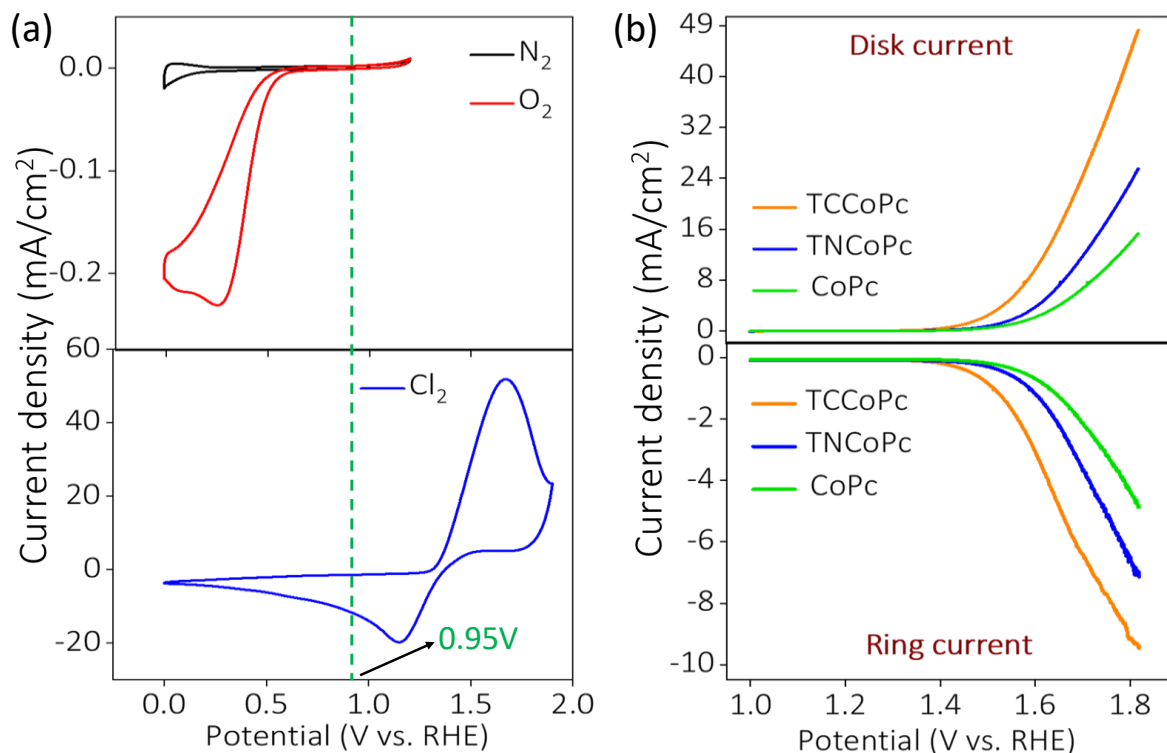
Figure 4.15. (a) CV of Pt electrode in nitrogen (black trace) and oxygen (red trace) purged solution containing (0.1 M HClO₄ + 1 M NaCl) as electrolytes (top panel). Chlorine evolution reaction (CER) and chloride reduction reaction (CRR) occurring on the same Pt electrode in nitrogen purged electrolytes (blue trace, bottom panel). (b) RRDE measurements of CER on TCCoPc, TNCoPc and CoPc catalysts in 0. 1 M HClO₄ containing 1 M NaCl. The measurements were carried out in Ar-saturated solutions at an electrode rotation speed of 1600 rpm at a scan rate of 10 mV/s. Top panel indicates disk currents for CER. Bottom panel shows the corresponding ring current for Cl₂ reduction obtained on a Pt ring electrode, whose potential was fixed at 0.95 V vs. RHE.

Subsequently, the solution was purged with oxygen and the current response on the same Pt electrode for ORR was recorded (red trace, Figure 4.15a). The ORR onset was found to be close to 0.7 V vs. RHE on Pt electrode in this electrolyte. The solution was again purged with nitrogen and scanned to a higher positive potential where CER occurred. As expected around 1.32

V vs. RHE an exponential rise in the current was seen and on reversing the scan, a reduction peak started appearing from nearly 1.44 V with a peak potential close to 1.2 V due to the reduction of Cl_2 to Cl^- (blue trace, Figure 4.15a). Reading this together, at 0.95V vs. RHE, only Cl_2 should get reduced and not O_2. And the presence of ring current under this condition should primarily correspond to Cl_2 reduction and not to ORR. Based on these experiments, a potential of 0.95 V vs. RHE was chosen for selective Cl_2 reduction without the complexity of ORR on the RRDE ring electrode. In the RRDE experiments, Figure 4.15b, an increase in the ring current was observed as soon as the disk current starts rising indicating that the Cl_2 generated at the disk was simultaneously getting reduced back at the ring. This confirms that oxygen generation is negligible, pointing to selective CER on these molecular electrocatalysts.
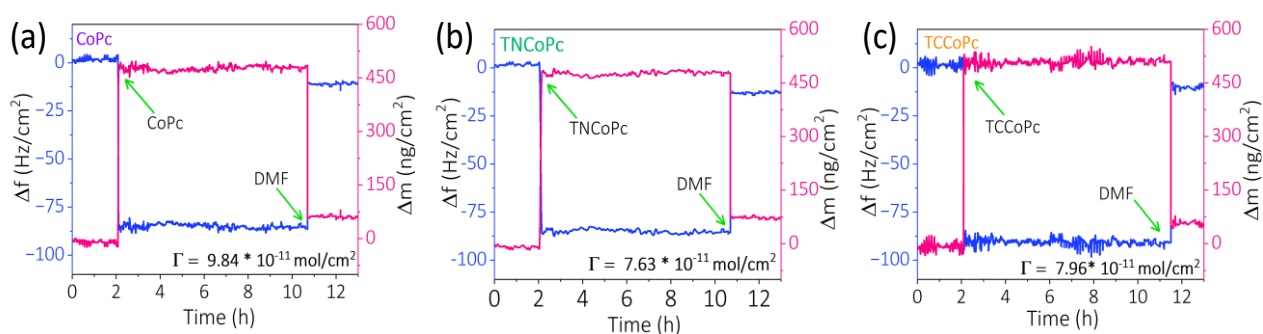
**Figure 4.16.** Quartz crystal microbalance (QCM) profile during the adsorption of the molecules from a 0.5 mM solution of (a) CoPc, (b) TNCoPc and (c) TCCoPc in dimethyl formamide (DMF). Blue trace shows the frequency change during adsorption and the pink trace shows the mass change calculated using Saurbrey equation. Surface coverage (Γ) values of the molecules are provided in respective images.

Table 4.4. Surface coverage (Γ) values of CoPc, TNCoPc and TCCoPc molecules.

System	Γ (mol/cm²)
TCCoPc	7.96×10^{-11}
TNCoPc	7.63×10^{-11}
CoPc	9.84×10^{-11}

To further show that this behavior is intrinsic to the molecules, CER was carried out by modifying the glassy carbon electrode with monolayers of CoPc, TNCoPc and TCCoPc molecules. To ensure successful formation of monolayer Quartz crystal microbalance studies (QCM) were performed (please refer to chapter 2, section 2.6, pages 60-61). Changes in mass during QCM studies indicate almost equal mass change for all the three molecules, Figure 4.16. The surface coverage values obtained according to Saurbrey equation are given in Table 4.4 for all the three catalysts. These values are close to the theoretically expected value of 1.1×10^{-10} mol/cm² for a perfectly flat phthalocyanine monolayer indicating that the orientation of the molecules is nearly flat on the GC electrode surface.[62, 63] When these monolayer modified electrodes were used as electrocatalysts for CER, TCCoPc molecule demonstrated higher activity over TNCoPc and CoPc molecules Figure 4.17 and the trends are analogues to the results in Figure 4.14.
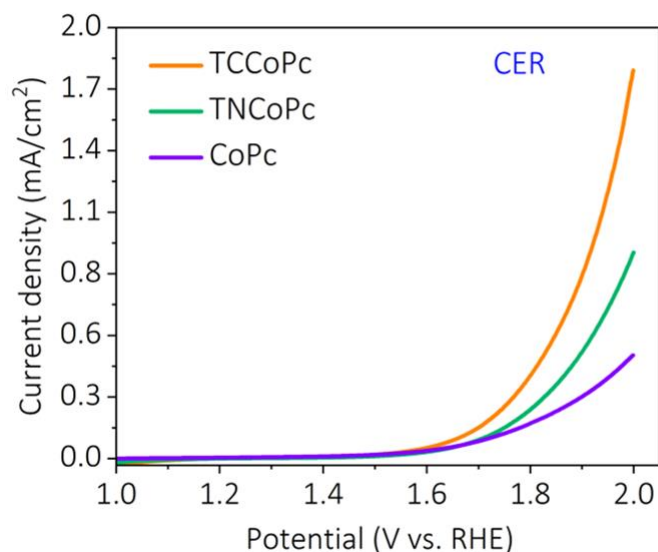
Figure 4.17. Linear sweep voltammetry curves for CER recorded at a scan rate of 10 mV/s in 0.1 M HClO$_4$ solution containing 1 M NaCl with monolayers of CoPc, TNCoPc and TCCoPc molecules on a glassy carbon electrode.

To further carry out the qualitative and quantitative analysis of Cl$_2$ formation with the catalysts, iodometric test and chronoamperometric method using RRDE were performed respectively.[59, 64, 65] Although, it is possible to quantify the amount of Cl$_2$ liberated with iodometric titration method, it does not give accurate results since some of the Cl$_2$ gas may escape into the surroundings during the titration. Therefore, the iodometric test was performed in order to prove Cl$_2$ gas is being generated by all the three catalysts. For this, chronoamperometry was carried out in a two-compartment cell for 120 seconds (refer to chapter 2, section 2.4.3, page 58 for details) and a few mL of the anodic electrolyte was transferred to a test tube containing an excess of KI solution as shown in Figure 4.18a. Initially the KI solution was colourless (test tube 1) but with addition of the Cl$_2$ containing electrolyte, it turned to yellowish brown in colour due to the

generation of triiodide ion (I_3^-) according to the following equations (test tube 2).

$$Cl_2 + 2\ KI \quad \rightleftharpoons \quad 2\ KCl + I_2 \qquad \text{....... (4.4)}$$

$$I_2 + I^- \quad \rightleftharpoons \quad I_3^- \qquad \text{....... (4.5)}$$

Following that, with the addition of hexane into the brown-coloured solution and after vigorously shaking it, two layers were observed getting separated which are the non-polar hexane layer on the top and the polar aqueous layer on the bottom (test tube 3). The non-polar layer gets a pink colouration as iodine is soluble in hexane, Figure 4.18a. This proves the presence of Cl_2 in the anodic electrolyte. After this, quantification of the Cl_2 gas by hydrodynamic technique was done. For each catalyst, Cl_2 was estimated by performing RRDE chronoamperometry at a rotation speed of 100 rpm for 500 seconds. The ring was biased at a constant potential of 0.95 V vs. RHE whereas the disk potential was fixed at 1.6 V vs. RHE. The amount of Cl_2 evolved or in other words the Cl_2 selectivity was calculated according to the following equation:

$$\text{Amount of } Cl_2\ (\%) = 100 \times \frac{2 \times iCER}{id + iCER} \ ; \text{ where } \ \text{....... (4.6)}$$

$$i_{CER} = \left| \frac{ir}{N} \right| \qquad \text{....... (4.7)}$$

where, i_d, i_r and N represent the disk current, ring current and collection efficiency respectively.[59] It is seen that the Cl_2 selectivity (%) is maximum for the TCCoPc catalyst giving a value of 93.7 ± 0.5 % whereas it is 92.2 ± 0.9 % and 88.1 ± 0.4 % for the TNCoPc and the unsubstituted CoPc catalysts
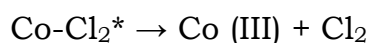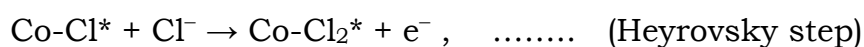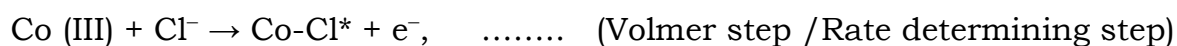
respectively, Figure 4.18b, c and d. This is direct evidence that the amount of Cl_2 produced is highest for the carboxy substituted cobalt phthalocyanine followed by nitro substituted and unsubstituted cobalt phthalocyanines at a fixed driving force of 1.6 V vs RHE.
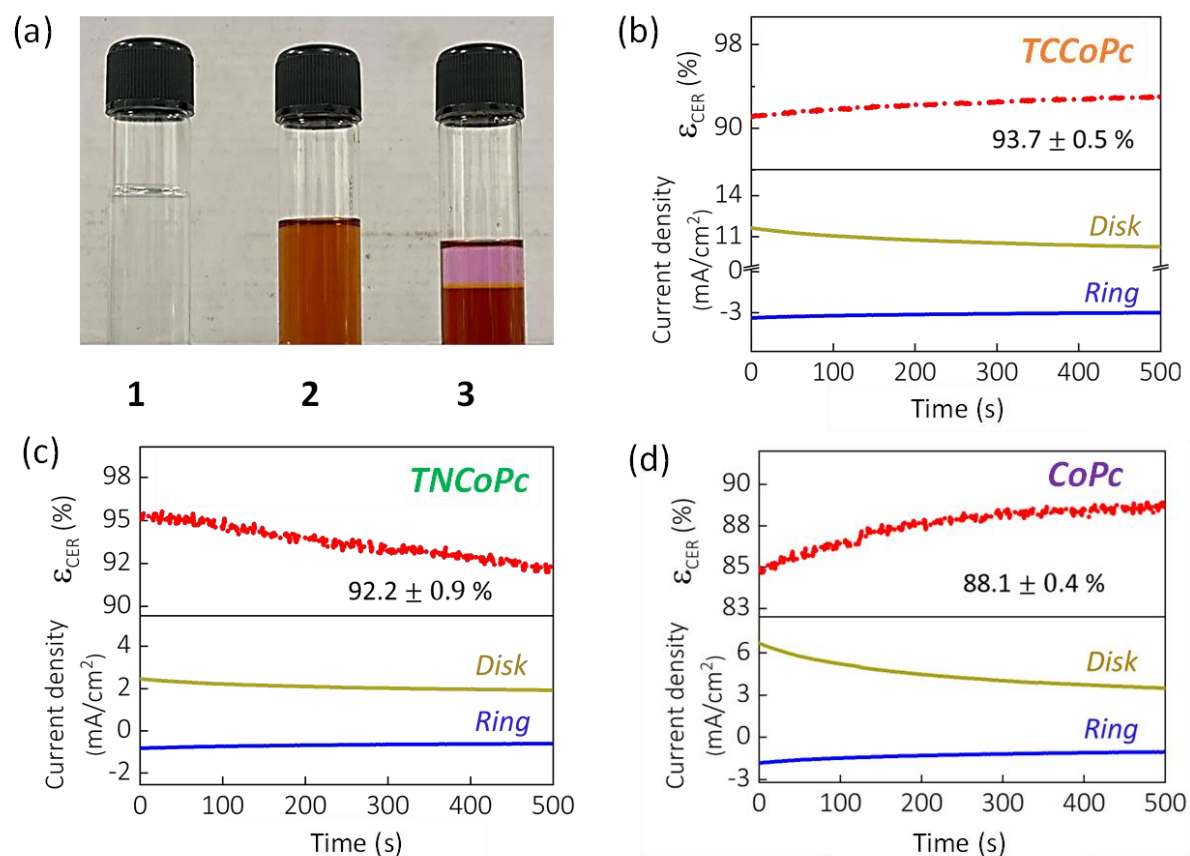
Figure 4.18. (a) Photographs of test tubes containing (1) only KI solution (colourless solution), (2) KI + anodic electrolyte (brown colour) and (3) KI + anodic electrolyte + hexane (pink layer and brown layer). Chronoamperograms of (b) TCCoPc, (c) TNCoPc and (d) CoPc catalysts measured by RRDE electrode in acidic media containing 1 M NaCl in an Ar-saturated 0.1 M $HClO_4$ electrolyte at an electrode rotation speed of 1600 rpm. The potential of the disc was fixed at 1.6V vs RHE and that of Pt ring electrode was fixed at 0.95 V vs. RHE for Cl_2 reduction.

As mentioned before, for oxidative electrocatalysis, oxidized Co species mediates the reaction in a complex sequence of events [66-68] and its enrichment in the TCCoPc in acidic medium (Figure 4.13) explains the higher activity of this electrocatalyst over the other. Further, the Tafel slope values on these electrocatalysts indicate a Volmer-Heyrovsky mechanism as explained before. Since the rate limiting Volmer step involves the adsorption of Cl^- ion on to the active site, the higher positive charge of the metal centre should result in a more favourable interaction with the negatively charged Cl^- ions. Based upon the Tafel slope and XPS data, the overall reaction was predicted to follow a Volmer-Heyrovsky mechanism as shown below,

$Co\ (III) + Cl^- \rightarrow Co\text{-}Cl^* + e^-$, ...   (Volmer step /Rate determining step)

$Co\text{-}Cl^* + Cl^- \rightarrow Co\text{-}Cl_2^* + e^-$, ...   (Heyrovsky step)

$Co\text{-}Cl_2^* \rightarrow Co\ (III) + Cl_2$

Taken together, this study suggests that in the domain of molecular electrocatalysis, the less obvious ligands can play indispensable roles by altering the EDL structure and this should be considered for the design of molecular platforms for challenging electrochemical transformations.

4.3. Conclusion:

A counter intuitive trend in electrocatalysis on the same catalytic metal center is demonstrated via the ability of the ligand functionality to undergo a proton charge assembly. Electrochemical analysis revealed that,

on the same catalytic entity, the carboxy functionalized ligand favoured the least Tafel slope, nearly 4 times higher exchange current density, ~5 times higher turn-over frequency and a chlorine selectivity as high as ~94% compared to unsubstituted ligand with a surprisingly higher activity than more aggressively electron withdrawing nitro functionalized ligands. XPS and UV-vis spectroscopy in combination with electrochemical analysis show the unexpected oxidative activation of the catalytic entity in carboxy functionalized ligand via proton charge assembly that in turn accelerates the overall CER process. This demonstration of less obvious ligand becoming indispensable in electrocatalysis via their ability to alter the EDL structure, suggest that a blind designing of the ligand by considering solely their inductive effect in the spectrochemical series will prevent the utilization of the maximum potential of the molecule in electrocatalysis.

4.4. References:

[1] Farghali, M.; Osman, A. I.; Mohamed, I. M. A.; Chen, Z.; Chen, L.; Ihara, I.; Yap, P. S.; Rooney, D. W. Strategies to Save Energy in the Context of the Energy Crisis: A Review. *Environ. Chem. Lett.* **2023**, *21*, 2003–2039.

[2] Shi, Y.; Lu, Y. C. Embedded order boosts battery membranes. *Nat Sustain.* **2022**, *5*, 1007–1008.

[3] Dufil, Y.; Favier, F.; Brousse, T.; Lethien, C.; Le Bideau, J.; Fontaine, O. Ionic Transport and Charge Distribution in Miniaturized Electrochemical Energy Storage Devices by Modeling Investigation. *J. Electrochem. Soc.* **2022**, *169* (6), 060551.

[4] Costentin, C.; Savéant, J. M. Towards an Intelligent Design of Molecular Electrocatalysts. *Nat. Rev. Chem.* **2017**, *1* (11), 1–8.

[5]   Yang, S.; Yu, Y.; Gao, X.; Zhang, Z.; Wang, F. Recent Advances in Electrocatalysis with Phthalocyanines. *Chem. Soc. Rev.* **2021**, *50* (23), 12985–13011.

[6]   Petit, Y. K.; Mourad, E.; Prehal, C.; Leypold, C.; Windischbacher, A.; Mijailovic, D.; Slugovc, C.; Borisov, S. M.; Zojer, E.; Brutti, S.; Fontaine, O.; Freunberger, S. A. Mechanism of Mediated Alkali Peroxide Oxidation and Triplet versus Singlet Oxygen Formation. *Nat. Chem.* **2021**, *13* (5), 465–471.

[7]   Cherevko, S. Stability and Dissolution of Electrocatalysts: Building the Bridge between Model and "Real World" Systems. *Curr. Opin. Electrochem.* **2018**, *8*, 118–125.

[8]   Cechanaviciute, I. A.; Antony, R. P.; Krysiak, O. A.; Quast, T.; Dieckhöfer, S.; Saddeler, S.; Telaar, P.; Chen, Y. T.; Muhler, M.; Schuhmann, W. Scalable Synthesis of Multi-Metal Electrocatalyst Powders and Electrodes and Their Application for Oxygen Evolution and Water Splitting. *Angew. Chemie - Int. Ed.* **2023**, *62*, e202218493.

[9]   Sorokin, A. B. Phthalocyanine Metal Complexes in Catalysis BT - Chemical Reviews. *Chem. Rev.* **2013**, *113* (10), 8152–8191.

[10]   Ji, W.; Wang, T.-X.; Ding, X.; Lei, S.; Han, B.-H. Porphyrin- and Phthalocyanine-Based Porous Organic Polymers: From Synthesis to Application. *Coord. Chem. Rev.* **2021**, *439*, 213875.

[11]   Laurs, H.; Heiland, G. Electrical and Optical Properties of Phthalocyanine Films. *Thin Solid Films* **1987**, *149* (2), 129–142.

[12]   Topal, S. Z.; Işci, Ü.; Kumru, U.; Atilla, D.; Gürek, A. G.; Hirel, C.; Durmuş, M.; Tommasino, J. B.; Luneau, D.; Berber, S.; Dumoulin, F.; Ahsen, V. Modulation of the Electronic and Spectroscopic Properties of Zn (II) Phthalocyanines by Their Substitution Pattern. *Dalt. Trans.* **2014**, *43* (18), 6897–6908.

[13]   Wöhrle, D.; Schnurpfeil, G.; Makarov, S. G.; Kazarin, A.; Suvorova, O. N. Practical Applications of Phthalocyanines – from Dyes and Pigments to Materials for Optical, Electronic and Photo-Electronic Devices. *Macroheterocycles,* **2012**, *5* (3), 191–202.

[14] Baygu, Y.; Soganci, T.; Kabay, N.; Gök, Y.; Ak, M. Phthalocyanine-Cored Conductive Polymer Design: Effect of Substitution Pattern and Chalcogen Nature on Optical and Electrical Properties of Zn (II)-Phthalocyanine–Cored Polycarbazoles. *Mater. Today Chem.* **2020**, *18*, 100360.

[15] Zhang, Y.; Lin, Y.; Duan, T.; Song, L. Interfacial Engineering of Heterogeneous Catalysts for Electrocatalysis. *Mater. Today* **2021**, *48*, 115–134.

[16] Huang, S.; Chen, K.; Li, T. T. Porphyrin and Phthalocyanine Based Covalent Organic Frameworks for Electrocatalysis. *Coord. Chem. Rev.* **2022**, *464*, 214563.

[17] Agboola, B. O.; Ozoemena, K. I.; Nyokong, T. Electrochemical Properties of Benzylmercapto and Dodecylmercapto Tetra Substituted Nickel Phthalocyanine Complexes: Electrocatalytic Oxidation of Nitrite. *Electrochim. Acta* **2006**, *51* (28), 6470–6478.

[18] Yu, F.; Yu, L.; Mishra, I. K.; Yu, Y.; Ren, Z. F.; Zhou, H. Q. Recent Developments in Earth-Abundant and Non-Noble Electrocatalysts for Water Electrolysis. *Mater. Today Phys.* **2018**, *7*, 121–138.

[19] Kumar, S.; Sharma, A. K.; Sohal, M. K.; Sharma, D. P.; Debnath, A. K.; Aswal, D. K.; Mahajan, A. Room Temperature Highly Sensitive Chlorine Sensor Based on Reduced Graphene Oxide Anchored with Substituted Copper Phthalocyanine. *Sens. Actuators, B Chem.* **2021**, *327*, 128925.

[20] Mukhopadhyay, S.; Devendrachari, M. C.; Kanade, S. C.; Vinod, C. P.; Nimbegondi Kotresh, H. M.; Thotiyl, M. O. Regio-Isomerism Directed Electrocatalysis for Energy Efficient Zinc-Air Battery. *iScience* **2022**, *25* (10), 105179.

[21] Li, R.; Zhang, X.; Zhu, P.; Ng, D. K. P.; Kobayashi, N.; Jiang, J. Electron-Donating or -Withdrawing Nature of Substituents Revealed by the Electrochemistry of Metal-Free Phthalocyanines. *Inorg. Chem.* **2006**, *45* (5), 2327–2334.

[22] Kaeffer, N.; Leitner, W. Electrocatalysis with Molecular Transition-Metal Complexes for Reductive Organic Synthesis. *JACS Au* **2022**, *2* (6), 1266–1289.

[23] Bedioui, F.; Griveau, S.; Nyokong, T.; John Appleby, A.; Caro, C. A.; Gulppi, M.; Ochoa, G.; Zagal, J. H. Tuning the Redox Properties of Metalloporphyrin- and Metallophthalocyanine-Based Molecular Electrodes for the Highest Electrocatalytic Activity in the Oxidation of Thiols. *Phys. Chem. Chem. Phys.* **2007**, *9* (26), 3383–3396.

[24] Jeong, D. S.; Shin, H. S.; Yang, J. Influence of the Molecular Structure of Metal-Phthalocyanine on Electrocatalytic Reactions. *Sci. China Mater.* **2022**, *65* (12), 3324–3333.

[25] Jiang, L.; Gu, M.; Zhao, S.; Wang, H.; Huang, X.; Gao, A.; Zhu, H.; Sun, P.; Liu, X.; Lin, H.; Zhang, X. Regulating the Active Sites of Metal–Phthalocyanine at the Molecular Level for Efficient Water Electrolysis: Double Deciphering of Electron-Withdrawing Groups and Bimetallic. *Small* **2022**, *2207243*, 1–10.

[26] Giraudeau, A.; Callot, H. J.; Gross, M. Effects of Electron-Withdrawing Substituents on the Electrochemical Oxidation of Porphyrins. *Inorg. Chem.* **1979**, *18* (1), 201–206.

[27] Kuzmina, E. A.; Dubinina, T. V.; Tomilova, L. G. Recent Advances in Chemistry of Phthalocyanines Bearing Electron-Withdrawing Halogen, Nitro and: N -Substituted Imide Functional Groups and Prospects for Their Practical Application. *New J. Chem.* **2019**, *43* (24), 9314–9327.

[28] Ici, Ü.; Afanasiev, P.; Millet, J. M. M.; Kudrik, E. V.; Ahsen, V.; Sorokin, A. B. Preparation and Characterization of μ-Nitrido Diiron Phthalocyanines with Electron-Withdrawing Substituents: Application for Catalytic Aromatic Oxidation. *Dalt. Trans.* **2009**, *36*, 7410–7420.

[29] Chen, K.; Cao, M.; Lin, Y.; Fu, J.; Liao, H.; Zhou, Y.; Li, H.; Qiu, X.; Hu, J.; Zheng, X.; Shakouri, M.; Xiao, Q.; Hu, Y.; Li, J.; Liu, J.; Cortés, E.; Liu, M. Ligand Engineering in Nickel Phthalocyanine to Boost the Electrocatalytic Reduction of CO_2. *Adv. Funct. Mater.* **2022**, *32*, 2111322.

[30] Li, M.; Yan, C.; Ramachandran, R.; Lan, Y.; Dai, H.; Shan, H.; Meng, X.; Cui, D.; Wang, F.; Xu, Z.-X. Non-Peripheral Octamethyl-Substituted Cobalt Phthalocyanine Nanorods Supported on N-Doped Reduced

Graphene Oxide Achieve Efficient Electrocatalytic CO_2 Reduction to CO. *Chem. Eng. J.* **2022**, *430*, 133050.

[31]   Baturhan Orman, E.; Sağlam, M. B.; Özkaya, A. R. Novel Peripherally Substituted Metal-Free, Zinc (II), and Cobalt (II) Phthalocyanines with 1,1'-Thiobis(2-Napthol) and Additional Tetraphthalonitrile Groups: Synthesis, Aggregation Behavior, Electrochemical Redox and Electrocatalytic Oxygen Reducing Properties. *Synth. Met.* **2020**, *263*, 116351.

[32]   Kumar, A.; Vashistha, V. K.; Sharma, V. Substituent Effect on Catalytic Activity of Co Phthalocyanines for Oxygen Reduction Reactions. *Inorg. Chem. Commun.* **2021**, *127*, 108518.

[33]   Luo, F.; Wang, M. S.; Luo, M. B.; Sun, G. M.; Song, Y. M.; Li, P. X.; Guo, G. C. Functionalizing the Pore Wall of Chiral Porous Metal–Organic Frameworks by Distinct –H, –OH, –NH2, –NO2, –COOH Shutters Showing Selective Adsorption of CO_2, Tunable Photoluminescence, and Direct White-Light Emission. *Chem. Commun.* **2012**, *48* (48), 5989–5991.

[34]   Tezcan, H.; Ozkan, N. Substituent Effects on the Spectral Properties of Some 3-Substituted Formazans. *Dye. Pigment.* **2003**, *56* (2), 159–166.

[35]   Stasyuk, O. A.; Szatylowicz, H.; Guerra, C. F.; Krygowski, T. M. Theoretical Study of Electron-Attracting Ability of the Nitro Group: Classical and Reverse Substituent Effects. *Struct. Chem.* **2015**, *26* (4), 905–913.

[36]   Mugadza, T.; Nyokong, T. Electrochemical, Microscopic and Spectroscopic Characterization of Benzene Diamine Functionalized Single Walled Carbon Nanotube-Cobalt (II) Tetracarboxy-Phthalocyanine Conjugates. *J. Colloid Interface Sci.* **2011**, *354* (2), 437–447.

[37]   Mounesh; Malathesh, P.; Praveen Kumara, N. Y.; Jilani, B. S.; Mruthyunjayachari, C. D.; Venugopala Reddy, K. R. Synthesis and Characterization of Tetra-Ganciclovir Cobalt (II) Phthalocyanine for Electroanalytical Applications of AA/DA/UA. *Heliyon* **2019**, *5* (7), e01946.

[38] Mohammed, I.; Nemakal, M.; Aralekallu, S.; Sajjan, V. A.; Divakara, T. R.; Palanna, M.; Keshavananda Prabu, C. P.; Sannegowda, L. K. Phthalocyanine Sheet Polymer Based Amperometric Sensor for the Selective Detection of 2,4-Dichlorophenol. *J. Electroanal. Chem.* **2020**, *871*, 114292.

[39] Sun, X.; Wang, L.; Tan, Z. Improved Synthesis of Soluble Metal-Free/Metal Phthalocyanine Tetracarboxylic Acids and Their Application in the Catalytic Epoxidation of Cyclohexene. *Catal. Letters* **2015**, *145* (4), 1094–1102.

[40] Achar, B. N.; Fohlen, G. M.; Parker, J. A.; Keshavayya, J. Preparation & Structural Investigations of Copper (II), Cobalt (II), Nickel (II) & Zinc (II) Derivatives of 2,9,16,23-Phthalocyanine Tetracarboxylic Acid. *Indian J. Chem.* **1988**, *27*, 411–416.

[41] Jiang, W.; Wang, T.; Chen, X.; Li, B.; Zeng, M.; Hu, N.; Su, Y.; Zhou, Z.; Zhang, Y.; Yang, Z. Enhancing Room-Temperature NO_2 detection of Cobalt Phthalocyanine Based Gas Sensor at an Ultralow Laser Exposure. *Phys. Chem. Chem. Phys.* **2020**, *22* (33), 18499–18506.

[42] Chidembo, A. T.; Ozoemena, K. I.; Agboola, B. O.; Gupta, V.; Wildgoose, G. G.; Compton, R. G. Nickel (II) Tetra-Aminophthalocyanine Modified MWCNTs as Potential Nanocomposite Materials for the Development of Supercapacitors. *Energy Environ. Sci.* **2010**, *3* (2), 228–236.

[43] Zhang, X.; Wu, Z.; Zhang, X.; Li, L.; Li, Y.; Xu, H.; Li, X.; Yu, X.; Zhang, Z.; Liang, Y.; Wang, H. Highly Selective and Active CO_2 Reduction Electrocatalysts Based on Cobalt Phthalocyanine/Carbon Nanotube Hybrid Structures. *Nat. Commun.* **2017**, *8*, 1–8.

[44] Abbaspour, A.; Mirahmadi, E. Electrocatalytic Activity of Iron and Nickel Phthalocyanines Supported on Multi-Walled Carbon Nanotubes towards Oxygen Evolution Reaction. *Electrochim. Acta* **2013**, *105*, 92–98.

[45] Zhang, M.; Gorski, W. Electrochemical Sensing Platform Based on the Carbon Nanotubes/Redox Mediators-Biopolymer System. *J. Am. Chem. Soc.* **2005**, *127* (7), 2058–2059.

[46] Zhu, J.; Li, Y.; Chen, Y.; Wang, J.; Zhang, B.; Zhang, J.; Blau, W. J. Graphene Oxide Covalently Functionalized with Zinc Phthalocyanine for Broadband Optical Limiting. *Carbon N. Y.* **2011**, *49* (6), 1900–1905.

[47] Kumar, A.; Prajapati, P. K.; Aathira, M. S.; Bansiwal, A.; Boukherroub, R.; Jain, S. L. Highly Improved Photoreduction of Carbon Dioxide to Methanol Using Cobalt Phthalocyanine Grafted to Graphitic Carbon Nitride as Photocatalyst under Visible Light Irradiation. *J. Colloid Interface Sci.* **2019**, *543*, 201–213.

[48] Zeng, X.; Yu, S.; Ye, L.; Li, M.; Pan, Z.; Sun, R.; Xu, J. Encapsulating Carbon Nanotubes with SiO2: A Strategy for Applying Them in Polymer Nanocomposites with High Mechanical Strength and Electrical Insulation. *J. Mater. Chem. C* **2015**, *3* (1), 187–195.

[49] Ralph G. P. The Principle of Maximum Hardness *Acc. Chem. Res.* **1993**, *26*, 250–255.

[50] Ralph G. P. Hard and Soft Acids and Bases *J. Am. Chem. Soc.* 1**963**, *85 (22),* 3533-3539.

[51] Ralph G. P. *Chemical Hardness*, Wiley-VCH; Weinheim, 1997.

[52] Ripin, D. H.; Evans, D. A. PKa's of Inorganic and Oxo-Acids *Chem*, **2020**, 206.

[53] March, J. Advanced Organic Chemistry: Reactions, Mechanisms, and Structure, 3rd Edition; *Wiley: New York,* **1985**.

[54] Silverstein, T. P.; Heller, S. T. pKa Values in the Undergraduate Curriculum: What Is the Real pKa of Water? *Chem. Educ.* **2017**, *94* (6), 690–695.

[55] Sohrabnejad-Eskan, I.; Goryachev, A.; Exner, K. S.; Kibler, L. A.; Hensen, E. J. M.; Hofmann, J. P.; Over, H. Temperature-Dependent Kinetic Studies of the Chlorine Evolution Reaction over RuO_2(110) Model Electrodes. *ACS Catal.* **2017**, *7* (4), 2403–2411.

[56] Exner, K. S. Beyond Thermodynamic-Based Material-Screening Concepts: Kinetic Scaling Relations Exemplified by the Chlorine Evolution Reaction over Transition-Metal Oxides. *Electrochim. Acta* **2020**, *334,* 135555.

[57] Dong, H.; Yu, W.; Hoffmann, M. R. Mixed Metal Oxide Electrodes and the Chlorine Evolution Reaction. *J. Phys. Chem. C* **2021**, *125* (38), 20745–20761.

[58] Exner, K. S. Beyond the Traditional Volcano Concept: Overpotential-Dependent Volcano Plots Exemplified by the Chlorine Evolution Reaction over Transition-Metal Oxides. *J. Phys. Chem. C* **2019**, *123* (27), 16921–16928.

[59] Lim, T.; Jung, G. Y.; Kim, J. H.; Park, S. O.; Park, J.; Kim, Y.-T.; Kang, S. J.; Jeong, H. Y.; Kwak, S. K.; Joo, S. H. Atomically Dispersed Pt–N₄ Sites as Efficient and Selective Electrocatalysts for the Chlorine Evolution Reaction. *Nat. Commun.* **2020**, *11* (1), 412.

[60] Ollo, K.; Guillaume, P. L. A.; Auguste, A. F. T.; Lassine, O. Anodic Oxidation of Chlorides on Platinum Modified by Metallic Oxides. *Int. J. Pure Appl. Sci. Technol.*, **2015**, *27*, 27–43.

[61] Lim, T.; Sung, M.; Kim, J. Oxygen Evolution Reaction at Microporous Pt Layers: Differentiated Electrochemical Activity between Acidic and Basic Media. *Sci. Rep.*, **2017**, *7*, 15382.

[62] Makinde, Z. O.; Louzada, M.; Mashazi, P.; Nyokong, T.; Khene, S. Electrocatalytic Behaviour of Surface Confined Pentanethio Cobalt (II) Binuclear Phthalocyanines towards the Oxidation of 4- Chlorophenol. *Appl. Surf. Sci.* **2017**, *425*, 702–712.

[63] Somashekarappa, M. P.; Keshavayya, J.; Sampath, S. Self-Assembled Molecular Films of Tetraamino Metal (Co, Cu, Fe) Phthalocyanines on Gold and Silver. Electrochemical and Spectroscopic Characterization. *Pure Appl. Chem.* **2002**, *74* (9), 1609–1620.

[64] Szabó, Z. G.; Csányi, L. On the Iodometric Determination of the Bromide Ion. *Anal. Chim. Acta* **1952**, *6*, 208–216.

[65] Hallinan, F. J. Test for Residual Chlorine. *Ind. Eng. Chem. Anal. Ed.* **1940**, *12* (8), 452–453.

[66] Hegner, F. S.; Garcés-Pineda, F. A.; González-Cobos, J.; Rodríguez-García, B.; Torréns, M.; Palomares, E.; López, N. Understanding the Catalytic Selectivity of Cobalt Hexacyanoferrate toward Oxygen

Evolution in Seawater Electrolysis. *ACS Catal.* **2021**, *11* (21), 13140–13148.

[67]   Da Silva, L. M.; Boodts, J. F. C.; De Faria, L. A. Chlorine Evolution Reaction at Ti/(RuO$_2$+Co$_3$O$_4$) Electrodes. *J. Braz. Chem. Soc.* **2003**, *14* (3), 388–395.

[68]   Ha, H.; Jin, K.; Park, S.; Lee, K. G.; Cho, K. H.; Seo, H.; Ahn, H. Y.; Lee, Y. H.; Nam, K. T. Highly Selective Active Chlorine Generation Electrocatalyzed by Co$_3$O$_4$ Nanoparticles: Mechanistic Investigation through in Situ Electrokinetic and Spectroscopic Analyses. *J. Phys. Chem. Lett.* **2019**, *10* (6), 1226–1233.

Chapter 5

Ligand Assisted Electrochemical Energy Storage via Proton Charge Assembly

ABSTRACT: This Chapter discusses how a ligand functionality that do not exhibit any redox activity, elevate the charge storage capability of the electric double layer via a proton charge assembly. The non-redox active carboxy ligand compared to the unsubstituted ligand demonstrated nearly 4 times elevated charge storage, impressive capacitive retention even at 900C rate and ~2 times lowered leakage currents with an enhancement in energy density up to ~70% via a non-electrochemical route of proton charge assembly. Generalizability of these findings are presented with various non redox active functionalities that can undergo proton charge assembly in the ligand. Contrary to conventional beliefs, this demonstration of non-redox active functionalities enriching the super capacitive charge storage via proton charge assembly contributes to the rationale design of ligands for energy storage applications.
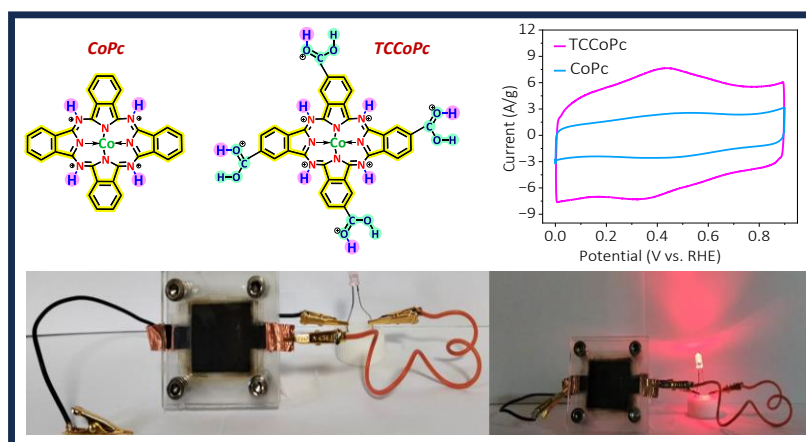
Chapter 5

5.1. Introduction:

This Chapter elucidates the role of the nature of ligands in electrochemical charge storage. In the previous Chapter, it is demonstrated that a non-electrochemical -COOH functionality tunes the kinetics of oxidative electrocatalysis via extensive proton charge assembly. In this Chapter, this ability to undergo a proton charge assembly is exploited for improving the charge storage in organic supercapacitors. Amidst the pressing need to address the escalating global energy demands and rapid industrialization, significant attention is focused on developing high-power, and high-energy-density energy storage/conversion devices.[1-7] In these contexts, electrochemical capacitors, or supercapacitors, have emerged as particularly promising candidates due to their superior power density, long lifetime and high cyclic stability in comparison to secondary batteries.[8-11] These electrochemical capacitors (ECs) can bridge the power-energy trade-off between batteries (high energy) and traditional dielectric capacitors (high power).[12-16] Supercapacitors are majorly classified into two categories; electrical double layer capacitors (EDLC) and pseudocapacitors. The EDLC operates by the non-Faradaic separation of charges at the electric double layer, whereas the pseudocapacitors majorly involve surface confined Faradaic redox reactions. EDLC-type materials such as activated carbon or carbon nanotube undergo reversible adsorption/desorption of electrolyte ions at the electrode-electrolyte interface during charging/discharging. This process is solely dependent on the active surface area of the electrodes, and since the charge storage mechanism depends only on the physical

reorientation of ion charge assembly at the interface, the energy density is much lower in EDLCs, as compared to pseudocapacitive materials. As mentioned earlier, the charge storage mechanism of pseudocapacitive materials primarily involve surface limited redox reactions.[17-20] Typically, during the process of charging/discharging, there will be a change in the redox state of the species involved, that in turn demand intercalation/deintercalation of counter ions.[21-23] Therefore, materials that can exhibit multiple redox transitions are often preferred in developing high energy density capacitor device. This conventional wisdom that multiple redox transition within the electrode has a direct link with the attainable energy density is affirmed by the classical demonstrations of charge storage in electrode materials including RuO_2, NiO, Co_3O_4, MnO_2, conducting polymers etc., and they all exhibited very high charge storage capability in their available potential window.[24-28]

In this chapter it is shown that for developing high energy supercapacitors, redox activity is not quintessential at least in the domain of molecular systems and even functionality without any capability for Faradaic redox transitions, can indeed enrich their energy storage capability. Our investigation with molecular systems containing functionalities like -$COOH/NH_2$ that do not exhibit any redox activity in the available potential window, elevate the charge storage capability nearly by four times with impressive performance metrics compared to non-functionalized ligands. Various physico chemical analyses affirmed that, it is the proton charge assembly on the electrode which contribute to

screening of repulsive interactions of the anions leading to dense anion storage within the EDL.

5.2. Results and Discussions:
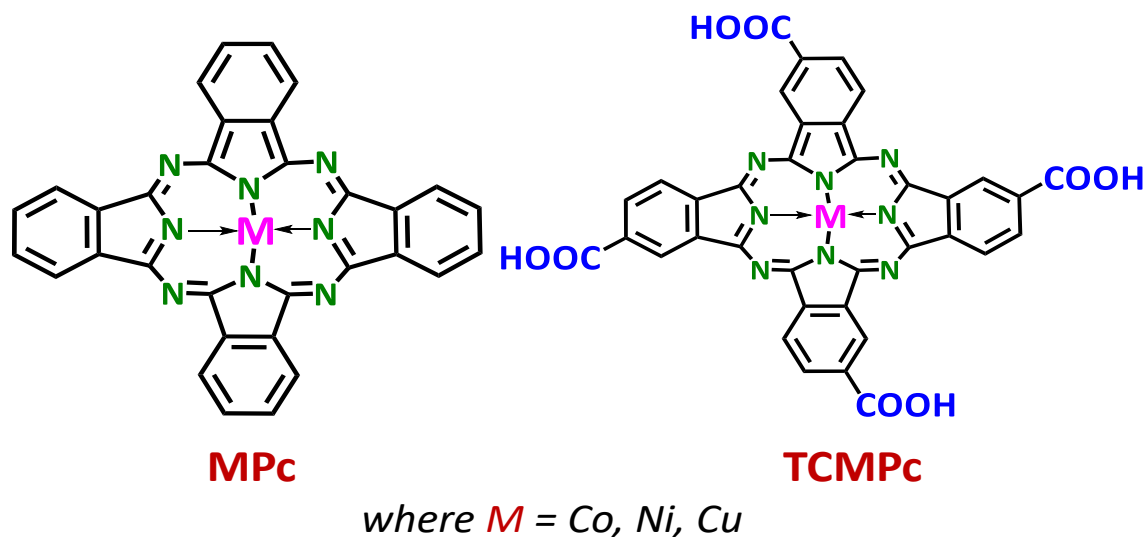
Scheme 5.1. Molecular structures of unsubstituted metal phthalocyanine (MPc) and tetra carboxy substituted metal phthalocyanine (TCMPc), where M = Co, Ni, Cu.

In the previous chapter, how the proton charge assembly can modulate the electrocatalytic behavior of Co based phthalocyanines via the modulation of the surface charge of the molecules was explored.[29] It is anticipated that this kind of proton charge assembly on the molecule should increase the local density of anions residing in the electric double layer, which in turn should make these molecules a suitable platform for charge storage applications. Specifically, in this chapter, it is shown how the functionalization of the ligand with non-redox active functionalities like -COOH/NH$_2$ can make the metal phthalocyanine molecule a potential platform for supercapacitive charge storage with enhanced energy and
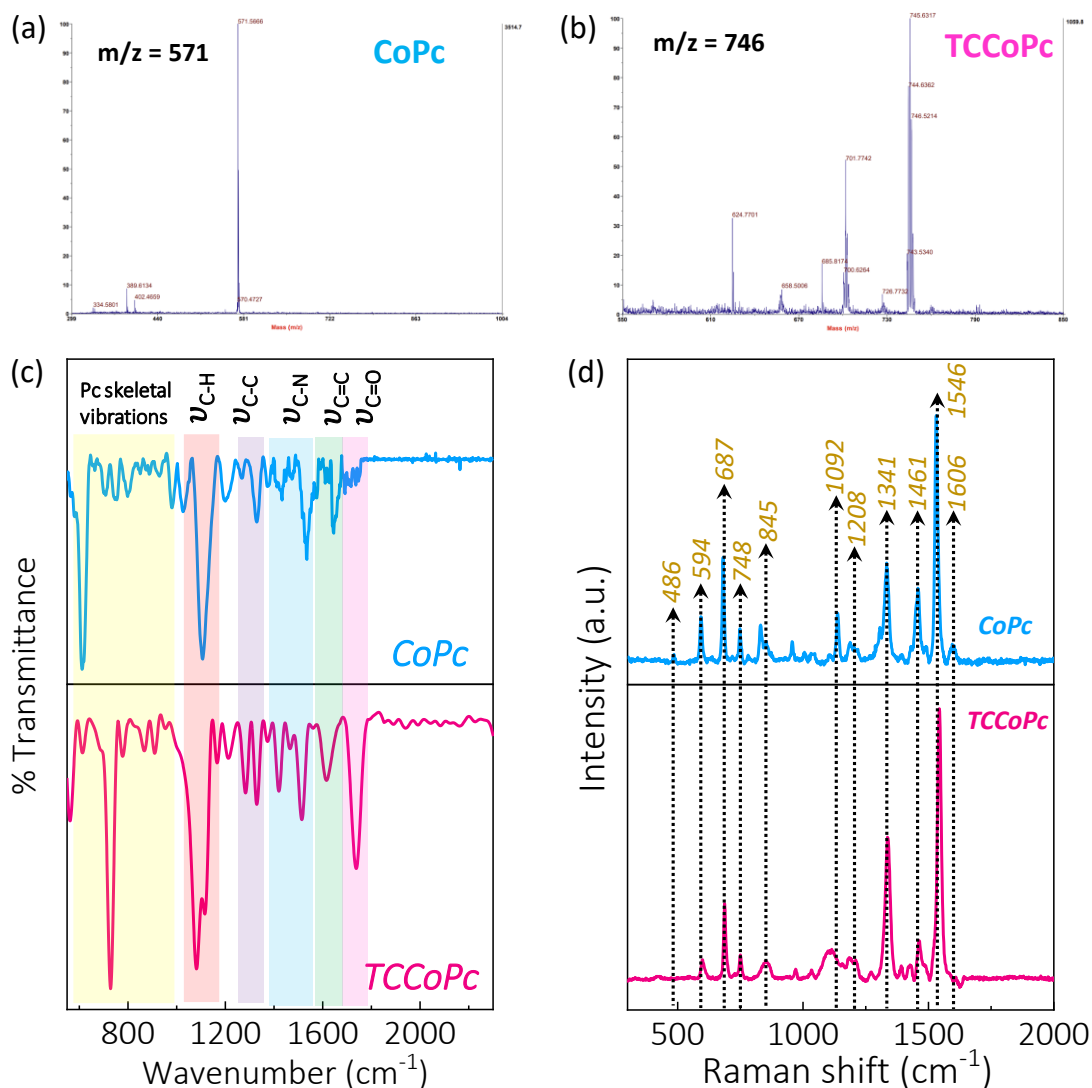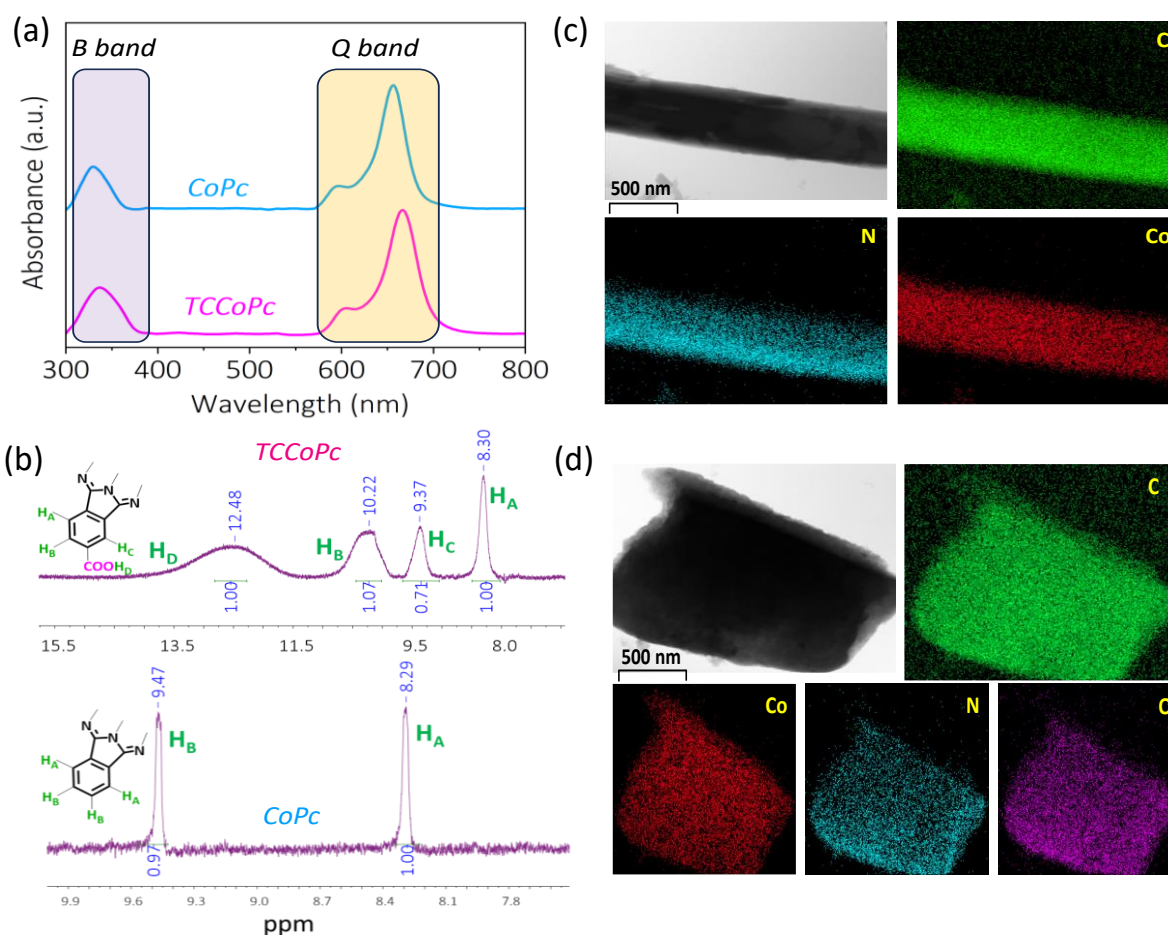
Figure 5.1. (a-b) Matrix-assisted laser desorption ionization time-of-flight mass spectrometry (MALDI-TOF), (c) FT-IR and (d) Raman spectra of CoPc and TCCoPc molecules.

power capability. To demonstrate this, cobalt (II) phthalocyanine (CoPc) and tetracarboxycobalt (II) phthalocyanine (TCCoPc) molecules were initially used. It is to be noted that -COOH functionality cannot exhibit any redox activity in the available potential window in aqueous medium. For a deeper analysis, tetraaminocobalt (II) phthalocyanine (TACoPc), tetranitrocobalt (II) phthalocyanine (TNCoPc), copper (II) phthalocyanine (CuPc) and tetracarboxycopper (II) phthalocyanine (TCCuPc) molecules were also used.

Table 5.1. Allotment of spectral peaks observed in the Raman spectra of CoPc and TCCoPc.

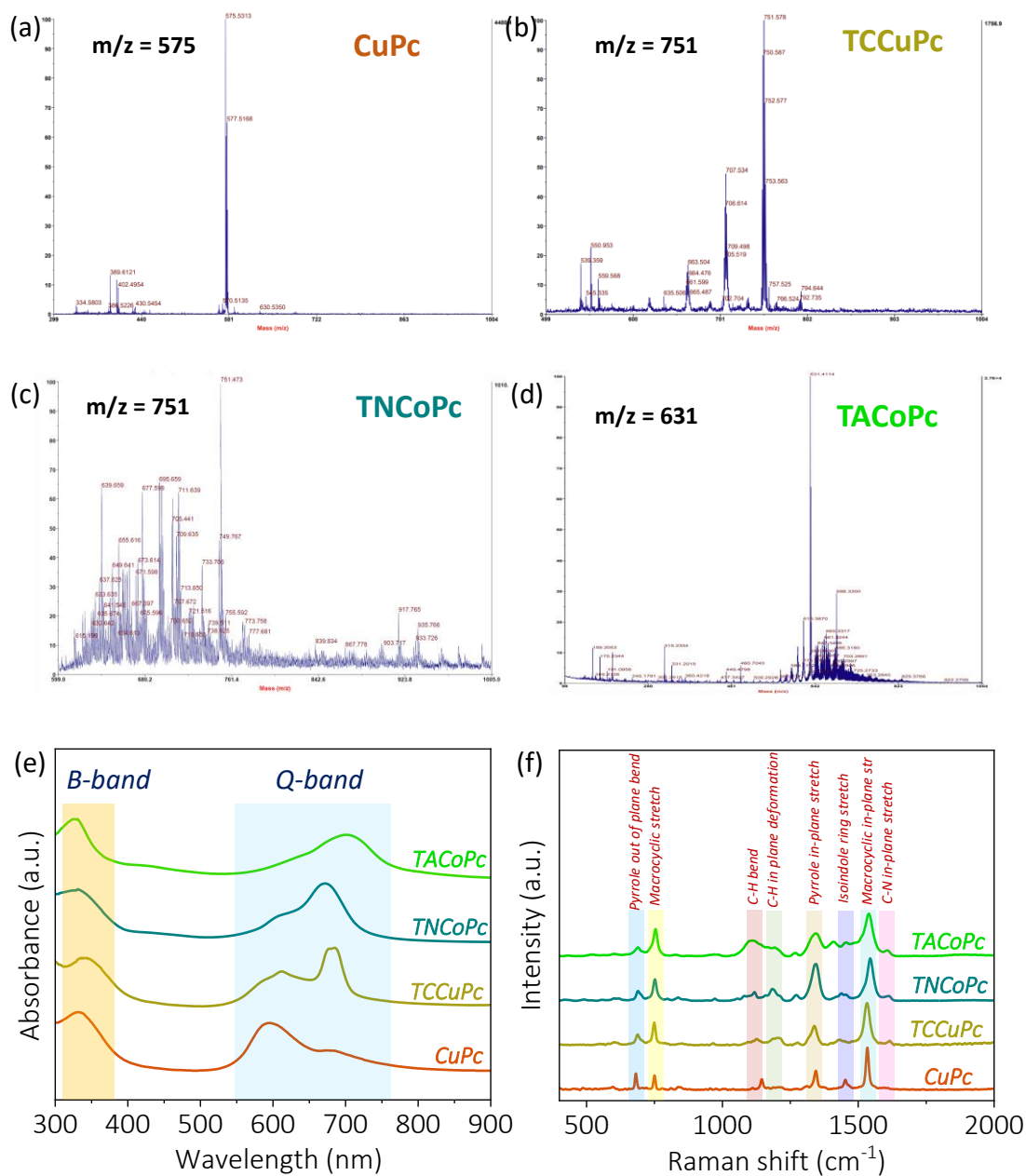| Raman shift (cm^{-1})	Band corresponding to
486	In plane bending of C-C-C
687	Out of plane bending of pyrrole ring
748	Macrocyclic stretching
845	Benzene breathing
1092	C-H bending
1208	In plane deformation of C-H
1341	In plane stretching of C-N
1461	Isoindole ring stretching
1546	In plane stretching of macrocycle
1606	In plane stretching of C-N

Figure 5.2. (a) UV-visible spectra, (b) ^{1}H NMR spectra of CoPc and TCCoPc molecules. HRTEM images along with elemental mapping of (c) CoPc and (d) TCCoPc molecules.

The molecules were first synthesized and characterized (please refer to chapter 2, section 2.2.1-2.2.3, pages 50-53 for details) and the structures of the unsubstituted and carboxy substituted molecules are as shown in Scheme 5.1.

5.2.1. Characterisation of CoPc, TCCoPc, TNCoPc, TACoPc, CuPc and TCCuPc.

Briefly, the matrix-assisted laser desorption ionization time-of-flight mass spectrometry (MALDI-TOF) demonstrated the parent ion peaks at m/z value of ~571 and ~746 for CoPc and TCCoPc respectively, ensuring their successful formation (Figure 5.1a, b). Fourier transform infrared spectroscopy (FTIR) exhibited peaks at ~1110, ~1280, ~1411 and ~1640 cm^{-1} corresponding to υ $_{C-H,}$ υ $_{C-C,}$ υ $_{C-N}$ and υ $_{C=C}$ macrocyclic ring vibration respectively. Phthalocyanine skeletal vibrations are observed at ~724, ~872, ~913 and ~1083 cm^{-1}.[30-37] The peak at ~1700 cm^{-1} in TCCoPc corresponds to υ $_{C=O}$ of the -COOH group, (Figure 5.1c). Raman spectra of both the molecules provided characteristic Raman shifts as detailed in (Figure 5.1d) and Table 5.1 which confirms successful formation of both the molecules. UV-visible spectra demonstrated the characteristic phthalocyanine bands such as B band and Q band for both the molecules (Figure 5.2a). Q-band was found to be red shifted in the case of the TCCoPc molecule than the CoPc molecule signaling that this band has more ligand characteristics.[30-35] This is further attributed to comparatively extensive electron delocalization in case of the TCCoPc molecule. ^{1}H NMR of these molecules further confirm the successful formation of these molecules, Figure 5.2b.

TCCoPc showed ^{1}H NMR peaks at 8.3 ppm, 9.37 ppm, 10.22 ppm and 12.48 ppm corresponding to four types of H atom. The broad peak at 12.48 ppm corresponds to the acidic proton. CoPc on the other hand demonstrated peaks at chemical shift values of 8.29 ppm and 9.47 ppm indicating the presence of only two different types of protons in it, Figure 5.2b. The morphology of the molecules was analyzed with the help of high-resolution transmission electron microscopy (HRTEM). The TEM images show rod like morphology for the CoPc molecule and sheet like morphology for the TCCoPc molecules, Figure 5.2c-d, indicating a difference in the way the molecule self-assemble. The morphology of CoPc is found to be mostly nanowire in nature in the literature.[38, 39] A similar nanowire kind of morphology for the CoPc system was also observed (Figure 5.2c). However, for TCCoPc system, the morphology was found to be sheet like and aggregated (Figure 5.2d). This may be because of the presence of intermolecular H-bonding between the -COOH groups in this molecule. In these lines, a randomly aggregated morphology was reported in the literature for carboxy substituted cobalt phthalocyanine.[33, 36, 40-41] Elemental mapping was further carried out to understand the composition of the molecules. CoPc showed a homogenous distribution of carbon, nitrogen and cobalt whereas TCCoPc demonstrated a uniform distribution of carbon, nitrogen, cobalt and oxygen, Figure 5.2 c and d respectively. The characterization of the nitro substituted cobalt phthalocyanine (TNCoPc), amino substituted cobalt phthalocyanine (TACoPc), unsubstituted copper phthalocyanine (CuPc) and carboxy substituted copper phthalocyanine (TCCuPc) molecules are demonstrated in Figure 5.3.

Figure 5.3. (a-d) MALDI-TOF, (e) UV-visible and (f) Raman spectra of TACoPc, TNCoPc, CuPc and TCCuPc molecules.

5.2.2. Self-assembled monolayer studies.

After successful formation of the molecules, the electrochemical behavior of these molecules in acidic medium was evaluated. For that they were anchored on a glassy carbon electrode as a monolayer via self-

assembly process. To ensure a proper formation of the monolayer, quartz crystal microbalance (QCM) studies were carried out. It has been observed that the value of surface coverage (obtained with the help of Saurbrey's equation) is in line with reported values for a flat monolayer, Figure 5.4 (please refer to chapter 2, section 2.6, pages 60-61 for details).[42-44]
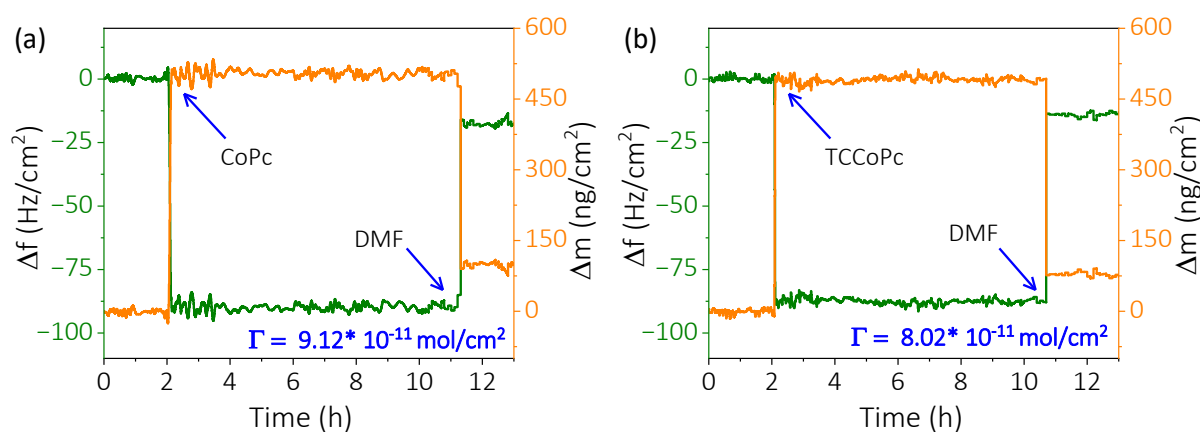

Figure 5.4. Quartz crystal microbalance (QCM) measurement data of CoPc and TCCoPc molecules on a quartz resonator (carbon coated) during the adsorption of the molecules. (a) CoPc (0.5 mM) and (b) TCCoPc (0.5 mM) in dimethyl formamide (DMF). Green trace corresponds to the frequency change during adsorption and the orange trace corresponds to the mass change calculated using Saurbrey equation. Surface coverage (Γ) values of the molecules are provided in each graph.

The surface coverage values were 9.12×10^{-11} mol/cm^2 and 8.02×10^{-11} mol/cm^2 for CoPc and TCCoPc molecules suggesting the electrode is modified with almost similar number of molecules. Following this, the cyclic voltammograms were recorded for the monolayer modified glassy carbon electrodes in 0.5 M H$_2$SO$_4$ solution. Though, both the molecules have similar number of redox active centers, on functionalization with a non-redox active -COOH functionality, the double layer current was found to be noticeably

enhanced, Figure 5.5a. The galvanostatic charge discharge data (Figure 5.5b) also indicate that the TCCoPc molecule has a much higher charge storage capability than the unsubstituted CoPc molecule.
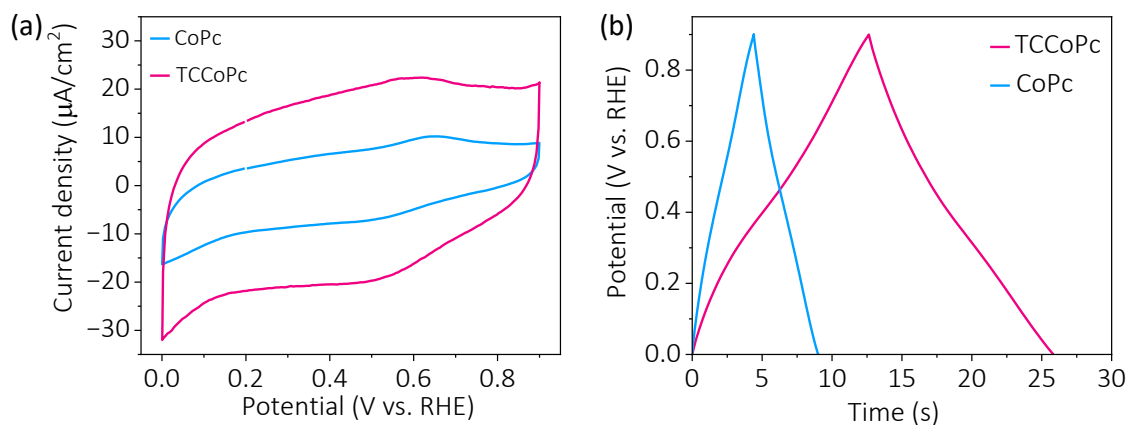

Figure 5.5. (a) Cyclic voltammogram of CoPc and TCCoPc molecules adsorbed as monolayer on a GC electrode at a scan rate of 5 mV/s. (b) Galvanostatic charge discharge of CoPc and TCCoPc molecules adsorbed as monolayer on a GC electrode at 0.1 mA/cm^2.

5.2.3. Characterisation of CoPc and TCCoPc composites with YP-50.

After ensuring their pristine behavior in acidic medium, composites of these molecules with YP-50 porous carbon support were made, in order to check their application in real life supercapacitor devices. The composites were synthesized with the help of reported procedure (please refer to chapter 2, section 2.2.5, page 54). They were characterized by various physicochemical techniques to confirm their successful formation. The Raman and FT-IR spectra demonstrated the respective phthalocyanine features, although they were suppressed because of the presence of the carbon material, Figure 5.6. In order to check the homogenous distribution

of all the elements in the YP-50 composites, elemental analysis as well as EDX mapping was carried out (Figure 5.7), which confirm homogenous distribution of the corresponding elements on YP-50 in both the composites.
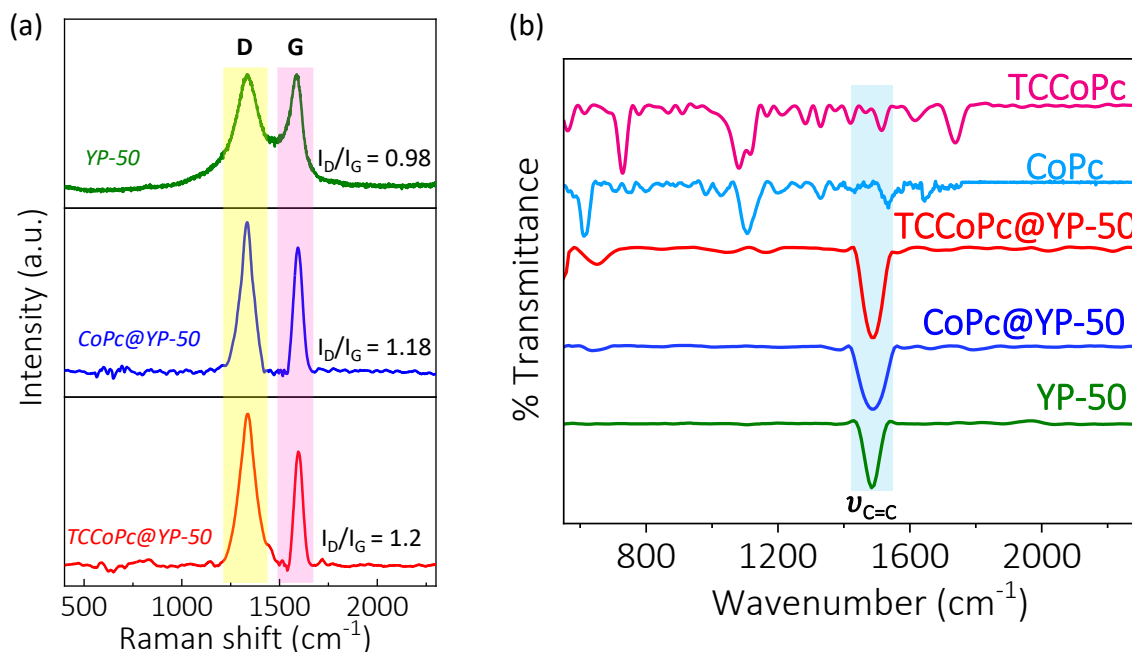

Figure 5.6. (a) Raman spectra of YP-50, CoPc@YP-50 and TCCoPc@YP-50 composite systems and (b) FT-IR spectra of YP-50, CoPc@YP-50, TCCoPc@YP-50 composite systems along with pristine CoPc and TCCoPc molecules.
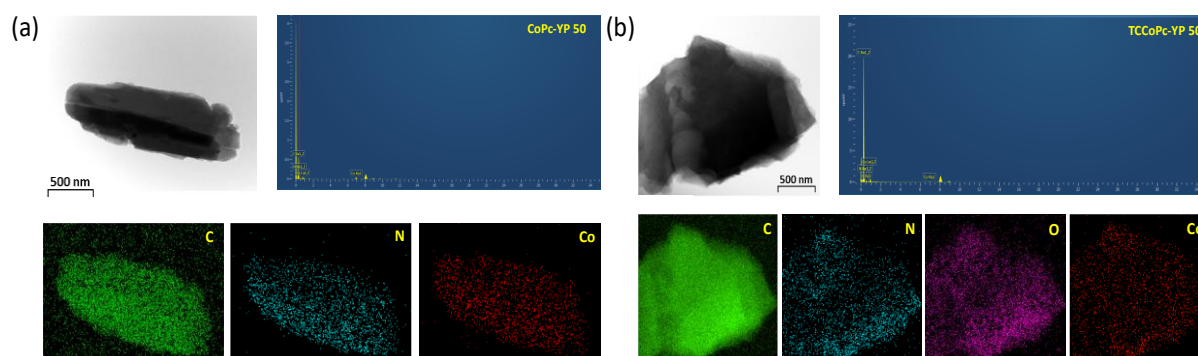
Figure 5.7. HRTEM image along with elemental mapping and EDX of (a) CoPc@YP-50 and (b) TCCoPc@YP-50 composite systems.

5.2.4. Electrochemical analysis for three electrode configurations.

After successfully confirming the formation of the composites, their electrochemical behavior was monitored in 0.5 M H_2SO_4 solution. The ratio of YP-50 to phthalocyanine molecule was optimised and a ratio of 2:1 (YP-50 to phthalocyanine) was found to furnish the highest capacitance. The data for different weight ratios along with their capacitance is shown in Figure 5.8 and Table 5.2 (please refer to chapter 2, section 2.9.1, pages 64-65 for details). The alterations in capacitance with respect to the weight ratio of individual counterparts in the composite electrode is attributed to the interplay between electronic conductivity of the composite electrode and the availability of phthalocyanine molecules for charge storage. It should be
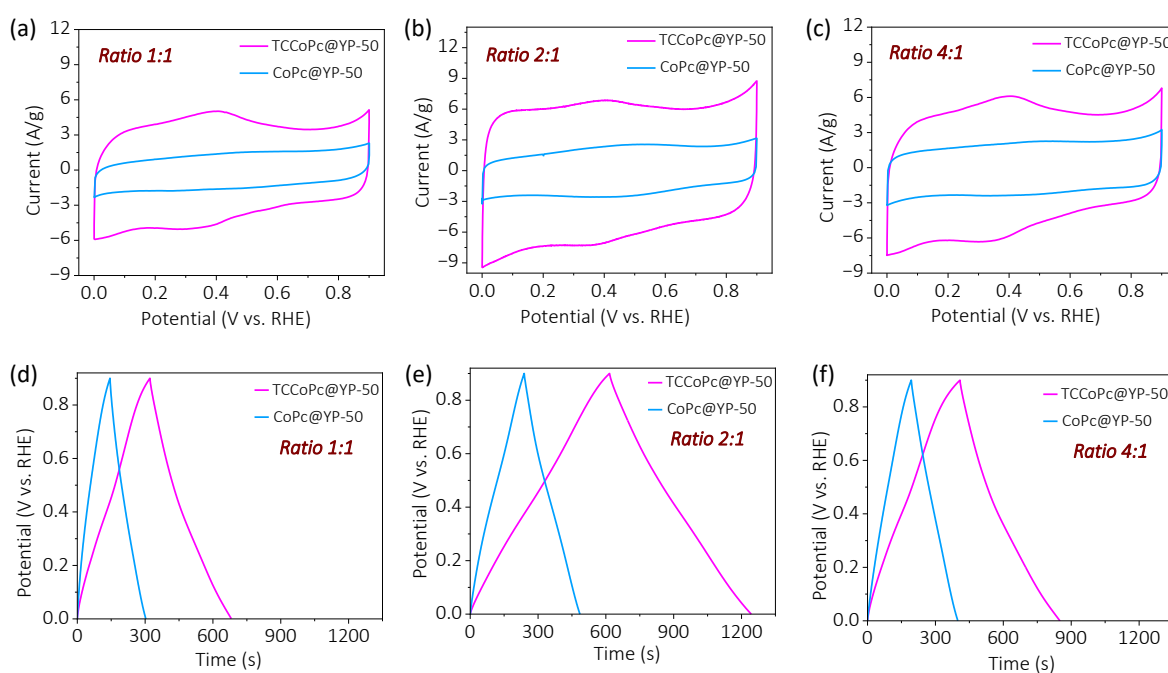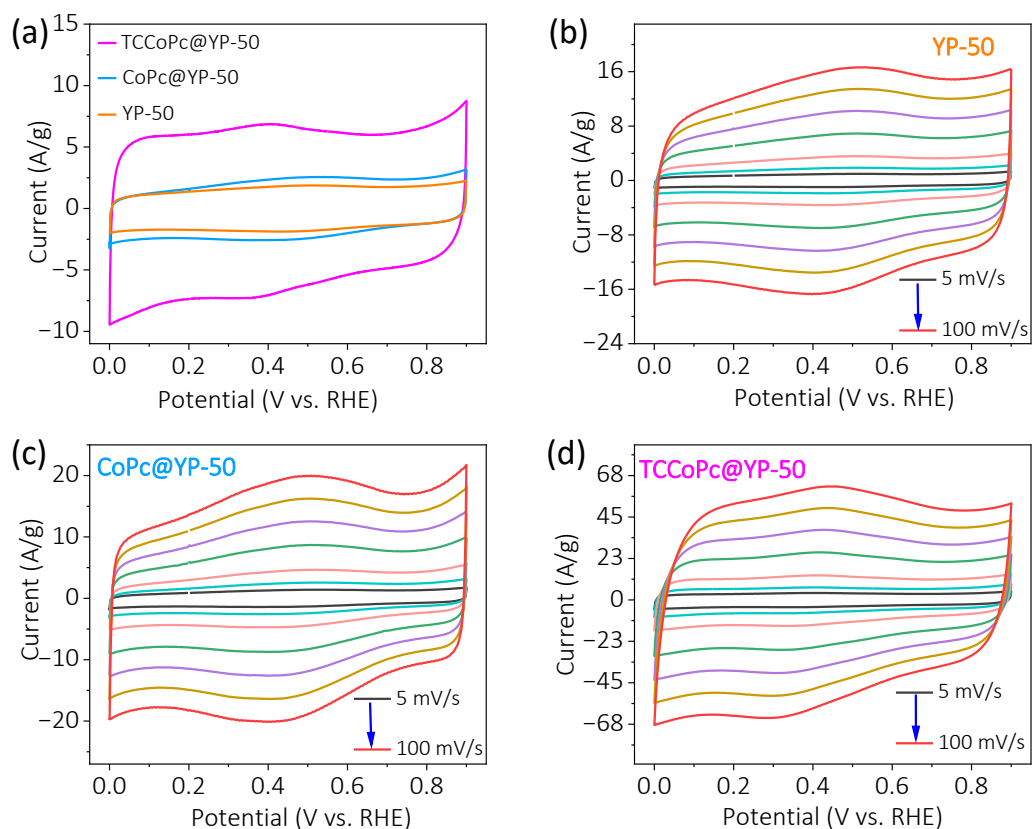

Figure 5.8. (a-c) Cyclic voltammetry at a scan rate of 5 mV/s and (d-f) galvanostatic charge-discharge profiles (at 1 A/g rate) for 1:1 (YP-50 to CoPc/TCCoPc), 2:1 (YP-50 to CoPc/TCCoPc) and 4:1 (YP-50 to CoPc/TCCoPc) weight ratio composition.

Table 5.2. Specific capacitance for different weight ratios of CoPc and TCCoPc composites with YP-50. The parameters are extracted from Figure 5.8.

| Ratio of composite (YP-50 : CoPc/TCCoPc	From cyclic voltammetry Csp (F/g)		From Galvanostatic charge-discharge Csp (F/g)	
	CoPc@YP-50	TCCoPc@YP-50	CoPc@YP-50	TCCoPc@YP-50
1:1	136	388	169	402
2:1	233	682	269	715
4:1	205	454	219	483

noted that the phthalocyanine molecules have a lower electronic conductivity than carbon-based materials.[45, 46] With surplus amount of YP-50 (4:1 ratio), the number of phthalocyanine molecules accessible for charge storage decreases that in turn leads to lower capacitance. Similarly, when the amount of phthalocyanine is increased as in 1:1 ratio, the overall capacitance decreases because of lowering of the electronic conductivity of the composite system. The enhanced capacitance in the 2:1 ratio composite system could be due to the overall enhancement in the electronic conductivity coupled with the sufficient availability of phthalocyanine molecules for charge storage. The double layer current obtained from the cyclic voltammograms was found to be nearly 4 times enhanced for the TCCoPc molecule than that of the CoPc (Figure 5.9a) which is almost in line with the monolayer data, Figure 5.5a. The scan rate dependance study ranging from 5 mV/s to 100 mV/s with all the three systems are shown in Figure 5.9b-d. The calculated specific capacitance (Csp) from the cyclic voltammograms at various scan rates, suggest the maintenance of high capacitance by TCCoPc than CoPc at all the studied scan rates, Figure 5.10.

Figure 5.9. (a) Cyclic voltammograms (CVs) for the composite electrodes with YP-50 at a scan rate of 5 mV/s. (b-d) Cyclic voltammograms at various scan rates from 5 mV/s to 100 mV/s for YP-50, CoPc@YP-50 and TCCoPc@YP-50 respectively.
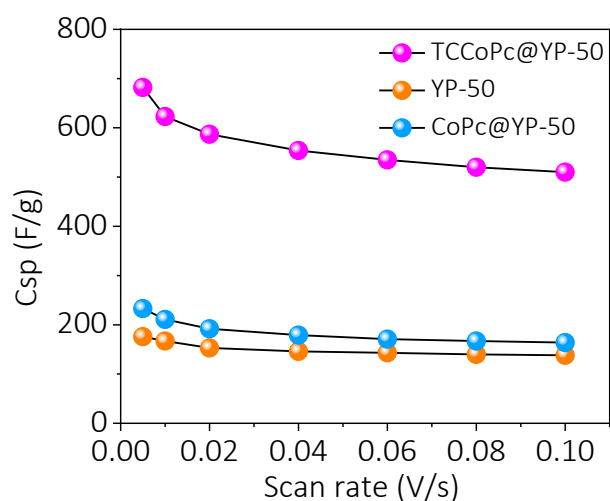
Figure 5.10. Rate profile extracted from the cyclic voltammograms at various scan rates from 5 mV/s to 100 mV/s for YP-50, CoPc@YP-50 and TCCoPc@YP-50.
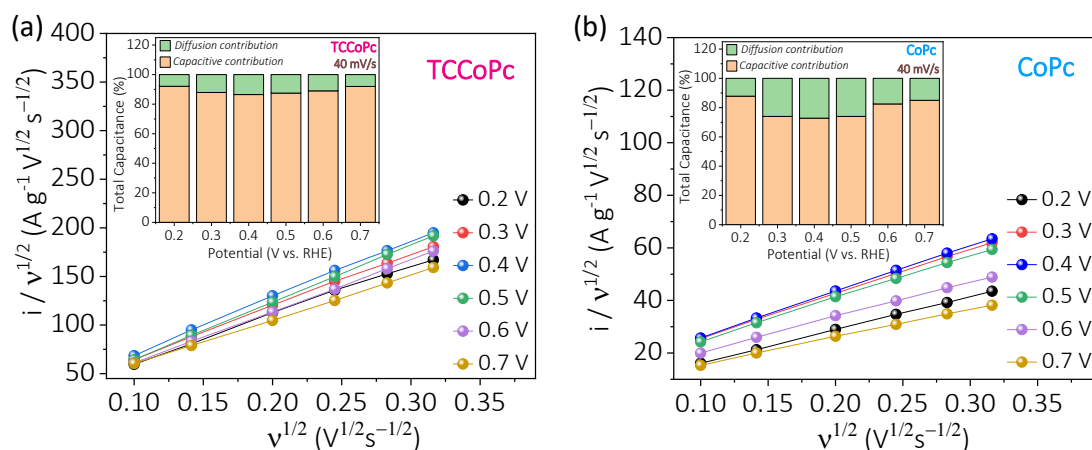
Figure 5.11. (a) Faradaic and capacitive contributions extracted from the CVs for (a) TCCoPc and (b) CoPc respectively. Inset shows their percentage contributions at different potentials.
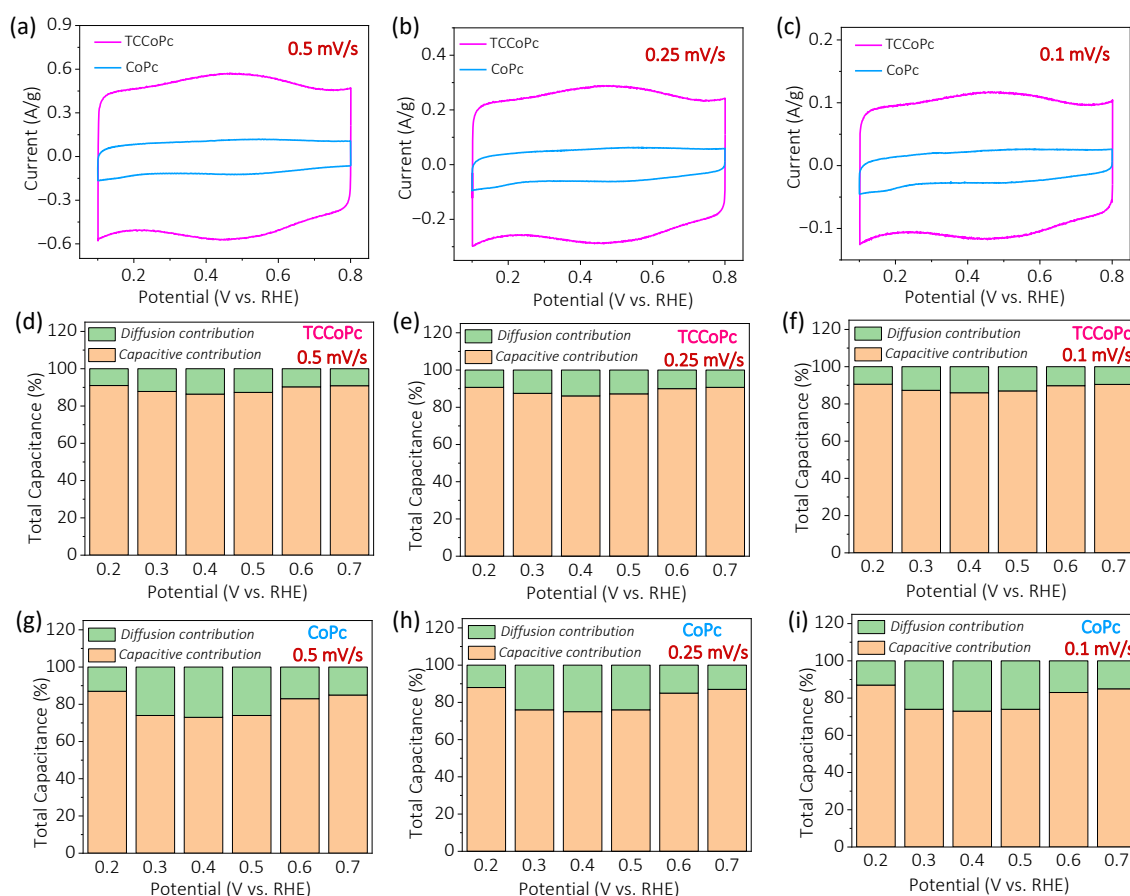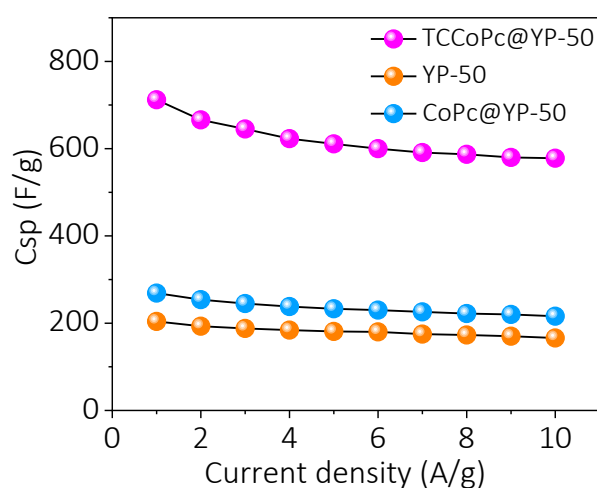

Figure 5.12. (a-c) Cyclic voltammograms of CoPc and TCCoPc from 0.5 mV/s to 0.1 mV/s. Histogram plots demonstrating the percentage of

capacitive and diffusional contributions at 0.5 mV/s, 0.25 mV/s and 0.1 mV/s scan rates for (d-f) TCCoPc and (g-i) CoPc molecules.

In order to check the contribution of pseudocapacitance to the overall capacitance, the Faradaic and capacitive contributions were extracted from the cyclic voltammograms (please refer to chapter 2, section 2.10, page 66 for details). Figure 5.11 show that the capacitive contribution is predominant for the TCCoPc molecule as compared to the CoPc molecule even in the potential range of 0.3 V - 0.5 V where Faradaic redox peaks appear for both the molecules. Even at low scan rates from 0.5 mV/s to 0.1 mV/s, the capacitive contribution dominated the charge storage as compared to the Faradaic contribution in CoPc as well as TCCoPc (Figure 5.12). Galvanostatic charge-discharge (GCD) study with these molecules at various current densities ranging from 1 A/g to 10 A/g as can be seen from Figure 5.13 demonstrate that the TCCoPc molecule is excelling the CoPc molecule in terms of rate capability (Figure 5.13a). The specific capacitance (Csp) values were extracted from these GCD studies (please refer to chapter 2, section 2.9.1, page 65 for calculations) and they were found to be in line with scan rate dependent studies. The TCCoPc molecule was found to maintain a higher value of capacitance over the CoPc molecule at all the studied rates, Figure 5.14. Table 5.3 compiles the specific capacitance of all the systems at 5 mV/s and 1 A/g which suggest that functionalization by a non-redox active -COOH functionality enhances the double layer charge storage significantly.
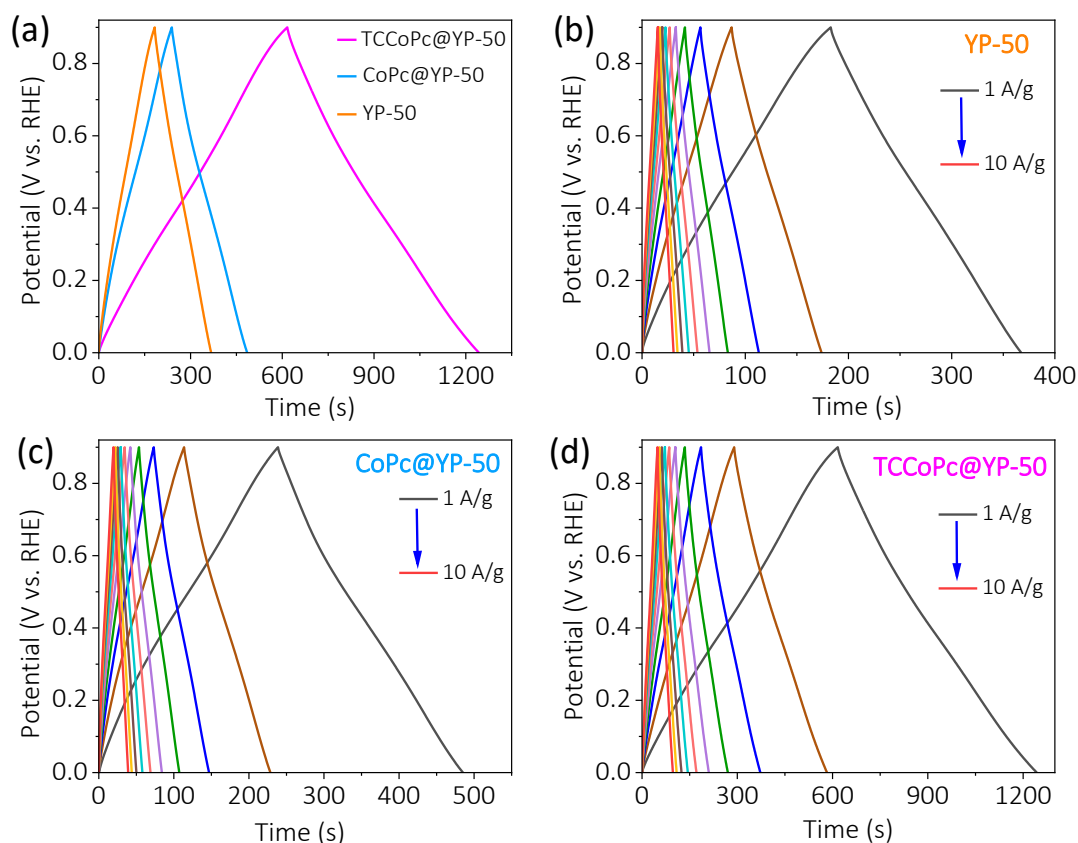
Figure 5.13. (a) Galvanostatic charge-discharge for the composite electrodes with YP-50 at a current rate of 1A/g. (b-d) Galvanostatic charge-discharge profiles at various rates for YP-50, CoPc@YP-50 and TCCoPc@YP-50 respectively.

Figure 5.14. Rate profile extracted from the cyclic voltammograms at various scan rates from 5 mV/s to 100 mV/s for YP-50, CoPc@YP-50 and TCCoPc@YP-50.

Table 5.3. Specific capacitance (Csp) extracted from the cyclic voltammogram at 5 mV/s and galvanostatic charge-discharge at 1 A/g for YP-50, CoPc@YP-50 and TCCoPc@YP-50 composites.

Composite electrodes	From Cyclic Voltammetry Csp (F/g)	From Galvanostatic charge-discharge Csp (F/g)
YP-50	176	204
CoPc@YP-50	233	269
TCCoPc@YP-50	682	715

5.2.5. Surface charge analysis.

In order to rule out the possibility of factors like wettability and surface area of the composite electrodes (CoPc@YP-50 and TCCoPc@YP-50) contributing to charge storage, these parameters were extracted by BET surface area and contact angle measurements. The surface area extracted from the N_2 adsorption isotherm was found to be 1029 m²/g, 1014 m²/g and 1682 m²/g for CoPc@YP-50, TCCoP@YP-50 and YP-50 respectively (Figure 5.15a), suggesting that both the composite electrodes have almost similar surface areas which are lower than that of pure YP-50. This is expected as the pores on YP-50 may get blocked while forming composites with phthalocyanine molecules. Figure 5.15b shows the pore size distribution for the composites and it was also found to be falling in a similar range. The pore volume for CoPc@YP-50 and TCCoPc@YP-50 were found to be 0.449 cc/g and 0.427 cc/g respectively, suggesting that these parameters are
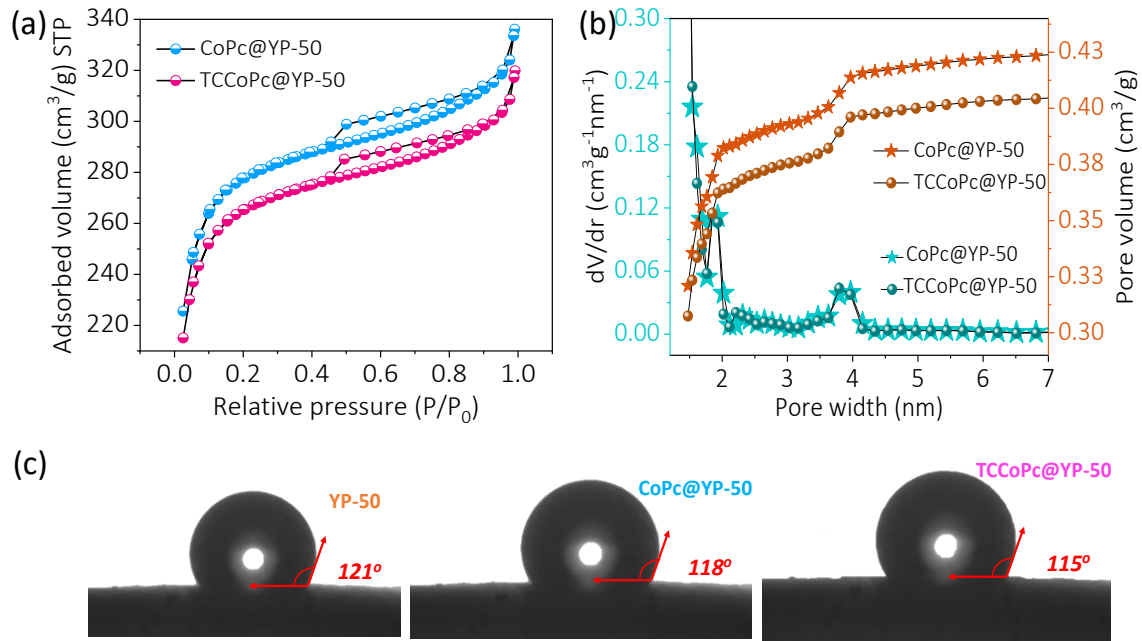
Figure 5.15. (a) BET N_2 adsorption isotherm along with (b) Pore size distribution plot by DFT method extracted from BET analysis for CoPc@YP-50 and TCCoPc@YP-50. (c) Contact angle measurement for YP-50, CoPc@YP-50 and TCCoPc@YP-50 electrodes.
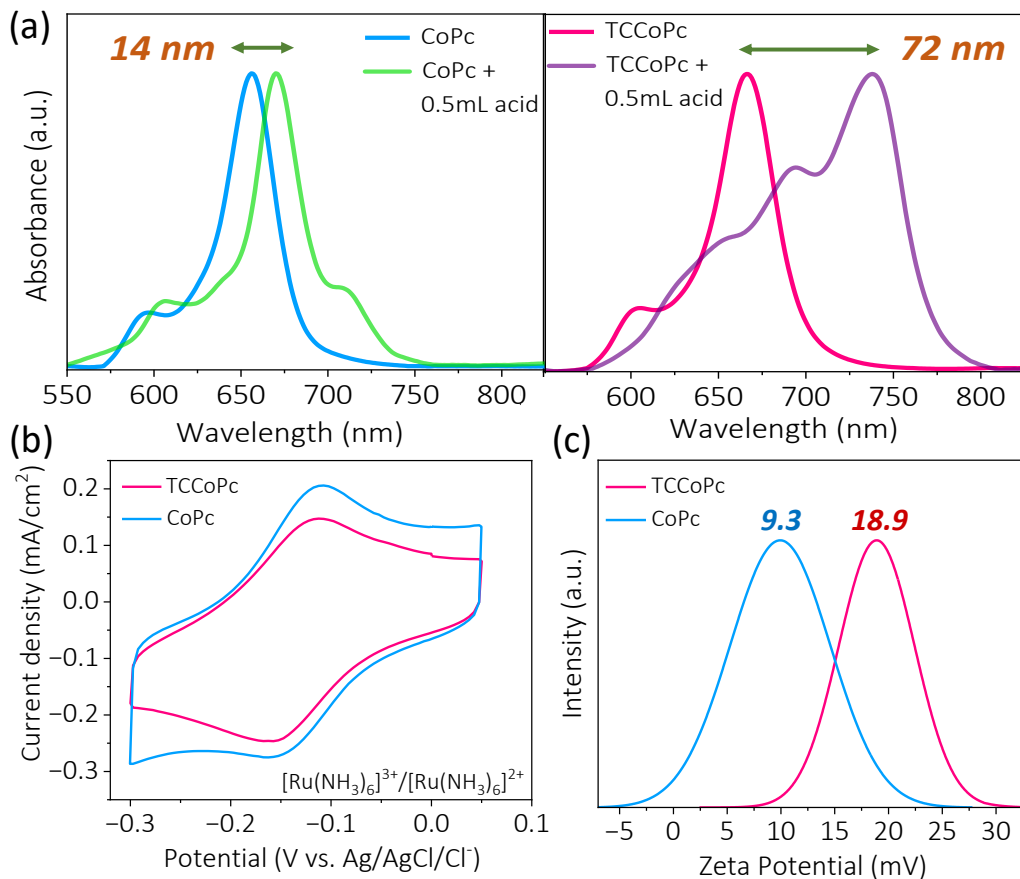
Figure 5.16. (a) UV-visible spectra for CoPc and TCCoPc molecule with and without acid treatment. (b) Cyclic voltammograms for 5 mM [Ru $(NH_3)_6]^{2+}$ in 0.5 M H_2SO_4 medium collected at a scan rate of 20 mV/s with CoPc and TCCoPc molecules. (c) Zeta potential measurement for CoPc and TCCoPc molecules in acidic medium.

almost similar in range for the composite materials. Figure 5.15c demonstrate both the composite molecules exhibit similar wettability. Taken together, wettability and surface area cannot be responsible factors for the alterations in the double layer current as shown in Figure 5.9.

To understand what could be the reason for the TCCoPc molecule to show better charge storage than the CoPc molecule, UV-Visible acid titration was carried out as shown in Figure 5.16a. It was observed that after addition of the same concentration of acid into the DMSO solution containing the molecules, the Q-band got significantly red shifted for the TCCoPc molecule than CoPc molecule. The red-shift in the Q-band is an indication of protonation of the molecule.[47-51] So, these results suggest that the extent of protonation is more pronounced for TCCoPc molecule than for the unsubstituted CoPc molecule. To substantiate this claim and to verify the nature of this surface charge, cyclic voltammograms of these two molecules were recorded in the presence of positively charged [Ru $(NH_3)_6]^{3+}$/ [Ru $(NH_3)_6]^{2+}$ redox probes in acidic medium. With the positively charged redox species in the medium, a relative decrease in current was observed for the TCCoPc molecule, suggesting electrostatic repulsion at play in the interfacial region, Figure 5.16b. To further verify this, Zeta potential measurements in presence of acid were performed and it suggest the surface

charge of TCCoPc molecule is more positive than CoPc (Figure 5.16c) in acidic medium.
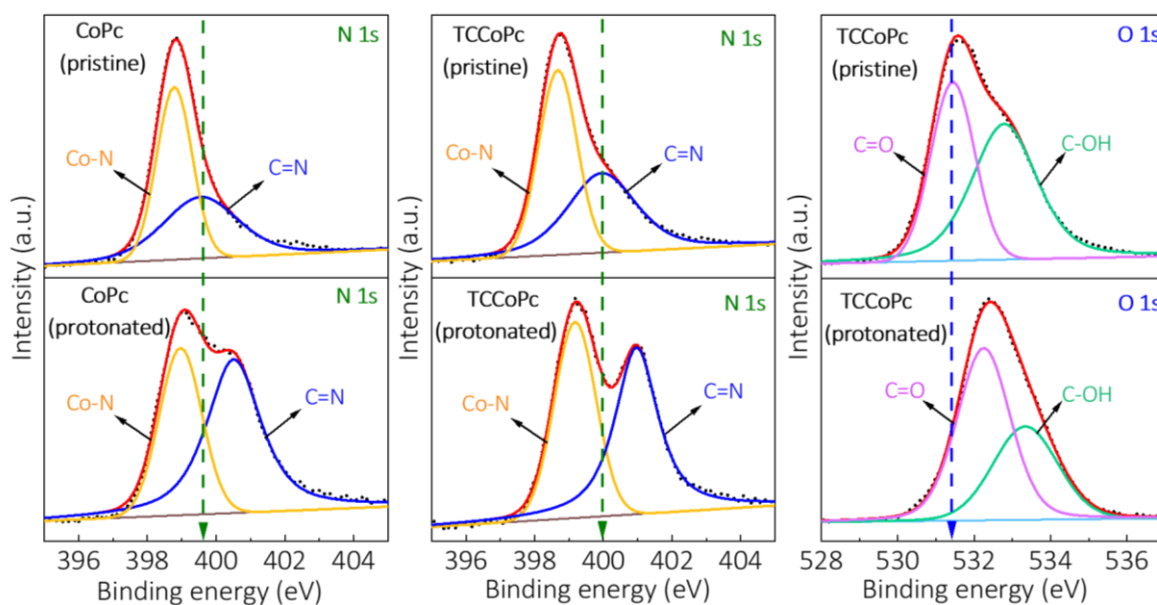
Figure 5.17. N1s and O1s XPS analysis of CoPc and TCCoPc with and without acid treatment.

Table 5.4. XPS analysis of CoPc and TCCoPc with and without acid treatment.

Molecules	CoPc	TCCoPc	
	C=N	C=N	C=O
Pristine B.E. (eV)	399.55	399.9	531.4
Protonated B.E. (eV)	400.3	400.97	532.2
Δ B.E. (eV) [protonated − pristine] (eV)	0.75	1.07	0.8

To unambiguously confirm this, XPS spectra of the molecules were recorded (Figure 5.17), which shows a significantly upshifted O1s binding energy (BE) in TCCoPc molecule upon acid treatment. N1s spectra in both the molecules demonstrated an upshift in BE on acid treatment, however,

the shift is much more pronounced in TCCoPc molecule than the unsubstituted molecule, Table 5.4.[52-57] It should be noted that the peak intensity of -C=N increased noticeably after the protonation, Figure 5.17. Generally, the peak intensity in the XPS spectra is related to the surface concentration of the species in question and it gives information about how much of that species is exposed at the surface. There are studies where the increase in intensity of a certain peak in the XPS spectra is attributed to the higher surface exposure of that species.[58-60] Thus, the increase in the peak intensity of C=N after protonation is attributed to its dominant surface exposure after the proton charge assembly. This behaviour is observed consistently in CoPc as well as TCCoPc molecules. Nevertheless, Co-N peak intensity did not demonstrate this intensity variation as this N is deeply embedded in the macrocyclic ligand.

To further prove that it is proton charge assembly contributing to enhanced charge storage, the performance of substituted CoPc with functionalities like -NH$_2$ which can also undergo protonation without exhibiting any redox activity was evaluated. As expected, the cyclic voltammograms suggest that tetraamino substituted CoPc (TACoPc) demonstrates an enhanced charge storage than unsubstituted CoPc with the former molecule exhibiting charge storage values almost similar to that of TCCoPc molecule, Figure 5.18a. The pH of the electrolyte (0.5 M H$_2$SO$_4$) was measured to be 0.2. The pKa values of aromatic Ph-COOH is ~4.2 and Ph-NH$_2$ is ~4.6.[61-63] According to Henderson-Hasselbalch equation, it is known that if the pKa of a compound is higher than the pH of the solution
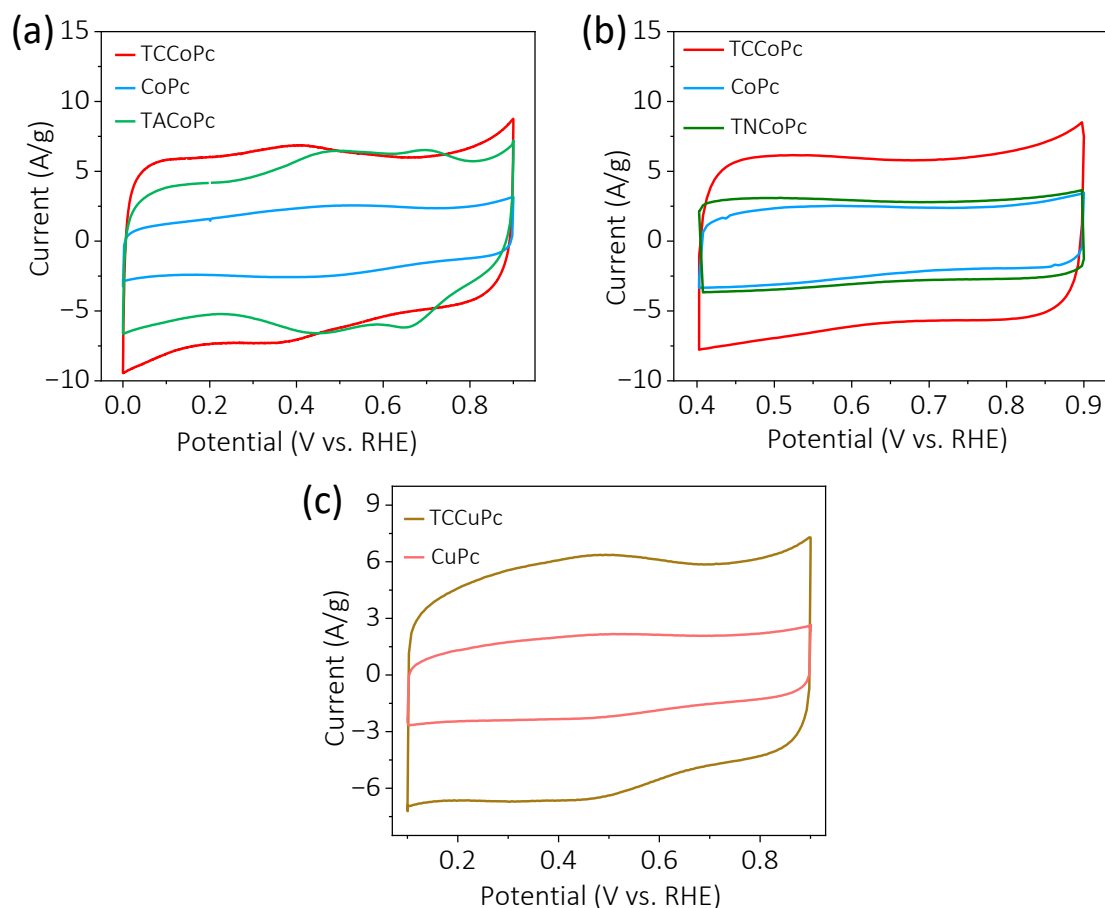
Figure 5.18. Comparative cyclic voltammograms at a scan rate of 5 mV/s in 0.5 M H_2SO_4 medium for (a) CoPc, TACoPc and TCCoPc molecules, (b) CoPc, TNCoPc and TCCoPc molecules and (c) CuPc and TCCuPc molecules.

Table 5.5. Specific capacitance (Csp) extracted from the cyclic voltammogram at 5 mV/s for CoPc, CuPc, TCCoPc and TCCuPc molecules.
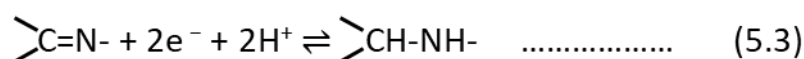
Catalyst	Csp (F/g)
CoPc	233
CuPc	211
TCCoPc	682
TCCuPc	657

where it is present, it will exist in its protonated form.[64] Therefore, since the pKa of both the amino substituent and carboxy substituent are more than pH of 0.5 M H_2SO_4 medium (pH is nearly 0.2), both the functionalities should have a proton charge assembly in this medium. Further, a nitro functionality which may not undergo protonation like TACoPc/TCCoPc demonstrated almost similar double layer features like unsubstituted CoPc molecule, Figure 5.18b. On changing the central metal ion from Co to Cu, a similar disparity in double layer features were evidently present between -COOH functionalized ligand and unsubstituted ligand, which in turn indicates that this enhanced double layer charge storage majorly stems from the ligand, Figure 5.18c and Table 5.5. All these indicate that the proton charge assembly in the ligand on functionalization with non-redox active functionality like -COOH and -NH_2 is extensive than unsubstituted ligand that in turn make the former ligands without any additional redox active
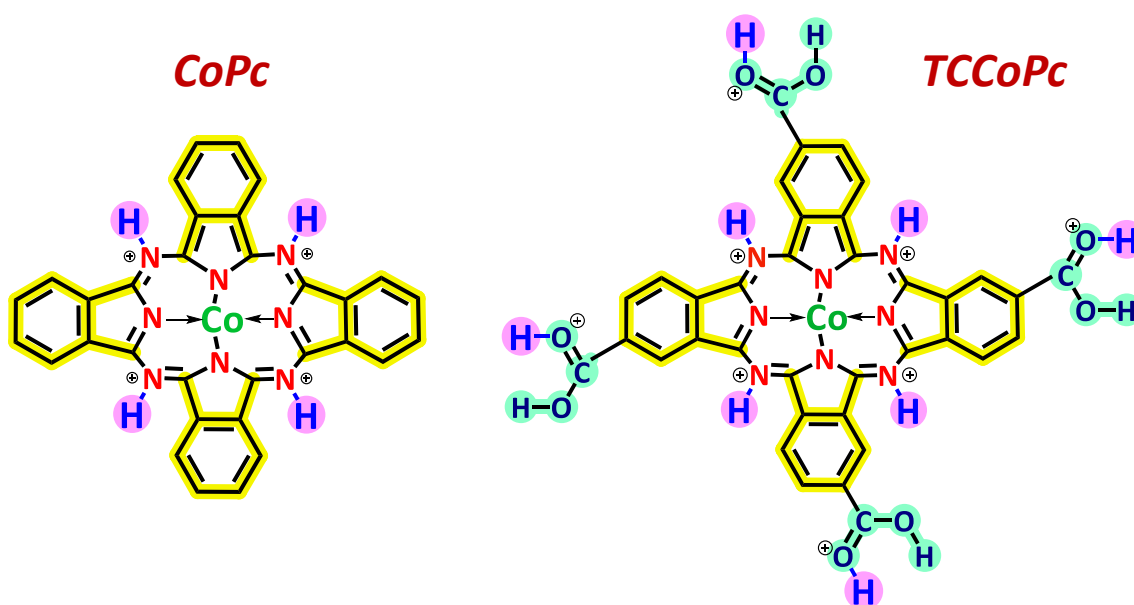
Scheme 5.2. Schematic illustration of proton charge assembly in CoPc and TCCoPc molecules in acidic medium.

functionality a potential platform for charge storage applications. Based on these, a schematic representation for the proton charge assembly in CoPc and TCCoPc is provided in Scheme 5.2. It is assumed that in an ideal situation TCCoPc can hold up to 8 protons which will be twice as that on unsubstituted CoPc (4 protons), Scheme 5.2. It is to be noted that, the redox peaks in the CV curve of TACoPc (Figure 5.18a) corresponds to the Faradaic reactions of the metal centre and phthalocyanine ligand as shown below:

$$Co^{3+}TAPc^{-2} + e^{-} \rightleftharpoons Co^{2+}TAPc^{-2} \quad \text{..................} \quad (5.1)$$

$$Co^{3+}TAPc^{-1} + e^{-} \rightleftharpoons Co^{3+}TAPc^{-2} \quad \text{..................} \quad (5.2)$$

$$\text{>C=N- } + 2e^{-} + 2H^{+} \rightleftharpoons \text{>CH-NH- } \quad \text{..................} \quad (5.3)$$

The redox peak at lower potential range is attributed to equation 5.1 and equation 5.3, whereas the redox peak at higher potential is attributed equation 5.2.[65, 66] However, for TCCoPc only a broad redox peak pair was observed, Figure 5.18a, which is attributed to merging of redox peaks corresponding to equations 5.1-5.3. Although, the reason for this behaviour between TCCoPc and TACoPc is unclear at the moment, it is believed it has something to do with the nature of the intermolecular interactions in TACoPc and TCCoPc molecules. To figure out the contribution of proton charge assembly specifically to pseudocapacitance, the Faradaic contributions for TCCoPc as well as CoPc were compared in the potential range from 0.3 V to 0.5 V where metal-nitrogen redox transition is observed, Figure 5.9a. Figure 5.19 shows that at 0.4 V, the pseudocapacitance is almost similar in magnitude for TCCoPc and CoPc molecules. The capacitive

and diffusional contributions, further suggest that the non-Faradaic contributions in the voltage range of 0.3 V to 0.5 V are noticeably enriched in TCCoPc compared to CoPc as shown in Figure 5.19. All these indicate that the proton charge assembly does not influence the Faradaic contribution noticeably, however, it majorly contributes to non-Faradaic capacitance.
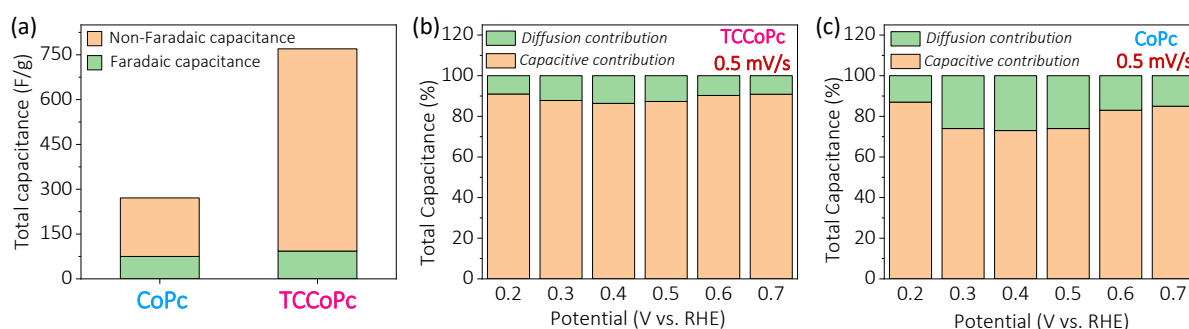

Figure 5.19. Histogram plot showing (a) Faradaic and non-Faradaic contributions with respect to total specific capacitance for CoPc and TCCoPc at 0.4 V. The percentage contribution of Faradaic and non-Faradaic capacitance in (b) TCCoPc molecule and (c) CoPc molecule.

5.2.6. Electrochemical analysis for two electrode configurations.

To demonstrate a practical supercapacitor device, a two-electrode asymmetric device architecture using the composite electrodes and activated carbon (AC) as the positive and negative electrodes respectively have been assembled. The two-electrode fabrication procedure is explained in chapter 2, section 2.4.4, pages 58-59. Cyclic voltammetry and galvanostatic charge–discharge measurements, (Figure 5.20a and 5.20b), using the two-electrode configuration suggest an enhanced charge storage
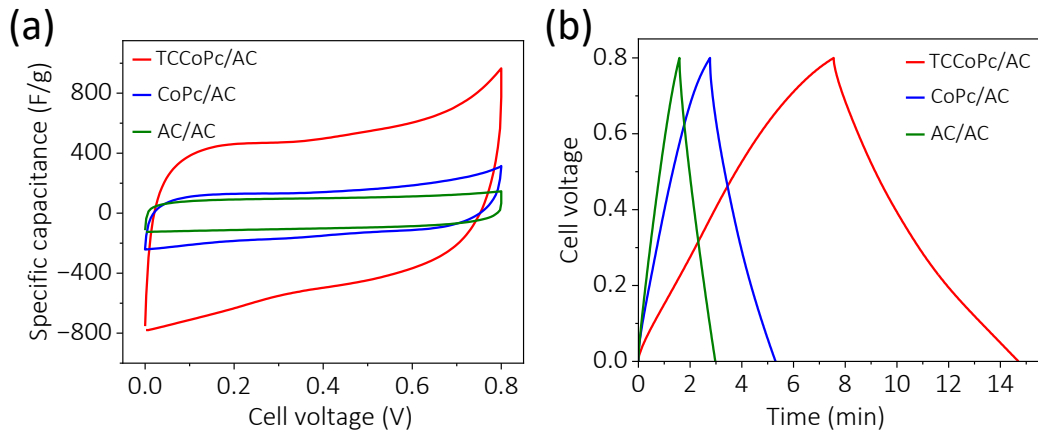
Figure 5.20. (a) Cyclic voltammogram of a two-electrode split cell in asymmetric configuration with TCCoPc and CoPc as (+) electrodes and activated carbon as (−) electrodes. (b) Galvanostatic charge–discharge profiles of the device.
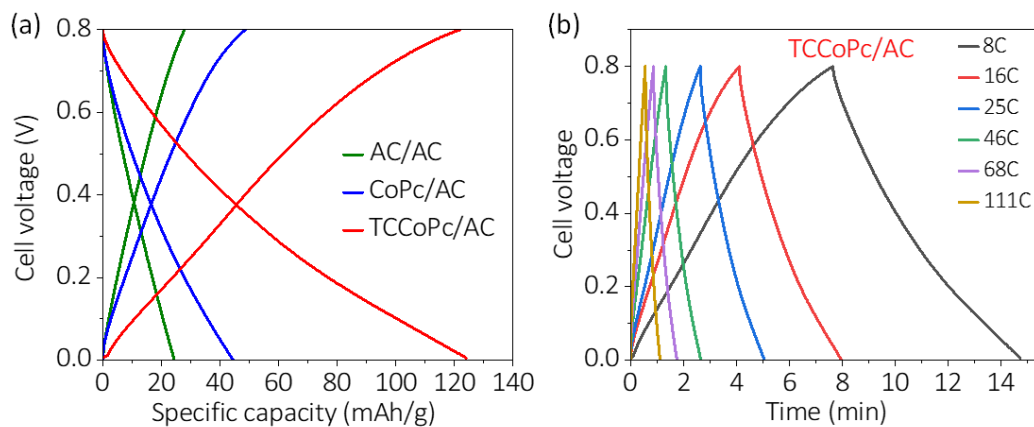
Figure 5.21. (a) Comparison of specific capacity of all the three composite electrodes at a current rate of 1A/g and (b) Galvanostatic charge discharge of TCCoPc/AC at various rates.

in TCCoPc system than unsubstituted CoPc as demonstrated in the case of three-electrode systems. The rate capability and cycling tests with the TCCoPc/AC two electrode device was carried out as it is the best performing system. Specific capacity and GCD measurements demonstrate the excellent charge storage capability of the TCCoPc/AC device, Figure 5.21.
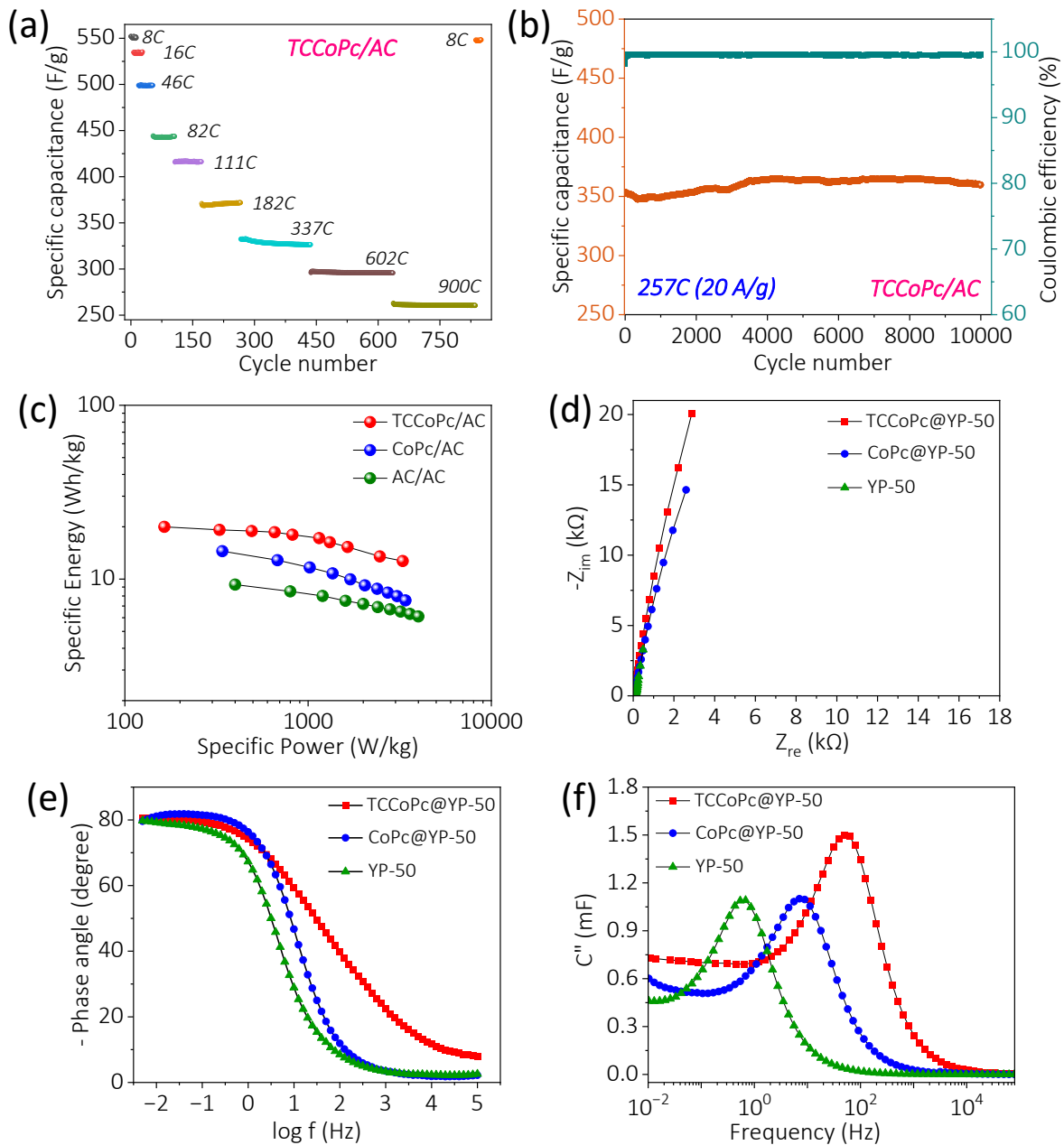
Figure 5.22. (a) Capacity retention plot for the TCCoPc/AC split cell with increasing C rates. The rate is brought back to 8C after cycling it up to a high rate of 900C. (b) Specific capacitance and coulombic efficiency of the split cell with TCCoPc/AC system over 10,000 cycles at a rate of 257 C (20 A/g). (c) Ragone plots for the asymmetric two-electrode split cell. (d) Nyquist plots and (e) Bode plots for YP-50, CoPc@YP-50 and TCCoPc@YP-50 electrodes. at 0 V vs. OCV. (f) Plot of the imaginary part of capacitance (C'') vs. frequency acquired in the frequency range of 100 kHz to 5 mHz with a 10 mV (peak to peak) AC excitation signal at the open circuit voltage (OCV).

The rate capability analysis with TCCoPc/AC device show stability even at a very high current rating of 900C (50 A/g), while maintaining a capacity of 270 F/g (please refer to chapter 2, section 2.9.2, page 65 for calculation). The device demonstrated swift returning to almost its original performance when the current rating is lowered to 8C, without compromising its initial capacity, Figure 5.22a. The long-term cycling at a current rate of 20 A/g for the TCCoPc molecule demonstrated a stable profile and a capacity retention of nearly 99.5% even after 10,000 cycles, Figure 5.22b. The Ragone plot, suggest that functionalization by a non-redox active functionality like -COOH group can dramatically influence the charge storage, by enhancing the energy density without compromising their power capability, Figure 5.22c (please refer to chapter 2, section 2.9.2, page 65 for calculation). Electrochemical impedance spectroscopy (EIS) with the composite electrodes (in a three-electrode configuration) and the corresponding Bode plot reveal a high frequency resistive to capacitive switching in TCCoPc@YP-50, however this switching occurs at a lower frequency in CoPc@YP-50, (Figure 5.22d and e). These further reflect the superior supercapacitor characteristics of TCCoPc over the CoPc molecule. From the frequency corresponding to the maximum of the imaginary part of the capacitance (C") in the C" *versus* frequency plot, which generally reflects the transition boundary between purely capacitive and purely resistive behavior,[18, 67-71] the knee frequency (f_0) reflecting the power capability of a supercapacitor was extracted, (Figure 5.22e and f). The f_0 was highest for TCCoPc (49 Hz) molecule than unsubstituted CoPc (10 Hz) and YP-50 (3 Hz), suggesting the higher power capability of the former molecule. The

relaxation time which is the inverse of the knee frequency ($\tau_0 = 1/f_o$) indicating the minimum time required to fully discharge the capacitor was shorter for the TCCoPc molecule than CoPc molecule, Figure 5.22f and Table 5.6 (please refer to chapter 2, section 2.11, pages 66-68 for details). The TCCoPc system as compared to the unsubstituted system demonstrated a remarkably lowered self-discharge rates and leakage currents, Figure 5.23 and Table 5.7 (chapter 2, section 2.11, pages 66-68).

Table 5.6. Knee frequency and relaxation time for YP-50 and its composite electrodes determined using the electrochemical impedance spectroscopy (EIS) method.

Composite electrodes	Knee frequency (f_0) in Hz	Time constant (τ_0) in ms
YP-50	3	333
CoPc@YP-50	10	100
TCCoPc@YP-50	49	20.4
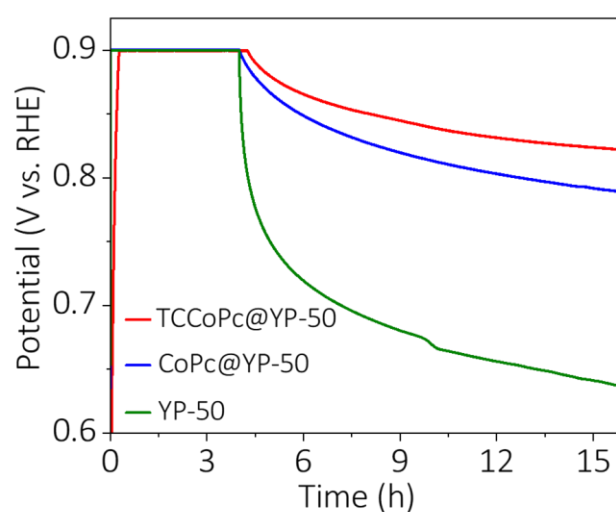
Figure 5.23. Self-discharge profiles of YP-50, CoPc@YP-50 and TCCoPc@YP-50 in a three-electrode configuration.

Table 5.7. Self-discharge current and leakage current values extracted from Figure 5.23.

Electrode Materials	TCCoPc@YP-50	CoPc@YP-50	YP-50
Specific capacitance (F/g)	715	269	204
Self discharge current (µA)	18.10^{-3}	26.10^{-3}	35.10^{-3}
Leakage current (mA/F/V)	77.10^{-3}	139.10^{-3}	192.10^{-3}

Electrode   **Composite electrode**   **(+) electrode**   **(-) electrode**

Assembled device powering a 2V LED
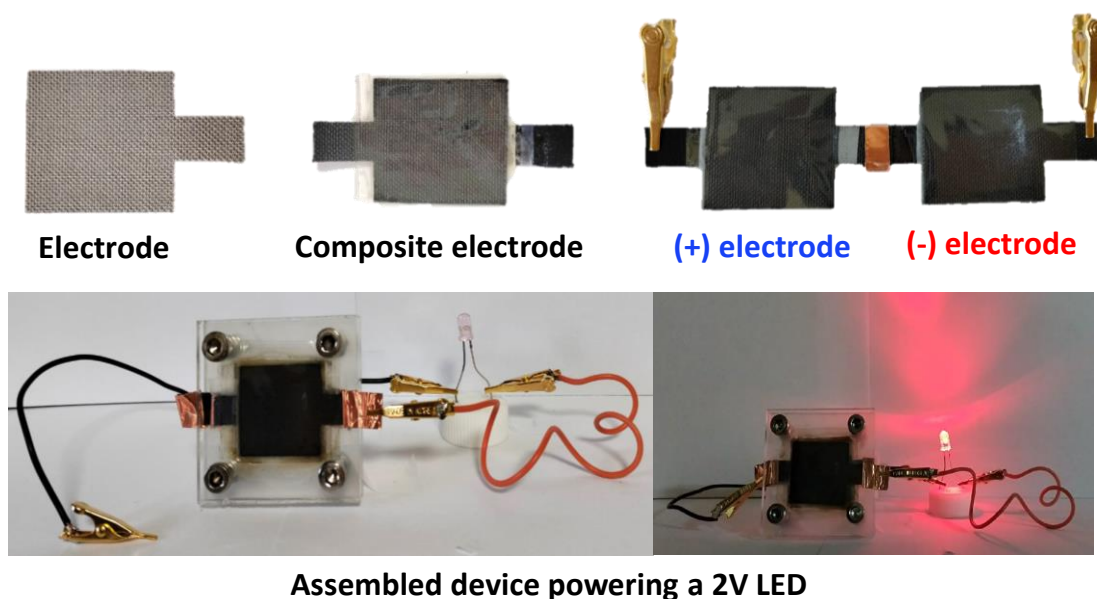
Scheme 5.3. Photographs showing the architectural components of the supercapacitor along with the assembled device powering a 2 V LED.

Practical viability of the device is demonstrated by powering a 2 V LED by a series of configuration of the asymmetric capacitor, Scheme 5.3. To position the work with respect to the literature, the results obtained with molecules containing non-redox active functionalities were compared with various phthalocyanine molecules-based supercapacitors. As shown in Table 5.8, the performance metrics of molecule-based supercapacitors can be noticeably enhanced with a non-redox active functionality that can

undergo a non-Faradaic proton charge assembly. Taken together, the approach detailed here shows that EDL structure can be altered by a non-redox active functionality via a non-Faradaic proton charge assembly that in turn can be exploited for designing ligands for potential molecule-based supercapacitor devices.

Table 5.8. Comparison of specific capacitance, specific energy and specific power of different phthalocyanine based supercapacitors (in three electrode configurations).

System	Electrolyte	Current rate (A/g)	Specific capacitance (F/g)	Specific Energy (Wh/kg)	Specific Power (W/kg)	References
NiPc NF-rGO	1M H_2SO_4	1	223	15	350	Appl. Surf. Sci., 2018, **449**, 528–536
CuPcTs-Ppy/ MWCNT	3M H_2SO_4	5	488	67.7	2500	Electrochim. Acta, 2018, **265**, 594–600
N-CuMe2Pc-GO	1M H_2SO_4	0.5	291.6	32.8	225	Electrochim. Acta, 2019, **298**, 770–777
Cu(II)Pc/acid activated MWCNT/Ppy	1M H_2SO_4	10	304	42	4973	Int. J. Energy Res., 2020, **44**, 9093–9111
CoPc@CNTs	6M KOH	1	1112	55.6	300	J. Mol. Liq., 2022, **359**, 119319
Co(NO$_2$)$_4$Pc-rGO	1M H_2SO_4	4	150	20.8	1994	Synth. Met., 2023, **293**, 117284
ZnPc-400//Zn Zn-ion	1M $ZnSO_4$	1	164	86.2	220	Chem. Eng. J., 2023, **468**, 143875
TCCoPc@YP-50	0.5M H_2SO_4	1	715	80.4	450	**This work**

5.3. Conclusion:

In this Chapter, how the nature of the ligand enhances the supercapacitive energy storage is demonstrated. It is shown that, a non-redox active substituent can alter the population of anions in the electric double layer (EDL) via a proton charge assembly over the molecule. It was observed that the double layer charge storage was enhanced for the

carboxylic substituted as well as the amine substituted molecules almost to similar magnitudes compared to unsubstituted ligand. However, for the nitro substituted molecule, the double layer storage was not elevated compared to unsubstituted ligand. Various physicochemical analyses indicate that -COOH and -NH$_2$ groups can undergo extensive proton charge assembly in acidic medium. This in turn leads to a higher local density of anions in EDL that in turn enhance the energy density of the supercapacitor device without compromising the power capability. This concept of a non-redox active functionality contributing to super capacitive charge storage via a non-electrochemical proton charge assembly can be harnessed for the design of ligands for charge storage applications.

5.4. References:

[1]   Zhu, Y.; Deng, J.; Fontaine, O. Breaking the Strength Barrier. *Nat. Energy* **2023**, *8* (7), 643–644.

[2]   Wang, X.; Zhang, C.; Sawczyk, M.; Sun, J.; Yuan, Q.; Chen, F.; Mendes, T. C.; Howlett, P. C.; Fu, C.; Wang, Y.; Tan, X.; Searles, D. J.; Král, P.; Hawker, C. J.; Whittaker, A. K.; Forsyth, M. Ultra-Stable All-Solid-State Sodium Metal Batteries Enabled by Perfluoropolyether-Based Electrolytes. *Nat. Mater.* **2022**, *21*, 1057–1066.

[3]   Linnell, S. F.; Kim, E. J.; Choi, Y. S.; Hirsbrunner, M.; Imada, S.; Pramanik, A.; Cuesta, A. F.; Miller, D. N.; Fusco, E.; Bode, B. E.; Irvine, J. T. S.; Duda, L. C.; Scanlon, D. O.; Armstrong, A. R. Enhanced Oxygen Redox Reversibility and Capacity Retention of Titanium-Substituted Na$_{4/7}$[$\square_{1/7}$Ti$_{1/7}$Mn$_{5/7}$] O$_2$ in Sodium-Ion Batteries. *J. Mater. Chem. A* **2022**, 10, 9941–9953.

[4]   Mahne, N.; Schafzahl, B.; Leypold, C.; Leypold, M.; Grumm, S.; Leitgeb, A.; Strohmeier, G. A.; Wilkening, M.; Fontaine, O.; Kramer, D.; Slugovc, C.; Borisov, S. M.; Freunberger, S. A. Singlet Oxygen Generation as a Major Cause for Parasitic Reactions during Cycling of Aprotic Lithium–Oxygen Batteries. *Nat. Energy* **2017**, *2* (5), 17036.

[5]   Nikman, S.; Zhao, D.; Gonzalez-Perez, V.; Hoster, H. E.; Mertens, S. F. L. Surface or Bulk? Real-Time Manganese Dissolution Detection in a Lithium-Ion Cathode. *Electrochim. Acta* **2021**, *386*, 138373.

[6]   Becker, J. M.; Lielpetere, A.; Szczesny, J.; Junqueira, J. R. C.; Rodríguez-Maciá, P.; Birrell, J. A.; Conzuelo, F.; Schuhmann, W. Bioelectrocatalytic CO_2 Reduction by Redox Polymer-Wired Carbon Monoxide Dehydrogenase Gas Diffusion Electrodes. *ACS Appl. Mater. Interfaces* **2022**, *14* (41), 46421–46426.

[7]   Phun, G. S.; Bhide, R.; Ardo, S. Detailed-Balance Limits for Sunlight-to-Protonic Energy Conversion from Aqueous Photoacids and Photobases Based on Reversible Mass-Action Kinetics. *Energy Environ. Sci.* **2023**, *16*, 4593–4611.

[8]   Bisquert, J. Current-Controlled Memristors: Resistive Switching Systems with Negative Capacitance and Inverted Hysteresis. *Phys. Rev. Appl.* **2023**, *20* (4), 44022.

[9]   Faqeeh, A. H.; Symes, M. D. A Standard Electrolyzer Test Cell Design for Evaluating Catalysts and Cell Components for Anion Exchange Membrane Water Electrolysis. *Electrochim. Acta* **2023**, *444*, 142030.

[10]   Lei, J.; Yao, Y.; Huang, Y.; Lu, Y. C. A Highly Reversible Low-Cost Aqueous Sulfur-Manganese Redox Flow Battery. *ACS Energy Lett.* **2023**, *8* (1), 429–435.

[11]   Salanne, M.; Rotenberg, B.; Naoi, K.; Kaneko, K.; Taberna, P.-L.; Grey, C. P.; Dunn, B.; Simon, P. Efficient Storage Mechanisms for Building Better Supercapacitors. *Nat. Energy* **2016**, *1* (6), 16070.

[12]   Lannelongue, P.; Bouchal, R.; Mourad, E.; Bodin, C.; Olarte, M.; le Vot, S.; Favier, F.; Fontaine, O. "Water-in-Salt" for Supercapacitors: A Compromise between Voltage, Power Density, Energy Density and Stability. *J. Electrochem. Soc.* **2018**, *165* (3), A657–A663.

[13] Oni, J.; Ozoemena, K. I. Phthalocyanines in Batteries and Supercapacitors. *J. Porphyr. Phthalocyanines* **2012**, *16* (7–8), 754–760.

[14] Li, T.; Wang, Y. F.; Yin, Z.; Li, J.; Peng, X.; Zeng, M. H. The Sequential Structural Transformation of a Heptanuclear Zinc Cluster towards Hierarchical Porous Carbon for Supercapacitor Applications. *Chem. Sci.* **2022**, *13* (36), 10786–10791.

[15] Mourad, E.; Coustan, L.; Lannelongue, P.; Zigah, D.; Mehdi, A.; Vioux, A.; Freunberger, S. A.; Favier, F.; Fontaine, O. Biredox Ionic Liquids with Solid-like Redox Density in the Liquid State for High-Energy Supercapacitors. *Nat. Mater.* **2017**, *16* (4), 446–454.

[16] Lekitima, J. N.; Ozoemena, K. I.; Jafta, C. J.; Kobayashi, N.; Song, Y.; Tong, D.; Chen, S.; Oyama, M. High-Performance Aqueous Asymmetric Electrochemical Capacitors Based on Graphene Oxide/Cobalt (II)-Tetrapyrazinoporphyrazine Hybrids. *J. Mater. Chem. A* **2013**, *1* (8), 2821–2826.

[17] Yuan, J.; Qiu, M.; Hu, X.; Liu, Y.; Zhong, G.; Zhan, H.; Wen, Z. Pseudocapacitive Vanadium Nitride Quantum Dots Modified One-Dimensional Carbon Cages Enable Highly Kinetics-Compatible Sodium Ion Capacitors. *ACS Nano* **2022**, *16* (9), 14807–14818.

[18] Chidembo, A. T.; Ozoemena, K. I.; Agboola, B. O.; Gupta, V.; Wildgoose, G. G.; Compton, R. G. Nickel (II) Tetra-Aminophthalocyanine Modified MWCNTs as Potential Nanocomposite Materials for the Development of Supercapacitors. *Energy Environ. Sci.* **2010**, *3* (2), 228–236.

[19] Gorduk, O.; Gencten, M.; Gorduk, S.; Sahin, M.; Sahin, Y. Electrochemical Fabrication and Supercapacitor Performances of Metallo Phthalocyanine/Functionalized-Multiwalled Carbon Nanotube/Polyaniline Modified Hybrid Electrode Materials. *J. Energy Storage* **2021**, *33*, 102049.

[20] Chen, J. J.; Ye, J. C.; Zhang, X. G.; Symes, M. D.; Fan, S. C.; Long, D. L.; Zheng, M. Sen; Wu, D. Y.; Cronin, L.; Dong, Q. F. Design and Performance of Rechargeable Sodium Ion Batteries, and Symmetrical Li-Ion Batteries with Supercapacitor-Like Power Density Based upon Polyoxovanadates. *Adv. Energy Mater.* **2018**, *8* (6), 1–6.

[21]   Sarkar, D.; Das, D.; Das, S.; Kumar, A.; Patil, S.; Nanda, K. K.; Sarma, D. D.; Shukla, A. Expanding Interlayer Spacing in MoS_2 for Realizing an Advanced Supercapacitor. *ACS Energy Lett.* **2019**, *4* (7), 1602–1609.

[22]   Åvall, G.; A. Ferrero, G.; Janßen, K. A.; Exner, M.; Son, Y.; Adelhelm, P. In Situ Pore Formation in Graphite Through Solvent Co-Intercalation: A New Model for The Formation of Ternary Graphite Intercalation Compounds Bridging Batteries and Supercapacitors. *Adv. Energy Mater.* **2023**, *2301944*, 1–13.

[23]   He, S.; Mo, Z.; Shuai, C.; Liu, W.; Yue, R.; Liu, G.; Pei, H.; Chen, Y.; Liu, N.; Guo, R. Pre-Intercalation δ-MnO_2 Zinc-Ion Hybrid Supercapacitor with High Energy Storage and Ultra-Long Cycle Life. *Appl. Surf. Sci.* **2022**, *577*, *151904*.

[24]   Zhang, Q. Z.; Zhang, D.; Miao, Z. C.; Zhang, X. L.; Chou, S. L. Research Progress in MnO_2–Carbon Based Supercapacitor Electrode Materials. *Small* **2018**, *14* (24), 1702883.

[25]   Alharbi, F. F.; Waheed, M. S.; Aman, S.; Ahmad, N.; Farid, H. M. T.; Mohaymen Taha, T. A. Facile Development of Mn Doped NiO Nanoarrays Supported on a Reduced Graphene Oxide Nanocomposite as a Supercapacitor. *Energy and Fuels* **2023**, *37* (16), 12225–12235.

[26]   Zhang, W.; Yu, S.; Hu, H.; Fei, Y.; Chen, L.; Zhang, T. Binder-Free Self-Supporting Electrodes Formed by Intercalation of RuO_2 on Wood-Derived Carbon for Supercapacitor. *Appl. Surf. Sci.* **2023**, *640*, 158285.

[27]   Halder, S.; Roy, S.; Roy, S.; Chakraborty, C. Enriching Oxygen Vacancy in Co_3O_4 by Solution Combustion Synthesis for Enhanced Supercapacitive Property. *J. Phys. Chem. C* **2023**, *127*, 18279–18290.

[28]   Arun Kumar, S.; Sarasamreen, I.; Balaji, C.; Gowdhaman, A.; Ramesh, R.; Anbarasan P. M. Elevates the electrochemical stability performance of hydrothermally synthesized Co_3O_4 nanowires/NF for hybrid supercapacitors. *Inorg. Chem. Commun.* **2023**, *158*, 111506.

[29]   Mukhopadhyay, S.; Kottaichamy, A. R.; Chame, P. V.; Ghosh, P.; Vinod, C. P.; Makri Nimbegondi Kotresh, H.; Kanade, S. C.; Thotiyl, M. O. Unusual Ligand Assistance in Molecular Electrocatalysis via Interfacial

Proton Charge Assembly. *J. Phys. Chem. Lett.* **2023**, *14* (23), 5377–5385.

[30] Mohammed, I.; Nemakal, M.; Aralekallu, S.; Sajjan, V. A.; Divakara, T. R.; Palanna, M.; Keshavananda Prabu, C. P.; Sannegowda, L. K. Phthalocyanine Sheet Polymer Based Amperometric Sensor for the Selective Detection of 2,4-Dichlorophenol. *J. Electroanal. Chem.* **2020**, *871*, 114292.

[31] Sun, X.; Wang, L.; Tan, Z. Improved Synthesis of Soluble Metal-Free/Metal Phthalocyanine Tetracarboxylic Acids and Their Application in the Catalytic Epoxidation of Cyclohexene. *Catal. Letters* **2015**, *145* (4), 1094–1102.

[32] Achar, B. N.; Fohlen, G. M.; Parker, J. A.; Keshavayya, J. Preparation & Structural Investigations of Copper (II), Cobalt (II), Nickel (II) & Zinc (II) Derivatives of 2,9, 16,23-Phthalocyanine Tetracarboxylic Acid. *Indian J. Chem.* **1988**, *27*, 411–416.

[33] Hosu, I. S.; Wang, Q.; Vasilescu, A.; Peteu, S. F.; Raditoiu, V.; Railian, S.; Zaitsev, V.; Turcheniuk, K.; Wang, Q.; Li, M.; Boukherroub, R.; Szunerits, S. Cobalt Phthalocyanine Tetracarboxylic Acid Modified Reduced Graphene Oxide: A Sensitive Matrix for the Electrocatalytic Detection of Peroxynitrite and Hydrogen Peroxide. *RSC Adv.* **2015**, *5* (2), 1474–1484.

[34] Mugadza, T.; Nyokong, T. Electrochemical, Microscopic and Spectroscopic Characterization of Benzene Diamine Functionalized Single Walled Carbon Nanotube-Cobalt (II) Tetracarboxy-Phthalocyanine Conjugates. *J. Colloid Interface Sci.* **2011**, *354* (2), 437–447.

[35] Mounesh; Malathesh, P.; Praveen Kumara, N. Y.; Jilani, B. S.; Mruthyunjayachari, C. D.; Venugopala Reddy, K. R. Synthesis and Characterization of Tetra-Ganciclovir Cobalt (II) Phthalocyanine for Electroanalytical Applications of AA/DA/UA. *Heliyon* **2019**, *5* (7), e01946.

[36] Mafuwe, P. T.; Moyo, M.; Mugadza, T.; Shumba, M.; Nyoni, S. Cobalt Oxide Nanoparticles Anchored Polyaniline-Appended Cobalt

Tetracarboxy Phthalocyanine, Modified Glassy Carbon Electrode for Facile Electrocatalysis of Amitrole. *J. Solid State Electrochem.* **2019**, *23* (1), 285–294.

[37] Shaposhnikov, G. P.; Maizlish, V. E.; Kulinich, V. P. Carboxy-Substituted Phthalocyanine Metal Complexes. *Russ. J. Gen. Chem.* **2005**, *75* (9), 1480–1488.

[38] Ji, X.; Zou, T.; Gong, H.; Wu, Q.; Qiao, Z.; Wu, W.; Wang, H. Cobalt Phthalocyanine Nanowires: Growth, Crystal Structure, and Optical Properties. *Cryst. Res. Technol.* **2016**, *51* (2), 154–159.

[39] Zhang, A.; Zhang, W.; Lu, J.; Wallace, G. G.; Chen, J. Electrocatalytic Reduction of Carbon Dioxide by Cobalt-Phthalocyanine- Incorporated Polypyrrole. *Electrochem. Solid-State Lett.* **2009**, *12* (8), 16–19.

[40] Chen, C.; Ma, Z.; Zhou, S.; Li, T.; Sun, X. Cobalt-Tetracarboxyl-Phthalocyanine Linked with Fe_3O_4/Chitosan Microsphereas—Efficient Catalyst for Dye Degradation. *Catal. Letters* **2017**, *147* (9), 2399–2409.

[41] Kumar, A.; Prajapati, P. K.; Aathira, M. S.; Bansiwal, A.; Boukherroub, R.; Jain, S. L. Highly Improved Photoreduction of Carbon Dioxide to Methanol Using Cobalt Phthalocyanine Grafted to Graphitic Carbon Nitride as Photocatalyst under Visible Light Irradiation. *J. Colloid Interface Sci.* **2019**, *543*, 201–213.

[42] Fleming, B. D.; Praporski, S.; Bond, A. M.; Martin, L. L. Electrochemical Quartz Crystal Microbalance Study of Azurin Adsorption onto an Alkanethiol Self-Assembled Monolayer on Gold. *Langmuir* **2008**, *24* (1), 323–327.

[43] Somashekarappa, M. P.; Keshavayya, J.; Sampath, S. Self-Assembled Molecular Films of Tetraamino Metal (Co, Cu, Fe) Phthalocyanines on Gold and Silver. Electrochemical and Spectroscopic Characterization. *Pure Appl. Chem.* **2002**, *74* (9), 1609–1620.

[44] Makinde, Z. O.; Louzada, M.; Mashazi, P.; Nyokong, T.; Khene, S. Electrocatalytic Behaviour of Surface Confined Pentanethio Cobalt (II) Binuclear Phthalocyanines towards the Oxidation of 4-Chlorophenol. *Appl. Surf. Sci.* **2017**, *425*, 702–712.

[45] Wang, A.; Ye, J.; Humphrey, M. G.; Zhang, C. Graphene and Carbon-Nanotube Nanohybrids Covalently Functionalized by Porphyrins and Phthalocyanines for Optoelectronic Properties. *Adv. Mater.* **2018**, *30* (17), 1–9.

[46] Chen, Y.; Qu, S.; Shi, W.; Yao, Q.; Chen, L. Enhanced Thermoelectric Properties of Copper Phthalocyanine/Single-Walled Carbon Nanotubes Hybrids. *Carbon N. Y.* **2020**, *159*, 471–477.

[47] Ogunsipe, A.; Nyokong, T. Effects of Substituents and Solvents on the Photochemical Properties of Zinc Phthalocyanine Complexes and Their Protonated Derivatives. *J. Mol. Struct.* **2004**, *689* (1–2), 89–97.

[48] Beeby, A.; FitzGerald, S.; Stanley, C. F. Protonation of Tetrasulfonated Zinc Phthalocyanine in Aqueous Acetonitrile Solution. *Photochem. Photobiol.* **2001**, *74* (4), 566.

[49] Yamada, Y.; Yoshida, S.; Honda, T.; Fukuzumi, S. Protonated Iron-Phthalocyanine Complex Used for Cathode Material of a Hydrogen Peroxide Fuel Cell Operated under Acidic Conditions. *Energy Environ. Sci.* **2011**, *4* (8), 2822–2825.

[50] Tokunaga, E.; Mori, S.; Sumii, Y.; Shibata, N. Super-Sensitive Protonation Behavior of Trifluoroethoxy-Substituted Phthalocyanines and Their Application to Solvent Discrimination. *ACS Omega* **2018**, *3* (9), 10912–10917.

[51] Bächle, F.; Maichle-Mössmer, C.; Ziegler, T. Helical Self-Assembly of Optically Active Glycoconjugated Phthalocyanine J-Aggregates. *Chempluschem* **2019**, *84* (8), 1081–1093.

[52] Gładysiak, A.; Nguyen, T. N.; Anderson, S. L.; Boyd, P. G.; Palgrave, R. G.; Bacsa, J.; Smit, B.; Rosseinsky, M. J.; Stylianou, K. C. Shedding Light on the Protonation States and Location of Protonated N Atoms of Adenine in Metal-Organic Frameworks. *Inorg. Chem.* **2018**, *57* (4), 1888–1900.

[53] Mthethwa, T.; Antunes, E.; Nyokong, T. Photophysical Properties of a New Water-Soluble Tetra Thiamine Substituted Zinc Phthalocyanine Conjugated to Gold Nanorods of Different Aspect Ratios. *Dalt. Trans.* **2014**, *43* (22), 8230–8240.

[54] Rojas, J. V; Toro-Gonzalez, M.; Molina-Higgins, M. C.; Castano, C. E. Facile Radiolytic Synthesis of Ruthenium Nanoparticles on Graphene Oxide and Carbon Nanotubes. *Mater. Sci. Eng. B* **2016**, *205*, 28–35.

[55] Quezada-Renteria, J. A.; Ania, C. O.; Chazaro-Ruiz, L. F.; Rangel-Mendez, J. R. Influence of Protons on Reduction Degree and Defect Formation in Electrochemically Reduced Graphene Oxide. *Carbon N. Y.* **2019**, *149*, 722–732.

[56] Sotoma, S.; Akagi, K.; Hosokawa, S.; Igarashi, R.; Tochio, H.; Harada, Y.; Shirakawa, M. Comprehensive and Quantitative Analysis for Controlling the Physical/Chemical States and Particle Properties of Nanodiamonds for Biological Applications. *RSC Adv.* **2015**, *5* (18), 13818–13827.

[57] Pedrosa, M.; Da Silva, E. S.; Pastrana-Martínez, L. M.; Drazic, G.; Falaras, P.; Faria, J. L.; Figueiredo, J. L.; Silva, A. M. T. Hummers' and Brodie's Graphene Oxides as Photocatalysts for Phenol Degradation. *J. Colloid Interface Sci.* **2020**, *567*, 243–255.

[58] Juodkazis, K.; Juodkazyt≐, J.; Jasulaitien≐, V.; Lukinskas, A.; Šebeka, B. XPS Studies on the Gold Oxide Surface Layer Formation. *Electrochem. commun.* **2000**, *2* (7), 503–507.

[59] Kumar, A.; Ganguly, A.; Papakonstantinou, P. Thermal Stability Study of Nitrogen Functionalities in a Graphene Network. *J. Phys. Condens. Matter* **2012**, *24*, 235503.

[60] Motejadded Emrooz, H. B.; Maleki, M.; Rashidi, A.; Shokouhimehr, M. Adsorption Mechanism of a Cationic Dye on a Biomass-Derived Micro- and Mesoporous Carbon: Structural, Kinetic, and Equilibrium Insight. *Biomass Convers. Biorefinery* **2021**, *11* (3), 943–954.

[61] Gomez, A.; Mullens, J.; Huyskens, P. Specific Interactions of Anilines with Water. *J. Phys. Chem.* **1972**, *76* (26), 4011–4014.

[62] Bryson, A. The Effects of m-Substituents on the pKa Values of Anilines, and on the Stretching Frequencies of the N-H Bonds. *J. Am. Chem. Soc.* **1960**, *82* (18), 4858–4862.

[63] Guillaume, M.; Botek, E.; Champagne, B.; Castet, F.; Ducasse, L. Substituent Effects on the Electronic Structure and PKa Benzoic Acid. *Int. J. Quantum Chem.* **2002**, *90* (4–5), 1396–1403.

[64] Po, H. N.; Senozan, N. M. The Henderson-Hasselbalch Equation: Its History and Limitations. *J. Chem. Educ.* **2001**, *78* (11), 1499–1503.

[65] Madhuri, K. P.; John, N. S. Supercapacitor Application of Nickel Phthalocyanine Nanofibres and Its Composite with Reduced Graphene Oxide. *Appl. Surf. Sci.* **2018**, *449*, 528–536.

[66] Qi, F.; Wang, Y.; Xu, J.; Wang, X.; Wang, J.; Shan, H.; Li, M.; Xu, J. Tetranitro-Substituted Cobalt Phthalocyanine Immobilized on Reduced Graphene Oxide as Supercapacitor Electrode Material with Enhanced Capacitance. *Synth. Met.* **2023**, *293*, 117284.

[67] Purkait, T.; Singh, G.; Kumar, D.; Singh, M.; Dey, R. S. High-Performance Flexible Supercapacitors Based on Electrochemically Tailored Three-Dimensional Reduced Graphene Oxide Networks. *Sci. Rep.* **2018**, *8* (1), 1–13.

[68] Shrestha, M.; Amatya, I.; Wang, K.; Zheng, B.; Gu, Z.; Fan, Q. H. Electrophoretic Deposition of Activated Carbon YP-50 with Ethyl Cellulose Binders for Supercapacitor Electrodes. *J. Energy Storage* **2017**, *13*, 206–210.

[69] Sheng, K.; Sun, Y.; Li, C.; Yuan, W.; Shi, G. Ultrahigh-Rate Supercapacitors Based on Eletrochemically Reduced Graphene Oxide for Ac Line-Filtering. *Sci. Rep.* **2012**, *2*, 3–7.

[70] Taberna, P. L.; Simon, P.; Fauvarque, J. F. Electrochemical Characteristics and Impedance Spectroscopy Studies of Carbon-Carbon Supercapacitors. *J. Electrochem. Soc.* **2003**, *150* (3), A292.

[71] Yoo, Y.; Kim, M. S.; Kim, J. K.; Kim, Y. S.; Kim, W. Fast-Response Supercapacitors with Graphitic Ordered Mesoporous Carbons and Carbon Nanotubes for AC Line Filtering. *J. Mater. Chem. A* **2016**, *4* (14), 5062–5068.

Chapter 6

Ligand Assisted Tuning of Mechanistic Pathway in Oxygen Reduction Reaction

Chapter 6

ABSTRACT: This chapter demonstrates how the ligand functionality influences the reaction mechanism in the oxygen reduction reaction. Typically, ORR with metal phthalocyanines in an aqueous medium follows either a 2-electron or a 4-electron pathway, resulting in peroxide or water as the main products, respectively. However, the unique combination of a cobalt central metal and a carboxy-functionalized ligand (TCCoPc) leads to an unexpected 1-electron ORR, forming superoxide in aqueous medium. Various analyses including hydrodynamic voltammetric techniques, indicate the formation of superoxide ion with TCCoPc molecule. Moreover, this 1-electron ORR phenomenon was not observed with other carboxy-substituted transition metal phthalocyanines (Fe, Cu, and Ni), making it unique to the cobalt and carboxy combination. The actual reason for this distinctive result is still unclear and theoretical investigations, coupled with in-situ studies, are being pursued to elucidate the underlying reasons behind this novel result.
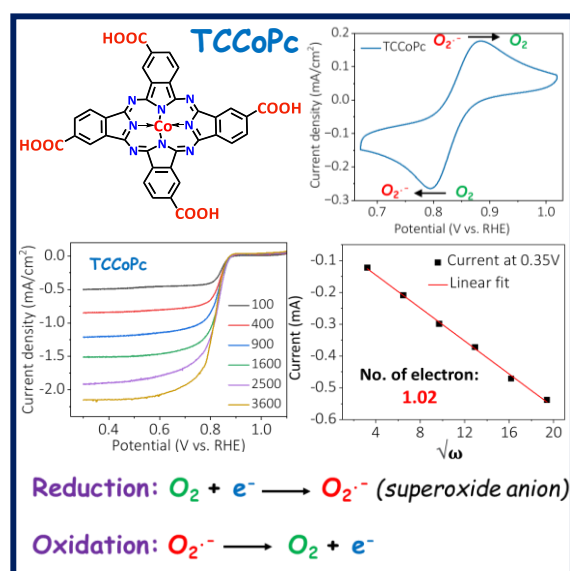
Declaration: The work in this chapter is original and has not yet been published anywhere. *(Manuscript under preparation)*

6.1. Introduction:

The electrochemical reduction of oxygen (ORR) is ubiquitous in most of the electrochemical energy systems including fuel cells [1-6] and metal-air batteries.[7-11] Molecular electrocatalysts such as metal phthalocyanines (MPcs) and metal porphyrins (MPs) are widely investigated towards ORR mainly because of their high degree of tunability of their electronic and geometric parameters.[12-16] The first study on the catalytic activity of cobalt phthalocyanine (CoPc) for oxygen reduction reaction (ORR) dates back to 1964 which was performed by Jasinski in alkaline medium.[17] Following this work, extensive research on catalytic activity towards ORR for various metallophthalocyanine (MPc) derivatives containing different substitutes on the peripheral organic skeleton in both acidic and alkaline electrolyte has been conducted.[18-28] Special attention has been directed toward Co and Fe based metal phthalocyanines in the context of oxygen reduction reaction (ORR) due to the high electrochemical activity of their respective central metal ions.[29-33] Most studies indicate that $Fe-N_4$ macrocyclic complexes could promote the reduction of oxygen to water via a 4 e- pathway whereas $Co-N_4$ macrocyclic complexes could catalyze only hydrogen peroxide formation via a 2 e- pathway.[34-37] In 1980, Zagal and coworkers examined the kinetics of ORR in both acid and alkaline solutions with the rotating ring-disk electrode technique by using monolayers of Co and Fe tetrasulfonate phthalocyanines (CoTSPc and FeTSPc) adsorbed on graphite surfaces and found that CoTSPc promotes the reduction process via two electrons to give peroxide whereas FeTSPc promotes a four-electron

reduction to give water.[21] In 1992, the same group did a comparative study of various substituted cobalt phthalocyanines (CoPc, CoTsPc, CoMeOPc, CoTNPc) for O_2 reduction in alkaline and acid media and observed that always it corresponds to a 2 e- reduction process.[38] In similar lines, Janda et al., studied the mechanism of dioxygen reduction with a monolayer of tetra neopentoxy phthalocyaninato cobalt (II) and ended up with a 2 e- reduction process.[27] Chen and coworkers in 2009, performed a detailed study on the mechanistic pathway of the ORR on CoPc and FePc in alkaline electrolyte through Koutecky–Levich and RRDE method and found nearly 4 e- reduction of oxygen on FePc and around 2 e- reduction on CoPc.[39] In the year 2012, Honda et al. reported two-electron reduction of O_2 on a saddle-distorted CoPc containing eight phenyl groups on the peripheral carbon rings.[40] Apart from experimental evidence, ORR pathways on substituted CoPc and FePc were also investigated using DFT studies and the theoretical calculations corroborate it.[41,42] For instance, in 2011, Sun and his group applied DFT for ORR and demonstrated CoPc reduces O_2 to H_2O_2 whereas FePc doesn't form any intermediate and directly reduces dioxygen to H_2O as the eg orbital of FePc is higher than that of CoPc.[43] In the following year, He et al. found that the O−O bond could be split on the Fe macrocyclic complexes but not on the Co macrocyclic complexes confirming the 4e- reduction route for Fe macrocyclic complexes whereas 2e- reduction route for Co macrocyclic complexes.[44]

Therefore, all the above examples demonstrate that unsubstituted as well as substituted cobalt phthalocyanine always follow the 2 e- reduction

pathway for ORR in aqueous medium. We found for the first time a 1 e-pathway for ORR with formation of superoxide in alkaline medium with a carboxy substituted cobalt phthalocyanine. In order to understand whether this 1 e- ORR is unique to the carboxy functionality, we have synthesised different transition metal substituted carboxy phthalocyanines namely iron carboxy (TCFePc), nickel carboxy (TCNiPc) and copper carboxy (TCCuPc) phthalocyanine molecules and evaluated their ORR activity in alkaline medium. None of the metal carboxy molecules other than cobalt provided this surprising result. Thus, this novel result is because of combined effect of both central metal cobalt and carboxy ligand functionality.

6.2. Results and Discussions:

The primary aim of this Chapter is to explore, whether the nature of a ligand functionality influences the reaction mechanism or reaction kinetics with respect to a specific reaction pathway. To demonstrate this, cobalt (II) phthalocyanine (CoPc) and tetracarboxycobalt (II) phthalocyanine (TCCoPc) molecules were initially synthesised. For a deeper analysis, tetracarboxyiron (II) phthalocyanine (TCFePc), tetracarboxynickel (II) phthalocyanine (TCNiPc) and tetracarboxycopper (II) phthalocyanine (TCCuPc) molecules were also used. Firstly, these molecules were synthesized and characterized (please refer to chapter 2, section 2.2.1-2.2.3, pages 50-53 for details) and the structures of the unsubstituted and carboxy substituted molecules are demonstrated in Scheme 6.1 and Scheme 6.2 respectively.
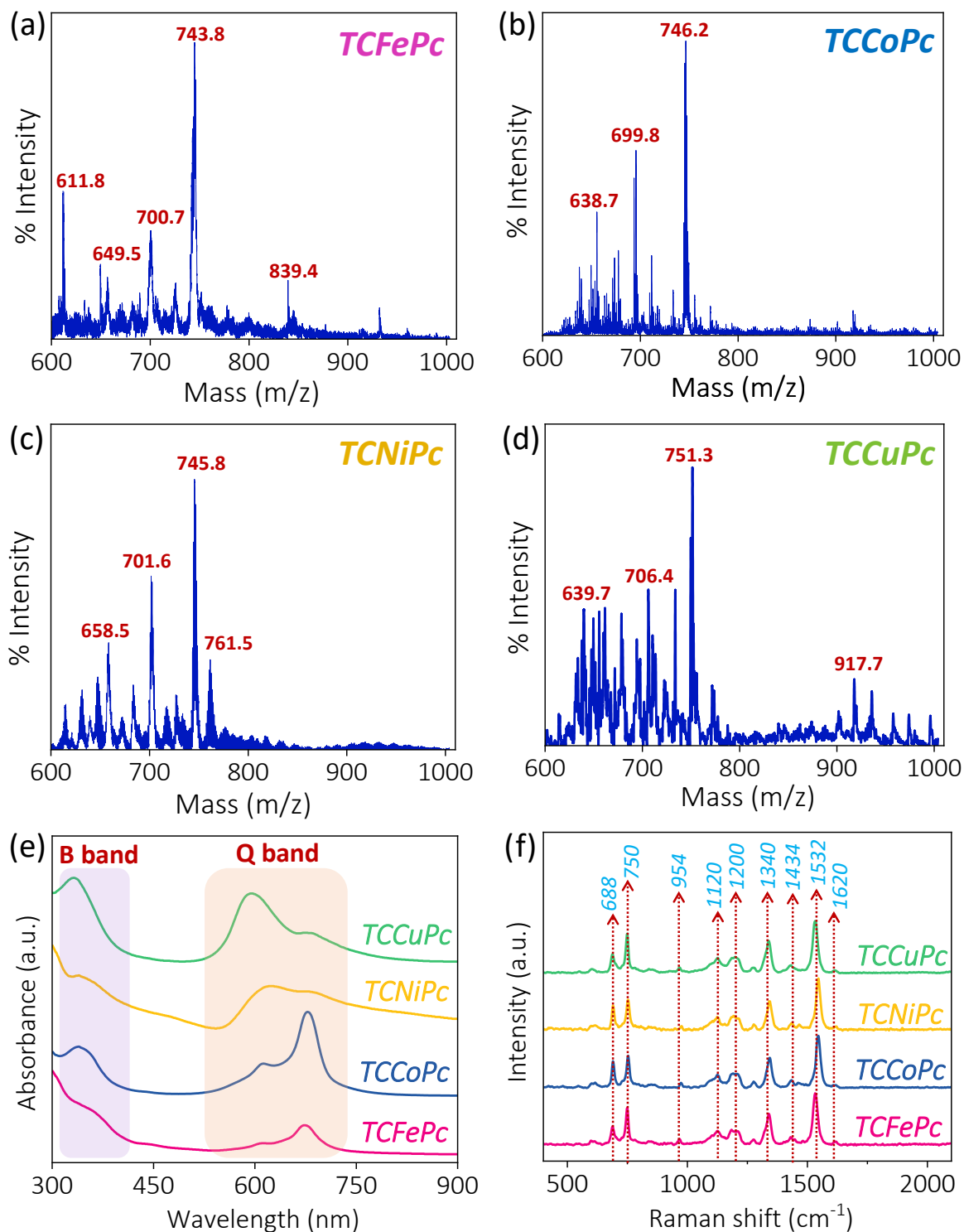
CoPc   **TCCoPc**
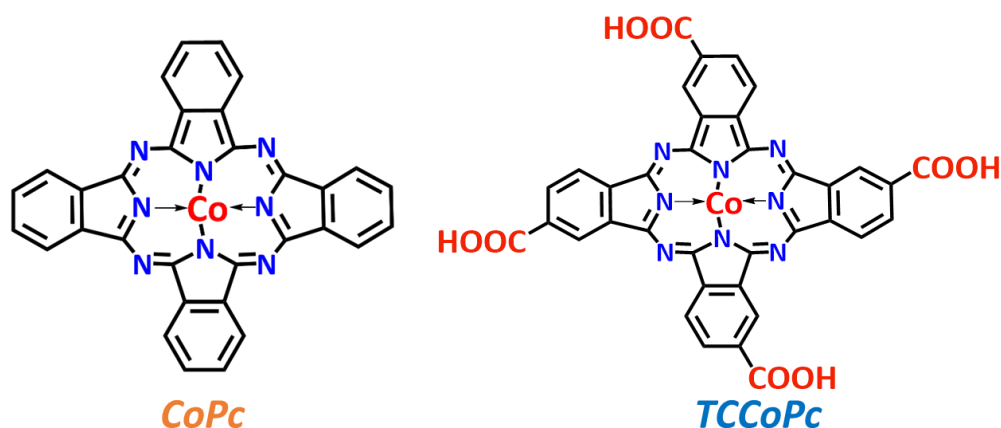
Scheme 6.1. Molecular structures of unsubstituted cobalt phthalocyanine CoPc (Left), and tetra carboxy substituted cobalt phthalocyanine TCCoPc (right) molecules.

TCFePc   **TCNiPc**   **TCCuPc**
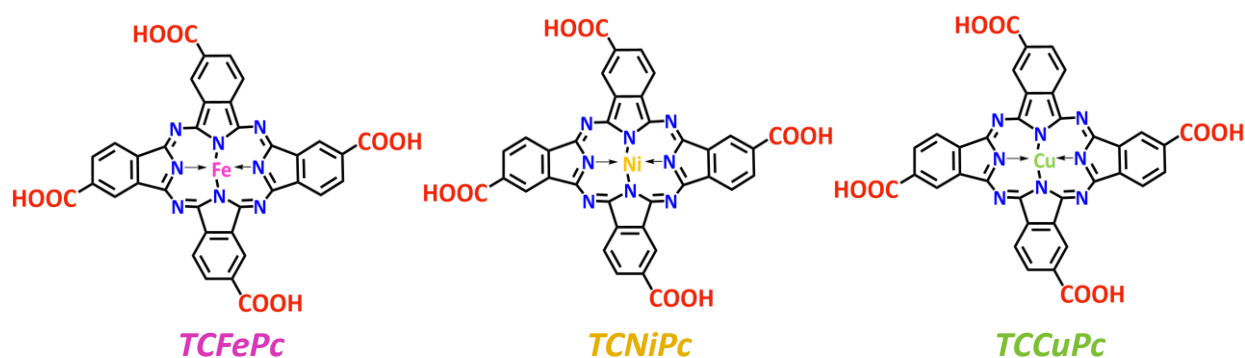
Scheme 6.2. Molecular structures of tetra carboxy substituted iron phthalocyanine TCFePc (left), nickel phthalocyanine TCNiPc (middle) and copper phthalocyanine TCCuPc (right) molecules.

6.2.1. Characterisation of CoPc, TCCoPc, TCFePc, TCNiPc, TCCuPc molecules and their composites with CNTs.

Matrix-assisted laser desorption ionization time-of-flight mass spectrometry (MALDI-TOF) demonstrated the parent ion peaks at m/z values of ~743, ~746, ~745 and ~751 for TCFePc, TCCoPc, TCNiPc and TCCuPc respectively, ensuring their successful formation (Figure 6.1 a-d). UV-visible spectra demonstrated the characteristic phthalocyanine bands

Figure 6.1. (a) Matrix-assisted laser desorption ionization time-of-flight mass spectrometry (MALDI-TOF) of (a) TCFePc (b) TCCoPc (c) TCNiPc and (d) TCCuPc molecules. (e) UV-visible spectra and (f) Raman spectra of TCFePc, TCCoPc, TCNiPc and TCCuPc molecules.

such as B band and Q band for all four molecules (Figure 6.1e). Raman spectra further aids in confirming the formation of the molecules. The formation of the molecules accompanies several characteristic Raman shifts related to various functionalities attached to the molecule. C-N stretching, C-C stretching and C-H bending vibrations are observed in the range 800-1200 cm^{-1}. The C-H in-plane deformation in the macrocyclic ring and the stretching vibration of the isoindole ring unit are respectively present at ~1200 cm^{-1} and ~1434 cm^{-1}. The C-N in-plane stretching vibrations are observed at ~1340 cm^{-1} and ~1620 cm^{-1}. C-C-C in-plane bending bands and the macrocyclic stretching vibration bands are present at a Raman shift between 400-600 cm^{-1} and ~750 cm^{-1} respectively, as shown in (Figure 6.1f).[45-50]

Following the successful formation of all the pristine molecules, their activity towards oxygen reduction reaction (ORR) was studied. To enhance the overall electronic conductivity, these metal phthalocyanines were anchored on carbon nanotubes (MWCNT).[51-53] The composites namely TCFePc/CNT, TCCoPc/CNT, TCNiPc/CNT and TCCuPc/CNT were synthesized according to procedure reported in chapter 2, section 2.2.4, page 53. UV-visible, Raman and other spectroscopic techniques were employed to examine the extent of integration of the molecules with the CNT. UV-vis spectra demonstrated the respective B band Q band for the composite molecules (Figure 6.2a). Raman spectroscopy has been performed which clearly exhibits defects and graphitic bands corresponding to the CNT substrate (Figure 6.2b). The incorporation of molecules into CNT
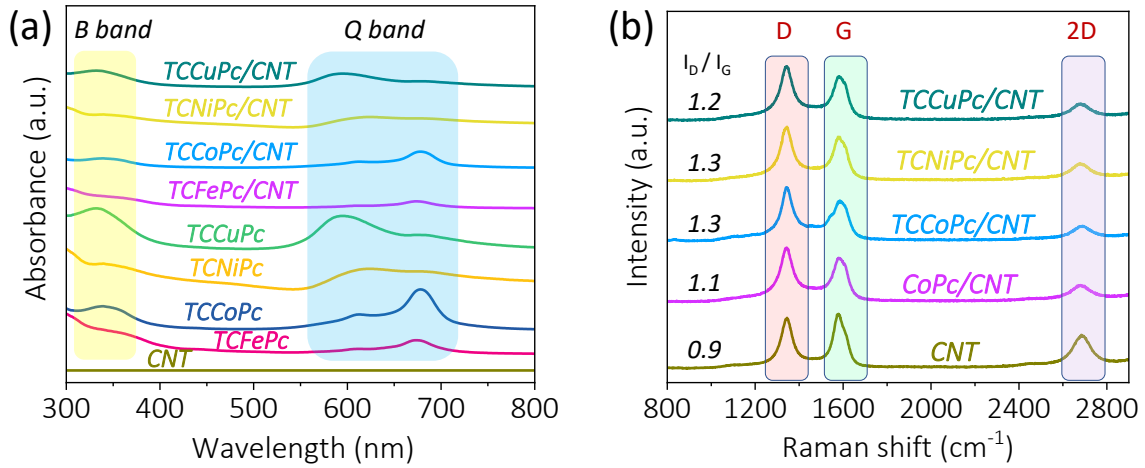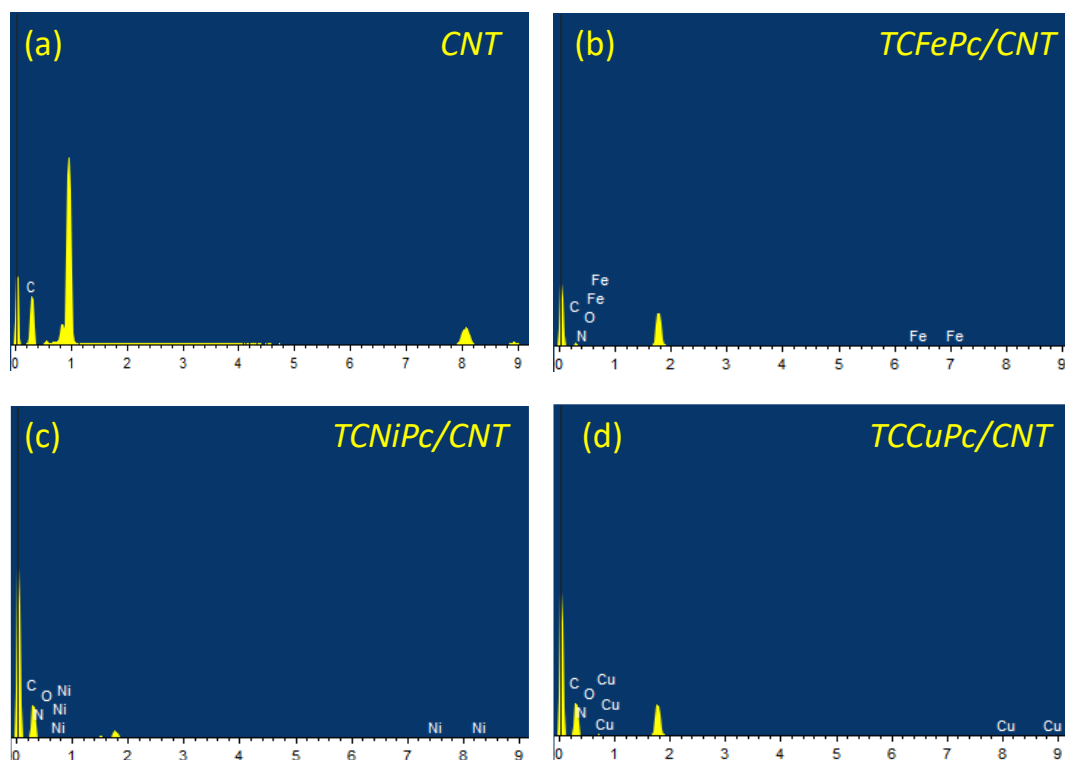
Figure 6.2. (a) UV-visible spectra, (b) Raman spectra of composite molecules namely TCFePc/CNT, TCCoPc/CNT, TCNiPc/CNT and TCCuPc/CNT.
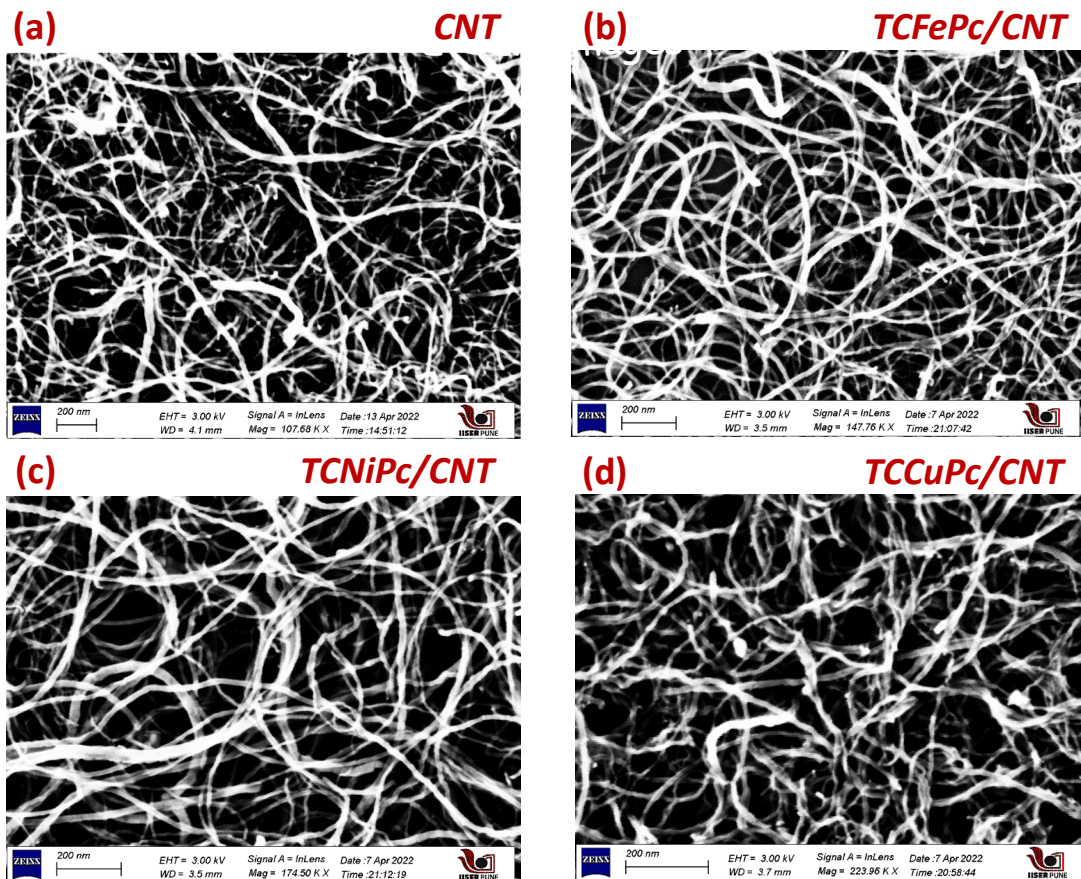
Figure 6.3. FE-SEM images of (a) CNT (b) TCFePc/CNT (c) TCNiPc/CNT and (d) TCCuPc/CNT.

Figure 6.4. EDS pattern along with the elemental composition of (a) CNT (b) TCFePc/CNT (c) TCNiPc/CNT and (d) TCCuPc/CNT.

Table 6.1. Weight and atomic percentage of the elements extracted from EDS data for all the catalysts.

TCFePc			TCCoPc			TCNiPc			TCCuPc		
Element	Weight %	Atomic %	Element	Weight %	Atomic %	Element	Weight %	Atomic %	Element	Weight %	Atomic %
C K	71.83	77.44	C K	75.12	80.79	C K	75.55	80.63	C K	73.35	78.85
N K	9.22	8.52	N K	8.08	7.45	N K	9.11	8.43	N K	8.80	8.15
Fe K	2.24	0.52	Co K	3.07	0.67	Ni K	2.55	0.58	Cu K	2.91	0.62
O K	16.71	13.52	O K	13.73	11.09	O K	12.79	10.36	O K	14.94	12.38
Total:	100.0		Total:	100.0		Total:	100.0		Total:	100.0	

can be discerned by evaluating the intensity ratio between defect (I_D) and graphitic (I_G) bands.[51-53] The successful integration of phthalocyanine into CNTs is confirmed by the observed increase in the I_D/I_G ratio after composite formation, indicative of enhanced defect creation (Figure 6.2b). Moreover,

the scanning electron microscopy (SEM) images (Figure 6.3), coupled with energy-dispersive X-ray spectroscopy (EDS), Figure 6.4 and Table 6.1, reveal distinctive features of CNT and verify the presence of C, N, and O along with the respective central metals (Fe, Ni and Cu) as per the EDS pattern in the composite CNT catalytic systems. These findings, combined with observations from UV-vis, FTIR, and Raman spectroscopy, provide evidence for the anchoring of phthalocyanine molecules on CNT.

6.2.2. Electrochemical analysis of oxygen reduction reaction (ORR).

After successfully confirming the formation of the molecules and their composites, oxygen reduction reaction (ORR) was performed with unsubstituted and carboxy substituted cobalt phthalocyanine molecules. The cyclic voltammograms obtained at a scan rate of 10 mV/s in 1 M KOH electrolytic medium while scanning the potential form right to left side demonstrates an unusual reversible oxidation peak in the case of the TCCoPc molecule. However, in case of CoPc the expected irreversible ORR was obtained (Figure 6.5).

In order to check the stability of this reversible oxidation peak scan rate dependance study was performed by varying the scan rates from 10 mV/s to 100 mV/s with the TCCoPc molecule (Figure 6.6a). The reversibility was found to be maintained at all scan rates indicating the species formed is quite stable. Moreover, to understand the species formed is on the surface of the electrode or in the solution, Randles Sevcik equation was used for
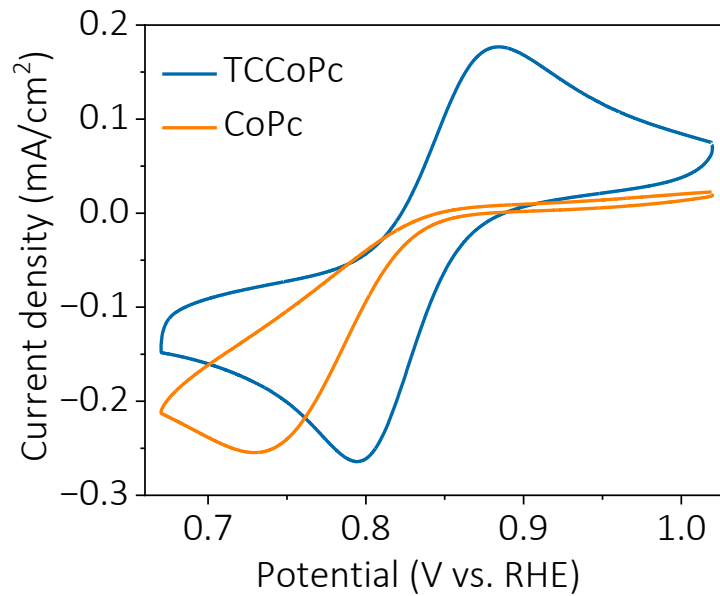
Figure 6.5. Cyclic voltammograms (CVs) of unsubstituted cobalt phthalocyanine (CoPc) and carboxy substituted cobalt phthalocyanine (TCCoPc) molecules in 1 M KOH at a scan rate of 10 mV/s.

the analysis. The equation is as follows:

$$I_{pc} = (2.69*10^5)\, n^{3/2}\, AD^{1/2}\, v^{1/2}\, C \qquad .... (6.1)$$

$$I_{pa} = (2.69*10^5)\, n^{3/2}\, AD^{1/2}\, v^{1/2}\, C \qquad .... (6.2)$$

where I_{pa} and I_{pc} represent the anodic and cathodic peak currents respectively, n is the number of electrons, A is the area of the electrode, D is the diffusion coefficient, C is the concentration of the substrate and v represents the scan rate. The plot of peak current with square root of v gives a linear profile indicating it is a diffusion controlled process (Figure 6.6b). It is known that for a surface controlled process the slope value obtained from the plot of log peak current to log scan rate is ~1, whereas for a solution process the slope value is ~0.5. On plotting the log anodic peak current and cathodic peak current with respect to log v, a linear plot with a slope value ~0.5 for both the anodic and cathodic peak currents was obtained (Figure

6.6c and 6.6d), indicating it is a solution process. This indicates that the species formed is in the solution and is not confined to the surface of the electrode.
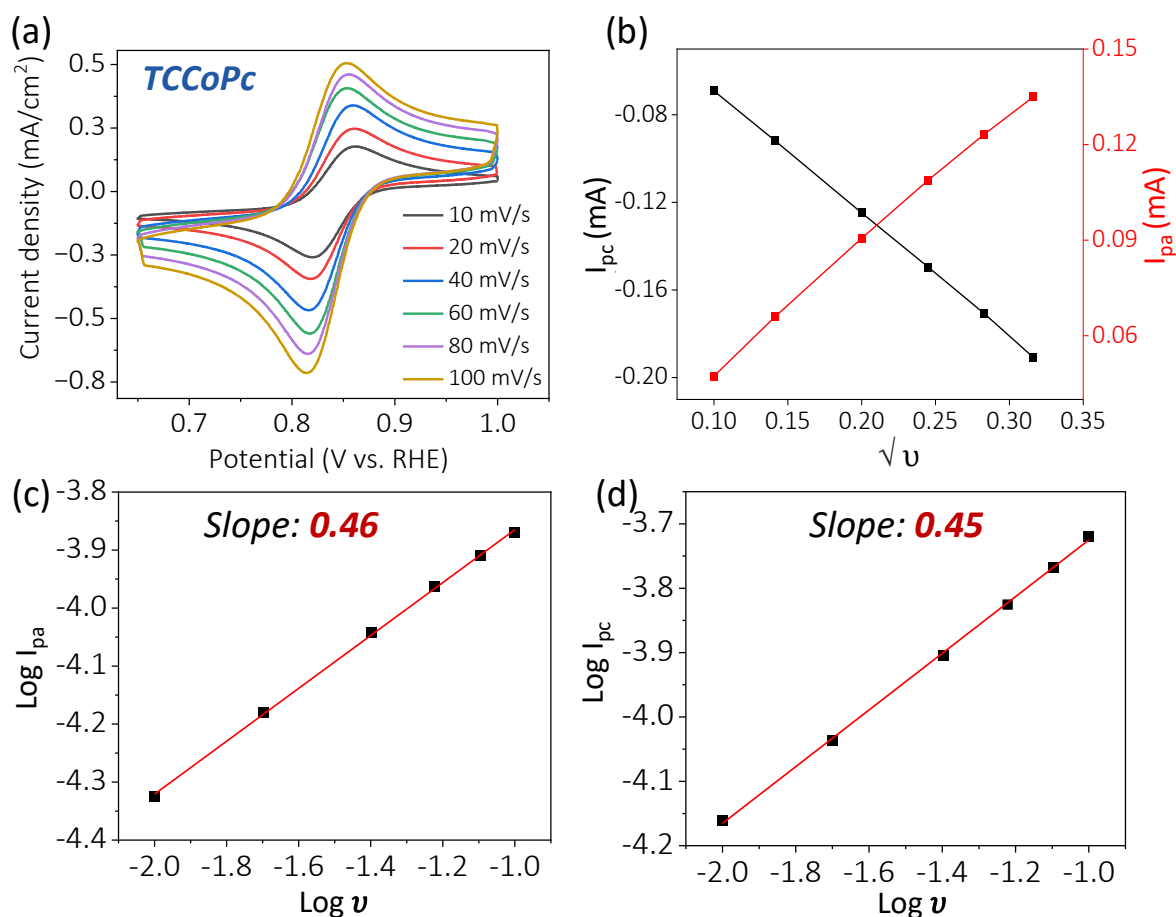

Figure 6.6. (a) Cyclic voltammograms (CVs) of carboxy substituted cobalt phthalocyanine (TCCoPc) molecule in 1 M KOH at various scan rates ranging from 10 mV/s to 100 mV/s. (b) Plot of cathodic peak current with square root of scan rate (black trace) and anodic peak current with square root of scan rate (red trace). (c) Plot of log anodic peak current with log scan rate and (d) plot of log cathodic peak current with log scan rate.

6.2.3. Hydrodynamic studies for oxygen reduction reaction (ORR).

In order to investigate the mechanistic pathway or the number of

electrons transferred during ORR, hydrodynamic voltametric technique like rotating disk electrode (RDE) and rotating ring disk electrode (RRDE) was utilised (please refer to chapter 2, section 2.8, pages 63-64 for details and calculations). For CoPc, a simultaneous increase in the ring current was observed along with the disk current on increasing the rotation rate (Figure 6.7a). The number of electrons was calculated to be 2 and the major product was found to be peroxide with a yield of ~80% which is in line with reported literatures (Figure 6.7b). However, in case of TCCoPc molecule, the number of electrons was found to be 1 (Figure 6.8).
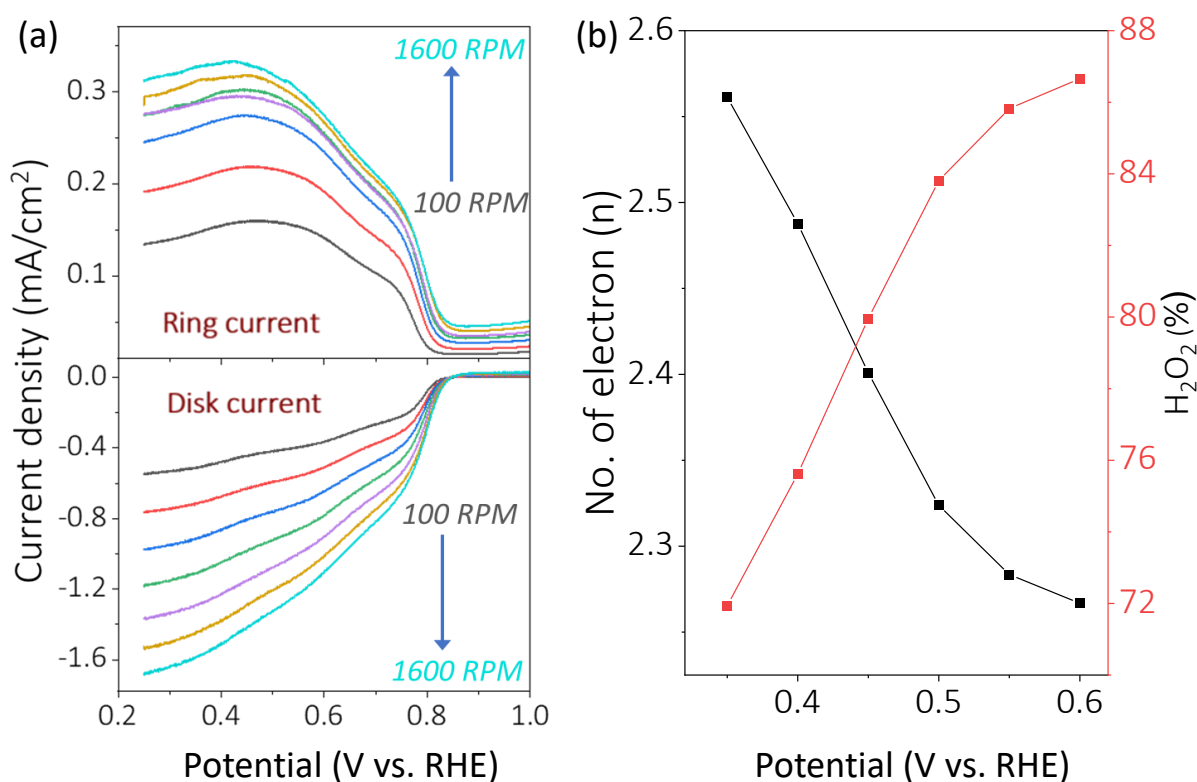
Figure 6.7. (a) RRDE measurement of CoPc molecule in 1 M KOH electrolyte at different rotation rates and (b) Plot showing number of electron and % of peroxide formed as a function of potential for CoPc molecule during ORR.
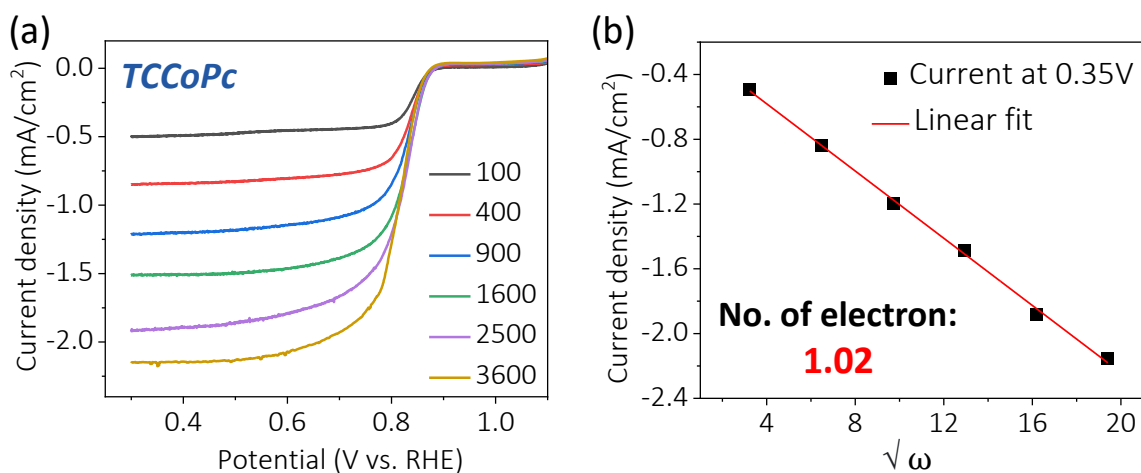
Figure 6.8. (a) RDE measurement of TCCoPc molecule in 1 M KOH electrolyte at different rotation rates ranging from 100 rpm to 3600 rpm. (b) Plot extracted with Levich equation demonstrating number of electrons transferred on TCCoPc during ORR.

6.2.4. Plausible mechanism of ORR.

The 1 electron ORR obtained in case of TCCoPc molecule indicates the ORR proceeds via formation of superoxide anion. The superoxide anion can quickly take one electron and get oxidised back to molecular oxygen as shown in equations 6.3 and 6.4 respectively.[54-57] This explains the reversible cyclic voltammogram obtained in case of TCCoPc molecule (Figure 6.9a).

$$O_2 + e^- \longrightarrow O_2^{\cdot -} \text{ (superoxide anion) } .... (6.3)$$

$$O_2^{\cdot -} \longrightarrow O_2 + e^- \qquad\qquad .... (6.4)$$

The formation of superoxide was further confirmed with a pH dependant study. It is known that superoxide anion is stable only in very high alkaline conditions (pH=14). All the electrochemical analyses in this chapter were performed in 1 M KOH solution which has a pH of 14. On decreasing the pH of the electrolyte from 14 to 12 the reversibility of the cyclic

voltammogram was lost (Figure 6.9b). This is mainly because at lower pH, superoxide is not stable and therefore it cannot be oxidised back to molecular oxygen.
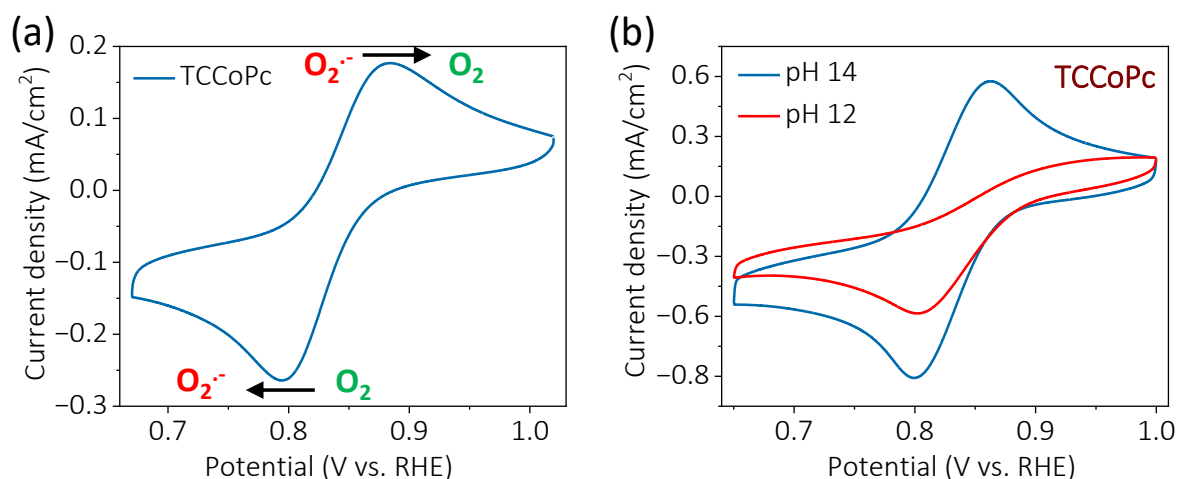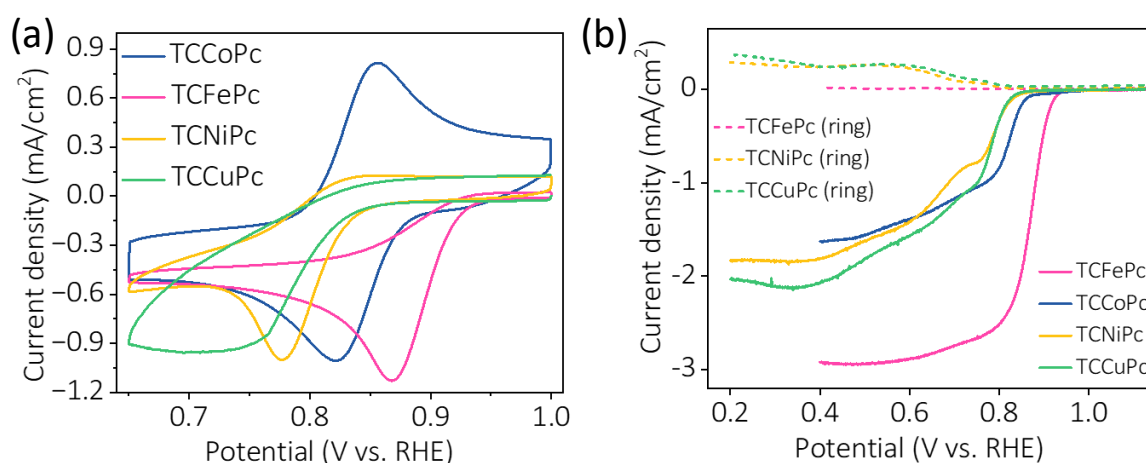

Figure 6.9. (a) Cyclic voltammograms of TCCoPc molecule in 1 M KOH at a scan rate of 10 mV/s indicating the reduction and oxidation peaks due to superoxide. (b) pH dependence study of TCCoPc molecule in O_2 purged 1 M KOH solution at a scan rate of 10 mV/s.

6.2.5. Electrochemical analysis of various metal carboxy phthalocyanines for ORR.

To further explore whether this unique behaviour of superoxide formation during ORR in alkaline medium is exclusively associated with the carboxy functionality or not, different carboxy substituted transition metal phthalocyanines namely the iron carboxy TCFePc, nickel carboxy TCNiPc and copper carboxy TCCuPc molecules were investigated. The cyclic voltammograms with all these metal carboxy phthalocyanines did not give any reversible oxidation peak unlike TCCoPc (Figure 6.10a). RRDE studies at a rotation rate of 1600 rpm demonstrated appreciable ring current in case

of TCNiPc and TCCuPc indicating they proceed via peroxide formation. For TCFePc no ring current was observed indicating it doesn't form peroxide and directly gives water as the final product (Figure 6.10b). The RRDE technique was used to check the number of electrons transferred during ORR for TCFePc, TCNiPc as well as TCCuPc. The data is given in Figure 6.11 and 6.12 respectively. The number of electrons and % of peroxide for all the three metal carboxy phthalocyanines were extracted from the data given in Figure 6.11 and 6.12. The number of electrons was found to be nearly 4 for TCFePc and the amount of peroxide formed was nearly zero indicating that it follows a 4-electron pathway forming water as the major product. For TCNiPc and TCCuPc the number of electrons came out to be nearly 3 for both the molecules which indicates ORR proceeds via an intermediary of peroxide and therefore the amount of peroxide formed was around 50 % for both the molecules (Figure 6.13).


Figure 6.10. (a) Comparison of cyclic voltammograms of TCFePc, TCCoPc, TCNiPc and TCCuPc for ORR in 1 M KOH at a scan rate of 10 mV/s. (b) RRDE study at a rotation rate of 1600 rpm with TCFePc, TCCoPc, TCNiPc and TCCuPc molecules.
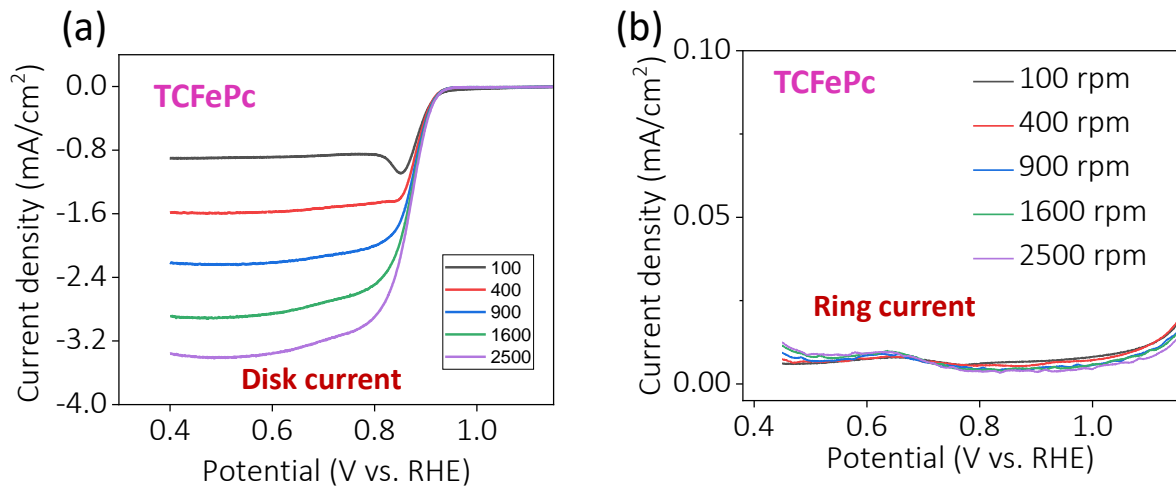
Figure 6.11. (a) Disk and (b) ring currents at various rotation rates from 100 rpm to 2500 rpm for TCFePc molecule.
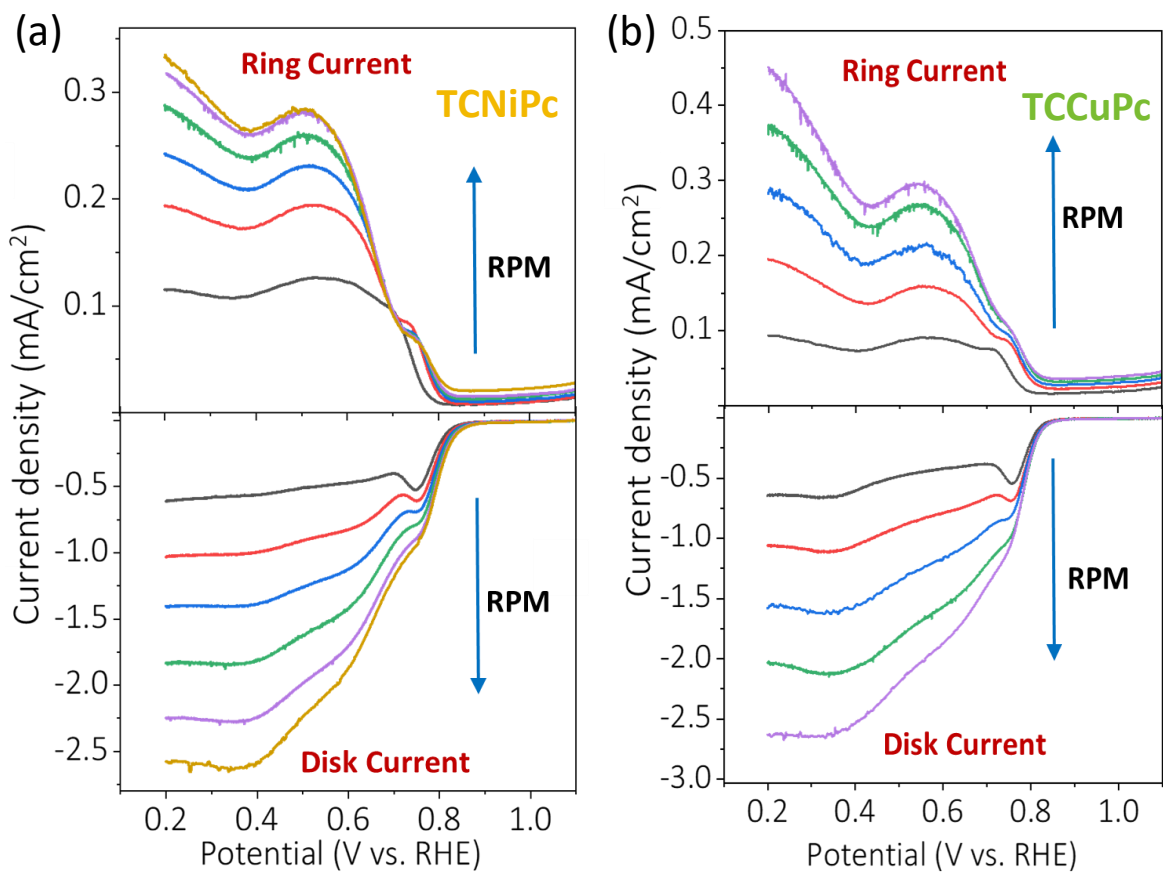
Figure 6.12. RRDE measurement of disk and ring currents at rotation rates 100 rpm to 3600 rpm towards ORR for (a) TCNiPc and (b) TCCuPc molecules.
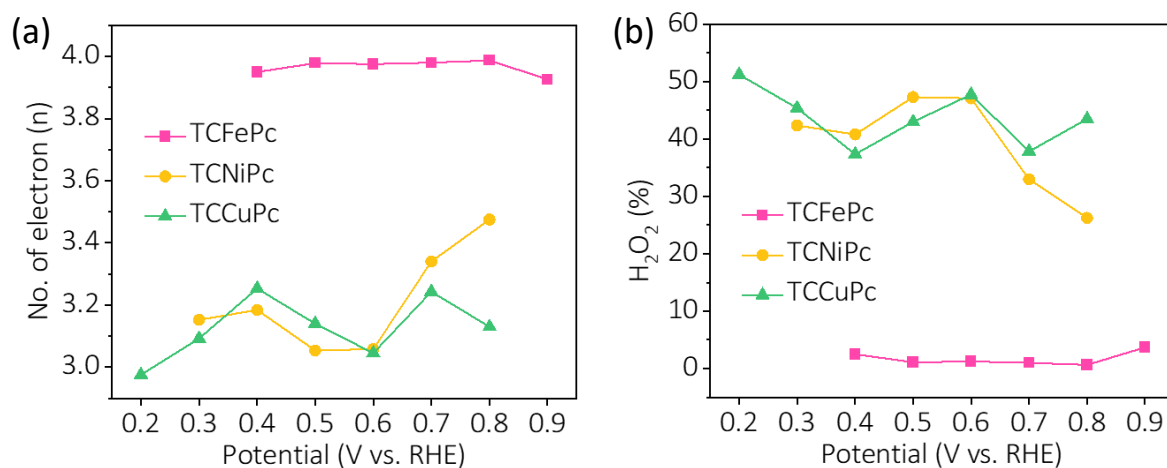
Figure 6.13. (a) Comparison of number of electrons transferred during ORR as a function of potentials for TCFePc, TCNiPc and TCCuPc molecules. (b) Comparison of % of peroxide produced as a function of potential for TCFePc, TCNiPc and TCCuPc molecules.

6.2.6. Plausible explanation for superoxide formation.

All the analyses indicate that the unique 1 electron ORR in aqueous medium is exclusive to the Co metal centre with carboxy ligand functionality. To understand the reason behind this, the binding of molecular oxygen with the metal centres have to be looked at. It is well established that O_2 binds in an end on mode with Co based phthalocyanine whereas it binds in a side on mode with iron based phthalocyanines [34,38,39,42-44] as demonstrated in Scheme 6.3. It is evident from the scheme that formation of superoxide is possible only in end on binding of oxygen as the side on binding will lead to breakage of the O-O bond. Thus, this points to the direction that superoxide formation is possible only with cobalt based phthalocyanines. However, unsubstituted cobalt phthalocyanine does not follow a 1 electron ORR and does not give rise to superoxide, and this result

Scheme 6.3. (a) Binding modes of molecular oxygen (O_2) in metal phthalocyanine complexes.
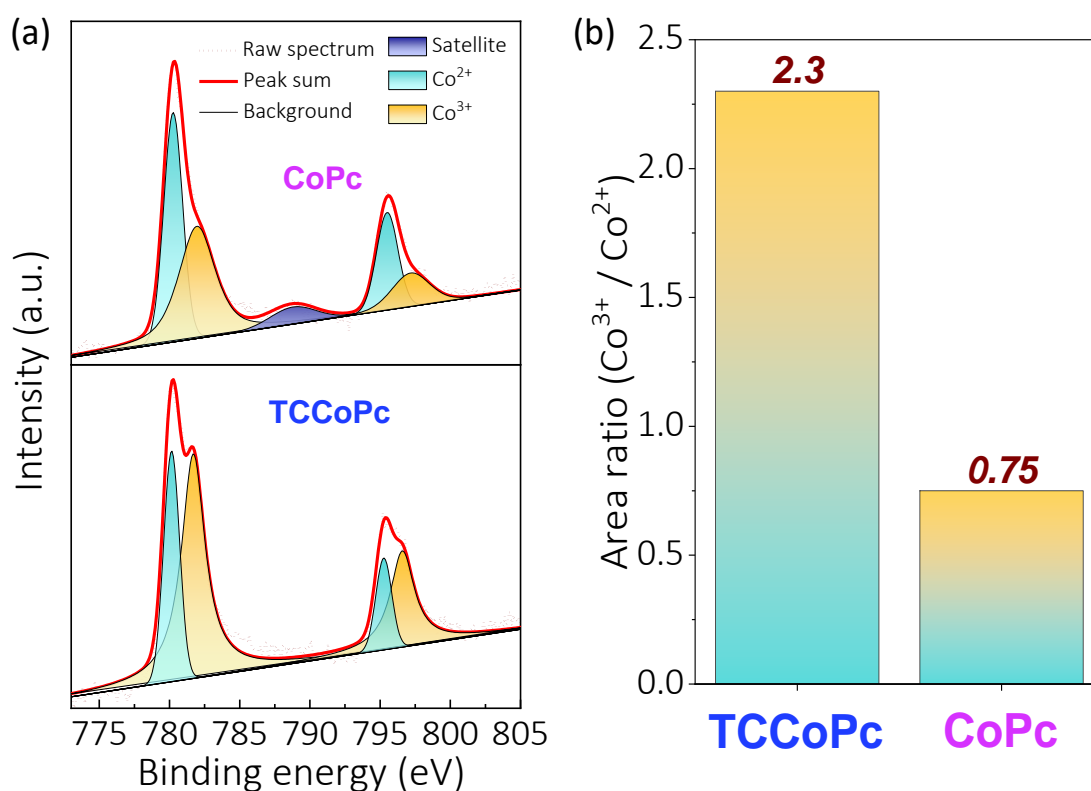
Figure 6.14. (a) Co 2p XPS spectra of CoPc and TCCoPc molecules and (b) area ratio of Co^{3+}/Co^{2+} species in both the molecules.

is obtained only with carboxy functionalised cobalt phthalocyanine. To understand the role of the carboxy functionality in case of cobalt phthalocyanine, XPS analysis of the pristine CoPc and TCCoPc molecules were performed (Figure 6.14). It was observed that the Co^{3+}/Co^{2+} ratio is

sharply altered when there is a -COOH functionality indicating an electron density modulation at the catalytic metal centre. The Raman spectra of alkali treated CoPc and TCCoPc molecules did not show much difference as demonstrated in Figure 6.15 indicating no such structural changes after alkali treatment. Therefore, the effect of the carboxy ligand in altering the electron density of the cobalt central metal together with the end on binding of dioxygen on cobalt may give rise to this unique 1 electron ORR in aqueous medium. To unambiguously verify this, theoretical investigation and in-situ spectro-electrochemical studies need to be performed.
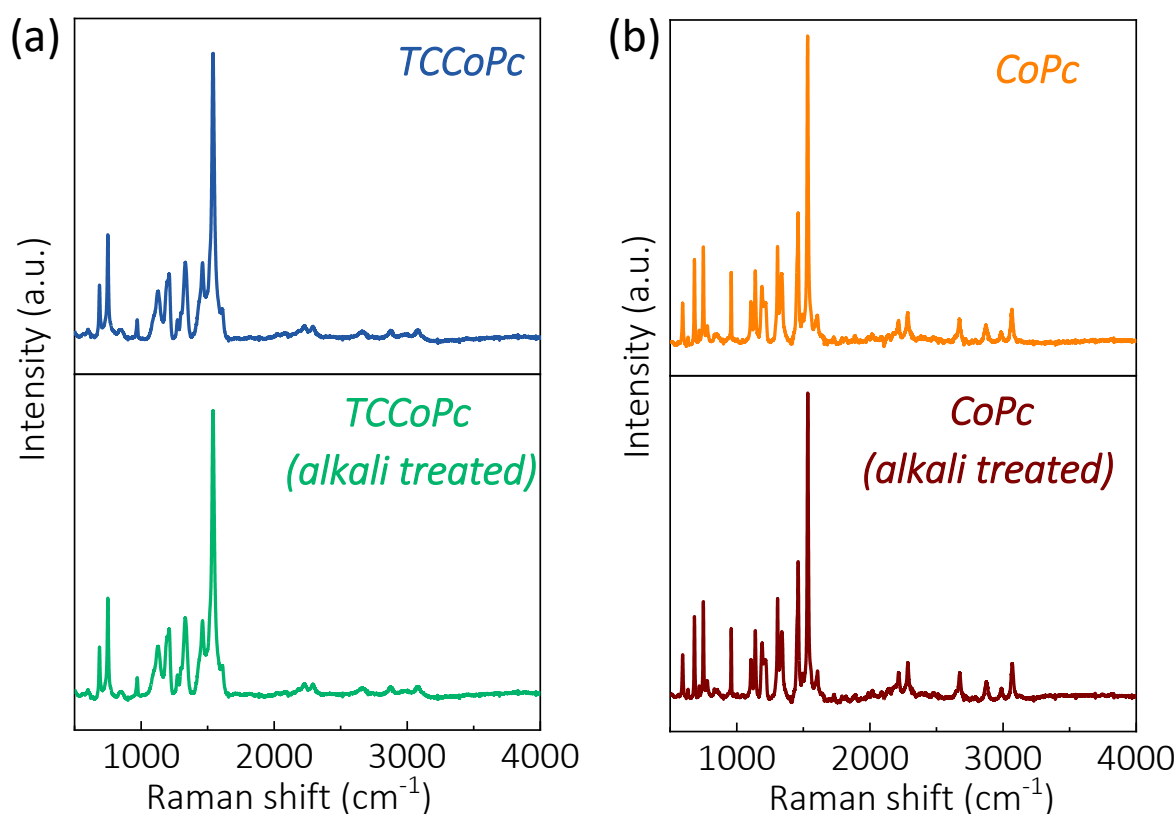
Figure 6.15. (a) Comparison of Raman spectra with and without alkali treatment for (a) TCCoPc and (b) CoPc molecules respectively.

6.3. Conclusion:

This chapter elucidates the role of ligand functionality in altering the reaction mechanism in oxygen reduction reaction. With the carboxy functionalized cobalt phthalocyanine, a unique 1 electron ORR was observed in aqueous medium. Comparative study with other carboxy substituted metal phthlocyanines led to the observation that this behaviour is exclusive to the cobalt central metal ion and the carboxy ligand. Various electrochemical analyses suggest the formation of superoxide during ORR in aqueous medium with TCCoPc molecule. However, the specific reason behind this unique outcome remains still unclear and further studies including ttheoretical investigations as well as in-situ analysis are required to explain the actual reason behind this result.

6.4. References:

[1] Bidault, F.; Brett, D. J. L.; Middleton, P. H.; Brandon, N. P. Review of Gas Diffusion Cathodes for Alkaline Fuel Cells. *J. Power Sources* **2009**, *187* (1), 39–48.

[2] Park, J. S.; Park, S. H.; Yim, S. D.; Yoon, Y. G.; Lee, W. Y.; Kim, C. S. Performance of Solid Alkaline Fuel Cells Employing Anion-Exchange Membranes. *J. Power Sources* **2008**, *178* (2), 620–626.

[3] Asazawa, K.; Yamada, K.; Tanaka, H.; Oka, A.; Taniguchi, M.; Kobayashi, T. A Platinum-Free Zero-Carbon-Emission Easy Fuelling Direct Hydrazine Fuel Cell for Vehicles. *Angew. Chemie* **2007**, *119* (42), 8170–8173.

[4] Kuttiyiel, K. A.; Sasaki, K.; Choi, Y.; Su, D.; Liu, P.; Adzic, R. R. Bimetallic IrNi Core Platinum Monolayer Shell Electrocatalysts for the

Oxygen Reduction Reaction. *Energy Environ. Sci.* **2012**, *5* (1), 5297–5304.

[5]   Xu, H.; Fu, Q.; Yao, Y.; Bao, X. Highly Active Pt-Fe Bicomponent Catalysts for CO Oxidation in the Presence and Absence of H_2. *Energy Environ. Sci.* **2012**, *5* (4), 6313–6320.

[6]   Oezaslan, M.; Hasché, F.; Strasser, P. $PtCu_3$, PtCu and Pt_3Cu Alloy Nanoparticle Electrocatalysts for Oxygen Reduction Reaction in Alkaline and Acidic Media. *J. Electrochem. Soc.* **2012**, *159* (4), B444–B454.

[7]   Park, H. W.; Lee, D. U.; Nazar, L. F.; Chen, Z. Oxygen Reduction Reaction Using MnO_2 Nanotubes/Nitrogen-Doped Exfoliated Graphene Hybrid Catalyst for $Li-O_2$ Battery Applications. *J. Electrochem. Soc.* **2013**, *160* (2), A344–A350.

[8]   Lee, D. U.; Park, H. W.; Higgins, D.; Nazar, L.; Chen, Z. Highly Active Graphene Nanosheets Prepared via Extremely Rapid Heating as Efficient Zinc-Air Battery Electrode Material. *J. Electrochem. Soc.* **2013**, *160* (9), F910–F915.

[9]   Zhang, H.; Zhong, X.; Shaw, J. C.; Liu, L.; Huang, Y.; Duan, X. Very High Energy Density Silicide-Air Primary Batteries. *Energy Environ. Sci.* **2013**, *6* (9), 2621–2625.

[10]   Shui, J. L.; Okasinski, J. S.; Kenesei, P.; Dobbs, H. A.; Zhao, D.; Almer, J. D.; Liu, D. J. Reversibility of Anodic Lithium in Rechargeable Lithium-Oxygen Batteries. *Nat. Commun.* **2013**, *4*, 1–7.

[11]   Chen, Z.; Higgins, D.; Chen, Z.; Lee, D. U. Activated and Nitrogen-Doped Exfoliated Graphene as Air Electrodes for Metal-Air Battery Applications. *J. Mater. Chem. A* **2013**, *1* (7), 2639–2645.

[12]   Wan, X.; Liu, X.; Li, Y.; Yu, R.; Zheng, L.; Yan, W.; Wang, H.; Xu, M.; Shui, J. Fe- N-C Electrocatalyst with Dense Active Sites and Efficient Mass Transport for High- Performance Proton Exchange Membrane Fuel Cells. *Nat. Catal.* **2019**, *2* (3), 259- 268.

[13]   Sorokin, A. B. Phthalocyanine Metal Complexes in Catalysis BT - Chemical Reviews. *Chem. Rev.* **2013**, *113* (10), 8152-8191.

[14] Sobbi, A. K.; Wöhrie, D.; Schlettwein, D. Photochemical Stability of Various Porphyrins in Solution and as Thin Film Electrodes. *J. Chem. Soc. Perkin Trans. 2* **1993**, *3*, 481-488.

[15] Rigsby, M. L.; Wasylenko, D. J.; Pegis, M. L.; Mayer, J. M. Medium Effects Are as Important as Catalyst Design for Selectivity in Electrocatalytic Oxygen Reduction by Iron-Porphyrin Complexes. *J. Am. Chem. Soc.* **2015**, *137* (13), 4296-4299.

[16] Bottari, G.; de la Torre, G.; Guldi, D. M.; Torres, T. Covalent and Noncovalent Phthalocyanine-Carbon Nanostructure Systems: Synthesis, Photoinduced Electron Transfer, and Application to Molecular Photovoltaics. *Chem. Rev.* **2010**, *110* (11), 6768-6816.

[17] Jasinski, R. A New Fuel Cell Cathode Catalyst. *Nature* **1964**, *201* (4925), 1212–1213.

[18] Jahnke, H.; Schonborn, M.; Zimmermann, G. Organic dyestuffs as catalysts for fuel cells. Top Curr Chem. **1976,** *61,* 133–181.

[19] Randin, J. P. Interpretation of the relative electrochemical activity of various metal phthalocyanines for the oxygen reduction reaction. *Electrochim. Acta* **1974,** *19,* 83–85.

[20] Zagal, J. H.; Sen, R. K.; Yeager, E. Oxygen reduction by Co (II) tetrasulfonatephthalocyanine irreversibly adsorbed on a stress-annealed pyrolytic graphite electrode surface. *J. Electroanal. Chem,* **1977,** *83,* 207–213.

[21] Zagal, J.; Bindra, P.; Yeager, E. A mechanistic study of O_2 reduction on water soluble phthalocyanines adsorbed on graphite electrodes. *J. Electrochem. Soc,* **1980,** *127,* 1506–1517.

[22] Van den Brink, F.; Visscher, W.; Barendrecht, E. Electrode catalysis of cathodic oxygen reduction by metal phthalocyanines—Part I. Introduction, cobalt phthalocyanine as electrocatalyst: experimental part. *J. Electroanal. Chem,* **1983,** *157,* 283–304.

[23] Van den Brink, F.; Visscher, W.; Barendrecht, E. Electrode catalysis of cathodic oxygen reduction by metal phthalocyanines—Part III. Iron phthalocyanine as electrocatalyst: experimental part. *J. Electroanal. Chem,* **1984,** *172,* 301–325.

[24] Zagal, J. H.; Paez, M.; Sturm, J.; Ureta-zanartu, S. Electroreduction of oxygen on mixtures of phthalocyanines co-adsorbed on a graphite electrode. *J. Electroanal. Chem,* **1984,** *181*, 295–300.

[25] Elzing, A.; Van der Putten, A.; Visscher, W.; Barendrecht, E.; The cathodic reduction of oxygen at cobalt phthalocyanine—influence of electrode preparation on electrode catalysis. *J. Electroanal. Chem,* **1986,** *200*, 313–322.

[26] Van der Putten, A.; Elzing, A.; Visscher, W.; Barendrecht, E. Oxygen reduction on vacuum-deposited and adsorbed transition-metal phthalocyanine films. *J. Electroanal. Chem*, **1986,** *214*, 523–533.

[27] Janda, P.; Kobayashi, N.; Auburn, P. R.; Lam, H.; Leznoff, C. C.; Lever, ABP. Dioxygen reduction at a graphite electrode modified by mononuclear tetraneopentoxyphthalocyaninatocobalt(II) and related polynuclear species. *Can. J. Chem,* **1989,** *67*, 1109–1119.

[28] Jiang, R.; Dong, S. Research on chemically modified electrodes—catalytic reduction of dioxygen at a cobalt phthalocyanine-doped polyaniline film electrode. *J. Electroanal. Chem,* **1988,** *246*, 101–117.

[29] Zagal, J. H. *Macrocycles, In Handbook of Fuel Cells Fundamentals, Technology and Applications*, John Wiley & Sons, Ltd.: Chichester, **2003**, *Vol. 2, Part 5*, 544.

[30] Zagal, J. H. Metallophthalocyanines as Catalysts in Electrochemical Reactions. *Coord. Chem. Rev.* **1992**, *119* (C), 89–136.

[31] Masa, J.; Ozoemena, K.; Schuhmann, W.; Zagal, J. H. Oxygen Reduction Reaction Using N_4-Metallomacrocyclic Catalysts: Fundamentals on Rational Catalyst Design. *J. Porphyr. Phthalocyanines* **2012**, *16* (7–8), 761–784.

[32] Jiang, Y.; Lu, Y.; Lv, X.; Han, D.; Zhang, Q.; Niu, L.; Chen, W. Enhanced Catalytic Performance of Pt-Free Iron Phthalocyanine by Graphene Support for Efficient Oxygen Reduction Reaction. *ACS Catal.* **2013**, *3* (6), 1263–1271.

[33] Cao, R.; Thapa, R.; Kim, H.; Xu, X.; Kim, M. G.; Li, Q.; Park, N.; Liu, M.; Cho, J. Promotion of Oxygen Reduction by a Bio-Inspired Tethered Iron

Phthalocyanine Carbon Nanotube-Based Catalyst. *Nat. Commun.* **2013**, *4*, 2076.

[34]   Zagal, J. H.; Griveau, S.; Silva, J. F.; Nyokong, T.; Bedioui, F. Metallophthalocynine-based molecular materials as catalysts for electrochemical reactions. *Coord. Chem. Rev.* **2010,** *254*, 2755–2791.

[35]   Van der Putten, A.; Elzing, A.; Visscher, W.; Barendrecht, E. Redox potential and electrocatalysis of O_2 reduction on transition metal chelates. *J. Electroanal. Chem.* **1987,** *221*, 95–104.

[36]   Vasudevan, P.; Santosh Mann, N.; Tyagi, S. Transition metal complexes of porphyrins and phthalocyanines as electrocatalysts for dioxygen reduction. *Transition Met Chem*, **1990,** *15*, 81–90.

[37]   Van den Brink, F.; Barendrecht, E.; Visscher, W. The cathodic reduction of oxygen—a review with emphasis on macrocyclic organic metal complexes as electrocatalysts. *Recl. Trav. Chim. Pays-B,* **1980,** *99*, 253–262.

[38]   Zagal, J.; Paez, M.; Tanaka, A. A.; dos Santos, J. R.; Linkous, C. A. Electrocatalytic activity of metal phthalocyanines for oxygen reduction. *J. Electroanal. Chem.* **1992,** *339*, 13–30.

[39]   Chen, R.; Li, H.; Chu, D.; Wang, G. Unraveling oxygen reduction reaction mechanisms on carbon-supported Fe-phthalocyanine and Co-phthalocyanine catalysts in alkaline solutions. *J. Phys Chem C,* **2009,** *113*, 20689–20697.

[40]   Honda, T.; Kojima, T.; Fukuzumi, S. Proton-coupled electron-transfer reduction of dioxygen catalysed by a saddle-distorted cobalt phthalocyanine. *J. Am Chem Soc.* **2012,** *134*, 4196–4206.

[41]   Wang, G.; Ramesh, N.; Hsu, A.; Chu, D.; Chen, R. Density functional theory study of the adsorption of oxygen molecule on iron phthalocyanine and cobalt phthalocyanine. *Mol. Simulat.* **2008,** *34*, 1051–1056.

[42]   Shi, Z.; Zhang, J. Density functional theory study of transitional metal macrocyclic complexes' dioxygen-binding abilities and their catalytic activities toward oxygen reduction reaction. *J. Phys Chem C,* **2007**, *111*, 7084.

[43] Sun, S.; Jiang, N.; Xia, D.; Density functional theory study of the oxygen reduction reaction on metalloporphyrins and metallophthalocyanines. *J. Phys Chem C*, **2011,** *115*, 9511–9517.

[44] He, H.; Lei, Y.; Xiao, C.; Chu, D.; Chen, R.; Wang, G. Molecular and electronic structures of transition-metal macrocyclic complexes as related to catalysing oxygen reduction reactions: a density functional theory study. *J. Phys Chem C*, **2012,** *116*, 16038–16046.

[45] Mugadza, T.; Nyokong, T. Electrochemical, Microscopic and Spectroscopic Characterization of Benzene Diamine Functionalized Single Walled Carbon Nanotube-Cobalt (II) Tetracarboxy-Phthalocyanine Conjugates. *J. Colloid Interface Sci.* **2011**, *354* (2), 437–447.

[46] Mounesh; Malathesh, P.; Praveen Kumara, N. Y.; Jilani, B. S.; Mruthyunjayachari, C. D.; Venugopala Reddy, K. R. Synthesis and Characterization of Tetra-Ganciclovir Cobalt (II) Phthalocyanine for Electroanalytical Applications of AA/DA/UA. *Heliyon* **2019**, *5* (7), e01946.

[47] Mohammed, I.; Nemakal, M.; Aralekallu, S.; Sajjan, V. A.; Divakara, T. R.; Palanna, M.; Keshavananda Prabu, C. P.; Sannegowda, L. K. Phthalocyanine Sheet Polymer Based Amperometric Sensor for the Selective Detection of 2,4-Dichlorophenol. *J. Electroanal. Chem.* **2020**, *871*, 114292.

[48] Sun, X.; Wang, L.; Tan, Z. Improved Synthesis of Soluble Metal-Free/Metal Phthalocyanine Tetracarboxylic Acids and Their Application in the Catalytic Epoxidation of Cyclohexene. *Catal. Letters* **2015**, *145* (4), 1094–1102.

[49] Achar, B. N.; Fohlen, G. M.; Parker, J. A.; Keshavayya, J. Preparation & Structural Investigations of Copper (II), Cobalt (II), Nickel (II) & Zinc (II) Derivatives of 2,9,16,23-Phthalocyanine Tetracarboxylic Acid. *Indian J. Chem.* **1988**, *27*, 411–416.

[50] Jiang, W.; Wang, T.; Chen, X.; Li, B.; Zeng, M.; Hu, N.; Su, Y.; Zhou, Z.; Zhang, Y.; Yang, Z. Enhancing Room-Temperature NO_2 detection of

Cobalt Phthalocyanine Based Gas Sensor at an Ultralow Laser Exposure. *Phys. Chem. Chem. Phys.* **2020**, *22* (33), 18499–18506.

[51] Abbaspour, A.; Mirahmadi, E. Electrocatalytic Activity of Iron and Nickel Phthalocyanines Supported on Multi-Walled Carbon Nanotubes towards Oxygen Evolution Reaction. *Electrochim. Acta* **2013**, *105*, 92–98.

[52] Zhu, J.; Li, Y.; Chen, Y.; Wang, J.; Zhang, B.; Zhang, J.; Blau, W. J. Graphene Oxide Covalently Functionalized with Zinc Phthalocyanine for Broadband Optical Limiting. *Carbon N. Y.* **2011**, *49* (6), 1900–1905.

[53] Kumar, A.; Prajapati, P. K.; Aathira, M. S.; Bansiwal, A.; Boukherroub, R.; Jain, S. L. Highly Improved Photoreduction of Carbon Dioxide to Methanol Using Cobalt Phthalocyanine Grafted to Graphitic Carbon Nitride as Photocatalyst under Visible Light Irradiation. *J. Colloid Interface Sci.* **2019**, *543*, 201–213.

[54] Lee-Ruff, E. The Organic Chemistry of Superoxide. *Chem. Soc. Rev.* **1977**, *6* (2), 195–214.

[55] Hayyan, M.; Hashim, M. A.; AlNashef, I. M. Superoxide Ion: Generation and Chemical Implications. *Chem. Rev.* **2016**, *116* (5), 3029–3085.

[56] Divišek, J.; Kastening, B. Electrochemical Generation and Reactivity of the Superoxide Ion in Aqueous Solutions. *J. Electroanal. Chem. Interfacial Electrochem.* **1975**, *65* (2), 603–621.

[57] Stoin, U.; Shames, A. I.; Malka, I.; Bar, I.; Sasson, Y. In Situ Generation of Superoxide Anion Radical in Aqueous Medium under Ambient Conditions. *ChemPhysChem* **2013**, *14* (18), 4158–4164.
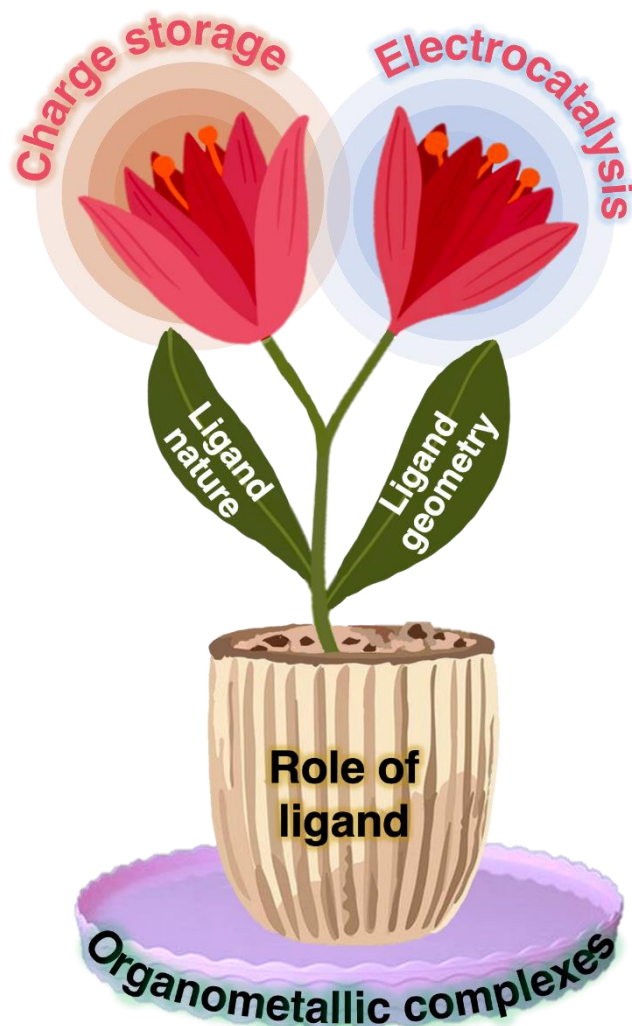
Chapter 7

Summary

Chapter 7

Summary of the thesis entitled "Ligand assisted molecular electrocatalysis and molecular charge storage"

This Chapter summarizes the work with a future outlook. The work presented in this thesis reveals the importance of ligand in the field of electrocatalysis as well as charge storage in molecular systems. While the central metal ion significantly influences electrocatalysis and charge storage, the ligand-induced contribution provides a distinctive avenue to exploit the molecule's maximum potential for complex electrochemical transformations and charge storage applications. Moreover, the structure-activity relations of molecules remain incomplete without considering the role of the ligand, as demonstrated by its significant impact. It is imperative to emphasize that this phenomenon lacks generalizability across the spectrochemical series, as the correlation is distinct for each substituent. This underscores the necessity for meticulous investigations at the molecular level for individual substituents to comprehend their specific activity or charge storage relationships. This is principally due to non-electrochemical interactions frequently intertwining the molecule's electrochemical properties with the nature of the functionality as well as its surrounding medium, as elucidated in this thesis. These interactions typically manifest as substituent-specific, presenting a myriad of prospects for researchers within the molecular electrocatalysis and charge storage domain. The elucidation of metal-ligand activity relationships, in tandem with the influence of the surrounding medium, within N_4-macrocyclic molecules, is expected to remedy deficiencies and knowledge gaps in their

structure-activity correlations. This contribution is expected to notably propel the evolution of next-generation electrodes applicable to electrocatalysis and energy storage and conversion devices.

The role of ligand in molecular electrocatalysis and

charge storage

List of Publications

❖ **Included in this thesis**

[1] **Mukhopadhyay, S.**; Kottaichamy, A. R.; Devendrachari, M. C.; Mendhe, R. M.; Nimbegondi Kotresh, H. M.; Vinod, C. P.; Thotiyl, M. O. Electrochemical energy storage in organic supercapacitor via a non-electrochemical proton charge assembly. *Chem. Sci.* **2024**, *15*, 1726–1735.

[2] **Mukhopadhyay, S.**; Kottaichamy, A. R.; Chame, P. V.; Ghosh, P.; Vinod, C. P.; Makri Nimbegondi Kotresh, H.; Kanade, S. C.; Thotiyl, M. O. Unusual Ligand Assistance in Molecular Electrocatalysis via Interfacial Proton Charge Assembly. *J. Phys. Chem. Lett.* **2023**, *14* (23), 5377–5385.

[3] **Mukhopadhyay, S.**; Devendrachari, M. C.; Kanade, S. C.; Vinod, C. P.; Nimbegondi Kotresh, H. M.; Thotiyl, M. O. Regio-Isomerism Directed Electrocatalysis for Energy Efficient Zinc-Air Battery. *iScience* **2022**, *25* (10), 105179.

[4] **Mukhopadhyay, S.**; Kottaichamy, A. R.; Bhat, Z. M.; Dargily, N. C.; Thotiyl, M. O. Isomerism-Activity Relation in Molecular Electrocatalysis: A Perspective. *Electroanalysis* **2020**, *32* (11), 2387–2392.

❖ **Not included in the thesis**

[5] Dhakar, S.; **Mukhopadhyay, S.**; Ottakam Thotiyl, M.; Sharma, S. Methanol Assisted Water Electrooxidation on Noble Metal Free Perovskite: RRDE Insight into the Catalyst's Behaviour. *J. Colloid Interface Sci.* **2024**, *654*, 688–697.

[6]   Sur, S.; Mondal, R.; Thimmappa, R.; **Mukhopadhyay, S.**; Thotiyl, M. O. Aqueous OH−/H+ Dual-Ion Gradient Assisted Electricity Effective Electro-Organic Synthesis of 2,5-Furandicarboxylic Acid Paired with Hydrogen Fuel Generation. *J. Colloid Interface Sci.* **2023**, *630*, 477–483.

[7]   Sur, S.; Thimmappa, R.; Manzoor Bhat, Z.; Dargily, N. C.; **Mukhopadhyay, S.**; Liu, X.; Cai, P.; Wen, Z.; Thotiyl, M. O. Hybrid Alkali-Salt-Acid Electrochemical Device for Electricity-Efficient Desalination and H2Generation. *ACS Sustain. Chem. Eng.* **2022**, *10* (33), 10781–10788.

[8]   Aralekallu, S.; Thimmappa, R.; Bhat, Z. M.; Devendrachari, M. C.; Dargily, N. C.; **Mukhopadhyay, S.**; Kottaichamy, A. R.; Thotiyl, M. O. Wireless Chemical Charging of a Metal-Ion Battery by Magnetic Particles. *ACS Sustain. Chem. Eng.* **2022**, *10* (1), 259–266.

[9]   Thimmappa, R.; Gautam, M.; Bhat, Z. M.; Thodika, A. R. A.; Devendrachari, M. C.; **Mukhopadhyay, S.**; Dargily, N. C.; Thotiyl, M. O. An Atmospheric Water Electrolyzer for Decentralized Green Hydrogen Production. *Cell Reports Phys. Sci.* **2021**, *2* (11), 100627.

Rights & Permissions

Isomerism-Activity Relation in Molecular Electrocatalysis: A Perspective
Author: Musthafa Ottakam Thotiyl, Neethu Christudas Dargily, Zahid Manzoor Bhat, et al
Publication: Electroanalysis
Publisher: John Wiley and Sons
Date: Sep 28, 2020

© 2020 Wiley-VCH GmbH

Order Completed

Thank you for your order.

This Agreement between Ms. Sanchayita Mukhopadhyay ("You") and John Wiley and Sons ("John Wiley and Sons") consists of your license details and the terms and conditions provided by John Wiley and Sons and Copyright Clearance Center.

Your confirmation email will contain your order number for future reference.

License Number	5698700643124	🖶 Printable Details
License date	Dec 30, 2023	

📄 Licensed Content

Licensed Content Publisher	John Wiley and Sons
Licensed Content Publication	Electroanalysis
Licensed Content Title	Isomerism-Activity Relation in Molecular Electrocatalysis: A Perspective
Licensed Content Author	Musthafa Ottakam Thotiyl, Neethu Christudas Dargily, Zahid Manzoor Bhat, et al
Licensed Content Date	Sep 28, 2020
Licensed Content Volume	32
Licensed Content Issue	11
Licensed Content Pages	6

🗐 Order Details

Type of use	Dissertation/Thesis
Requestor type	Author of this Wiley article
Format	Print and electronic
Portion	Full article
Will you be translating?	No

📄 About Your Work

Title of new work	PhD student
Institution name	IISER Pune
Expected presentation date	Apr 2024

📁 Additional Data

📍 Requestor Location

Requestor Location	Ms. Sanchayita Mukhopadhyay
	Lab: C-302, Chemistry wing
	Main building
	Pune, Maharashtra 411008
	India
	Attn: Indian Institute of Science Education and Research, Pune

📄 Tax Details

Publisher Tax ID	EU826007151